NATIONAL AERONAUTICS AND SPACE ADMINISTRATION

Space Programs Summary 37-60, Vol. II

The Deep Space Network

For the Period September 1 to October 31, 1969

JET PROPULSION LABORATORY
CALIFORNIA INSTITUTE OF TECHNOLOGY
PASADENA, CALIFORNIA

November 30, 1969

NATIONAL AERONAUTICS AND SPACE ADMINISTRATION

Space Programs Summary 37-60, Vol. II

The Deep Space Network

For the Period September 1 to October 31, 1969

JET PROPULSION LABORATORY
CALIFORNIA INSTITUTE OF TECHNOLOGY
PASADENA, CALIFORNIA

November 30, 1969

SPACE PROGRAMS SUMMARY 37-60, VOL. II

Preface

The Space Programs Summary is a multivolume, bimonthly publication that presents a review of technical information resulting from current engineering and scientific work performed, or managed, by the Jet Propulsion Laboratory for the National Aeronautics and Space Administration. The Space Programs Summary is currently composed of four volumes:

Vol. I. *Flight Projects* (Unclassified)

Vol. II. *The Deep Space Network* (Unclassified)

Vol. III. *Supporting Research and Advanced Development* (Unclassified)

Vol. IV. *Flight Projects and Supporting Research and Advanced Development* (Confidential)

Foreword

Volume II of the Space Programs Summary reports the results of work performed by the Deep Space Network (DSN). Information is presented, as appropriate, in the following categories:

Introduction
   Description of the DSN
   Description of DSN Systems

Mission Support
   Interplanetary Flight Projects
   Planetary Flight Projects
   Manned Space Flight Project
   Advanced Flight Projects

Advanced Engineering
   Tracking and Navigational Accuracy Analysis
   Communications Systems Research
   Communications Elements Research
   Supporting Research and Technology

Development and Implementation
   Space Flight Operations Facility Development
   Ground Communications Facility Development
   Deep Space Instrumentation Facility Development
   DSN Project and System Development

Operations and Facilities
   DSN Operations
   Space Flight Operations Facility Operations
   Ground Communications Facility Operations
   Deep Space Instrumentation Facility Operations
   Facility Engineering

In each issue, the section entitled "Description of DSN Systems" reports the current configuration of one of the six DSN systems (tracking, telemetry, command, monitoring, simulation, and operations control). The fundamental research carried out in support of the DSN is reported in Vol. III.

Contents

Contents (contd)

Contents (contd)

Contents (contd)

I. Introduction

A. Description of the DSN

The Deep Space Network (DSN), established by the NASA Office of Tracking and Data Acquisition under the system management and technical direction of JPL, is designed for two-way communications with unmanned spacecraft traveling approximately 10,000 mi from earth to planetary distances. It supports, or has supported, the following NASA deep space exploration projects: *Ranger*, *Surveyor*, *Mariner* Venus 1962, *Mariner* Mars 1964, *Mariner* Venus 67, *Mariner* Mars 1969, *Mariner* Mars 1971 (JPL); *Lunar Orbiter* and *Viking* (Langley Research Center); *Pioneer* (Ames Research Center); *Helios* (West Germany); and *Apollo* (Manned Spacecraft Center), to supplement the Manned Space Flight Network (MSFN).

The DSN is distinct from other NASA networks such as the MSFN, which has primary responsibility for tracking the manned spacecraft of the *Apollo* Project, and the Space Tracking and Data Acquisition Network (STADAN), which tracks earth-orbiting scientific and communications satellites. With no future unmanned lunar spacecraft presently planned, the primary objective of the DSN is to continue its support of planetary and interplanetary flight projects.

To support flight projects, the DSN simultaneously performs advanced engineering on components and systems, integrates proven equipment and methods into the network,[1] and provides direct support of each project through that project's Tracking and Data System. This management element and the project's Mission Operations personnel are responsible for the design and operation of the data, software, and operations systems required for the conduct of flight operations. The organization and procedures necessary to carry out these activities are described in SPS 37-50, Vol. II, pp. 15–17.

By tracking the spacecraft, the DSN is involved in the following data types:

(1) *Metric:* generate angles, one- and two-way doppler, and range.

(2) *Telemetry:* receive, record, and retransmit engineering and scientific data.

---

[1] When a new piece of equipment or new method has been accepted for integration into the network, it is classed as Goldstone duplicate standard (GSDS), thus standardizing the design and operation of identical items throughout the network.

(3) *Command:* send coded signals to the spacecraft to activate equipment to initiate spacecraft functions.

The DSN operation is characterized by six DSN systems: (1) tracking, (2) telemetry, (3) command, (4) monitoring, (5) simulation, and (6) operations control.

The DSN can be characterized as being comprised of three facilities: the Deep Space Instrumentation Facility (DSIF), the Ground Communications Facility (GCF), and the Space Flight Operations Facility (SFOF).

1. Deep Space Instrumentation Facility

a. Tracking and data acquisition facilities. A worldwide set of deep space stations (DSSs) with large antennas, low-noise phase-lock receiving systems, and high-power transmitters provide radio communications with spacecraft. The DSSs and the deep space communications complexes (DSCCs) they comprise are given in Table 1.

Radio contact with a spacecraft usually begins when the spacecraft is on the launch vehicle at Cape Kennedy, and it is maintained throughout the mission. The early part of the trajectory is covered by selected network stations of the Air Force Eastern Test Range (AFETR) and the MSFN of the Goddard Space Flight Center.[2] Nor-

---

[2]The 30-ft-diam-antenna station established by the DSN on Ascension Island during 1965 to act in conjunction with the MSFN orbital support 30-ft-diam-antenna station was transferred to the MSFN in July 1968.

mally, two-way communications are established between the spacecraft and the DSN within 30 min after the spacecraft has been injected into lunar, planetary, or interplanetary flight. A compatibility test station at Cape Kennedy (discussed later) monitors the spacecraft continuously during the launch phase until it passes over the local horizon. The deep space phase begins with acquisition by either DSS 51, 41, or 42. These and the remaining DSSs given in Table 1 provide radio communications to the end of the flight.

To enable continuous radio contact with spacecraft, the DSSs are located approximately 120 deg apart in longitude; thus, a spacecraft in deep space flight is always within the field-of-view of at least one DSS, and for several hours each day may be seen by two DSSs. Furthermore, since most spacecraft on deep space missions travel within 30 deg of the equatorial plane, the DSSs are located within latitudes of 45 deg north or south of the equator. All DSSs operate at S-band frequencies: 2110–2120 MHz for earth-to-spacecraft transmission and 2290–2300 MHz for spacecraft-to-earth transmission.

To provide sufficient tracking capability to enable useful data returns from around the planets and from the edge of the solar system, a 210-ft-diam-antenna network will be required. Two additional 210-ft-diam-antenna DSSs are under construction at Madrid and Canberra, which will operate in conjunction with DSS 14 to provide this capability. These stations are scheduled to be operational by early 1973.

Table 1. Tracking and data acquisition stations of the DSN

DSCC	Location	DSS	DSS serial designation	Antenna		Year of initial operation
				Diameter, ft	Type of mounting	
Goldstone	California	Pioneer	11	85	Polar	1958
		Echo[a]	12	85	Polar	1962
		(Venus)[b]	13	(85)	(Az–El)	(1962)
		Mars	14	210	Az–El	1966
Canberra	Australia	Woomera[c]	41	85	Polar	1960
		Tidbinbilla[c]	42	85	Polar	1965
—	South Africa	Johannesburg[c]	51	85	Polar	1961[d]
Madrid	Spain	Robledo[c]	61	85	Polar	1965
		Cebreros[c]	62	85	Polar	1967

[a]Established in 1959 to support NASA's Echo Project to explore the feasibility of transcontinental two-way communications using a passive satellite; DSS 12 was originally configured with an 85-ft-diam az–el-mounted antenna. In 1962, when the need arose for a second 85-ft-diam polar-mounted antenna at the Goldstone site, the 85-ft-diam az–el-mounted antenna was moved to DSS 13, and an 85-ft-diam polar-mounted antenna was constructed at DSS 12.

[b]A research-and-development facility used to demonstrate the feasibility of new equipment and methods to be integrated into the operational network. Besides the 85-ft-diam az–el-mounted antenna, DSS 13 has a 30-ft-diam az–el-mounted antenna that is used for testing the design and operation of the feed system for the DSS 14 210-ft-diam antenna.

[c]Normally staffed and operated by government agencies of the respective countries (except for a temporary staff of the Madrid DSCC), with some assistance of U.S. support personnel.

[d]Between 1958 and 1962, a temporary mobile tracking station was located near Johannesburg to provide L-band communications required by the *Ranger* and *Mariner* Venus 1962 spacecraft.

b. Compatibility test facilities. In 1959, a mobile L-band compatibility test station was established at Cape Kennedy to verify flight-spacecraft DSN compatibility prior to the launch of the *Ranger* and *Mariner* Venus 1962 spacecraft. Experience revealed the need for a permanent facility at Cape Kennedy for this function. An S-band compatibility test station with a 4-ft-diam antenna became operational in 1965. In addition to supporting the preflight compatibility tests, this station monitors the spacecraft continuously during the launch phase until it passes over the local horizon.

Spacecraft telecommunications compatibility in the design and prototype development phases was formerly verified by tests at the Goldstone DSCC. To provide a more economical means for conducting such work and because of the increasing use of multiple-mission telemetry and command equipment by the DSN, a compatibility test area (CTA) was established at JPL in 1968. In all essential characteristics, the configuration of this facility is identical to that of the 85- and 210-ft-diam-antenna stations.

The JPL CTA is used during spacecraft system tests to establish the compatibility with the DSN of the proof test model and development models of spacecraft, and the Cape Kennedy compatibility test station is used for final flight spacecraft compatibility validation testing prior to launch.

2. Ground Communications Facility

The GCF, using, in part, facilities of the worldwide NASA Communications Network (NASCOM),[3] provides

---

[3]Managed and directed by the Goddard Space Flight Center.

voice, high-speed data, and teletype communications between the SFOF and all DSSs, except those of the Goldstone DSCC. Communications between the Goldstone DSCC and the SFOF are provided by a microwave link leased from a common carrier. Early missions were supported with voice and teletype circuits only, but increased data rates necessitated the use of wide-band circuits from all DSSs.

3. Space Flight Operations Facility

Network and mission control functions are performed by the SFOF at JPL. (Prior to 1964, these functions were performed in temporary facilities at JPL.) The SFOF receives data from all DSSs and processes that information required by the flight project to conduct mission operations. The following services are provided: (1) real-time processing and display of metric data; (2) real-time and non-real-time processing and display of telemetry data; (3) simulation of flight operations; (4) near-real-time evaluation of DSN performance; (5) operations control, and status and operational data display; and (6) general support such as internal communications by telephone, intercom, public address, closed-circuit TV, documentation, and reproduction of data packages. Master data records of science data received from spacecraft are generated. Technical areas are provided for flight project personnel who analyze spacecraft performance, trajectories, and generation of commands.

The SFOF is equipped to support many spacecraft in flight and those under test in preparation for flight. Over a 24-h period in 1967, as many as eight in-flight spacecraft or operational-readiness tests for flight were supported by the SFOF.

II. Mission Support

A. Planetary Flight Projects

1. Mariner Mars 1971 Mission Support, R. P. Laeser

a. Introduction. In the last four issues of this volume, functional descriptions of the DSN tracking, telemetry, command and monitor systems, which are planned for support of the *Mariner* Mars 1971 Mission, have been described.

There have been two major changes which significantly affect the previously described systems. First, the data processing configuration in the SFOF has been changed by the adoption of configuration C (Fig. 1). Secondly, the flow of data in the GCF to and from the DSIF stations has been changed by the scheduled replacement of the 2400-bits/s capability with a 4800-bit/s capability.

b. SFOF data processing. Configuration C was adopted to replace the obsolescent IBM 7044 and 7094 computers and to upgrade DSN/SFOF capability to be consistent with the requirements of *Mariner* Mars 1971 and future projects. The configuration consists of two parallel IBM 360/75 computers, electrically connected to the dual processor Univac 1108 computer of the scientific computer facility (SCF). It is intended that the two 360/75's be used for real-time processing in a redundant mode— one backing up the other. Either one should be more

than capable of handling all *Mariner* Mars 1971 real-time processing requirements. The 360/75 system will be designed to handle analysis programs as well as the real-time processing. However, because of schedule constraints, most analysis programs will have to be processed on the 1108.

A more detailed 360/75 configuration is shown in Fig. 2. The 360/75 communicates with the DSIF via teletype (through the communications processor), high-speed data lines, and the new digital wide-band data line. Keyboard/cathode ray tube input/output devices will be provided in the user areas along with computer-formatted digital TV displays, computer-reconstructed spacecraft video displays, and a computer-driven mission display board in the DSN operations area.

The DSN simulation computer, the ASI 6050, is electrically connected to the scientific computing facility (SCF) Univac 1108, which will perform spacecraft mathematical modeling. The SFOF PDP-7 computer performs the off-line media conversion tasks. The project-supplied mission and test computer (MTC) (Univac 1219/1230 complex) remains unchanged, as does the TV processing system. However, the TV processing system can receive its data from either the 360/75 or the MTC.
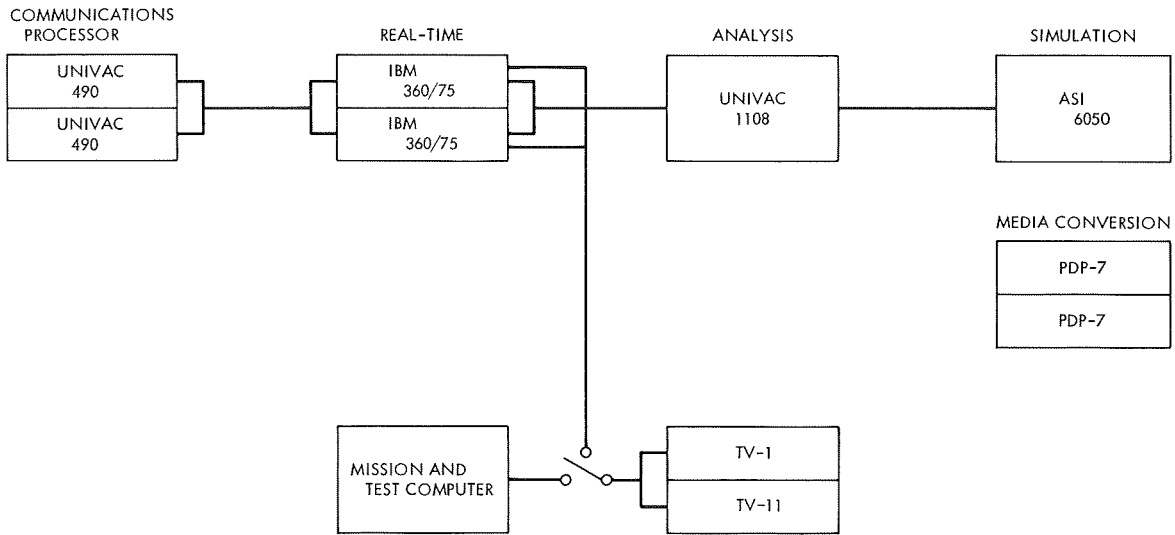
Fig. 1. SFOF configuration C data-processing system for *Mariner* Mars 1971
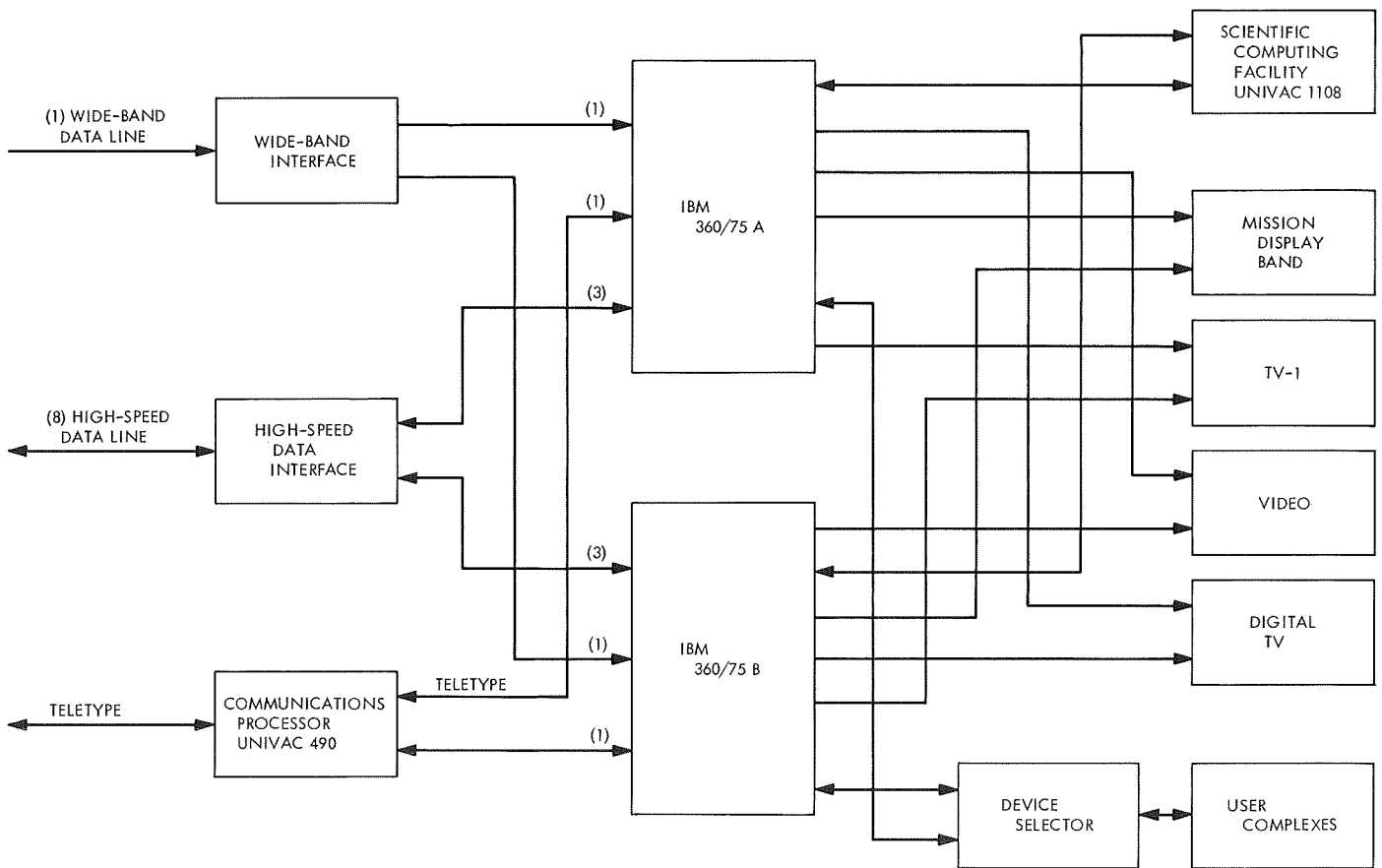
Fig. 2. SFOF *Mariner* Mars 1971 IBM 360/75 computer configuration

c. Effect of configuration C or DSN systems. A change of this magnitude obviously has a major effect on the DSN tracking, telemetry, command and monitor systems. In the tracking system, the tape interface between the DSN editing and original data record (ODR) generation functions in the 7094, and the project orbit determination function in the 1108 has been eliminated. Instead, there is now an electrical interface between the 360/75 and the 1108, with the 360/75 performing the editing, ODR generation, and pseudoresidual processing, and the 1108 performing all other functions, including DSIF prediction generation. An additional capability of the configuration is to process the high-speed tracking data which will be generated by the prototype DSIF tracking subsystem at DSS 14.

The telemetry system has the added capability of processing high-rate data from two spacecraft simultaneously as it is received over the new 50-kilobit/s digital wideband line from DSS 14. The capability of the 360/75 also allows generation in near real-time of master data records (MDR) for all telemetry data. The exact plans for MDRs have not yet been formulated. The new display capabilities of the 360/75 should be appreciated by all telemetry analysts, because silent, high-speed, large-volume devices will be provided.

The changes to the DSN command system are similar to those already described. The tape interface between the project command generation programs and the SFOF terminal of the automatic command transmission system will be eliminated and replaced with an electrical interface, and sophisticated input/output will be provided to expedite the command transmission process.

The DSN monitor system will undergo major physical change, but minor functional change as a result of the new configuration. The display buffer will be eliminated, and all DSN monitor functions will be performed by the 360/75.

d. 4800-bits/s high-speed data. A new development, the Model 203 modem, is the device which provides this expanded capability. It replaces the Model 205 modem which operated at 2400 bits/s, and it uses the same physical circuits as the 205. With this new capability, the same quantity of data can be carried on one half the number of circuits. The rest of the GCF high-speed data system is not changed: block multiplexers, demultiplexers, and error detection encoders and decoders.

e. Effect of 4800-bits/s high-speed data. All DSN systems share the use of high-speed data lines. The total high-speed data transmission capacity for *Mariner* Mars 1971 will not change. Where each DSS previously interfaced with the SFOF over two 2400-bits/s circuits, it will now interface over one 4800-bits/s circuit. However, since there will no longer be an artificial barrier between the lines, the task of assigning data by type to one of two lines will disappear, thereby simplifying software at the DSS. The overall reduction in circuit quantity provides a simpler and easier-to-operate system.

f. Other changes. Two other changes are noteworthy. Open-loop receivers for support of the S-band occultation experiment will be provided at DSS 41 and DSS 62 as well as DSS 14. However, real-time digitization will be provided only at DSS 14. At the overseas stations, the open-loop data will be analog-recorded on FR-1400 recorders, and these recordings will be made available to the experimenter.

Three separate DSIF telemetry and command processor (TCP) programs are now planned. The first will be the standard operations program and will provide command processing, data recording, and transmission of one engineering and one science stream for one spacecraft for any allowable combination of spacecraft data rates, except for high-rate data of 4 kilobits/s and above; an optional use of this program will allow processing of high-rate data in excess of 4 kilobits/s when no other processing is performed. The second program will provide for playback of TCP recordings after the pass in order to fill in gaps in the master data record. The third program will be used at DSS 14 only and will provide processing of two engineering streams, one from each spacecraft, and command processing for one spacecraft.

III. Advanced Engineering

A. Communications Systems Research

1. Digital Telemetry and Command: Efficient Estimates of Noise Variance in Block-Coded Telemetry,
J. K. Holmes

a. Introduction. Recently, a simple estimator of the noise variance was presented for biorthogonal block-coded telemetry systems, such as that used on *Mariner* Mars 1969. This estimator, using an order statistic (SPS 37-46, Vol. IV, pp. 242–245; SPS 37-58, Vol. II, pp. 37–39), provides a monitor for the signal-to-noise ratio.

In SPS 37-46, an asymptotic formula was used to evaluate the variance of the estimator. More accurate results (to eight places) were obtained in SPS 37-58 by a direct calculation via the computer. In this article, the single-sample maximum likelihood estimate (MLE) of σ, for a single-sample drawn from the largest of the absolute noise-only correlation values, is derived and compared to the one of SPS 37-58. It is shown that the single-sample estimator of SPS 37-58 is asymptotically a MLE. Also, the equation defining the M-sample MLE is

derived and shown to have a solution (estimate) different from the average of the single-sample MLE. Furthermore, it is shown that the estimator of SPS 37-58 has a very high asymptotic efficiency when compared to the M-sample MLE and, therefore, under the existing ground rules, is best suited for the purpose of noise variance estimation.

b. Review. The system for which the noise estimator was developed in SPSs 37-46 and -58 is a biorthogonal block-coded telemetry system. Since the code is biorthogonal, only the upper half of the code dictionary need be correlated with the input, since the lower half will correlate to the negative of the first half. The code word presumed to be present corresponds to the correlator with the largest absolute value, the sign determining to which half of the code dictionary the code word belongs. The estimate of the noise variance considered here is obtained from the second largest absolute correlation value which is with high probability due to noise only, with the largest absolute correlation corresponding to the transmitted signal. This largest absolute correlation can, therefore, be used to estimate the relative signal level.

c. Single-sample MLE. The MLE for the noise variance that is obtained here is for a single sample obtained from the largest noise-only absolute correlation term. For M samples, the estimate suggested in SPSs 37-46 and -58 is the average of the single-sample estimator. If we have available the n-vector

$$(x_1, x_2, \cdots, x_n)$$

of noise-only absolute correlation values [$n + 1 = 32$ in the (32,6) code] which can be rearranged in increasing order to form the order statistic

$$(x_{(1)}, x_{(2)}, \cdots, x_{(n)})$$

then $x_{(n)}$ will be the largest absolute correlation value. Because of the ground rules on the complexity of the estimator, only one of the "n" absolute correlation values can be used to estimate the noise variance.

It has been shown (SPS 37-46) that, if ordering is allowed, the best estimator restricted to one correlation will use $x_{(n)}$, the largest absolute correlation value. Since the samples are absolute values of gaussian random variables, the x_i have a distribution function

$$F(x) = 2 \left[\Phi(x) - \frac{1}{2} \right] \tag{1}$$

where

$$\Phi(x) = \int_{-\infty}^{x} \frac{1}{(2\pi)^{1/2} \sigma} \exp\left(\frac{-t^2}{2\sigma^2}\right) dt \tag{2}$$

The distribution of the largest is given by

$$F(x_{(n)} \leq x) = [2\Phi(x) - 1]^n, \qquad x \geq 0 \tag{3}$$

To obtain the MLE, we must solve the following equation:

$$\frac{\partial}{\partial \hat{\sigma}} \ln [p(x)] = 0 \tag{4}$$

where $p(x)$ is the density function associated with the distribution $F(x)$. From Eq. (3), we have

$$\ln [p(x)] = \ln (2n) + (n-1) \ln [2\Phi(x) - 1] + \ln [\Phi'(x)] \tag{5}$$

Differentiating and setting this equal to zero produces

$$1 = \left(\frac{x}{\hat{\sigma}}\right)^2 - \frac{n-1}{\Phi(x) - \frac{1}{2}}$$
$$\times \left[\Phi(x) - \int_{-\infty}^{x} \frac{t^2}{\hat{\sigma}^2} \frac{1}{(2\pi)^{1/2} \hat{\sigma}} \exp\left(\frac{-t^2}{2\hat{\sigma}^2}\right) dt \right] \tag{6}$$

Integrating by parts and letting $x/\hat{\sigma} = r$, we have

$$1 = r^2 - \frac{n-1}{\Phi(r) - \frac{1}{2}} \cdot \frac{r}{(2\pi)^{1/2}} \exp\left(-\frac{r^2}{2}\right) \tag{7}$$

Once we have the solution to Eq. (7), the single-sample MLE is given by

$$\hat{\sigma} = \frac{1}{r} x_{(n)} \tag{8}$$

For the M-sample average, we would then use

$$\hat{\sigma} = \frac{1}{Mr} \sum_{i=1}^{M} x_{(n)}^i \tag{9}$$

For $n = 1$, the solution to Eq. (7) is trivial, and our single-sample MLE becomes

$$\hat{\sigma} = x_1 \tag{10}$$

But it is biased, since

$$E(\hat{\sigma}) = \int_0^\infty \frac{2x}{(2\pi)^{1/2} \sigma} \exp\left(\frac{-x^2}{2\sigma^2}\right) dx = \left(\frac{2}{\pi} \sigma\right)^{1/2} \tag{11}$$

The estimate of SPS 37-58 for $n = 1$ is given by

$$\tilde{\sigma} = \left(\frac{\pi}{2}\right)^{1/2} x_1 \tag{12}$$

which is, from Eq. (11), unbiased. In fact, all estimates of SPS 37-58 are unbiased for all n. Next, we show that the MLE and the estimate $\tilde{\sigma}$ of SPS 37-58 are asymptotically (in n) the same.

d. Comparison of estimates for large n. The estimate $\widetilde{\sigma}$ is defined by

$$\widetilde{\sigma} = \lambda_n x_{(n)} \tag{13}$$

where λ_n is tabulated in SPS 37-58 and is defined by the condition $\lambda_n E(x_{(n)}) = \sigma$; moreover, in SPS 37-46, $\widetilde{\sigma}$ was shown to be asymptotic to

$$\widetilde{\sigma} = \frac{x_{(n)}}{[2\ln(n)]^{1/2}} \tag{14}$$

Now consider the MLE $\widehat{\sigma}$ for large n. Note that as n increases, r must increase in order that Eq. (7) is satisfied. Now, rewrite Eq. (7) as

$$\frac{\ln(r^2-1)}{\dfrac{r^2}{2}} = \frac{\ln(2\pi)^{1/2}}{\dfrac{r^2}{2}} + \frac{\ln(n)}{\dfrac{r^2}{2}} + \frac{\ln(r)}{\dfrac{r^2}{2}} - 1 + \frac{\ln\left(\dfrac{n-1}{n}\right)}{\dfrac{r^2}{2}} \tag{15}$$

We have, therefore, that as $n \to \infty$ (and, therefore, as $r \to \infty$)

$$r = [2\ln(n)]^{1/2} + o(1) \tag{16}$$

Hence,

$$\widehat{\sigma} = \frac{x_{(n)}}{[2\ln(n)]^{1/2} + o(1)}$$

Consequently, the two single-sample estimators in consideration are asymptotically equal, and, therefore, we conclude that the estimate proposed in SPS 37-58 is asymptotically a single-sample MLE.

e. MLE for M samples. We now obtain the maximum likelihood equation which defines the MLE for M samples and show that it is not the same as the average of the single-sample MLE. The distribution function of M independent samples of a random variable distributed as the largest absolute noise correlation is given by

$$F(\underline{x}_{(n)}) = \prod_{i=1}^{M} [2\Phi(x_{(n)}^i) - 1]^n,$$

$$\underline{x}_{(n)} = \left(x_{(n)}^1, x_{(n)}^2, \cdots, x_{(n)}^M\right)$$

If we take logarithms and differentiate and set the results equal to zero, we obtain an implicit equation for $\widehat{\sigma}$:

$$\widehat{\sigma}^2 = \frac{1}{M}\sum_{i=1}^{M}(x_{(n)}^i)^2 - \frac{\widehat{\sigma}^2(n-1)}{M}\sum_{i=1}^{M}\frac{\left(\dfrac{x_{(n)}^i}{\widehat{\sigma}}\right)\exp\left[-\dfrac{(x_{(n)}^i)^2}{2\widehat{\sigma}^2}\right]}{\left[\Phi\left(\dfrac{x_{(n)}^i}{\widehat{\sigma}}\right) - \dfrac{1}{2}\right](2\pi)^{1/2}} \tag{17}$$

It is clear that the average of the single-sample estimate (Eq. 9) is not a solution to Eq. (17). In fact, it appears to be very difficult to obtain an explicit expression for $\widehat{\sigma}$ from Eq. (17). However, the large-sample variance of this MLE can be found from a result given in Ref. 1 where, under rather general conditions satisfied here, it is shown that for a MLE $\widehat{\sigma}$ of a single parameter σ, we have

$$\mathrm{var}(\widehat{\sigma}) \cong \left\{ - M E\left[\frac{\partial^2}{\partial \sigma^2}\ln p(x\mid\sigma)\right]\right\}^{-1} \tag{18}$$

for large M. The coefficient B_n^2 defined by

$$\sigma^2 B_n^2 = \left\{ - E\left[\frac{\partial^2}{\partial \sigma^2}\ln p(x\mid\sigma)\right]\right\}^{-1} \tag{19}$$

has been obtained by use of the SDS 930 computer and is compared in Table 1 with C_n^2 of SPS 37-58. The coefficient C_n^2 is defined by

$$\mathrm{var}(\widetilde{\sigma}) = C_n^2\,\sigma^2 \tag{20}$$

As can be seen from Table 1, the asymptotic (in M) efficiency of the estimator proposed in SPS 37-58 is quite high for all n considered. Clearly, any improvement by the use of nonlinear estimates would not be worth the

Table 1. Comparison of numerical results

n	C_n^2	B_n^2	Efficiency, %
3	0.195	0.188	96.4
7	0.0962	0.0961	99.8
15	0.0566	0.0563	99.5
31	0.0372	0.0360	96.8
63	0.0259	0.0245	94.6

added complexity. Since for very large n it has been shown that both estimators are identical, it follows that

$$\lim_{n \to \infty} \left(\frac{B_n^2}{C_n^2} \right) = 1 \qquad (21)$$

It is easy to show that the unrestricted MLE uses all the noise samples available and is given by

$$\widehat{\sigma}_{UML} = \left[\frac{1}{Mn} \sum_{i=1}^{n} \sum_{i=1}^{M} (x_j^i)^2 \right]^{1/2} \qquad (22)$$

And its associated large-sample variance (asymptotic in M) is given by

$$\text{var} \left(\widehat{\sigma}_{UML} \right) \cong \frac{\sigma^2}{2 Mn} \qquad (23)$$

It is not hard to show that for large, fixed M that

$$\lim_{n \to \infty} \left[\frac{\text{var} \left(\widehat{\sigma}_{UML} \right)}{\text{var} \left(\widetilde{\sigma} \right) + \text{var} \left(\widehat{\sigma} \right)} \right] = 0$$

since both the variance of $\widehat{\sigma}$ and $\widetilde{\sigma}$ decrease as $[\ln (n)]^{-2}$ for large n, whereas the variance of $\widehat{\sigma}_{UML}$ decreases as n^{-1}. Therefore, MLEs based on the largest noise-only samples are asymptotically (in n) inefficient compared to unrestricted maximum likelihood samples, but require more equipment complexity. However, for the (32,6) code the unrestricted MLE is only about 3 dB better than the restricted one proposed in SPSs 37-46 and -58.

Reference

1. Mood, A. M., *Introduction to the Theory of Statistics.* McGraw-Hill Book Co., Inc., New York, N.Y., 1950.

2. Digital Telemetry and Command: Quantization Requirements for the Multimission Telemetry System,
J. K. Holmes

a. Introduction. Quantization requirements for the data channel quantizers (Fig. 1) are considered here for the multimission telemetry system (MMTS). The requirements are determined for the following constraints:

(1) Degradation of performance in the block-coded mode.

(2) Degradation of performance in the uncoded mode.

(3) Degradation of the accuracy of the signal-to-noise ratio (SNR) estimate in the block-coded mode.

(4) Degradation of the accuracy of the SNR estimates in the uncoded mode.

(5) Dynamic range considerations.

This article considers biorthogonal codes which have been adopted in the MMTS to provide a block-code capability. Both a (32,6) and (16,5) code are provided. The receiver is composed of M ($M = 32$ or 16) correlators, even though there are $2M$ code words. This reduction by a factor of two is possible since the upper half of the code words is a complement of the lower half. If the receiver waveform is designated by $r(t)$, then the correlation values r_i are given by

$$r_i = \int_0^{MT_s} r(t) \, W_i(t) \, dt, \qquad i = 1, \cdots, M \qquad (1)$$

where T_s is the code symbol time and $W_i(t)$ is the ith code word. Hence, if r_j is the r_i of largest absolute value, $W_j(t)$ is chosen as the transmitted word if $r_j > 0$; otherwise, $-W_j$ is chosen. After each symbol time, the symbol integrator values are quantized and used to form the correlation with the M-stored code words.

In the uncoded mode, since the bits are decoded directly, there is no degradation in bit error probability. However, quantization increases the variance of the SNR estimate, and thereby degrades it. The accuracy of SNR estimates in the coded case is degraded by quantization as in the uncoded case.

Dynamic range variations can be compensated by increasing the quantizer range and number of levels simultaneously so that the quantum levels remain at the same spacing.
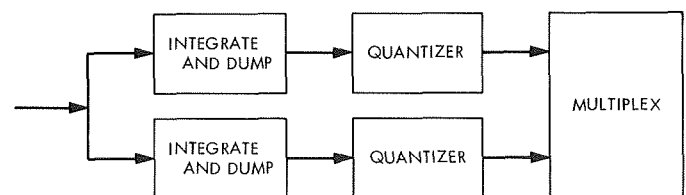
Fig. 1. Data channel

b. Quantizer model. To model the effect of the quantization, the quantizer's effect on the input signal plus noise must be developed. We consider the following model (SPS 37-45, Vol. IV, pp. 290–296) as illustrated in Fig. 2 for eight levels. Each input quantization level is L volts wide, and each corresponding output is at the center of its respective level, the dots in the figure. Altogether, there are 2^k levels (k bit quantization) so, if DR denotes the dynamic range, then the spacing between levels is given by

$$L = \frac{DR}{2^k} \text{ volts} \tag{2}$$

The dynamic range is the range of input voltages that can be quantized with a maximum quantization error of $L/2$ volts. A voltage exceeding the dynamic range is truncated to the last level with an associated increase in quantization error. The basic assumption made here is that the distribution, given that the input voltage falls in a given level (of range L volts), is uniform in that level. The accuracy of this characterization would increase as the level size becomes smaller. Also, at the extremes of the quantizer the error probability density function is actually a section of a gaussian density. However, if the quantization is fine enough, the uniform density will still be a valid assumption. Hence, with the assumption of a uniform density in each level, we have that the mean square of the quantization error at each level is given by

$$\sigma_q^2 = \frac{L^2}{12} \tag{3}$$

Since the range of the quantizer must be large enough to quantize the sum of the signal plus noise, one-half of the dynamic range is taken equal to the integrated signal
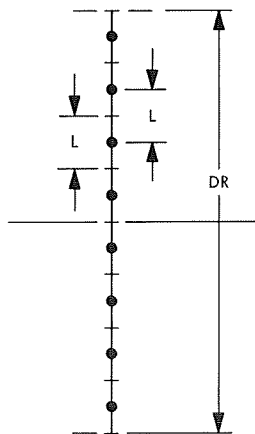
Fig. 2. Quantization scheme for eight levels

symbol AT_s plus three times the standard deviation σ of the integrated noise (SPS 37-45). Any larger samples are truncated, but they only occur with low probability and are assumed to have little effect. Therefore, the level size is given by

$$L = \frac{AT_s + 3\sigma}{2^{k-1}} \tag{4}$$

since $DR = 2(AT_s + 3\sigma)$.

c. Word signal plus noise. We assume that a signal of amplitude A plus white gaussian noise of spectral density $N_0/2$ is the input to the integrator over the symbol time T_s. The output of the integrator, assuming perfect synchronization, is

$$AT_s + N \tag{5}$$

where

$$N = \int_0^{T_s} N(t)\, dt \tag{6}$$

The variance of N is given by

$$\text{var}\,(N) = \frac{N_0}{2} T_s \tag{7}$$

and, hence, the output symbol SNR, without quantization, is given by

$$\text{SNR} = \frac{(AT_s)^2}{\dfrac{N_0}{2} T_s} = \frac{2E_s}{N_0} \tag{8}$$

where E_s is the symbol energy and is equal to $A^2 T_s$.

Now with quantization after the integration, more noise is added to the correlation with every symbol. Since in the coded mode 16 or 32 samples, each having uniformly distributed random errors, are added up, we may assume that the effect of the quantization is to add gaussian noise of variance $M\sigma_q^2$ to the word correlator outputs. This follows from the central limit theorem.

The total variance becomes

$$M\left(\frac{N_0}{2} T_s + \sigma_q^2\right) \tag{9}$$

The new word signal-to-noise ratio, say SNR′, with the quantization effects included, is given by

$$\text{SNR}' = \frac{M(AT_s)^2}{\frac{N_0}{2}\,T_s + \sigma_q^2} \qquad (10)$$

If we allow a maximum degradation to the SNR of D dB, then we require

$$10\log\left[\frac{M(AT_s)^2}{\frac{N_0}{2}\,T_s}\right] \le 10\log\left[\frac{M(AT_s)^2}{\frac{N_0}{2}\,T_s + \sigma_q^2}\right] + D \qquad (11)$$

or

$$\sigma_q^2 \le \frac{N_0}{2}\,T_s\,(10^{D/10} - 1) \qquad (12)$$

So, if $D = 0.1$ dB, then we have

$$\sigma_q^2 \le 0.023\,\frac{N_0}{2}\,T_s \qquad (13)$$

d. *Quantizer equation.* Now we can write the quantizer noise variance from Eq. (3) as

$$\sigma_q^2 = \frac{\left[AT_s + 3\left(\frac{N_0}{2}\,T_s\right)^{1/2}\right]^2}{12\,(2^{k-1})^2} \qquad (14)$$

At this point, it is assumed that AT_s and σ are known exactly so that the dynamic range is known exactly. Since they are actually unknown, extra quantizer bits must be added to compensate for their variation. Using Eq. (14) in Eq. (12) produces

$$\frac{\left[AT_s + 3\left(\frac{N_0}{2}\,T_s\right)^{1/2}\right]^2}{12\,(2^{k-1})^2} \le (10^{D/10} - 1)\frac{N_0}{2}\,T_s \qquad (15)$$

This inequality yields a bound on the required number of bits of quantization. Solving, using Eq. (8), we have, letting $\rho = E_s/N_0$,

$$2^{2k} \ge \frac{2\rho\left[1 + 3\left(\frac{1}{2\rho}\right)^{1/2}\right]^2}{3\cdot 10^D - 1} \qquad (16)$$

which is the quantizer equation relating the required number of bits k versus ρ and the allowable degradation D dB.

e. *Requirements at threshold for the (32,6) and (16,5) codes.* At threshold, which corresponds to a probability of word error equal to 10^{-2}, the allowable degradation is 0.1 dB. For this error probability, for the (32,6) code, we have, denoting E_B as the bit energy,

$$\frac{E_B}{N_0} = 2.9\,\text{dB}$$

so that the symbol energy per N_0 is given by

$$\frac{E_s}{N_0} = 2.9\,\text{dB} - 10\log_{10}\frac{32}{6} = -4.37\,\text{dB} \qquad (17)$$

In evaluating the quantizer equation we find that we must have $k \ge 4$ for a maximum degradation of 0.1 dB.

For the (16,5) code, it is found that $E_s/N_0 = -1.64$ dB or again that $k \ge 4$. Hence, at threshold $k = 4$ is sufficient for both the (32,6) and the (16,5) block codes if AT_s and σ are known *a priori*.

f. *Requirements at $PE_w = 10^{-5}$ for the (32,6) and (16,5) codes.* At $PE_w = 10^{-5}$, $E_s/N_0 = -0.82$ dB, and with an allowable degradation of 0.2 dB for the (32,6) code, we have, from the quantizer equation, that we must have $k \ge 4$ bits. Under the same conditions for the (16,5) code, it is found that we must have $k \ge 4$ bits also.

We summarize the results in Table 2. This table assumes that $2(AT_s + 3\sigma) = DR$ is held constant. In practice, this is, of course, not true and an additional number of bits must be used to take up signal and automatic gain control variations.

Table 2. Quantization requirements

Block code	Allowable degradation, dB	PE_W	Required k
(32,6)	0.1	10^{-2}	4
(16,5)	0.1	10^{-2}	4
(32,6)	0.2	10^{-5}	4
(16,5)	0.2	10^{-5}	4

g. Quantization effect on PE in the uncoded case. In the uncoded case, since decisions are made bit by bit, there is no degradation for any value of quantization as long as $k \geq 1$.

h. Quantization effect on the var ($\widehat{SNR}$) in the coded case.

Absolute magnitude method, random noise sample. This method estimates the square of the mean output and the variance from the word correlation outputs and forms the ratio to estimate the SNR; call it R. The square of the mean is estimated with the signal presumed present (highest correlation), and the noise variance is formed from a random noise-only correlation. Due to the method involved, it is possible with probability $1/M$ that a random selection will not be available and, so in this case, a zero is outputed for the random noise-only correlation. This effect increases the variance by approximately $M/(M-1)$. Its effect is neglected in what follows.

The estimator is of the form (SPS 37-49, Vol. III, pp. 306–311)

$$\widehat{R} = \frac{\left(\frac{1}{n}\sum_1^n |x_i^s|\right)^2}{\frac{\pi}{2}\left(\frac{1}{n}\sum_1^n |x_i|\right)^2} \tag{18}$$

where $|x_i^s|$ is the word correlation value with the signal present and $|x_i|$ is the correlation value of a randomly

chosen noise-only correlation. To analyze this expression, we may rewrite $\widehat{R}$ in a manner similar to that given in SPS 37-48, Vol. III, pp. 209–212

$$\widehat{R} = \frac{(AT_s)^2\left[1 + \frac{\delta_n}{(AT_s)^2}\right]}{\sigma^2\left[1 + \frac{\gamma_n}{\sigma^2}\right]} \tag{19}$$

where δ_n and γ_n are, respectively, the random parts of the numerator and denominator.

Under the assumption that with probability approaching one

$$\frac{\delta_n}{(AT_s)^2} \ll 1 \text{ and } \frac{\gamma_n}{\sigma^2} \ll 1 \tag{20}$$

we have, to a good approximation, for n large enough

$$\widehat{R} = \frac{(AT_s)^2}{\sigma^2}\left[1 + \frac{\delta_n}{(AT_s)^2} - \frac{\gamma_n}{\sigma^2} + O(\delta_n\gamma_n) + O(\gamma_n^2)\right] \tag{21}$$

Since the numerator and denominator of the estimate are unbiased, we have

$$E(\delta_n) = E(\gamma_n) = 0 \tag{22}$$

The variance of $\widehat{R}$ is given by

$$\text{var}(\widehat{R}) = \frac{(AT_s)^4}{\sigma^4}\left\{\text{var}\left[\frac{\delta_n}{(AT_s)^2}\right] + \text{var}\left(\frac{\gamma_n}{\sigma^2}\right) - 2E\left[\frac{\delta_n}{(AT_s)^2}\frac{\gamma_n}{\sigma^2}\right]\right\} \tag{23}$$

After some algebra, we have

$$\text{var}\left[\frac{\delta_n}{(AT_s)^2}\right] = \frac{4\sigma^2}{n(AT_s)^2}, \qquad \text{var}\left(\frac{\gamma_n}{\sigma^2}\right) = \frac{2(\pi-2)}{n}, \qquad 2E\left[\frac{\delta_n\gamma_n}{(AT_s\sigma)^2}\right] = \frac{1}{n}\left[\frac{2\sigma^2}{(AT_s)^2} - (\pi-2)\right] \tag{24}$$

Therefore, the variance is given by

$$\text{var}(\widehat{R}) = \frac{(AT_s)^4}{\sigma^4}\left[\frac{2\sigma^2}{n(AT_s)^2} + \frac{(\pi-2)}{n}\right] \tag{25}$$

and the relative variance is given by

$$\text{var}\left(\frac{\widehat{R}}{R}\right) = \frac{1}{n}\left[\frac{2\sigma^2}{(AT_s)^2} + \pi - 2\right] \tag{26}$$

Hence, the relative accuracy depends on two terms, one proportional to the noise-to-signal ratio and another that is constant. If we write σ^2 (denoting the thermal noise by σ_{th}^2) as

$$\sigma^2 = \sigma_{th}^2 + \sigma_q^2 \tag{27}$$

we see that a degradation of 0.1 dB due to quantization produces an increase in the relative variance of the esti-

mate that is less than 0.1 dB. This degradation in accuracy can be easily removed, by increasing n by a factor of 1.023. At a degradation of 0.2 dB due to quantization, n can thus be increased to only $(1.023)^2 n$ to remove the effects of quantization.

Largest noise-only method. This estimate uses a new denominator of the form (SPS 37-58, Vol. II, pp. 37–39)

$$(\widehat{\sigma})^2 = \left(\lambda_n \frac{1}{n}\sum_1^n x_i\right)^2 \tag{28}$$

where x_i is the largest noise correlation in absolute value (excluding the signal correlation) from the ith received word. This method is described in SPS 37-58 in detail. Since this estimate has been shown to have a much lower variance for the estimate of the noise variance than the estimate used in the preceding paragraphs, the estimate for R using this noise estimate has lower variance than the estimate described in the preceding paragraphs. The saving is 10.75 dB for the (16,5) code and 11.9 dB for the (32,6) code.

i. Quantization effect on var $(\widehat{SNR})$ in the uncoded case. In this case, the estimator (SPS 37-48) uses symbol values directly to estimate the SNR and is of the form

$$\widehat{R}_L = \frac{\frac{1}{2}\left(\frac{1}{n}\sum_1^n |I_i|\right)^2}{\frac{1}{n-1}\sum_1^n \left(|I_i| - \frac{1}{n}\sum_1^n |I_i|\right)^2} \tag{29}$$

which estimates (1/2) SNR. Since this estimate is biased, an improved estimate is used and is of the form

$$\widehat{R}_L' = \widehat{R}_L^{-1}(R_L) \tag{30}$$

where R_L^{-1} is a function which has less bias than $\widehat{R}_L$ and is asymptotically unbiased for large n for all values of R_L. Its variance is given approximately by

$$\text{var}\,(\widehat{R}') = \frac{1}{n}\,(2R_L + 2R_L^2) \tag{31}$$

assuming that the noise is strictly gaussian. This assumption is reasonable since the sum of a gaussian plus a uniform random variable is essentially gaussian as long

as the variance of the uniform is much smaller than that of the gaussian. The relative variance is given by

$$\text{var}\left(\frac{\widehat{R}}{R}\right) = \frac{1}{n}\left[\frac{4\sigma^2}{(AT_s)^2} + 2\right] \tag{32}$$

So if the variance σ^2 is composed of both quantization noise and thermal noise (gaussian), and if the quantization noise increases the total noise by 0.1 dB, we see that the increase in the relative variance is less than 0.1 dB.

j. Dynamic range considerations. Once the number of bits of quantization is determined for the case when the dynamic range is known, the variation in dynamic range must be included. However, once this factor F is known, the additional number of bits needed, k_a, can be obtained from the equation

$$\min k_a:\ 2^{k_a} \geq F \tag{33}$$

k. Conclusions. The number of quantization levels needed for the MMTS has been obtained under the assumption that the dynamic range was set equal to a fixed value of $AT_s + 3\sigma$. Under actual operating conditions, $AT_s + 3\sigma$ will vary by a factor to be determined so that additional bits are needed.

Two error levels were considered for the coded case, the first with the word error probability equal to 10^{-2} and the second with the word error equal to 10^{-5}. The resulting degradation was shown to be negligible in each case if the number of levels derived here is adopted.

3. Digital Telemetry and Command: Maximum Data Rate and Optimum Data Modulation Index, *U. Timor*

a. Introduction. In a coherent communication system using a phase-locked loop to track the carrier, the average error probability P_E is a function of the total loop signal-to-noise ratio ρ_L, the data modulation index I^2, and the data rate. If P_E is specified, then, for each ρ_L, the data modulation index will determine the data rate which yields P_E. Thus, given P_E and ρ_L, the rate is a function of the data modulation index. The purpose of this work is to find the optimum modulation index and the maximum possible data rate which yield a given error probability P_E; this is done for all data-rate-to-loop-bandwidth ratios.

b. Analysis of the system. Consider a coherent communication system using a phase-locked loop with one-sided bandwidth of b_L to track the carrier. If P is the total

received power and I^2 is the data modulation index, the probability density of the phase error ϕ is given by

$$p(\phi) = \frac{\exp[\rho_L(1-I^2)]}{2\pi I_0[\rho_L(1-I^2)]}$$

where $\rho_L \triangleq P/N_+ b_L$ is the total loop signal-to-noise ratio and N_+ is the one-sided spectral density of the noise. Let $1/T$ be the data rate and define

$$\delta = \frac{1}{Tb_L}$$

to be the rate-to-loop bandwidth ratio.

Then, for a completely coherent reception (no phase error), the data signal-to-noise ratio is

$$R = \frac{(PI^2)T}{N_+} = \frac{\rho_L I^2}{\delta}$$

However, there is a degradation of the performance due to the phase error, and the actual signal-to-noise ratio is $R\eta$, where $\eta < 1$ is the detection efficiency.

The behavior of η was investigated by Tausworthe (SPS 37-54, Vol. III, pp. 195–201), with these results. For $\delta \ll 1$, the efficiency is given by

$$\eta_0 = \left[\frac{I_1(\alpha)}{I_0(\alpha)}\right]^2$$

where

$$\alpha = \frac{r+1}{r}\rho_L(1-I^2) - \frac{1}{r\sigma_{\sin\phi}^2}$$

$\sigma_{\sin\phi}^2$ is the variance of $\sin\phi$, $r = 4\xi^2$, and ξ is the damping factor of the phase-locked loop.

For $\delta \gg 1$, the efficiency is given by

$$\eta_\infty = \frac{2}{kR}\left(\text{erfc}^{-1}\left\{\int_{-\pi}^{\pi} \text{erfc}\left[\left(\frac{kR}{2}\right)^{1/2}\cos\phi\right]p(\phi)d\phi\right\}\right)^2$$

where

$$\text{erfc } x = \frac{1}{(2\pi)^{1/2}}\int_x^\infty e^{-y^2/2}\, dy$$

and

$$k = \begin{cases} 2 & \text{uncoded or antipodal binary signals} \\ 1 & \text{coded (orthogonal/biorthogonal) signals} \end{cases}$$

For intermediate values of δ, the detection efficiency can be expressed as

$$\eta = (1 - a)\eta_0 + a\eta_\infty$$

where the interpolation factor a is a monotone increasing function of δ and is given by

$$a = \frac{\delta}{4}\left[1 - \frac{\delta}{8}(1 - e^{-8/\delta})\right]$$

Thus, given ρ_L, I^2, and δ, the detection efficiency η can be determined.

c. The maximum rate-to-bandwidth ratio. Let R_{eq} be the required signal-to-noise ratio to achieve an error probability of P_E. The R_{eq} must satisfy

$$R_{eq} = R\eta$$

Substituting the expressions for R and η, we get the following relation between R_{eq}, ρ_L, I^2, and δ:

$$R_{eq} = \frac{\rho_L I^2}{\delta}\eta_0(1 - a)$$
$$+ \frac{2a}{k}\left(\text{erfc}^{-1}\left\{\int_{-\pi}^{\pi} \text{erfc}\left[\left(\frac{k\rho_L I^2}{2\delta}\right)^{1/2}\cos\phi\right]p(\phi)d\phi\right\}\right)^2$$

where η_0 and $p(\phi)$ depend on $\rho_L(1 - I^2)$, and a is a function of δ.

Let the error probability, or equivalently R_{eq}, be given. Then for each ρ_L, δ is a function of I^2, given implicitly by the above integral equation. In particular, we are interested in finding the maximum of this function $\delta_{\max}(\rho_L, R_{eq})$, and the corresponding data modulation index $I^2_{\text{opt}}(\rho_L, R_{eq})$ which achieves this maximum. For a given total received power, noise density, and loop bandwidth, $\delta_{\max}$ will give us the maximum possible rate at the required error probabilities.

Since the integral equation cannot be solved analytically, we must resort to numerical methods. The following algorithm was used:

(1) R_{eq} and ρ_L are fixed and a coarse search is made, to restrict I^2_{opt} to an interval of length $2h$. We start with an arbitrary value I^2_0 and compute $\delta_0(I^2_0)$ and $\delta_1(I^2_0 + h)$ by solving, for each case, the integral equation. If $\delta_1 > \delta_0$, we compute $\delta_2(I^2_0 + 2h)$, $\cdots$, $\delta_n(I^2_0 + nh)$ until $\delta_n < \delta_{n-1}$. We then have

$$I^2_{\text{opt}} \ \epsilon \left[I^2_0 + (n-2)\,h, \ I^2_0 + nh \right]$$

If $\delta_1 < \delta_0$, we compute $\delta_{-1} = \delta(I^2_0 - h)$ and so on, to get a similar interval of length $2h$ containing I^2_{opt}.

(2) We pick some I^2_1 in the above interval and repeat the procedure with $h_1 < h_0$ (e.g., $h_1 = h_0/10$). We then have I^2_{opt} with an accuracy of $\pm h_1$ and

$$\delta_{n-1} \leq \delta_{\max} < \delta_{n-1} + \Delta\delta$$

where

$$\Delta\delta = \max\left[(\delta_{n-1} - \delta_n), (\delta_{n-1} - \delta_{n-2}) \right]$$

We can repeat the procedure with $h_2 < h_1$ until the accuracies of ΔI^2 and $\Delta\delta$ are accepted.

In the example computed, we took $h_0 = 0.1$, $h_1 = 0.01$, and got $\delta_{\max}$ within 0.5%.

(3) The computations are repeated for other values of ρ_L.

d. Numerical results. When ρ_L is large, $I^2_{\text{opt}} \to 1$, since a very small fraction of the total power will be enough to get an almost coherent reception. Similarly, $\eta \to 1$, since the phase error is very small. Therefore, asymptotically we have

$$\delta_{\max}(\rho_L) \xrightarrow[\rho_L \to \infty]{} \frac{\rho_L}{R_{eq}}$$

For other values of ρ_L, numerical calculations are necessary. The resulting values of $\delta_{\max}$ and I^2_{opt} for several values of R_{eq} and a wide range of ρ_L are given in Fig. 3 (uncoded signals) and Fig. 4 (coded, orthogonal/biorthogonal signals). In both cases, the damping factor was taken to be $\xi = 1/2^{1/2}$ (corresponding to $r = 2$).

e. Application. The described results can be used in the design of coherent communication systems. Given
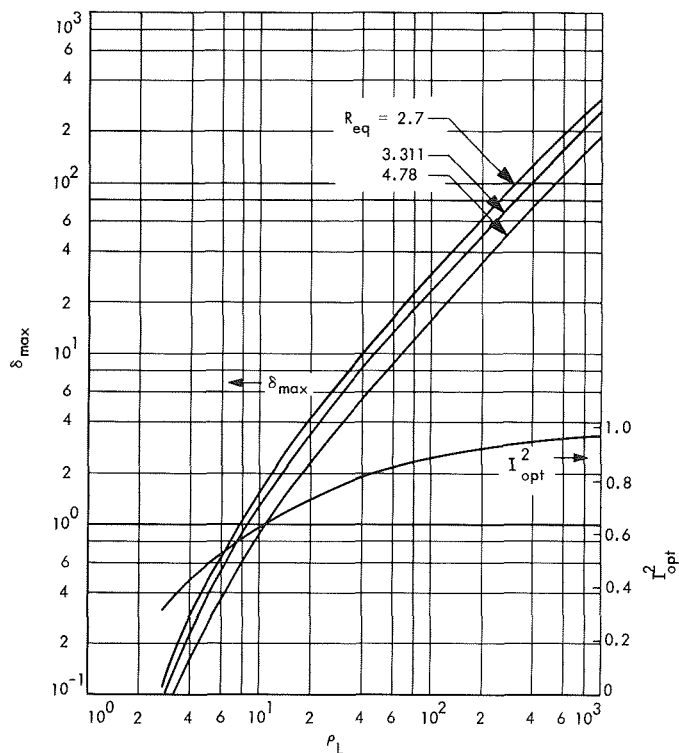
Fig. 3. Maximum rate/bandwidth and optimum data modulation index for uncoded signals
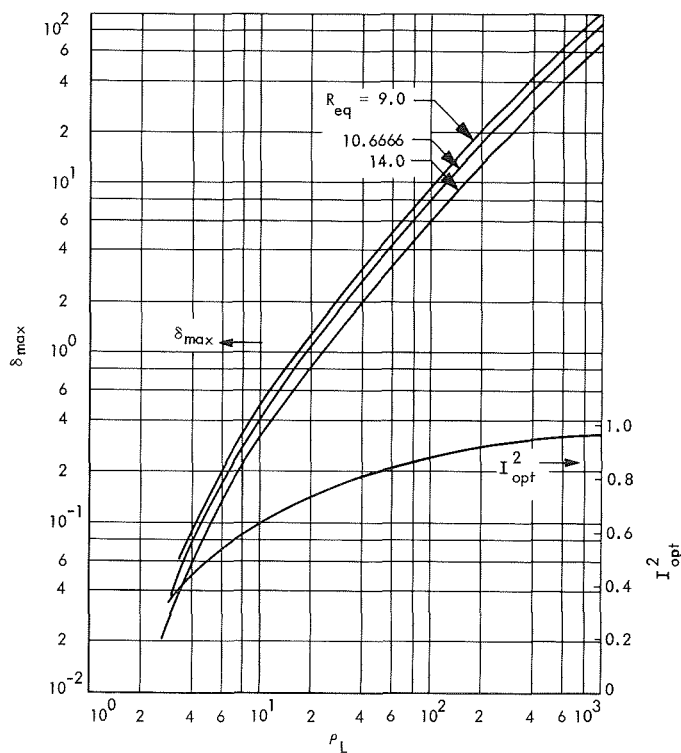
Fig. 4. Maximum rate/bandwidth and optimum data modulation index for coded (orthogonal) signals

the total loop signal-to-noise ratio and the required data signal-to-noise ratio, we can find the maximum possible data rate and the optimum data modulation index. For example, if

$$P = -157.5 \text{ dBmW}$$

$$N_+ = -180.5 \text{ dBmW/Hz}$$

$$b_L = 6 \text{ Hz} = 7.8 \text{ dBHz}$$

then

$$\rho_L = 15.2 \text{ dB} = 33.1$$

If the data are uncoded, then from Fig. 3 we have the following results:

(1) The optimum data modulation index is $I^2 = 0.7$.

(2) The maximum possible rate at $R_{eq} = 3.311$ ($P_E = 5 \cdot 10^{-3}$) is $\delta \cdot b_L = 39.5$ bit/s.

If we want a margin of Δ in the received data signal-to-noise ratio, we have to take the rate from the curve corresponding to $R'_{eq} = R_{eq} + \Delta$.

f. Conclusion. The design curves presented here can be used to select the optimum modulation index for uncoded as well as biorthogonal coherent communication systems over the entire range of possible loop signal-to-noise ratios and data rates. In the past, such design data were available in the form of approximation formulas (SPS 37-44, Vol. IV, pp. 282–290) that were good only at high loop signal-to-noise ratios $\rho_L > 10$ and high rates $\delta \gg 10$, or at very low rates $\delta \ll 10$. The middle range, which covers the *Mariner* Mars 1969 low- and medium-rate

systems, had to be designed by trial and error. The graphical data presented here will considerably reduce the design effort for future missions.

4. Digital Devices Development: Screening Test Method for Low-Noise Voltage-Controlled Oscillators,
R. Winkelstein

a. Introduction. A simple straightforward laboratory method has been developed for testing frequency noise in high-stability voltage-controlled oscillators (VCO). Such oscillators are key components in digitally controlled programmed oscillators (SPS 37-36, Vol. III, pp. 54–67) in which control accuracies are desired to better than 10 parts per million. Since the VCO is controlled in a sampled-data feedback system, with a sampling period of 1 s, oscillator frequency stability between sampling times is highly important.

The developed test method makes possible quantitative comparisons between similar VCOs, and has been used to screen out VCOs with unacceptably high noise levels.

b. System block diagram. Figure 5 is a block diagram of the test system. The VCO being tested is the search oscillator of a commercial frequency synthesizer and is referred to as "search oscillator." The output of the search oscillator is mixed with the output of a reference synthesizer and the difference frequency measured by a frequency meter. A dc voltage proportional to the input frequency is generated by the frequency meter and is used as the output test point of the system. This voltage also goes to an integrator which closes the loop by supplying the control voltage to the search oscillator. The
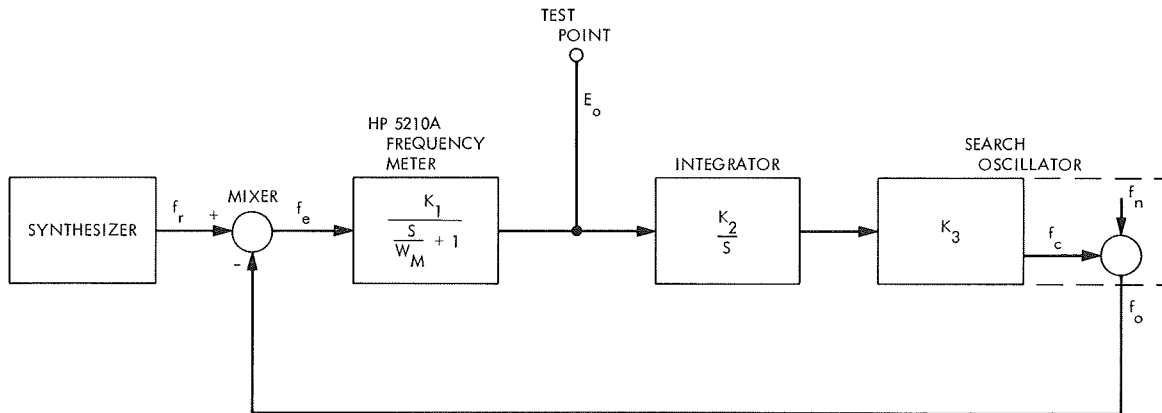
Fig. 5. Test system block diagram

constants of the system allow the loop to control long-term frequency drifts of the search oscillator, but permit short-term frequency deviations to be readily visible at the output test point.

Within each block of interest in Fig. 5 is shown the approximate Laplace transform gain function for the block. The frequency meter is a Hewlett–Packard Model 5210 A with the calibrated offset option. When used in the loop, the meter range switch is set to 1 kHz, the meter scale expanded to "× 10," and the offset to 10. The dc output, taken from the discriminator output jack, is +1 V for a full-scale deflection of 1.1 kHz. Zero voltage output results from an input of 1.0 kHz, and −1 V is obtained when the input is 0.9 kHz. Thus, the gain constant K_1 is 0.01 V/Hz. The "× 10" amplifier within the meter has a frequency cutoff of 10 Hz, which can be approximated by a single pole in the transfer function shown by the term $s/W_M + 1$. The parameter W_M, being 2π times the cutoff frequency, is thus 62.8 rad/s, and s is the complex Laplace transform frequency.

A schematic of the integrator is shown in Fig. 6. It consists of a unity gain inverter followed by an operational integrator. Feedback polarity is set by means of the "feedback" switch. The gain switch, when used in conjunction with the frequency meter range switch, is useful in initially locking the loop. During locked-loop operation, the gain switch is set to the 0.001 position, thus making K_2 equal to 0.001. The 741s are integrated circuit operational amplifiers and the 100-μF capacitor is a subminiature polycarbonate capacitor with greater than 2000-MΩ insulation resistance, made by Component Research Co. Offset currents within the loop are cancelled by the offset control.

The search oscillators tested by the loop were contained in modified Fluke synthesizers Model 644 A. The modification consisted of providing an expanded output of the search oscillator itself, independent of the front panel dial settings. The −1.0 digit on the search oscillator dial produces an output frequency of 1.0 MHz, and +1.0 digit on the dial produces a frequency of 5.0 MHz. For remote control, the −10 to +10 control voltage range could, therefore, produce a frequency swing of 4 MHz. Thus, K_3 is equal to 0.2×10^6 Hz/V. The search oscillator output f_o is considered to be the sum of an ideal controlled frequency f_c and a noise frequency f_n. The purpose of this test method is to measure the effect of f_n.

c. Loop analysis. Multiplying the individual transfer functions, the open loop gain G_o is found to be

$$G_o = \frac{K_1 K_2 K_3 W_M}{S(S + W_M)} = \frac{125.6}{S(S + 62.8)}$$

Since the phase shift is less than 180 deg at the unity gain point of approximately 0.3 Hz, the closed loop is stable. It may be noted that phase shifts in the frequency meter beyond that shown by the approximate transfer function in Fig. 5 caused the loop to become unstable when the loop gain was increased by switching the integrator gain control from 0.001 to 0.01.

Since the purpose of the loop is to measure f_n by monitoring the voltage E_o, the closed-loop transfer function G between f_n and E_o is of prime interest:

$$G = \frac{\text{gain of frequency meter}}{1 + G_o}$$
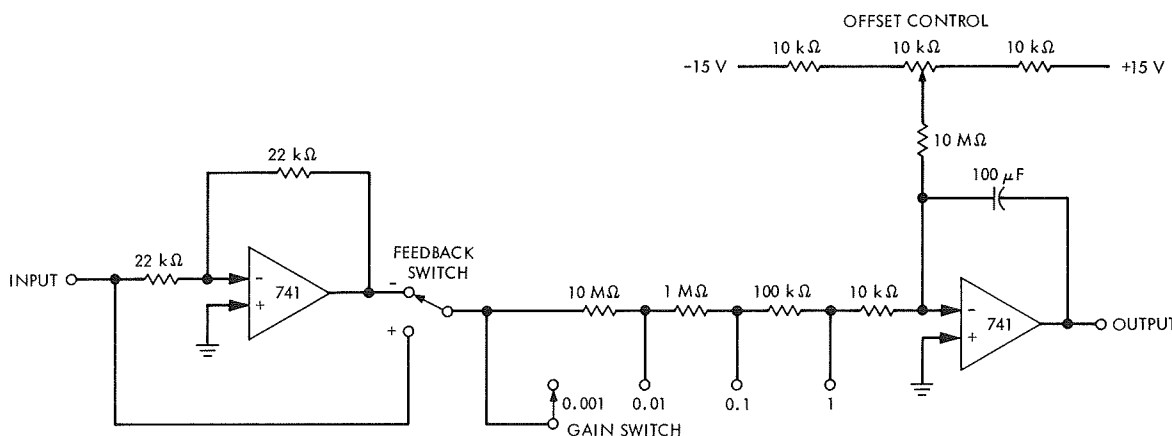
Fig. 6. Integrator

After substitution and algebraic manipulation,

$$G = \frac{S \, K_1 \, W_M}{S^2 + S \, W_M + W_M \, K_1 \, K_2 \, K_3}$$

Factoring the denominator gives

$$G = \frac{S \, K_1 \, W_M}{\left[S + \dfrac{W_M}{2} - \left(\dfrac{W_M^2}{4} - W_M \, K_1 \, K_2 \, K_3 \right)^{1/2} \right] \left[S + \dfrac{W_M}{2} + \left(\dfrac{W_M^2}{4} - W_M \, K_1 \, K_2 \, K_3 \right)^{1/2} \right]}$$

Since W_M is much larger than $K_1 K_2 K_3$, the radical may be simplified by approximating it with the first two terms of its binomial expansion

$$\left(\frac{W_M^2}{4} - W_M \, K_1 \, K_2 \, K_3 \right)^{1/2} = \frac{W_M}{2} - K_1 \, K_2 \, K_3$$

and so

$$G = \frac{SK_1 \, W_M}{(S + K_1 \, K_2 \, K_3)(S + W_M)} = \frac{0.628 \, S}{(S + 2)(S + 62.8)}$$

Thus, the transfer function is equivalent to a bandpass filter with corner frequencies at 0.3 and 10 Hz. Gain in the passband is K_1, which is equal to a 0.01-V/Hz deviation.

d. Test results. Figure 7 is a portion of a strip chart recording of a particular test run. The reference synthesizer was set to 1,001,000 Hz, forcing the search oscillator output to be approximately 1 MHz. From the record, it is

2 s/cm
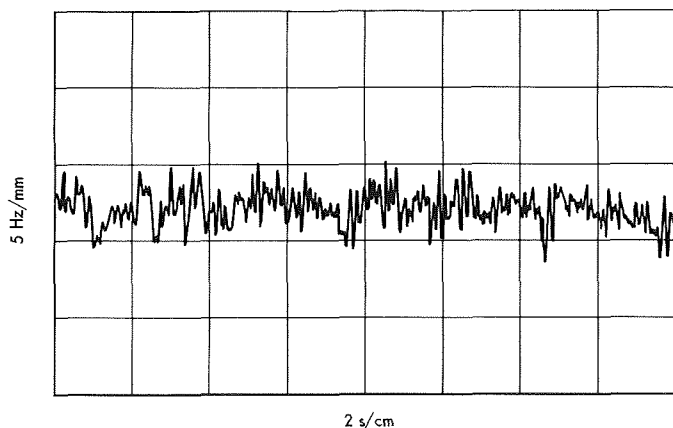
Fig. 7. Test run

seen that the maximum peak-to-peak deviation in a 1-s interval can be as high as 50 Hz, although the root-mean-square deviation is considerably less. At search oscillator frequencies of 3 and 5 MHz, observed deviations were reduced by a factor of 2.

This type of performance was acceptable. Of three modified synthesizers tested, the response of the first was as shown in Fig. 7; a second unit had periodic deviations in the order of 200 Hz, and the third unit had deviations in the order of 500 Hz peak-to-peak. Seven more search oscillator VCO units were supplied by the manufacturer and two units whose performance was equivalent to Fig. 7 were substituted in the second and third synthesizers. These test results show that it would be highly desirable to include this test in the test specifications of synthesizers with VCO-type search oscillators.

5. Information Systems: Toward Deep Space Station Automation Software—REGEN, A Binary-to-Symbolic Translator for the SDS 900 Series Languages,
J. W. Layland

a. Introduction. One article in SPS 37-59, Vol. II (pp. 48–54) and two subsequent articles in this volume (pp. 22–31) discuss algorithmic methods for assembling multiprogramming software packages. These algorithms could be applied manually to the symbolic decks of the programs, automatically to the symbolic decks by a program-combining program, or automatically to the binary load modules by a very sophisticated loader. This latter alternative is desirable for conservation of time and storage if several packages utilizing almost the same set of programs are to be generated on demand. This, of course, requires that timing information be supplied via the binary language and that programs must be written which interpret the binary language in greater detail than does the manufacturer-supplied loader.

With relatively few additional programs, the programs necessary to interpret the binary language for a multi-program scheduler can become a binary-to-symbolic language translator. Because its duties are well defined and its product is more visible, the translator can be written and "debugged" much more easily than could the multiprogram scheduler. Programming of the scheduler when it is eventually done will be an easier task with the important binary language interpreting routines already extant.

The binary-to-symbolic translator is also interesting and useful in its own right for the modification and manipulation of programs for which only the universal binary language version is available, the symbolic version having been lost or being otherwise not available. This article describes REGEN, a binary-to-symbolic translator for the SDS 900 series languages.

b. Program operation. The binary-to-symbolic translation program operates under control of the SDS MONARCH system. All input/output operations are performed by the system library routines MTAPE, CDRP, PYTIO, and PRINT. The input and output devices are selected by a "ΔASSIGN" message to MONARCH prior to loading REGEN. In this assignment message, "BO" specifies the source of the binary program to be translated "X1" specifies a scratch magnetic tape, "SO" specifies the symbolic output device, and "LO" specifies the list output device. REGEN will produce, under breakpoint control, either a symbolic deck which may subsequently be modified and assembled, a code listing whose format closely approximates the format of the listing produced when the input program was initially assembled, or both. If they are set during the initialization for any program, breakpoint 3 deletes the list output and breakpoint 4 deletes the symbolic output. If breakpoint 1 is set, REGEN will pause before translating each program.

Figure 8 shows an example of translator operation. Figure 8a shows the assembly listing of a very short program, Fig. 8b shows an octal dump of the binary tape for this same program, while Fig. 8c shows the listing produced by REGEN from that binary tape. Although it is not nearly as understandable as the original annotated listing, the regenerated listing is far more useful than the octal dump, should the original listing be unavailable. All external labels, both references and definitions, are inserted at the appropriate place in the regenerated deck. Locations which are referenced but do not have an external label are provided with an internal label based upon their address. This internal label consists of an alphabetic–hexadecimal address with $z = 0$, $I = 1, \cdots, Y = 15$, preceded by a prefix which is A9, R9, or C9, depending upon whether that location is absolute, relocatable, or common relocatable. Because the problem of differentiating data from instructions is simplified when all program addresses are relocatable, the output from the translation of a relocatable program will be much more understandable than the output of an absolute program.

c. SDS binary language. The SDS universal binary language can be used to express many more varied descriptions than can be expressed by any of the existing 900-series language processors. Here the basic organization of that language is described. A complete description may be found in the SDS MONARCH or real-time MONITOR manuals (Refs. 1 and 2).

A binary *record* consists of up to 31 words of data. The first word of the record is a control word which specifies the record type, word count, and mode (binary), and contains a parity check on the words of the record. The first three bits of the control word designate the record type: types 000 through 011 are text records, external references and definitions, programmed operator references and definitions, and END records, respectively; type 101 is a data statement record for FORTRAN IV.

The second word of a text record contains the address at which this text group is to be written, two one-bit flags which specify whether this address is absolute, relocatable, or common relocatable, and four one-bit flags which signify the presence of address modifier words for the text words of the record. This is followed by up to twenty-four text words, and, if specified by the flags in word 2, up to four address modifier words. Each modifier word contains one bit for each text word. This bit is a *one* if the associated word is to be modified for load, common, programmed operator, or special input/output relocation.

Type 001 and type 010 records contain up to ten three-word label items. The first two words of each item contain the eight-character binary-coded decimal name. The third word contains a two-bit subtype designator, and for most subtypes, the address to which that name applies and the address modifier flags. For type 010 records, this third word also contains the programmed operator sequence number.

External references are described by "chaining." The external reference item address is the address in the text of the last reference to that label. The address in that

```
( a )
        00000   0 00 00000      1  $KFILT  PZE                    DIGITAL FILTER SUBROUTINE
*       00001   0 53 0 00000    2          SKN     KGAIN
        00002   0 01 0 00004    3          BRU     $+2
        00003   0 51 0 00000    4          BRP     KFILT          DON'T FILTER
*       00004   0 54 0 00000    5          SUB     K1OUT
*       00005   0 64 0 00001    6          MUL     KGAIN
        00006   0 46 00014      7          XAB                    DOUBLEPRECISION INTERMEDIATE
        00007   0 55 0 00015    8          ADD     K2OUT
        00010   0 46 00014      9          XAB
*       00011   0 57 0 00004    10         ADC     K1OUT
*       00012   0 35 0 00011    11         STA     K1OUT
        00013   0 36 0 00015    12         STB     K2OUT
        00014   0 51 0 00000    13         BRR     KFILT
        00015   0 00 00000      14 K2OUT   PZE
                                15         END
        00005                      KGAIN
        00012                      K1OUT


( b )
10455747   42263143   63606060   40100000
02152475   02100000   00000000   05300000   00100004   05100000   05400000   06400001
04600014   05500015   04600014   05700004   03500011   03600015   05100000   00000000
15274000
10752666   42272131   45606060   20100005   42014664   63606060   20100012
30254754   00100016


( c )
                         1           RORG    000000                         REGEN
00000   0 00 00000       2  $KFILT   HLT     000000                         REGEN
00001   0 53 00000       3           SKN     KGAIN                          REGEN
00002   0 01 00004       4           BRU     R9L                            REGEN
00003   0 51 00000       5           BRP     KFILT                          REGEN
00004   0 54 00000       6  R9L      SUB     K1OUT                          REGEN
00005   0 64 00001       7           MUL     KGAIN                          REGEN
00006   0 46 00014       8           RCH     000014                         REGEN
00007   0 55 00015       9           ADD     R9W                            REGEN
00010   0 46 00014       10          RCH     000014                         REGEN
00011   0 57 00004       11          ADC     K1OUT                          REGEN
00012   0 35 00011       12          STA     K1OUT                          REGEN
00013   0 36 00015       13          STB     R9W                            REGEN
00014   0 51 00000       14          BRR     KFILT                          REGEN
00015   0 00 00000       15 R9W      HLT     000000                         REGEN
00016                    16          END                                    REGEN
00005   KGAIN
00012   K1OUT
```

Fig. 8. Short example of program translation: (a) assembly listing, (b) binary tape, and (c) REGENerated listing

cell points in turn to an earlier reference to the label, ultimately pointing in the program text to the first reference to the external reference label.

The second word of an END record contains the address of the next available location after the current program. A transfer address word and modifier word follow optionally. The data statement record is not generated by any of the processors under MONARCH.

d. Program organization. REGEN makes three passes through the binary text of a program, as it translates it. During the first pass, the input records are read, checked for conformity to the syntax of the binary language, and all legal records are transferred to the X1 file. Illegal records are identified if possible and their identity added to the list output. Data statement records, should they be encountered, are octally dumped onto the list output during pass 1 and not used again.

Three lists are built during pass 1 for later processing. A list of all addresses which are the arguments of instructions begins at the end of the REGEN program and its input/output handlers, and grows upwards. A list of external definition items begins just below the MONARCH resident in upper memory and grows downwards. Since all external definition records must precede all external reference records, the definition list is closed before any external references are encountered. A list of external references begins at the end of the definition list and

grows downwards. List formats are compatible with the formats of the external definition items in the SDS binary language. Pass 1 is complete whenever the end record is encountered.

If any external references appear during pass 1, their chains must be completely identified before actual translation can begin. During pass 2, the X1 file is read backwards and the reference chains are followed through the text records. Each new location where a reference occurs is inserted into the address portion of the external reference item in its list. This location is also removed from the address list where it was placed during pass 1. Pass 2 is complete whenever all reference chains have been followed to the first reference in each.

Actual translation and output formatting is performed during the third pass. Prior to performing the third pass, the address list is sorted into monotonic order for ease in searching, and a program block list is established which designates the range over which the location counter varies within the program being translated. The block list ensures that all cells which are referenced are assigned a location. During pass 3, the location counter is stepped sequentially through the range of the program while the text records are read from X1. If the location appears on the external definition list, the appropriate external label is inserted in the output format. If it appears in the external reference list, the instruction operand is replaced by the appropriate external label. If it appears in the address list but is not externally defined, a hexadecimal label is manufactured for it as described previously. If it is required by the instruction in the text word, a hexadecimal label is similarly manufactured for the instruction operand.

The final listing output line format closely approximates the listing format for a symbol assembly, consisting of an octal representation of the text word, the card number, and the label, operation mnemonic, and operand for the symbolic card image. REGEN's symbolic output consists of only the symbolic card image portion of the same line. Pass 3 is complete when the end record is again encountered.

REGEN consists of approximately 2200 METASYM-BOL cards, and assembles into a program which occupies approximately 3K words, exclusive of the input/output subroutines. Except for the sorting of the address list between pass 2 and pass 3, all operations are limited by input/output speed on the SDS 930.

e. Conclusion. This article describes the operation of a binary-to-symbolic translator for the SDS 900 series languages. Although this effort was initiated merely with the intent of familiarization with the SDS binary language—the ultimate goal is a sophisticated multiprogram scheduling loader—this translator can be an extremely useful tool for the examination and manipulation of programs whenever their symbolic source is not readily available but their binary version is.

References

1. *MONARCH manual,* #90-05-66C. Scientific Data Systems, Santa Monica, Calif., July 1967.
2. *Real-Time MONITOR manual,* #90-11-08C. Scientific Data Systems, Santa Monica, Calif., July 1967.

6. Information Systems: Range-Doppler Display System, *A. I. Zygielbaum*

a. Introduction. Advances in the transmitter and receiver capability of the Goldstone DSN Development Facility prior to the most recent Venus conjunction have necessitated the use of more sophisticated processing than was used on previous planetary range-doppler radar observations. In particular, a real-time display of the data and partial maps were required to permit experimenter intervention in the process of iterative averaging of data from mapping many days. A digital video display system (DVDS) was designed to provide this display.

The display consists of an interface to the SDS 930 computer, a data handler, an oscilloscope interface, and a large-screen oscilloscope. With appropriate software support, the display provides the real-time interaction required by the Venus range-doppler mapping effort.

b. Design considerations. For the display of the Venus radar data, the DVDS had to be capable of displaying an image of 80,000 picture elements flicker-free with a maximum number of grey shades. To present a satisfactory image, human visual response had to be considered.

The human observer detects logarithmic brightness change (Ref. 1). A grey scale is defined by equal decibel graduations. Oscilloscope manufacturers (Tektronix and Hewlett–Packard) claim that eight grey shades can be distinguished on a cathode ray tube (CRT). Experiments by the author indicate, however, that twelve grey shades are discernible, although barely.

The displayed image must be stable and linear. Linearity differences of less than 1% are easily noticeable. Also, any "breathing" or jitter of the image is bothersome because the human eye has reflexive motion sensors.

To prevent flicker, the projected image must be refreshed frequently. A human observer sees flicker if a light source is interrupted at a frequency lower than the critical flicker frequency (CFF). Figure 9 plots CFF with respect to the light-to-dark ratio (LDR) and the image luminance (Ref. 1).

The CFF is an important factor in the selection of a CRT phosphor. As the LDR is increased, the CFF decreases. A CRT with longer persistence will require lower refresh rate. Table 3 lists various phosphors and their corresponding decay and required refresh rates for a variable contrast picture (Refs. 1 and 2). A nearly full bright picture necessitates a higher refresh rate. The P 1 phosphor was chosen for the DVDS. This phosphor
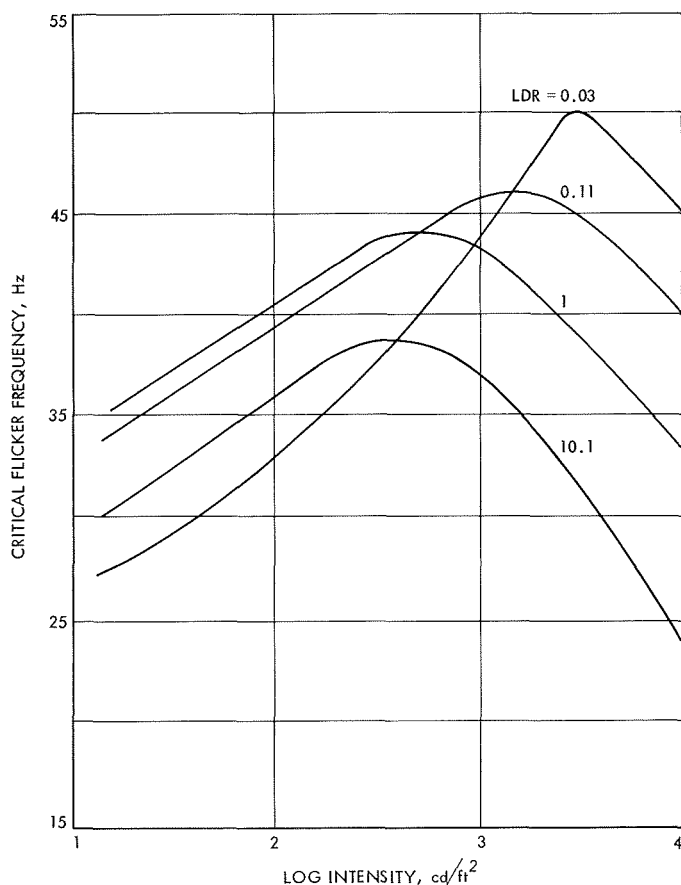
Table 3. Representative phosphors and their characteristics

Characteristic	P 1	P 4	P 7	P 31	P 39	P 40
Color	Yellow-green	White	Blue	Yellow-green	Yellow-green	White
Refresh rate, Hz	32	40	27	55	25	30
Decay to 0.1%, ms	95	20	1500	32	to 10% 150	to 10% 500

requires a 26-Hz refresh rate at low contrast and approximately 40 Hz at high contrast.

c. System design. The DVDS requires a high data transfer rate. To satisfy this, the data multiplex system (DMS) is used to take data from the SDS 930 computer memory. The DMS can operate at nearly full memory bandwidth and needs only minimal software and hardware interfacing.

The format of the data is a two-dimensional array of points. Each point is designated by position and intensity. This format lends itself to display by a TV-type raster scan.

To make the display as versatile as possible, the system was designed to project a picture of up to 120,000 elements. Since at least 40 frames/s must be presented to eliminate flicker, a picture element rate of 4.8 MHz is required. This requirement, together with the memory transfer bandwidth of 13.7 Mbits, limits each picture element to three bits, i.e., eight grey shades. A four grey shade (2-bit) and an on–off mode are also implemented for flexibility in future use.

d. Data multiplex system. The SDS 930 computer has three well-defined input/output interfaces. Referring to Fig. 10, which is the SDS 930 organization, the available paths to memory include the time-multiplexed communications channel (TMCC), the parallel input/parallel output (PIN/POT) channel, and the DMS. The TMCC is the normal input/output path for peripherals such as magnetic tapes and line printers. PIN/POT channels are used for 24-bit parallel word transfers at slow transfer rates. Both paths are controlled directly by the central processing unit (CPU).

The DMS is a device-controlled second path to memory. Although the CPU must supply word count and

Fig. 9. Human visual response to flicker (taken from Ref. 3)
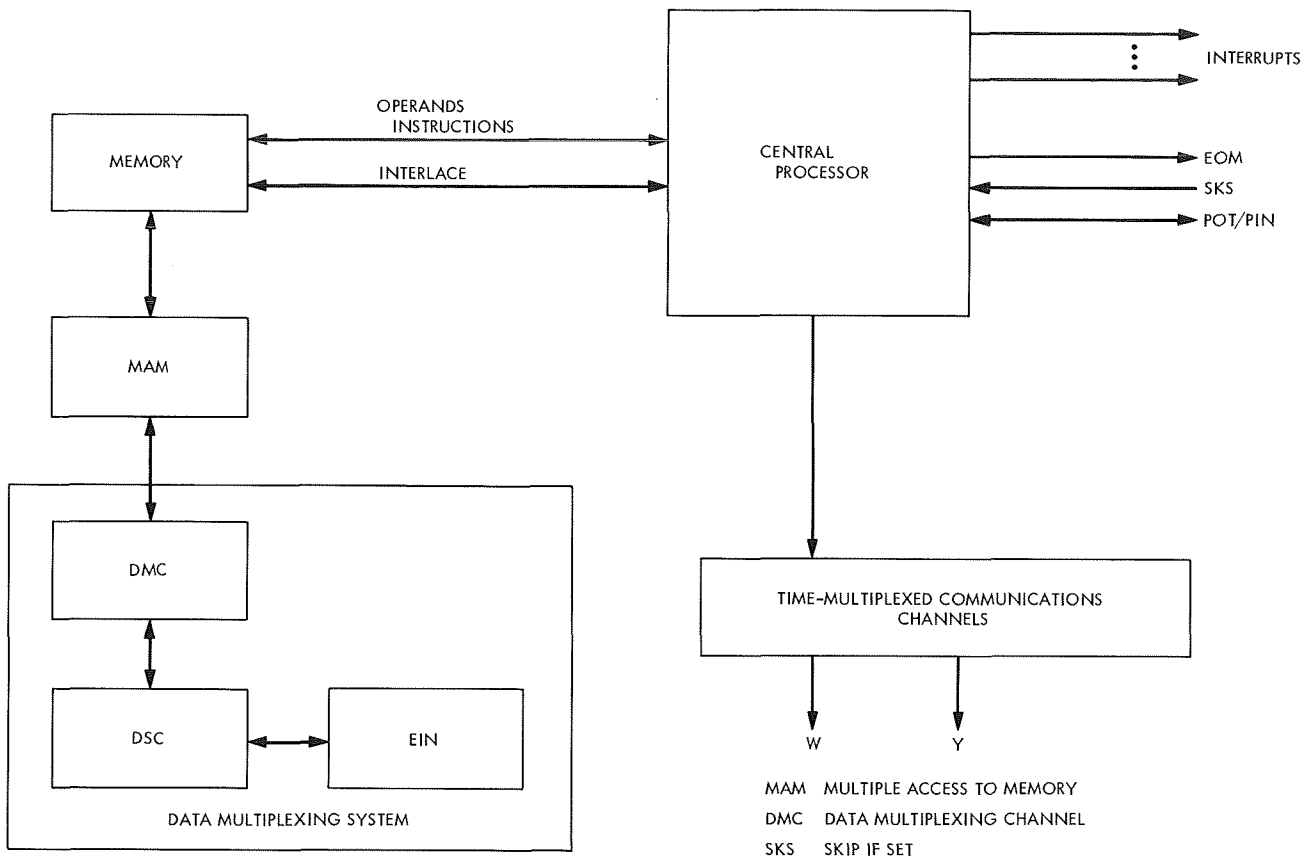
Fig. 10. SDS 930 organization

starting location to the external interlace, an external device can write into, read from, and increment core cells without CPU intervention until word count is exhausted. In the current application, the DMS is used only for readout.

The DMS is controlled through three data lines. Upon activation by the CPU, the DVDS moves these lines to the proper levels for readout under control of the external interlace (EIN). From this point until zero word count, the DVDS requests data from the core memory as needed to fill its buffers.

Two memory locations, even and odd interlace words, are reserved for use by the DMS. The programmer can command the DMS to use the data in either interlace word first and then cycle between the two. Upon activation, the DMS reads out the first interlace word. When the DVDS requests data, the word count is decremented by one and the starting address incremented by one immediately before data is outputted. When the zero word count is reached, an interrupt (ZWC) fires to alert

the CPU. The DMS then replaces the exhausted interlace word and reads the other interlace word. Since the DVDS outputs one line per interlace word, the ZWC interrupt indicates end of line.

It is important to note that the DMS has priority over the CPU in accessing any memory location. Therefore, in the accessing and replacing of the interlace words, the DMS steals two cycles from the CPU. This, of course, prohibits operating the DMS at full bandwidth in a bank of memory containing the program because the DMS would lock out the CPU.

e. Data display. Data to be displayed are stored in core as an array of X scan lines. The first word of each line contains the Y-axis location. For example, refer to Fig. 11, picture array segment. The Y axis is controlled by a 9-bit digital-to-analog converter. The Y location is thus randomly selectable.

Data can be presented in three modes: (1) three bits of Z modulation (8 grey shades), (2) two bits (4 shades),

Fig. 11. Picture array segment

MSD MOST SIGNIFICANT DIGIT
LSD LEAST SIGNIFICANT DIGIT

Fig. 12. Picture array organization

or (3) one bit (on–off). Therefore, 8, 12, or 24 picture elements are packed per computer word in the three modes. The data are read out to the display, the most significant digit first. A typical picture array is shown in Fig. 12.

The X axis can be stepped one, two, or four units for every picture element. Between-word blanking, as well as blanking between scan lines, is provided by the Z channel in order to allow the X and Y channels to settle.

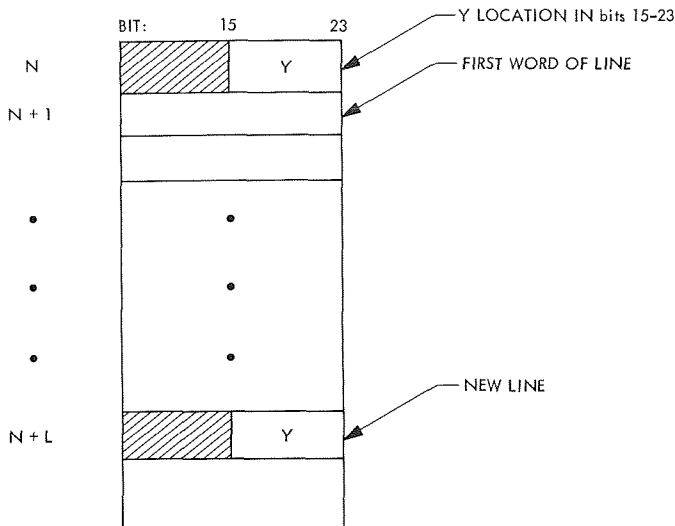Picture elements are presented for an equal time, regardless of the Z mode. Therefore, in the 3-bit mode, data are read out every machine cycle. In the 2-bit mode, data are needed in 2 out of 3 cycles, while only 1 in 3 cycles is accessed in the 1-bit mode.

f. Hardware description. Referring to Fig. 13, DVDS block diagram, the DVDS is divided into three parts. The computer interface control (CIC) commands the DMS to access and output data. It also senses, by means of the ZWC interrupt, that the end of line has been reached, in order to reset the X axis and route the first word of the next line into the Y-axis digital-to-analog buffer.

The mode control is set to its desired state by an EOM–POT sequence. Two octal digits in the POT command designate the Z-axis mode (1, 2, or 3 bits) and the X step (1, 2, or 4 units). The mode control also selects the DMS request rate to once each machine cycle, twice in three cycles or once in three cycles, as explained earlier.

The data control routes data into the Y-axis digital-to-analog buffer or Z-axis shift register. Data (24-bits) are stored in the data acquisition buffer until the Z-axis shift register is emptied. The data control also functions to inform the oscilloscope digital control (ODC) that data is ready for transfer.

The CIC operates at SDS 930 speed and uses the 1.75-μs computer clocks. The ODC operates on an internally generated 15-MHz clock. This clock is turned on only when needed and is turned off after the Z-axis shift register has been emptied.

The ODC operates on a basic cycle of three clock pulses (Fig. 14). The basic controller, the display timing control (DTC), is a three-counter with a fourth state for initialization. The DTC is set to the fourth state at the beginning of the processing of one computer word. This state enables the parallel data transfer from the data acquisition buffer to the Z-axis shift register. The Z register can be shifted one, two, or three steps per cycle depending upon the Z-axis mode selected.

The X axis is stepped once at the beginning of each cycle by adding a known charge to the operational amplifier integrator. At the end of the line, a reset pulse discharges the integrator storage capacitor and sets the beam back to the beginning of the line.

During retrace and X step, the beam is blanked. The Z channel is unblanked at the end of the X step. Because the turn-on time of the Z channel approximately equals the settling time of the X channel, a stable picture element is projected.
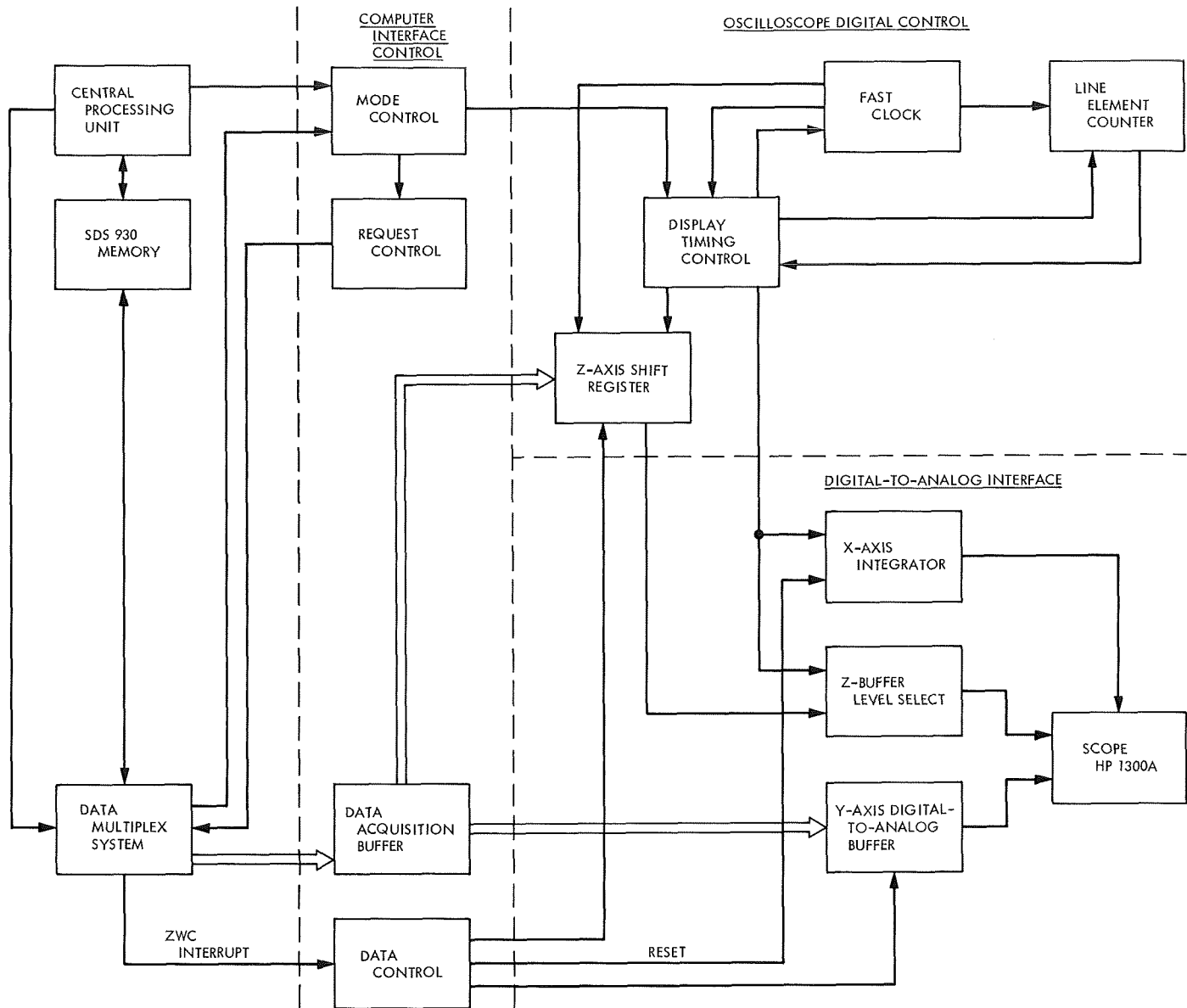
Fig. 13. DVDS block diagram

The line element counter counts the number of Z channel enables. After one word has been processed, the ODC is initialized for the next word.

As stated earlier, the Y-axis word is the first word of the line. After the end of line interrupt, this first word is gated into the Y-axis digital-to-analog buffer. This digital-to-analog converter, a 9-bit device, is allowed 2.25 μs to settle before projection of the first picture element. The Z-channel digital-to-analog converter is an 8-level current select network. It provides one out of

eight, one out of four, or on–off levels. A ninth level is provided by the blanking override which has priority over all other levels.

Due to the extremely high speeds required, a 20-MHz oscilloscope—the Hewlett–Packard 1300A—was chosen as the display oscilloscope. The Z-channel amplifier of this oscilloscope has been slightly modified to improve its transient response.

g. DVDS programming. The DMS has an activation sequence consisting of two EOM–POT instructions. The
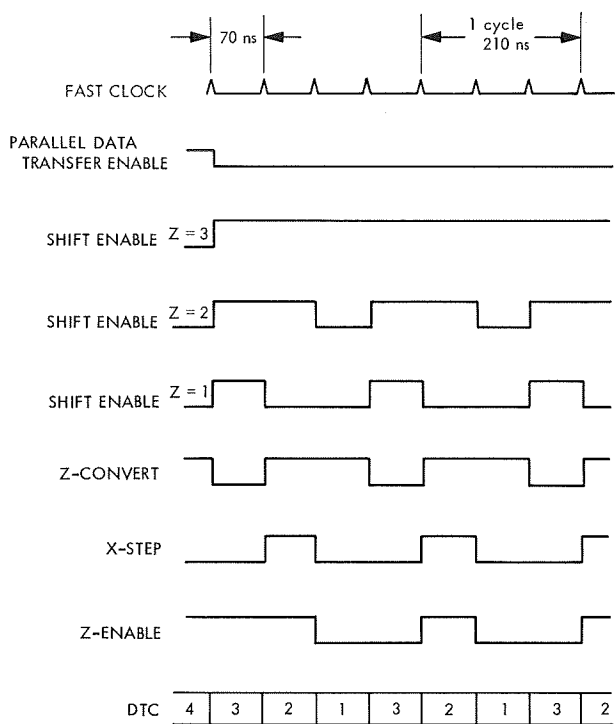
Fig. 14. Display timing

first EOM activates the DMS to control mode. The associated POT controls the end of record or zero word count interrupt arming, interlace word cycling, and designates the first interlace word.

The second EOM sets the DMS to buffer control mode. The lower 12 bits of the succeeding POT'ed word are decoded by devices attached to the DMS. Thus, the *activate* sequence is

EOM	72<u>234</u>	234 is the DSC number
POT	= 6	6 designates ZWC interrupt and cycling
EOM	70234	
POT	= Z X <u>21</u>	21 is the DVDS designation

The octal digits Z and X have the following meaning:

Value	X	Z
1	step X − 4 units	1-bit intensity mode
2	step X − 2 units	2-bit intensity mode
3	step X − 1 unit	3-bit intensity mode

The *deactivate* sequence is simply

EOM	70234
POT	= 0

As indicated previously, at the ZWC interrupt, the last interlace word must be replaced, since it is destroyed by the DMS. The interlace words contain the word count in bits 0–8 and the starting location minus one in bits 9–23. Thus, to output one line, the interlace is loaded with the number of computer words in the line as well as the location of the Y-word minus one.

Table 4. Typical ZWC interrupt routine

LC = number of lines (i.e., 200) less 1

LCA = decremented line count

WL = number of words/line (39)

LIW = last interlace word used

FIW = first interlace word, i.e.,

0	8	23
47	17777	
WL	1st LINE Y LOC − 1	

064	BRM	600	
600	PZE		
	XMA	LIW	save A and LDA with LIW
	SKR	LCA	skip if line count < 0
	BRU	700	to continue frame
	LDA	LC	reset to original
	STA	LCA	word count
	LDA	FIW	reset to FIW
	STA	0234	even interlace word
	STA	0235	odd interlace word
	XMA	LIW	reload A
	BRU	*600	
700	XXA		continue frame, put LIW into X
	EAX	18,2	increment X by 18
	STX	0234	
	STX	0235	
	XXA		LIW to A
	XMA	LIW	reload A
	BRU	*600	

A typical ZWC interrupt routine for a line length of 304 picture elements in the 3-bit Z-mode (38 computer words plus one Y-word or 39 computer words) is given in Table 4.

h. Applications. The DVDS is used to display planetary radar maps of Venus. Successive iterations can be shown so that convergence of the algorithm can be checked. The DVDS can be used to produce motion pictures or moving displays, such as can be used to examine the behavior of the Viterbi decoder for convolutional codes (SPS 37-54, Vol. III, pp. 171–177). Finally, the system is useful as a very fast *X–Y* plotter. Current software plots approximately 7000 data points per second into the raster scan line array.

References

1. Luxemberg, H. R., and Kuehn, R. L., *Display Systems Engineering.* McGraw–Hill Book Co., New York, N.Y., 1968.

2. *General Catalog,* p. 5. Tektronix Corp., Beaverton, Oregon, 1969.

3. Bartlett, S., "The Neural Determination of Critical Flicker Frequency," *J. Exp. Psychol.,* Vol. 21, 1937.

7. Information Systems: Scheduling Algorithms for Multiprocessors in a Hard Real-Time Environment,
C. L. Liu

a. Introduction. Scheduling algorithms for a single processor in the hard real-time environment were studied in SPS 37-59, Vol. II, pp. 48–54, and in a companion article in this SPS (pp. 31–37). In this article, we report some results on scheduling algorithms for multiple rather than single processors. Few of the results obtained for a single processor generalize directly to the multiple processor case; bringing in additional processors adds a new dimension to the scheduling problem. The simple fact that a task can use only one processor even when several processors are free at the same time adds a sur-

prising amount of difficulty to the scheduling of multiple processors. As in the single-processor studies, we assume that all tasks to be executed on a priority basis have periodic requests, fixed computation time at each request, and deadlines which correspond to the subsequent request for each task. A discussion of the appropriateness of these assumptions to the DSIF can be found in SPS 37-59, Vol. II, pp. 48–54.

b. Period-driven scheduling algorithm for multiprocessors. Suppose m tasks are to be scheduled on n processors by the period-driven scheduling algorithm. At any instant, then, among those tasks demanding processor time, the n tasks with the shortest periods will be executed. (Of course, if there are less than n tasks demanding processor time, all of these tasks will be executed.) As is expected, the period-driven scheduling algorithm for multiprocessors is not optimum. To see this, we note that for two processors and a set of three tasks with $T_1 = 4$, $C_1 = 3$, $T_2 = 4$, $C_2 = 3$, $T_3 = 5$, and $C_3 = 2.5$, the period-driven scheduling algorithm is not even feasible.

We have not been able to obtain a necessary and sufficient condition on the feasibility of the period-driven scheduling algorithm. The results here provide a sufficiency test on feasibility.

We study first a special case where $n + 1$ tasks are to be scheduled on n processors. Without loss of generality, we assign each of the n tasks with the shortest periods to a dedicated processor. The task with the longest period will run on any of the n processors whenever a processor becomes free. In other words, the task with the longest period will be run as a background task to the n tasks with shorter periods. Given the values of T_1, T_2, $\cdots$, T_{n+1}, C_1, C_2, $\cdots$, C_n, theorem 1 gives a lower bound to the value of C_{n+1} such that the period-driven scheduling algorithm is feasible.

We define two sets of functions:

$$
f_j(t) = \begin{cases}
0, & t \le T_j - \delta_j \\
t - (T_j - \delta_j), & T_j - \delta_j \le t \le 2T_j - \delta_j - C_j \\
T_j - C_j, & 2T_j - \delta_j - C_j \le t \le 3T_j - C_j - 2\delta_j \\
t - 2(t_j - \delta_j), & 3T_j - C_j - 2\delta_j \le t
\end{cases}
$$

$$g_j(t) = \begin{cases} \left(\left[\dfrac{t}{T_j} \right] - 1 \right) \delta_j + f_j \left(\left\{ \dfrac{t}{T_j} \right\} + T_j \right), & t \geq T_j \\[1em] f_j(t), & t \leq T_j \end{cases}$$

for $j = 1, \cdots, n$, where the δ_j's are computed recursively as

$$\delta_1 = T_1 - C_1$$

$$\delta_i = T_i - C_i + \max \left(g_1(C_i), g_2(C_i), \cdots, g_{i-1}(C_i) \right)$$

for $i = 2, \cdots, n$. The notation $[x]$ means the greatest integer less than x and $\{x\} = x - [x]$, the fractional part of x.

Theorem 1. A lower bound δ_{n+1} to the value of C_{n+1} such that the period-driven scheduling algorithm is feasible for $C_{n+1} \leq \delta_{n+1}$ is

$$\delta_{n+1} = \max \left(g_1(T_{n+1}), g_2(T_{n+1}), \cdots, g_n(T_{n+1}) \right)$$

Proof. By the *background computation time* on a set of processors, we mean the total amount of non-overlapping processor time on these processors available to a background task. Note that the word "non-overlapping" is important, because even when several processors are free at a certain instant, the background task can make use of only one of these processors.

We show first that δ_i, $i = 1, 2, \cdots, n$, is a lower bound to the background computation time on processors $1, 2, \cdots, i$ within each cycle or task i. We note that within a cycle of task i, the ith processor will be occupied by the ith task for C_i seconds and will then be free for the subsequent $T_i - C_i$ seconds. We now want to estimate the background computation time on processors $1, 2, \cdots, i - 1$ during the C_i seconds when the ith processor is occupied by the ith task. We claim that within any C_i contiguous seconds, the background computation time on processors $1, 2, \cdots, j$ is lower-bounded by $g_j(C_i)$. We note that within each cycle of task j there are at least δ_j seconds of background computation time on processors $1, 2, \cdots, j$. Moreover, at least C_j of these δ_j seconds are available at the end of a cycle. Within C_i contiguous seconds, there must be at least $[C_i/T_j] - 1$ complete cycles of task j, as illustrated in Fig. 15. In these $[C_i/T_j] - 1$ complete cycles, the background computation time on processors $1, 2, \cdots, j$ is at least $([C_i/T_j] - 1) \delta_j$ seconds. To estimate the background computation time on processors $1, 2, \cdots, j$, within $\Delta_1 + \Delta_2$, we see that Fig. 15 shows the most unfavorable distribution of background computation time in the two cycles at the ends of the C_i seconds. We, thus, have the estimation

$$\text{background processor time within } \Delta_1 + \Delta_2 \geq \begin{cases} 0, & \Delta_1 + \Delta_2 \leq T_j - \delta_j \\ (\Delta_1 + \Delta_2) - (T_j - \delta_j), & T_j - \delta_j \leq \Delta_1 + \Delta_2 \leq 2T_j - \delta_j - C_j \\ T_j - C_j, & 2T_j - \delta_j - C_j \leq \Delta_1 + \Delta_2 \leq 3T_j - C_j - 2\delta_j \\ (\Delta_1 + \Delta_2) - 2(T_j - \delta_j), & 3T_j - C_j - 2\delta_j \leq \Delta_1 + \Delta_2 \end{cases}$$

It follows that $g_j(C_i)$ is a lower bound to the background computation time on processors $1, 2, \cdots, j$ within any C_i contiguous seconds. This proves the theorem.

To illustrate the application of Theorem 1, let us consider the problem of scheduling three tasks with $T_1 = 3$, $C_1 = 2$, $T_2 = 4$, $C_2 = 3$, and $T_3 = 7$ on two processors. We want to estimate the value of C_3 such that the deadline scheduling algorithm is applicable. We have

$$\delta_1 = T_1 - C_1 = 3 - 2 = 1$$

$$\delta_2 = T_2 - C_2 + g_1(C_2)$$

$$= 4 - 3 + g_1(3)$$

$$= 4 - 3 + 1 = 2$$

$$\delta_3 = \max \left(g_1(T_3), g_2(T_3) \right)$$

$$= \max \left(g_1(7), g_2(7) \right)$$
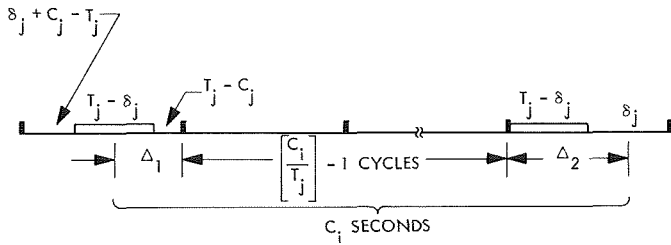
$$= \max (2, 3)$$

$$= 3$$

Fig. 15. Background computation time within C_i

As it turns out, the largest possible value of C_3, such that the period-driven scheduling algorithm is feasible, is also 3, so the deadline-driven and period-driven scheduling algorithms are equally efficient for this situation.

It is interesting to compare the lower bound in Theorem 1 and the actual largest possible value of C_n. Some results are tabulated in Table 5.

The results in Theorem 1 can be applied to the general case when m tasks are to be scheduled on n processors. After computing δ_{n+1} according to Theorem 1, we can lower-bound the background computation time on processors $1, 2, \cdots, m$ in every cycle of task $n + 2$ by

$$\delta_{n+2} = \left(\left[\frac{T_n + 2}{T_n + 1}\right] - 1\right)(\delta_{n+1} - C_{n+1})$$

Similarly, we can have

$$\delta_{n+3} = \left(\left[\frac{T_n + 3}{T_n + 2}\right] - 1\right)(\delta_{n+2} - C_{n+2})$$

and so on. As can be expected, such lower bounds deteriorate very rapidly as the number of tasks increases.

c. Deadline-driven scheduling algorithm for multiprocessors. We want to investigate now the deadline scheduling algorithm for multiprocessors. Unfortunately, we have not yet been able to obtain a necessary and sufficient condition on the feasibility of the algorithm. Neither were we able to obtain a sufficient condition similar to Theorem 1. However, there are some interesting observations.

First, we note that the deadline-driven scheduling algorithm is not always optimum, as the following example illustrates. Let $T_1 = 4$, $C_1 = 3$, $T_2 = 4$, $C_2 = 3$, $T_3 = 5$, and $C_3 = 2.5$. The utilization factor will be 100% if these three tasks can be scheduled on two processors. It is easy to see that for this set of tasks the deadline

Table 5. Comparison of lower bound and actual background computation time for period-driven scheduling of $n + 1$ tasks on n processors

T_i	C_i	T_{n+1}	Lower bound according to theorem 1	Actual maximum
3 4	2 3	7	3	3
3 5	2 4	7	2	2
5 7	2 2	9	5	7
5 7	2 2	31	21	27
5 31	2 7	41	33	34
5 7	4 2	15	10	11
5 20	4 17	30	6	8
5 31	4 27	41	8	11
13 27	9 25	41	12	12
5 7 9	2 2 3	11	7	9
3 5 13 25	2 4 11 21	41	15	21
5 7 9 13 15 31	4 6 7 11 12 27	35	11	18

scheduling algorithm is not feasible. However, these three tasks can be scheduled on two processors, as shown in Fig. 16.

Second, unlike the single-processor case, the deadline scheduling algorithm is not always superior to the period-driven scheduling algorithm. In other words, there are examples in which the period-driven schedule is feasible while the deadline scheduling algorithm is not. Although
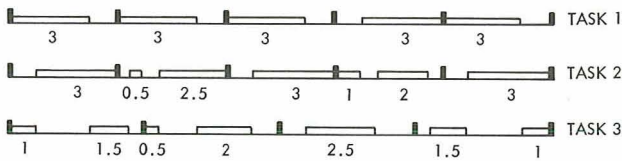
Fig. 16. A feasible schedule for three tasks with 100% utilization of two processors: $T_1 = 4$, $C_1 = 3$, $T_2 = 4$, $C_2 = 3$, $T_3 = 5$, $C_3 = 2.5$

this might sound surprising at first, a moment of reflection indicates that indeed this should have been anticipated. Without complete knowledge of the future timing structure of the tasks to be scheduled, both the period-driven and deadline-driven scheduling algorithms make their decisions on the basis of some local information. Therefore, we should not expect one scheduling algorithm to be always better than another. Table 6 contains some comparison.

In view of the results in Table 6, we conjecture that there is no particular advantage in employing the deadline scheduling algorithm in the case of multiprocessors.

d. Conclusion. Many problems concerning scheduling algorithms for multiprocessors in a hard real-time environment are still open for further investigation, for ex-

ample, proving or disproving the existence of optimum scheduling algorithms and finding such algorithms if they do exist. One difficulty in designing "good" scheduling algorithms is the problem of predicting the global timing structures of the tasks on the basis of some local information (e.g., the deadlines of the current requests). Both the period-driven scheduling algorithm and the deadline-driven scheduling algorithm offer some very simple decision rules for scheduling a set of tasks on several processors. However, we have not yet obtained any measurement on the effectiveness of the algorithms as compared to other scheduling algorithms.

8. Information Systems: Scheduling Algorithms for Hard Real-Time Multiprogramming of a Single Processor, C. L. Liu

a. Introduction. In SPS 37-59, Vol. II, pp. 48–54, Layland studied an algorithmic method for scheduling tasks with periodic requests on a time-shared computer. In this article, another algorithmic method is proposed for single processors and investigated. This method is optimum in the sense that if a set of tasks can be scheduled by some algorithmic method, it can also be scheduled by this method. In other words, the least upper bound on processor efficiency using this algorithm is uniformly 100%, and this efficiency can be attained by adjusting

Table 6. Comparison of period-driven and deadline-driven scheduling

Number of processors	Number of jobs	T_i	C_i	T_{n+1}	Maximum C_{n+1} using period-driven scheduling algorithm	Maximum C_{n+1} using deadline-driven scheduling algorithm
2	3	4 4	3 3	5	1	2
2	3	3 4	2 3	7	3	3
2	3	5 20	4 17	30	8	9
2	3	5 7	2 2	9	7	7
2	3	5 7	2 2	15	11	11
2	3	5 31	4 27	41	11	9
4	5	3 5 13 25	2 4 11 21	41	21	17

either the period or the computation time of any one of the tasks to be scheduled.

We follow the assumptions discussed in SPS 37-59, Vol. II, on the hard real-time environment. We shall refer to the scheduling algorithm in that article as the *period-driven scheduling algorithm* because priorities are assigned to tasks according to their periods. When a set of tasks are scheduled by some scheduling algorithm, we say that there is an overflow at time t if a request that should have been satisfied by time t was not satisfied at that time. For a given set of tasks, a scheduling algorithm is said to be *feasible* if the tasks are scheduled such that no overflow occurs.

b. Deadline scheduling algorithm.

We define a *deadline-driven scheduling algorithm* as one in which priorities are assigned to tasks according to the deadlines of their current requests. A task will be assigned the highest priority if the deadline of its current request is the nearest, and will be assigned the lowest priority if the deadline of its current request is the farthest. At any instant, the task of the highest priority with a yet unfulfilled request will be executed. Such a method of assigning priorities to the tasks is a dynamic one, in contrast to a static assignment in which priorities of tasks do not change with time.

Given a set of tasks with periods $T_1, T_2, \cdots, T_m$ and computation time $C_1, C_2, \cdots, C_m$, we want to establish a necessary and sufficient condition for the feasibility of the deadline-driven scheduling algorithm. We have first a lemma:

Lemma 1. When the deadline-driven scheduling algorithm is used to schedule a set of tasks on a single processor, there is no processor idle-time prior to an overflow.

Proof. Suppose that there are processor idle-periods prior to an overflow. To be specific, starting at time 0, let t_3 denote the time at which an overflow occurs, and let
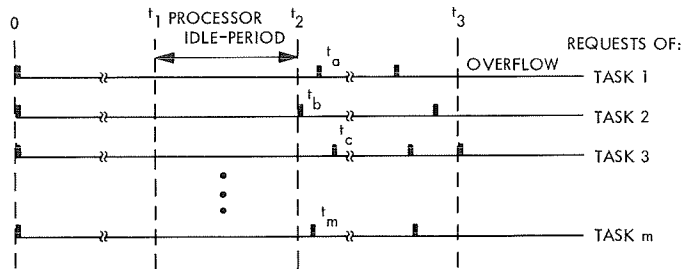
Fig. 17. Processing overflow following a processor idle period

t_1 and t_2 denote the beginning and the end, respectively, of the processor idle-period closest to t_3 (that is, there is no processor idle-time between t_2 and t_3). The situation is illustrated in Fig. 17, where the request-times of the first request of the m tasks after the processor idle-period are denoted $t_a, t_b, \cdots, t_m$.

Suppose that from t_2 on we move all requests of task 1 up so that t_a will coincide with t_2. Since there was no processor idle-time between t_2 and t_3, there will be no processor idle-time after t_a is moved up. Moreover, an overflow will occur either at or before t_3. Repeating the same argument for all other tasks, we conclude that if all tasks are initiated at t_2, there will be an overflow with no processor idle-period prior to it. However, this is a contradiction to the assumption that starting at time 0 there is a processor idle-period prior to an overflow. This proves Lemma 1.

We are now ready to establish the following theorem:

Theorem 1. For a given set of m tasks, the deadline-driven scheduling algorithm is feasible if and only if

$$\frac{C_1}{T_1} + \frac{C_2}{T_2} + \cdots + \frac{C_m}{T_m} \leq 1$$

Proof. To show the necessity, let us calculate the total demand of computation time by all tasks between $t = 0$ and $t = T_1 T_2 \cdots T_m$, which is

$$(T_2 T_3, \cdots, T_m) C_1 + (T_1 T_3, \cdots, T_m) C_2 + \cdots + (T_1 T_2, \cdots, T_{m-1}) C_m$$

If the total demand exceeds the available processor time, that is, if

$$(T_2 T_3, \cdots, T_m) C_1 + (T_1 T_3, \cdots, T_m) C_2 + \cdots + (T_1 T_2, \cdots, T_{m-1}) C_m > T_1 T_2, \cdots, T_m \tag{1}$$

there is clearly no feasible scheduling algorithm. Inequality (1) can be written as

$$\frac{C_1}{T_1} + \frac{C_2}{T_2} + \cdots + \frac{C_m}{T_m} > 1$$

To show the sufficiency, let us assume that the condition

$$\frac{C_1}{T_1} + \frac{C_2}{T_2} + \cdots + \frac{C_m}{T_m} \leq 1$$

is satisfied and yet the scheduling algorithm is not feasible. That is, there is an overflow between $t = 0$ and $t = T_1 T_2 \cdots T_m$. Moreover, according to Lemma 1, there is a time $(0 \leq T \leq T_1 T_2 \cdots T_m)$ at which there is an overflow with no processor idle-time between 0 and T. To be specific, let $a_1, a_2, \cdots, b_1, b_2, \cdots$ denote the request-times of the m tasks immediately prior to T, where $a_1, a_2, \cdots$ are the request-times of tasks with deadlines at T, and $b_1, b_2, \cdots$ are the request-times of tasks with deadlines beyond T. This situation is illustrated in Fig. 18.

In the following, we use $[x]$ to denote the greatest integer less than x. We examine two cases:

Case 1. None of the computations requested at $b_1, b_2, \cdots$ is carried out before T. In this case, the total demand of computation time between 0 and T is

$$\left[\frac{T}{T_1}\right] C_1 + \left[\frac{T}{T_2}\right] C_2 + \cdots + \left[\frac{T}{T_m}\right] C_m$$

Since there is no processor idle-period, we have

$$\left[\frac{T}{T_1}\right] C_1 + \left[\frac{T}{T_2}\right] C_2 + \cdots + \left[\frac{T}{T_m}\right] C_m > T$$
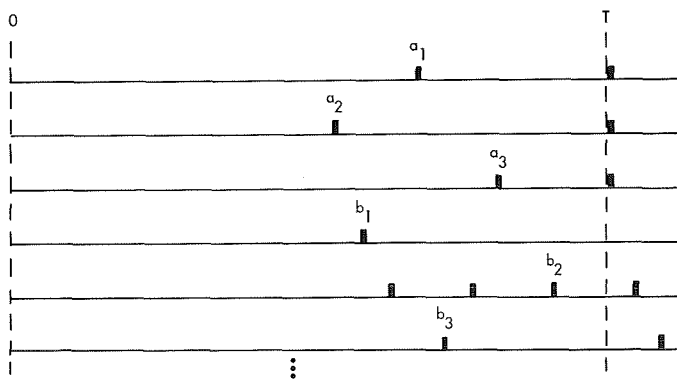
Fig. 18. Processing overflow at time T
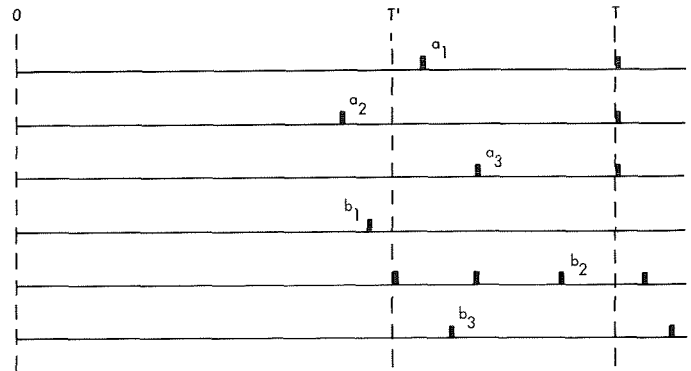
REQUESTS WITH DEADLINES AT a_1 AND a_3 WERE FULFILLED BEFORE T'

Fig. 19. Processing overflow at time T without execution of $\{b_i\}$ following T'

Since

$$\frac{T}{T_1} > \left[\frac{T}{T_1}\right], \frac{T}{T_2} \geq \left[\frac{T}{T_2}\right], \cdots, \frac{T}{T_m} \geq \left[\frac{T}{T_m}\right]$$

we have

$$\frac{T}{T_1} C_1 + \frac{T}{T_2} C_2 + \cdots + \frac{T}{T_m} C_m > T$$

or

$$\frac{C_1}{T_1} + \frac{C_2}{T_2} + \cdots + \frac{C_m}{T_m} > 1$$

which is a contradiction to Inequality (1).

Case 2. Some of the computations requested at $b_1, b_2, \cdots$ were carried out before T. Since an overflow occurs at T, there must exist a point T' such that none of the requests at $b_1, b_2, \cdots$ is carried out within the interval $T' \leq t \leq T$. In other words, within $T' \leq t \leq T$, only those requests with deadlines at or before T will be executed, as illustrated in Fig. 19. Moreover, the fact that one or more of the tasks having requests at the b_i's is executed until $t = T'$ means that all those requests initiated before T' with deadlines at or before T have been fulfilled before T'. Therefore, the total demand of processor time within $T' \leq t \leq T$ is less than or equal to

$$\left[\frac{T - T'}{T_1}\right] C_1 + \left[\frac{T - T'}{T_2}\right] C_2 + \cdots + \left[\frac{T - T'}{T_m}\right] C_m$$

That an overflow occurs at T means that

$$\left[\frac{T-T'}{T_1}\right]C_1 + \left[\frac{T-T'}{T_2}\right]C_2 + \cdots + \left[\frac{T-T'}{T_m}\right]C_m > T - T'$$

which implies again

$$\frac{C_1}{T_1} + \frac{C_2}{T_2} + \cdots + \frac{C_m}{T_m} > 1$$

and we have a contradiction to Inequality (1). Theorem 1 is proved.

Corollary 1-1. The deadline-driven scheduling algorithm is optimum.

Proof. No scheduling algorithm at all is feasible for a set of tasks if

$$\frac{C_1}{T_1} + \frac{C_2}{T_1} + \cdots + \frac{C_m}{T_m} > 1$$

which is the converse of the necessary and sufficient conditions for the deadline-driven algorithm to work.

c. Combination of period-driven and deadline-driven scheduling algorithm. We now derive the necessary and sufficient condition for the feasibility of a class of scheduling algorithms which are combinations of the period-driven scheduling algorithm and the deadline-driven scheduling algorithm. We call such a scheduling algorithm a *mixed* scheduling algorithm. The study of the mixed algorithms is motivated by the observation that the interrupt hardware of present-day computers acts as a fixed-priority scheduler. The deadline-driven scheduler could perhaps be best implemented as a software scheduler for the slower tasks. This implementation should be considerably cheaper than a hardware deadline-driven scheduler, and, as will be seen, will provide most of the advantages of one. To be specific, let tasks 1, 2, $\cdots$, k, the k tasks of shortest periods, be scheduled according to the period-driven scheduling algorithm, and let the remaining tasks, tasks $k+1$, $k+2$, $\cdots$, m, be scheduled according to the deadline-driven scheduling algorithm when the processor is not occupied by tasks 1, 2, $\cdots$, k.

Let $a(t)$ be a non-decreasing function of t; $a(t)$ is said to be sublinear if, for all t and all T,

$$a(T) \leq a(t+T) - a(t)$$

We define the availability function of a processor for a set of tasks as the accumulated processor time from 0 to t available to this set of tasks. Suppose that k tasks have been scheduled on a processor by the period-driven scheduling algorithm. We let $a_k(t)$ denote the availability function of the processor for tasks $k+1$, $k+2$, $\cdots$, m. Clearly, $a_k(t)$ is non-decreasing.

Lemma 2. $a_k(t)$ is sublinear.

Proof. Use the critical time zone argument as in SPS 37-59, Vol. II, pp. 48–54.

Lemma 3. If a set of tasks are scheduled by the deadline-driven scheduling algorithm on a processor whose availability function is sublinear, then there is no processor idle-period prior to an overflow.

Proof. Similar to that of Lemma 1.

Theorem 2. A necessary and sufficient condition for the feasibility of the deadline-driven scheduling algorithm with respect to a processor with availability function $a_k(t)$ is

$$\left[\frac{t}{T_{k+1}}\right]C_{k+1} + \left[\frac{t}{T_{k+2}}\right]C_{k+2} + \cdots + \left[\frac{t}{T_m}\right]C_m \leq a_k(t)$$

for all t's which are multiples of T_{k+1}, or of T_{k+2}, $\cdots$, or of T_m.

Proof. The proof is quite similar to that of Theorem 1. To show the necessity, we observe that at any moment, the total demand of processor time cannot exceed the total available processor time. Thus, we must have

$$\left[\frac{t}{T_{k+1}}\right]C_{k+1} + \left[\frac{t}{T_{k+2}}\right]C_{k+2} + \cdots + \left[\frac{t}{T_m}\right]C_m \leq a_k(t)$$

for all t.

To show the sufficiency, we assume that the condition stated in the theorem is satisfied and yet there is an overflow at T. We examine the two cases considered in the proof of Theorem 1. For case 1, we have the inequality

$$\left[\frac{T}{T_{k+1}}\right]C_{k+1} + \left[\frac{T}{T_{k+2}}\right]C_{k+2} + \cdots + \left[\frac{T}{T_m}\right]C_m > a_k(T)$$

which is a contradiction to our assumption. Note that T is multiple of T_{k+1}, or T_{k+2}, $\cdots$, or T_m. For case 2, we have the inequality

$$\left[\frac{T-T'}{T_{k+1}}\right]C_{k+1} + \left[\frac{T}{T_{k+1}}\right]C_{k+2} + \cdots + \left[\frac{T-T'}{T_m}\right]C_m > a_k(T-T')$$

Let ϵ be the smallest non-negative quantity such that $T - T' - \epsilon$ is a multiple of T_{k-1}, or T_{k-2}, $\cdots$, or T_m. We have

$$\left[\frac{T-T'-\epsilon}{T_{k-1}}\right] = \left[\frac{T-T'}{T_{k-1}}\right], \left[\frac{T-T'-\epsilon}{T_{k-2}}\right] = \left[\frac{T-T'}{T_{k+2}}\right], \cdots, \left[\frac{T-T'-\epsilon}{T_m}\right] = \left[\frac{T-T'}{T_m}\right]$$

and thus

$$\left[\frac{T-T'-\epsilon}{T_{k+1}}\right]C_{k+1} + \left[\frac{T-T'-\epsilon}{T_{k+2}}\right]C_{k+2} + \cdots + \left[\frac{T-T'-\epsilon}{T_m}\right]C_m > a_k(T-T') \text{ and } \geq a_k(T-T'-\epsilon)$$

which is a contradiction to our assumption.

d. A special case of the mixed scheduling algorithm. Although the result in Theorem 2 is a useful general result, its application involves the solution of a large set of inequalities. We investigate now a special case in which three tasks are scheduled by the mixed scheduling algorithm such that the task with the shortest period is scheduled by the period-driven scheduling and the other two tasks are scheduled by the deadline-driven scheduling algorithm. We want to illustrate how sufficient conditions on feasibility can be derived from the result in Theorem 2. We have:

Theorem 3. If

$$1 - \frac{C_1}{T_1} - \min\left(\frac{T_1-C_1}{T_2}, \frac{C_1}{T_2}\right) \geq \frac{C_2}{T_2} + \frac{C_3}{T_3}$$

then the mixed scheduling algorithm is feasible.

Proof. According to Theorem 2, a necessary and sufficient condition for the mixed scheduling algorithm to be feasible is

$$\left[\frac{t}{T_2}\right]C_2 + \left[\frac{t}{T_3}\right]C_3 \leq f(t, T_1, C_1) \qquad (2)$$

for all t's which are multiples of T_2 or T_3;$f(t, A, B)$ denotes

$$\left[\frac{t}{A}\right](A - B) + \max\left(o, \left\{\frac{t}{A}\right\} - B\right)$$

$\{x\}$ denotes $x - [x]$, the fractional part of x.

Since

$$f(t, T_1, C_1) \geq \left[\frac{t}{T_1}\right](T_1 - C_1) + \left\{\frac{t}{T_1}\right\} - C_1$$

and

$$f(t, T_1, C_1) \geq \left[\frac{t}{T_1}\right](T_1 - C_1)$$

Inequality (2) is implied either by

$$\left[\frac{t}{T_2}\right]C_2 + \left[\frac{t}{T_3}\right]C_3 \leq \left[\frac{t}{T_1}\right](T_1 - C_1) + \left\{\frac{t}{T_1}\right\} - C_1$$

$$(3)$$

or by

$$\left[\frac{t}{t_2}\right]C_2 + \left[\frac{t}{T_3}\right]C_3 \leq \left[\frac{t}{T_1}\right](T_1 - C) \qquad (4)$$

Since

$$\left[\frac{t}{T_1}\right](T_1 - C_1) + \left\{\frac{t}{T_1}\right\} - C_1$$

$$= \left[\frac{t}{T_1}\right]T_1 - \left[\frac{t}{T_1}\right]C_1 + t - \left[\frac{t}{T_1}\right]T_1 - C_1$$

$$= t - \left[\frac{t}{T_1}\right]C_1 - C_1$$

$$\geq t - \frac{t}{T_1}C_1 - C_1$$

Inequality (3) is implied by

$$\left[\frac{t}{T_2}\right] C_2 + \left[\frac{t}{T_3}\right] C_3 \leq t - \frac{t}{T_1} C_1 - C_1$$

which, in turn, is implied by

$$\frac{t}{T_2} C_2 + \frac{t}{T_3} C_3 \leq t - \frac{t}{T_1} C_1 - C_1$$

which can be written as

$$\frac{C_2}{T_2} + \frac{C_3}{T_3} \leq 1 - \frac{C_1}{T_1} - \frac{C_1}{t}$$

Since

$$1 - \frac{C_1}{T_1} - \frac{C_1}{t} \geq 1 - \frac{C_1}{T_1} - \frac{C_1}{T_2}$$

for all t's which are multiples of T_2 or T_3, we conclude that Inequality (3) is implied by the inequality

$$\frac{C_2}{T_2} + \frac{C_3}{T_3} \leq 1 - \frac{C_1}{T_1} - \frac{C_1}{T_2}$$

Since

$$\left[\frac{t}{T_1}\right] (T_1 - C_1) \geq \left(\frac{t}{T_1} - 1\right) (T_1 - C_1)$$

Inequality (4) is implied by

$$\left[\frac{t}{T_2}\right] C_2 + \left[\frac{t}{T_3}\right] C_3 \leq \left(\frac{t}{T_1} - 1\right) (T_1 - C_1)$$

which is, in turn, implied by

$$\frac{t}{T_2} C_2 + \frac{t}{T_3} C_3 \leq \frac{t}{T_1} (T_1 - C_1) - (T_1 - C_1)$$

which can be written

$$\frac{C_2}{T_2} + \frac{C_3}{T_3} \leq \frac{T_1 - C_1}{T_1} - \frac{T_1 - C_1}{t} \qquad (5)$$

Again, Inequality (5) is implied by

$$\frac{C_2}{T_2} + \frac{C_3}{T_3} \leq 1 - \frac{C_1}{T_1} - \frac{T_1 - C_1}{T_2}$$

which proves the result. We also have:

Theorem 4. If the following three inequalities hold,

$$C_2 \leq a_1(T_2)$$

$$\left[\frac{T_3}{T_2}\right] C_2 + C_3 \leq a_1 \left(\left[\frac{T_3}{T_2}\right] T_2\right)$$

$$\left(\left[\frac{T_3}{T_2}\right] + 1\right) C_2 + C_3 \leq a_1 (T_3)$$

then the mixed scheduling algorithm is feasible.

Proof. To simplify the notations, let $k = [T_3/T_2]$. According to Theorem 2, the following two inequalities must be satisfied:

$$iC_2 + \left[\frac{iT_2}{T_3}\right] C_3 \leq a_1 (i T_2), \qquad i = 1, 2, \cdots$$

$$(6)$$

$$\left[\frac{iT_3}{T_2}\right] C_2 + iC_3 \leq a_1 (iT_3), \qquad i = 1, 2, \cdots$$

$$(7)$$

Since $j\, a_1(T_2) \leq a_1(jT_2)$ for any $j \geq 0$, the inequality

$$C_2 \leq a_1(T_2) \qquad (8)$$

implies all inequalities of the form

$$j\, C_2 \leq a_1(j T_2), \qquad j \geq 0$$

We now claim that Inequality (8), together with

$$k\, C_2 + C_3 \leq a_1(kT_2) \qquad (9)$$

implies all inequalities in Inequality (6). Let

$$\left[\frac{iT_2}{T_3} = p\right]$$

Then $i > pk$. Let $i = pk + d, d > 0$. Addition of Inequalities (8) and (9) weighted by d and p, respectively, gives

$$(pk + d)\, C_2 + pC_3 \leq p\, a_1(kT_2) + d\, a_1(T_2)$$
$$\leq a_1 (pk\, T_2) + a_1(d\, T_2)$$
$$\leq a_1 ((pk + d)\, T_2)$$

That is,

$$i\,C_2 + \left[\frac{iT_2}{T_3}\right] C_3 \leq a_1(iT_2)$$

We show next that the inequality

$$(k+1)\,C_2 + C_3 \leq a_1(T_3)$$

implies all inequalities in Inequality (2). Since $i(k+1) \geq [iT_2/T_2]$, the inequality

$$i(k+1)\,C_2 + i\,C_3 \leq i\,a_1(T_3)$$

implies

$$\left[\frac{iT_3}{T_2}\right] C_2 + i\,C_3 \leq i\,a_1(T_3)$$

which in turn implies

$$\left[\frac{iT_3}{T_2}\right] C_2 + i\,C_3 \leq a_1(iT_3)$$

The theorem is proved.

e. Comparison and comment. The constraints developed by Theorems 2 to 4 strongly suggest that 100% utilization is not achievable universally by the mixed scheduling algorithm. The following simple example will illustrate: Let $T_1 = 3$, $T_2 = 4$, $T_3 = 5$, and $C_1 = C_2 = 1$. Since $a_1(20) = 13$, it can be easily seen that the maximum allowable $C_3 = 2$. The corresponding utilization factor is

$$\mu = \frac{1}{3} + \frac{1}{4} + \frac{2}{5} = 98.3\%$$

If these three tasks are scheduled by the deadline scheduling algorithm, C_2 can increase to $2.0833\cdots$ and achieve 100% utilization. If they are all scheduled by the period-driven scheduling algorithm, C_2 is restricted to 1 or less and utilization is restricted to at most

$$\mu = \frac{1}{3} + \frac{1}{4} + \frac{1}{5} = 78.3\%$$

which is only slightly greater than the worst-case three-task utilization bound.

Although a closed-form expression for the least upper bound to processor utilization has not been found for the mixed scheduling algorithm, this example strongly suggests that the bound is considerably less restrictive for the mixed algorithm than for the period-driven algorithm. The mixed algorithm may thus be appropriate for many applications, since it can be implemented via the interrupt hardware of present day computers, and provides most of the capability of the fully deadline-driven algorithm.

B. Communications Elements Research

1. Improved RF Calibration Techniques: System-Operating Noise-Temperature Calibrations of the JPL Research Cones, C. T. Stelzried

The system-operating noise-temperature performance of the low-noise research cones is reported. The operating noise-temperature calibrations are performed with the ambient termination technique (SPS 37-42, Vol. III, pp. 25–32). The principal advantage of this method is the stability and reliability of the ambient termination.

The research cones using this operational technique during this reporting period are:

(1) S-band planetary radar (SPR) cone.

(2) S-band research operational (SRO) cone.

(3) S-band cassegrain ultra (SCU) cone.

These cones are operated at the DSS 13 and 14 antennas in a cassegrain configuration.[1] The calibration parameters of the JPL research cones are summarized in Table 7.

The averaged operating noise-temperature calibrations were taken for the various research cone configurations during the period June 1 through October 1, 1969. The various cases are defined in Table 8. The calibrations are presented in Table 9. The data taken at DSS 14 with maser 2 (cases 7 and 8) used an aperture load placed in position by hand over the horn opening.

The operating noise-temperature data were reduced with JPL computer program ID 5841000, CTS 20B. The indicated errors in Table 9 are the standard deviation of the individual measurements and of the means, and

---

[1]The calibration data were taken by Goldstone DSCC personnel at the stations indicated.

Table 7. Calibration parameters of the JPL research cones

Cone			Con-struction date	Fre-quency, MHz	Maser		Noise box correction, dB		VSWR[c]			Approximate zenith low-noise path operating noise temperature, °K		Comments
Model	SN	Mod			SN	Temperature, °K	C_1 (gain)[a]	C_2 (VSWR)[b]	S_A	S_e	S_P	Ground-located	Antenna-mounted	
SPR	01	02	5/68	2295		5.3	26.0	20.0	1.250	1.174	1.280			SPS 37-53, Vol. II, pp. 87–90
				2388		5.0	26.0	20.0	1.084	1.463	1.020	17.5	21.0	
SRO	01	00	7/69	2295	02	5.3	33.0	33.0	1.020	1.174	1.128		18.8	SPS 37-56, Vol. II, pp. 110–113
				2388		5.0	33.0	33.0	1.040	1.463	1.010		17.1	
SCU				2297	05	4.2	33.0	33.0	1.061	1.135	1.001	13.1	16.9	SPS 37-58, Vol. II, pp. 55–56
				2388		4.2	33.0	33.0	1.130	1.300[d]	1.081		22.6	
	01	02	6/69											
SCU (3A)				2297	03	5.5	33.0	33.0	1.004	1.135	1.003		22.1	
				2388		5.5	33.0	33.0	1.284	1.300[d]	1.292			

[a]C_1 = Path loss to maser input referenced to maser output.

[b]C_2 = Path loss to maser input referenced to termination or antenna under evaluation.

[c]S_A, S_e, S_P = VSWR, defined at maser input, of antenna (right-handed circular polarization), maser input, and ambient termination, respectively.

[d]Estimated.

do not include instrumentation systematic errors. The averages were computed using only data with:

(1) Antenna at zenith.

(2) Clear weather.

(3) No RF spur in receiving passband.

(4) $PE_{T_{op}}D$ less than $0.1°K$ (from computer program).

Figure 20 shows a graph of the measurement results taken with the SPR and SRO cones operating on the 85-ft-diam DSS 13 antenna.

Some data have been taken with the SCU cone on the DSS 14 210-ft-diam antenna as a function of elevation angle (Fig. 21). It will be of interest to compare this profile with that taken when the cone is installed on the tri-cone configuration. The operating noise temperature at an elevation angle θ is related to that at zenith by

$$T_{op}(\theta) = T_{op}(90) + \left(\frac{1}{L_0} - \frac{1}{L}\right)(T_{sky} - T_{cosmic}) \quad (1)$$

where

L_0 = atmospheric loss at zenith, ratio

L = atmospheric loss at elevation angle θ, ratio

T_{sky} = "equivalent" temperature of atmosphere, °K

T_{cosmic} = cosmic noise temperature, °K

Assuming a flat earth with an atmosphere of finite height and uniform density,

$$L, dB = \frac{L_0, dB}{\sin \theta} \quad (2)$$

so that

$$L_0 = \exp\left(\frac{\ln 10}{10} L_0, dB\right) \quad (3)$$

and

$$L = \exp\left(\frac{\ln 10}{10}\frac{L_0, dB}{\sin \theta}\right) = (L_0)\frac{1}{\sin \theta} \quad (4)$$

Equation (1) is shown for comparison with measurements in Fig. 21, assuming $(T_{sky} - T_{cosmic}) = 260°K$ for values of zenith atmospheric loss which straddle the data. Additional data are shown in Fig. 22, indicating the small effect of azimuth on system-operating noise temperature as a function of elevation angle for DSS 14.

Table 8. Case number definition for the various cone calibration configurations

Case Number	DSS	Frequency, MHz	Cone	Configuration
1	13	2388	SPR	
2	13	2388	SRO	
3	13	2295	SRO	
4	13	2297	SCU	Cone on ground
5	14	2388	SCU	Maser 1, R&D receiver
6	14	2297	SCU	Maser 1, DSN receiver
7	14	2297	SCU	Maser 2, DSN receiver
8	14	2297	SCU	Maser 2, DSN receiver, diplexed

Table 9. Averaged system-operating noise-temperature calibrations of the various research cones operational from June 1 through October 1, 1969

Case Number	Maser gain, dB	Follow-up noise temperature contribution, °K	System-operating noise temperature, °K
1	37.9 ±0.33/0.05 (48 measurements)	0.94 ±0.09/0.01 (36 measurements)	21.3 ±0.41/0.07 (36 measurements)
2	36.7 ±1.8/0.32 (31 measurements)	0.83 ±0.08/0.01 (29 measurements)	17.1 ±0.51/0.01 (29 measurements)
3	—	0.05 ±0.02/0.01 (3 measurements)	18.8 ±0.43/0.25 (3 measurements)
4	49.1 ±0.56/0.11 (25 measurements)	0.07 ±0.01/0.00 (6 measurements)	13.1 ±1.1/0.43 (6 measurements)
5	34.6 ±0.32/0.08 (17 measurements)	2.5 ±0.53/0.16 (11 measurements)	22.6 ±0.82/0.25 (11 measurements)
6	48.0 ±0.38/0.05 (51 measurements)	1.2 ±0.91/0.13 (51 measurements)	16.9 ±0.96/0.13 (51 measurements)
7	50.0 ±0.81/0.23 (12 measurements)	0.26 ±0.23/0.07 (12 measurements)	22.1 ±0.40/0.12 (12 measurements)
8	50.1 ±0.30/0.12 (6 measurements)	0.58 ±0.31/0.13 (6 measurements)	24.6 ±5.1/2.1 (6 measurements)

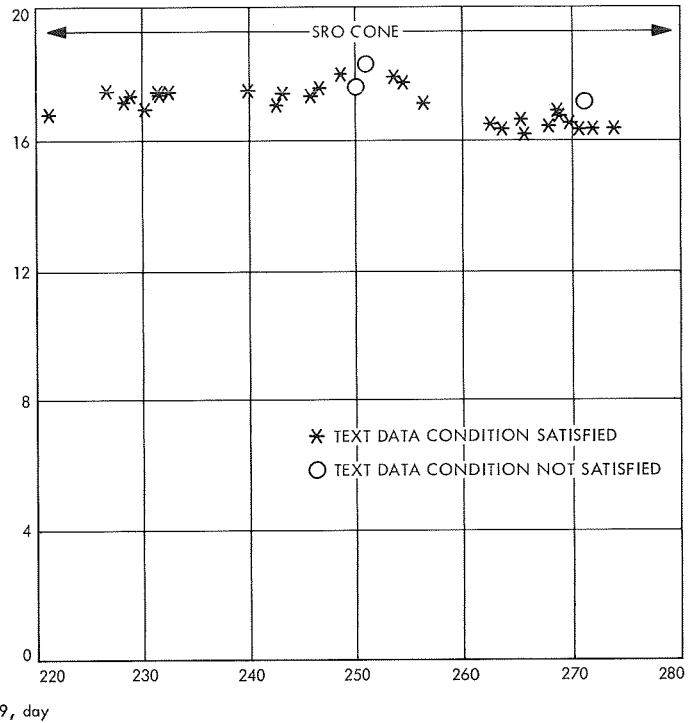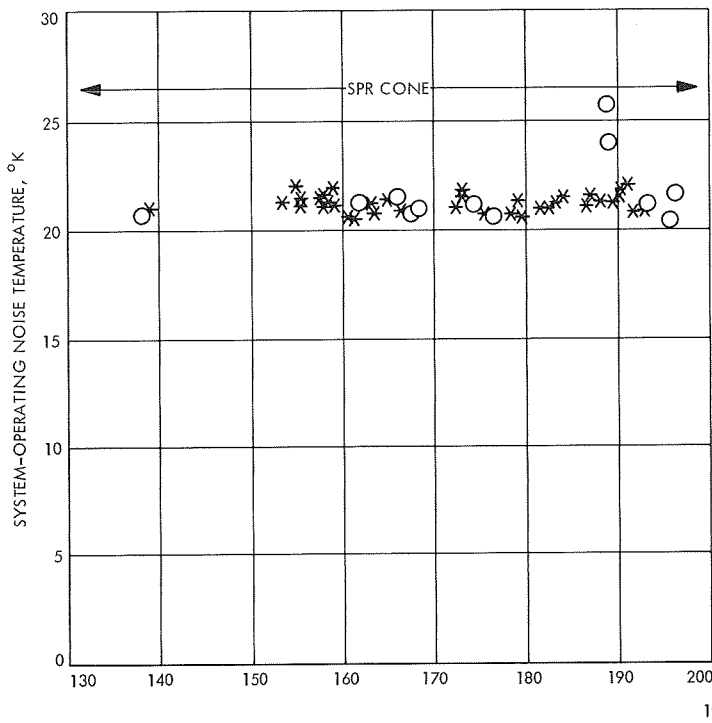**Fig. 20. System-operating noise temperature of SPR and SRO cones operational on DSS 13 antenna from June 1 through October 1, 1969**
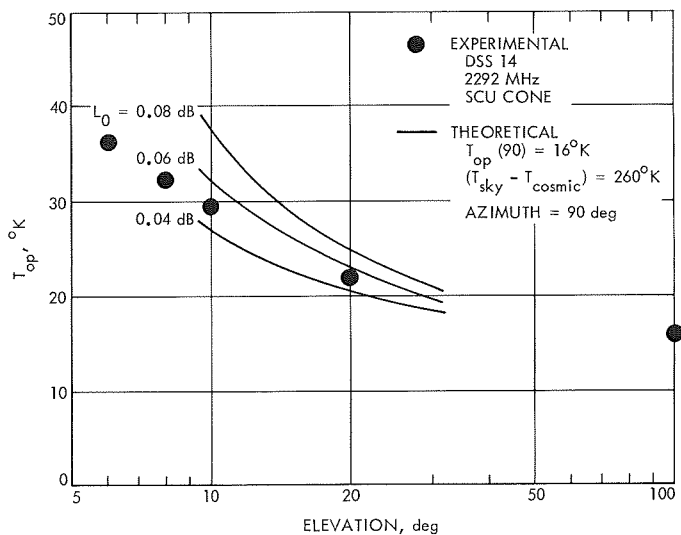

Fig. 21. System-operating noise temperature versus elevation angle for DSS 14 SCU cone (10/5/69, symmetrical mounting)
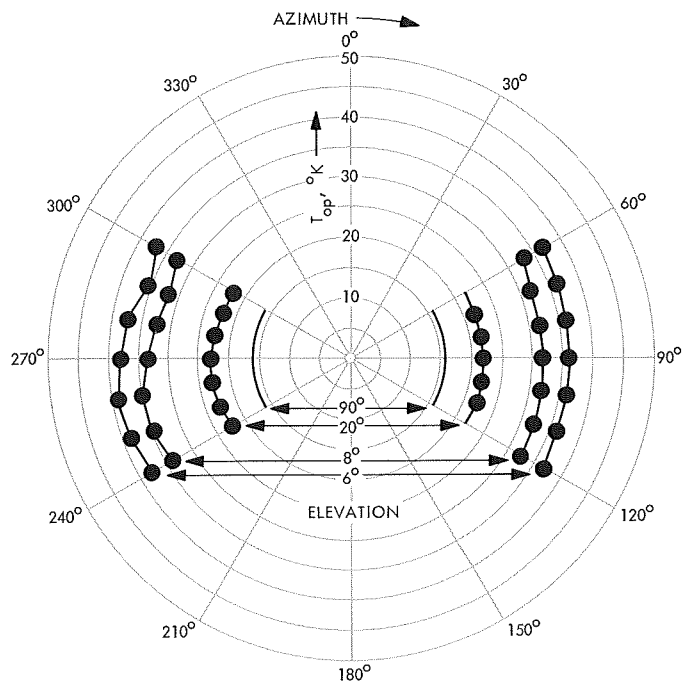

Fig. 22. System-operating noise temperature versus azimuth and elevation angles for DSS 14 SCU cone (10/5/69, symmetrical mountings)

2. Improved RF Calibration Techniques: Rotary Vane Attenuator Calibrations, *T. Y. Otoshi*

a. Introduction. In SPS 37-46, Vol. III, pp. 73–82, a modified theoretical attenuation law was derived for rotary vane attenuators. It is believed that precision attenuators can be made to obey the modified law up to 60 dB within tolerances of ±0.001 dB or ±0.15% of the attenuation in dB, whichever is greater. Through the use of the modified law, it should also be possible to design very short and compact rotary vane attenuators that are accurate over a 20- to 30-dB attenuation range (Ref. 1).

This article presents some preliminary results of an experimental program that was initiated to (1) test the validity of the modified law and (2) develop compact S- and X-band rotary vane attenuators for calibration of low-noise antenna systems.

b. Modified attenuation law. As derived in the referenced SPS, the modified attenuation law for rotary vane attenuators is

$$A_{dB} = -10 \log_{10} \left[\cos^4\theta \right.$$
$$\left. + 10^{-L_{dB}/20} (2 \cos\phi \cos^2\theta \sin^2\theta) + 10^{-L_{dB}/10} \sin^4\theta \right]$$

$$(1)$$

where

θ = the true rotary vane angle measured relative to the plane of the vanes in the stators. (It is assumed that there is no misalignment between the vanes in the stators.)

L_{dB} = attenuation of the tangential component relative to the normal component at the rotor output, dB. (It is related to the power-loss ratio L by $L_{dB} = 10 \log_{10} L$.)

ϕ = phase-shift difference between the tangential and normal electric-field components at the rotor output, deg.

The electrical parameters L_{dB} and ϕ are unique properties of the attenuator and, hence, they must be experimentally determined for the particular attenuator being calibrated. Over a narrow frequency range, however, these parameters should essentially remain constant. Note that when L_{dB} approaches infinity, Eq. (1) will reduce to the familiar unmodified law.

For most attenuators, there will be some deviations between the indicated and true vane angle due to bore-sight and other readout errors. The true vane angle can be expressed as

$$\theta = \theta_I + \alpha_1 + \alpha_2 \qquad (2)$$

where

θ_I = indicated vane angle

α_1 = boresight error

α_2 = angle runout error calibrated relative to $\theta_I = 0$ setting. (It is due to gearing errors, bearing runout, eccentricities, etc.)

The vane angle errors α_1 and α_2 must be calibrated to insure that the attenuator follows the law given by Eq. (1). With proper mechanical design and use of high-precision components, the angular errors α_1 and α_2 can often be made negligibly small.

c. Experimental results. To demonstrate that the modified law can be applied to improve the agreement between the actual and theoretical attenuations of a rotary vane attenuator, the results of some previous S-band calibrations (Ref. 2) were analyzed. Table 10 shows the deviations of corrected theoretical attenuations from measured attenuations. The two corrected theoretical attenuation cases shown are based, respectively, on the unmodified and modified laws; both cases include corrections made for vane angle readout errors. It can be seen that for attenuations greater than 40 dB, the agreement between measured and corrected theoretical attenuations was improved by about an order of magnitude[2] when the modified law was applied.

It should be mentioned that the values of L_{dB} = 88 dB and ϕ = 1.0 deg were measured by Rantec Corp. at 2295 MHz (Ref. 3), and the measured attenuations for Table 10 were obtained by JPL at 2388 MHz. However, because the values of the parameters L_{dB} and ϕ should change only slightly over a narrow frequency range, only small errors should result if the 2295-MHz values are also used at 2388 MHz. An error analysis given in the referenced SPS and in SPS 37-46, Vol. IV, pp. 253–258, indicates that small errors in determining the values of L_{dB} and ϕ will result in only second-order-type errors on the corrected attenuations.

---

[2]This type of improvement may not always be possible if other errors (such as those caused by mismatch and stator vane misalignment) become significant at the higher vane-angle settings.

Table 10. Comparison of theoretical and measured attenuations for the S-band rotary vane attenuator at 2388 MHz

Indicated vane angle θ_i, deg	Apparent theoretical attenuation A_i, dB	Measured vane angle[a] θ, deg	Runout error[b] α_2, deg	Unmodified law		Modified law	
				Corrected theoretical attenuation A, dB	Deviation from measured attenuation $(A - A_m)$, dB	Corrected theoretical attenuation[c] A, dB	Deviation from measured attenuation $(A - A_m)$, dB
2.749	0.0200	2.755	0.006	0.0201	0.0004	0.0201	0.0004
3.887	0.0400	3.887	0.000	0.0400	0.0006	0.0400	0.0006
4.759	0.0600	4.761	0.002	0.0601	0.0006	0.0600	0.0005
5.495	0.0800	5.499	0.004	0.0801	0.0008	0.0801	0.0008
6.142	0.1000	6.146	0.004	0.1001	0.0008	0.1001	0.0008
8.678	0.2000	8.684	0.006	0.2003	0.0008	0.2003	0.0008
12.248	0.4000	12.258	0.010	0.4007	0.0014	0.4006	0.0013
14.972	0.6000	14.989	0.017	0.6014	0.0021	0.6013	0.0020
17.255	0.8000	17.271	0.016	0.8015	0.0026	0.8014	0.0025
19.255	1.0000	19.272	0.017	1.0018	0.0003	1.0018	0.0003
26.969	2.0000	26.987	0.018	2.0028	−0.0011	2.0027	−0.0012
32.712	3.0000	32.734	0.022	3.0043	−0.0017	3.0041	−0.0019
37.408	4.0000	37.429	0.021	4.0049	−0.0026	4.0046	−0.0029
41.419	5.0000	41.446	0.027	5.0072	−0.0016	5.0070	−0.0018
44.932	6.0000	44.964	0.032	6.0097	−0.0008	6.0093	−0.0012
48.061	7.0000	48.095	0.034	7.0115	0.0000	7.0112	−0.0003
50.879	8.0000	50.911	0.032	8.0119	−0.0006	8.0113	−0.0012
53.440	9.0000	53.476	0.036	9.0147	−0.0015	9.0140	−0.0022
55.782	10.0000	55.822	0.040	10.0178	0.0019	10.0170	0.0011
59.921	12.0000	59.955	0.034	12.0178	−0.0018	12.0166	−0.0030
63.469	14.0000	63.505	0.036	14.0219	−0.0040	14.0206	−0.0053
66.540	16.0000	66.578	0.038	16.0266	−0.0019	16.0247	−0.0038
69.218	18.0000	69.257	0.039	18.0312	−0.0006	18.0288	−0.0030
71.565	20.0000	71.607	0.042	20.0382	0.0029	20.0351	−0.0002
76.282	25.0000	76.330	0.048	25.0597	0.0021	25.0534	−0.0042
79.757	30.0000	79.799	0.042	30.0706	0.0010	30.0604	−0.0092
82.337	35.0000	82.381	0.044	35.0994	0.0064	35.0809	−0.0121
84.261	40.0000	84.306	0.045	40.1363	0.0090	40.1021	−0.0252
85.699	45.0000	85.758	0.059	45.2395	0.0829	45.1753	0.0187
86.776	50.0000	86.829	0.053	50.2877	0.1140	50.1740	0.0003
87.583	55.0000	87.632	0.049	55.3556	0.1744	55.1547	−0.0265
88.188	60.0000	88.242	0.054	60.5254	0.3265	60.1674	−0.0315

[a]Measured by the JPL Mechanical Inspection Department.

[b]$\alpha_2 = \theta - \theta_i$ because it was determined that the boresight error $\alpha_1 = 0$ deg. See Eq. (2).

[c]Experimental values of 88 dB and 1.0 deg were used for L_{dB} and ϕ, respectively.

Some experimental data have recently been obtained on a compact X-band attenuator. Preliminary measurements indicate that the short attenuator follows the modified law very closely. More data are currently being obtained.

References

1. Stelzried, C. T., Otoshi, T. Y., Nixon, D. L., *Compact Precision Rotary Vane Attenuator*, Invention Report 30-1212. Jet Propulsion Laboratory, Pasadena, Calif., Mar. 5, 1968.

2. Finnie, C. J., Schuster, D., Otoshi, T. Y., *AC Ratio Transformer Technique for Precision Insertion Loss Measurements*, Technical Report 32-690. Jet Propulsion Laboratory, Pasadena, Calif., Nov. 30, 1964.

3. *Test Report on Relative Phase Shift Measurements Performed on a Rotary Vane Attenuator*, Report 70122-FR. Rantec Corp., Calabassas, Calif., Mar. 29, 1967.

3. Improved RF Calibration Techniques: Noise Source Instrumentation at DSSs 13 and 14, K. B. Wallace

Low-noise receiver instrumentation usually includes some type of noise source for calibration purposes. For example, in radiometric measurements of planets and boresight measurements using radio stars, it is helpful to have a well-calibrated multi-valued noise source to bracket unknown noise temperatures. Gas tubes have been the most useful noise sources and are still in use in the DSN to calibrate system temperature measurements.

The noise-source method of system temperature measurement has been supplanted by an ambient termination technique at DSSs 13 and 14, but noise sources have not been eliminated from the systems. The aforementioned radiometric and source measurements, as well as noise-adding gain stabilization research, are reasons enough to retain noise sources.

The recent development of solid-state microwave noise sources has revived interest in the use of noise sources for calibration and has been instrumental in an improvement in overall system temperature (Fig. 23). These noise sources have several advantages compared with gas tubes. Gas tubes require high voltages to operate. The aging and failure rates require frequent calibration. The devices are relatively large and fragile and difficult to temperature-stabilize. The excess noise realizable is about 20,000°K. After injection to the receiver through several directional couplers, the usable excess noise is typically about 50°K. Noise diodes are low-voltage devices, 28 Vdc being typical. They are quite small and compact. The largest now in use is ¾ in. square by 2 in. long. Some of these units are installed in constant temperature ovens at DSS 14. No data on failure rate are yet available, but the devices are operated in a low-power dissipation mode and long life is anticipated. Stability of noise output appears as good as a well-aged gas tube, although sufficient data to define stability limits have yet to be accumulated. The excess noise available is typically about 400,000°K. Using the same couplers as for a gas-tube system, the injected noise can be as high as 1000°K. At present, there is no need for such high values of injected noise; therefore, higher-valued couplers are used. For example, a 26-dB coupler was replaced with a 33-dB coupler. This reduced total system temperature by approximately 0.5°K. The small size of the devices permits the installation of several units in a system, to provide a greater range of noise values. Noise-adding radiometric gain stabilization techniques require switching of the noise source at various rates, e.g., 8 Hz. DSS 13 and 14 instrumentation systems have been designed to accommodate this requirement. The exact needs of the experimenters are not known, so the systems have been made more flexible than required for ordinary station operation. At DSS 14, the noise diodes are in ovens, with temperature and voltage readouts. The ovens may be switched off if desired. Modulation instrumentation is provided (Fig. 24). DSS 13 is similarly instrumented, except ovens are omitted.

It was recently demonstrated at DSS 13 that noise diodes can be square-wave modulated up to at least 100 Hz (Fig. 25).

Noise source values of injected noise temperature are:

Source	Temperature (DSS 13), °K	Temperature (DSS 14), °K
High noise	45	133
Medium noise	3	11 (maser 2), 36 (maser 1)
Low noise	2	3

These values are preliminary and are subject to refinement. Limits on accuracy and stability will be provided as more data are accumulated. Voltage standing-wave ratio (VSWR) and VSWR change of noise diodes are parameters requiring investigation. Presently, available devices are not particularly good in these respects.

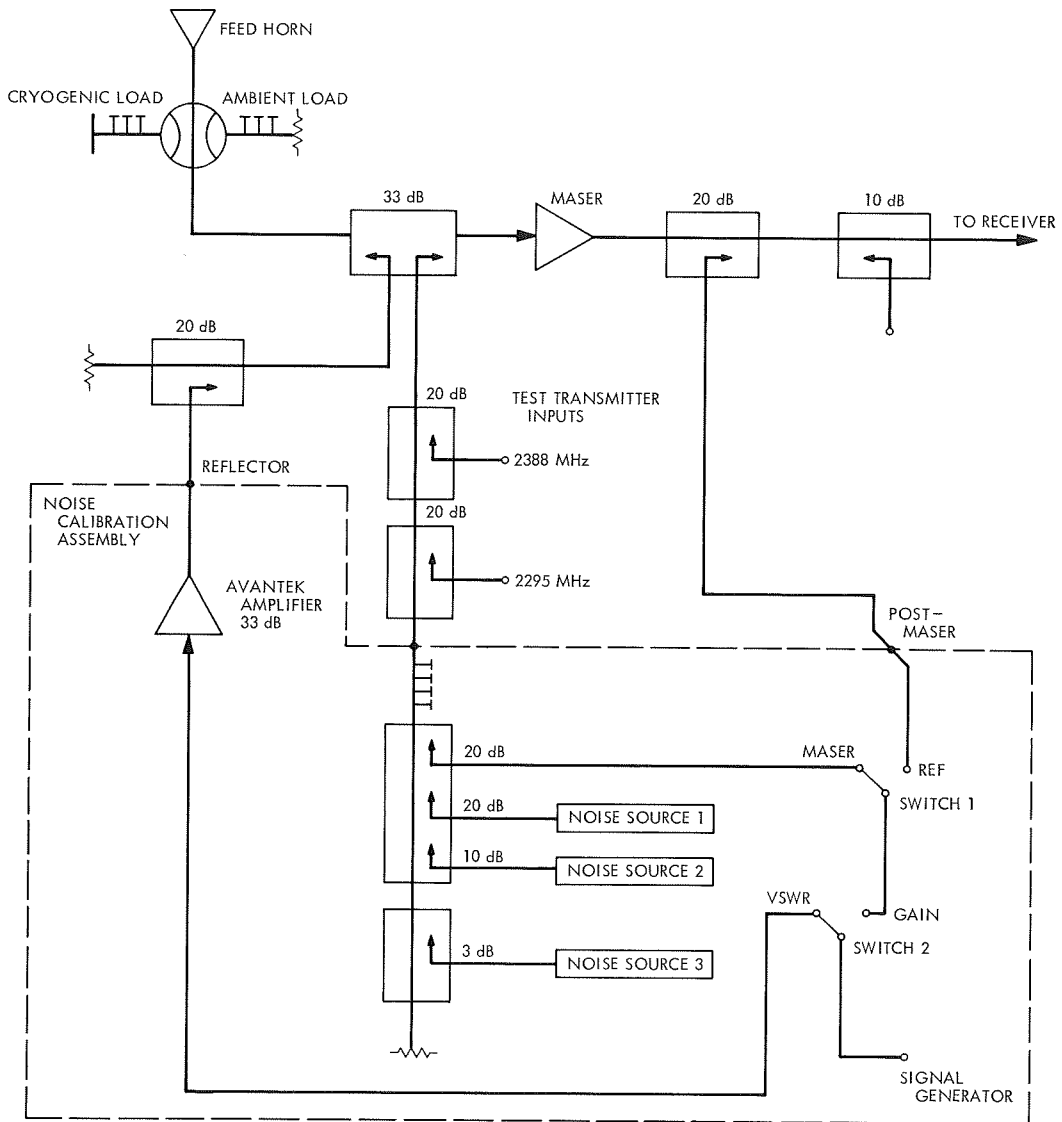An evaluation program is under way to determine the capabilities and limitations of these new devices.

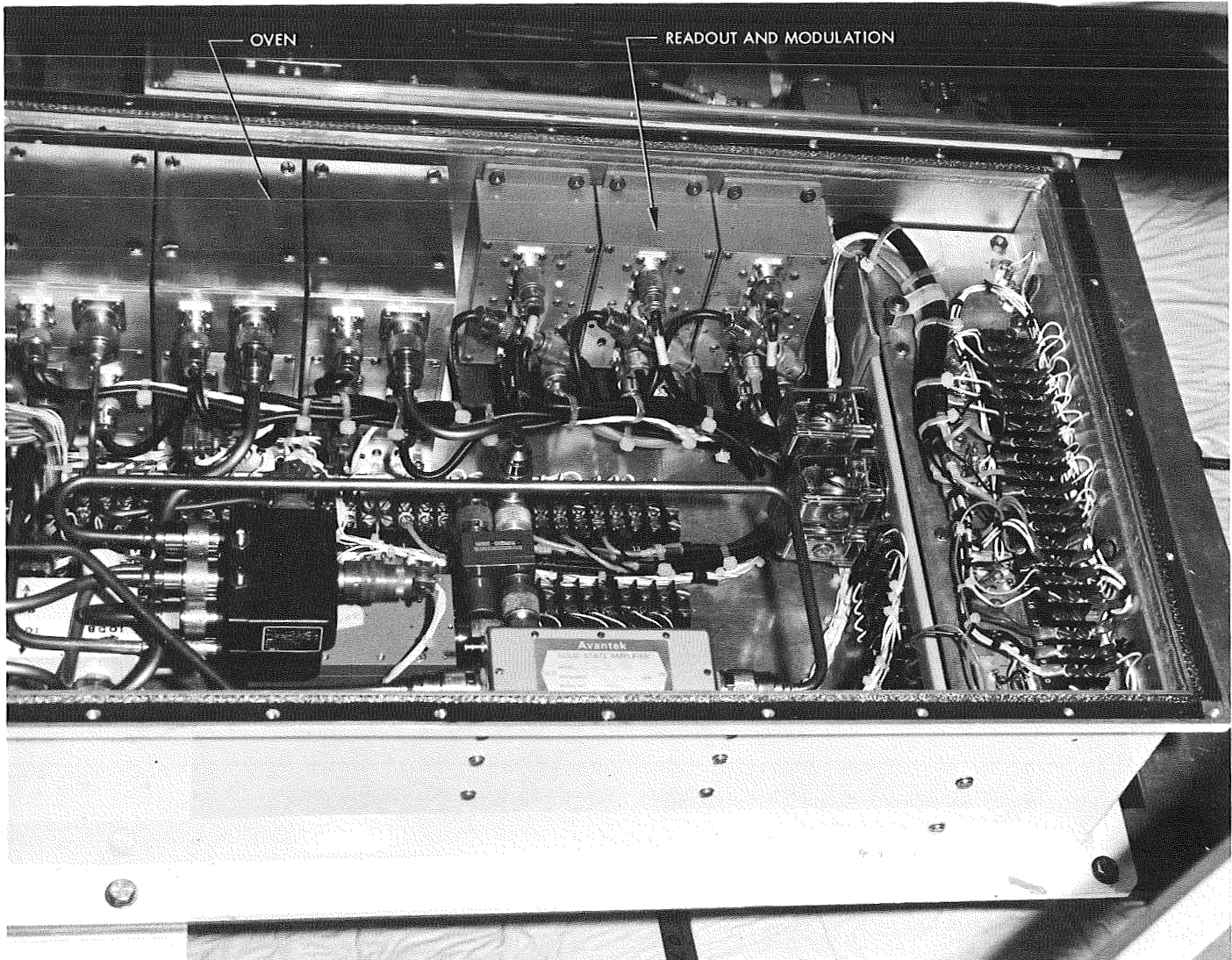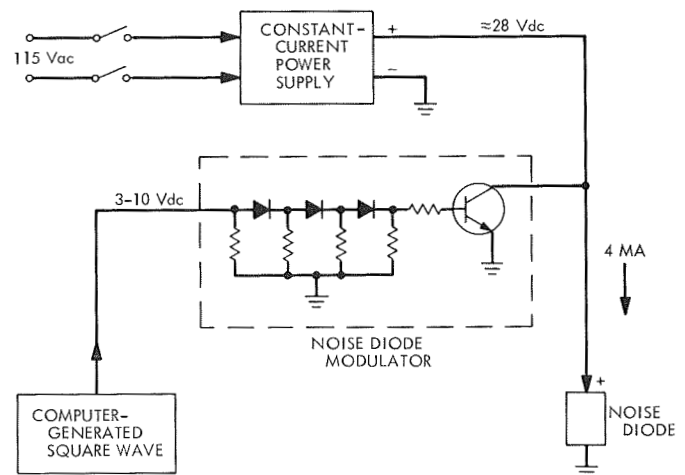**Fig. 23. Noise instrumentation of S-band cassegrain ultra cone at DSS 14**

Fig. 24. Noise calibration assembly at DSS 14

Fig. 25. Noise diode modulation

C. Supporting Research and Technology

1. An Executive Program for Telemetry Simulation,
J. A. Flynn

a. Introduction. In preceding articles, various features of the supervisory program (SPS 37-57, Vol. II, pp. 117–121), the user-oriented source-language (SPS 37-58, Vol. II, pp. 87–97), and means of communication among program components (SPS 37-59, Vol. II, pp. 74–78) have been described. The present article describes the manner in which simulated engineering telemetry is produced.

b. Input. The prototype for these researches in spacecraft simulation is the *Mariner* Mars 1969 vehicle. The simulation described, therefore, is structured about a pseudonoise (PN) sequence to identify position in the telemetry bit stream, a high-rate deck comprising multiple subcommutated channels, and a code word to identify the effects of subcommutation.

The foregoing structure is enabled by user-supplied input of the items described in Table 11. The syntax of these inputs is displayed in Table 12; the notation is

Table 11. Inputs for commutator definition

PNSEQ	An arbitrary sequence of 15 *zeros* and *ones* to define the PN sequence. The Hollerith 0–1 sequence will be mapped one-for-one into the PN bit string. Alternatively, input the letter "D" followed by the appropriate 5 octal digits.
DECK	A sequence of integer pairs naming the first and last channels in each deck.
SUBCOM	A sequence of integer pairs connecting each subcommutated channel with the first channel of the deck it points to.
CHANT	Channels to be computed as explicit functions of time.
INDEX	A sequence of ordered $(n + 1)$-tuples, to define the index word associated with each combination of subcommutated channels.

Table 12. Syntax of commutator input[a]

$<$ commutator input $>$ $:= <\ell> <$ com. hdr $> <\ell> \{[<p> | <d> | <s> | <c> | <i>]\}_5^{5/<t>}$

$<\ell>$ $:=$ a new line

$<$ com. hdr $>$ $:=$ *COMMUTATOR $\{\underline{b}\}_{61}^{61}$

$<p>$ $:=$ PNSEQ $= \{0|1\}_{15}^{15} | D \{0|1|2|3|4|5|6|7\}_5^5$

$<d>$ $:=$ DECK $= \{<C_F> - <C_L>\}_1^{/'}$

$<s>$ $:=$ SUBCOM $= \{(<S>, <C_F>)\}_1^{/'}$

$<c>$ $:=$ CHANT $= \{<C> | <C> - <C>\}_1^{/'}$

$<i>$ $:=$ INDEX $= \{(<\sigma_1>, \cdots, <\sigma_n>, <i\text{word}>),\}_1 (CCS \underline{b} RO, <i\text{word}>)$

$<blank>$ $:= \underline{b}$

$<C>$ $:=$ a channel name

$<C_F>$ $:=$ name of first channel in deck

$<C_L>$ $:=$ name of last channel in deck

$<S>$ $:=$ name of a subcommutated channel

$<\sigma_k>$ $:=$ name of channel pointed to by kth subcommutated channel

$<i\text{word}>$ $:=$ decimal digit ≤ 63

[a]Unless the contrary is indicated, embedded blanks are ignored.

adapted from Lee (Ref. 1) and is described in *Paragraph e*. Table 13 displays the *Mariner* Mars 1969 commutation inputs. To facilitate both narrative and computational references to the inputs, the definitions in Table 14 have been devised.

In Tables 11–14, the terms "deck name," "channel name," and "channel index number" are used. The "channel name" is the number by which the channel is known, e.g., 100, 213, 437. The "channel index number" is the ordinal number of the channel in question, given that the channels are arranged in channel-name sequence. The "deck name" is the same as the name of the first channel in the deck.

The following relationships are established by inspection.

$$C_{ij} = i + D_j - 1 \qquad (1)$$

$$K_{ij} = i + \sum_{v=0}^{j-1} N_v, \qquad N_0 = 0, j \geq 1 \qquad (2)$$

Eliminating i between Eqs. (1) and (2) and introducing F_j from Table 14, there results

$$K_{ij} = C_{ij} - F_j \qquad (3)$$

where

$$F_j = D_j - \sum_{v=0}^{j-1} N_v - 1 \qquad (4)$$

Table 15 shows the way the *Mariner* Mars 1969 DECK and SUBCOM data are transformed into program-usable form.

c. Environment. The program enters the telemetry publication phase following step termination. During

Table 13. *Mariner* Mars 1969 commutator-defining inputs

```
*COMMUTATOR
PNSEQ    = D03545
DECK     = 100-109, 110-119, 200-209, 210-219, 220-229, 300-309,
           400-409, 410-419, 420-429, 430-439
SUBCOM = (103,200), (104,210), (110,220), (202,300), (211,400),
           (211,410), (212,420), (212,430)
CHANT    = 305, 401, 404-414, 416-419, 430-439
INDEX    = (200,210,220, 1), (203,213,223, 2), (204,214,224, 3),
           (205,215,225, 4), (206,216,226, 5), (207,217,227, 6),
           (208,218,228, 7), (209,219,229, 8), (201,400,221, 9),
           (201,401,221,10), (201,402,221,11), (201,403,221,12),
           (201,404,221,13), (201,405,221,14), (201,406,221,15),
           (201,407,221,16), (201,408,221,17), (201,409,221,18),
           (300,420,222,19), (301,421,222,20), (302,422,222,21),
           (303,423,222,22), (304,424,222,23), (305,425,222,24),
           (306,426,222,25), (307,427,222,26), (308,428,222,27),
           (309,429,222,28), (201,410,221,41), (201,411,221,42),
           (201,412,221,43), (201,413,221,44), (201,414,221,45),
           (201,415,221,46), (201,416,221,47), (201,417,221,48),
           (201,418,221,49), (201,419,221,50), (300,430,222,51),
           (301,431,222,52), (302,432,222,53), (303,433,222,54),
           (304,434,222,55), (305,435,222,56), (306,436,222,57),
           (307,437,222,58), (308,438,222,59), (309,439,222,60),
           (CCS R/O, 31)
```

that period, all channels which do not depend explicitly on time were evaluated at t_R, the right-hand side of the integration interval, via source language statements of the following sort:

$$C = \mathcal{E}_1, \mathcal{E}_2, \mathcal{E}_3 \qquad (5)$$

The left side of this equation is an integer denoting the channel name. The $\mathcal{E}$'s are arithmetic expressions, $\mathcal{E}_1$

Table 14. Deck and channel parameters

D_j	name of deck j
N_j	number of channels in deck j
P_j	name of (subcommutated) channel that points to deck j
F_j	quantity that converts deck j channel names into channel index numbers
C	a channel name
K	a channel index number

Subscripts may be used on C or K to draw attention to some specific characteristic:

Subscript	C, K characteristic emphasized
ij	ith channel of deck j
L	first publishable channel in $[t_L, t_R]$
R	last publishable channel in $[t_L, t_R]$
ν	νth C or K in sequence (note that $K_\nu = \nu$ by definition)

being the computed telemetry value for the channel, while $\mathcal{E}_2$ and $\mathcal{E}_3$ are factors used to scale $\mathcal{E}_1$. A typical instance of Eq. (5) might be

$$106 = EY, 1.0, 10.0$$

The source statement Eq. (5) gives rise to the target language statement,

$$\text{CALL CHAN} (\mathcal{E}_1, \mathcal{E}_2, \mathcal{E}_3, C) \qquad (6)$$

Subroutine CHAN performs three functions:

(1) It maps the channel name C into the channel index number K.

(2) It maps $\mathcal{E}_1$ into the interval $[0, 1]$ by

$$\mathcal{E}_1 \leftarrow \frac{\mathcal{E}_1 - \mathcal{E}_2}{\mathcal{E}_3 - \mathcal{E}_2} \qquad (7)$$

(3) It stores the scaled $\mathcal{E}_1$ into the Kth cell of the telemetry array ZR.

d. Program action. Given the foregoing array ZR of telemetry values at t_R for all channels (except as noted), the publication problem consists of (1) deciding which channels to publish, (2) determining the publication time for each publishable channel, and (3) obtaining the correct telemetry values for these channels at the proper times. Most of the complexity at this stage can be traced to the requirements for subcommutation.

Table 15. DECK and SUBCOM inputs (*Mariner Mars* 1969)[a]

DK	Deck number, j									
	1	2	3	4	5	6	7	8	9	10
C_{1j}	100	110	200	210	220	300	400	410	420	430
$C_{N_j j}$	109	119	209	219	229	309	409	419	429	439
P_j	0	0	103	104	110	202	211	211	212	212
N_j	10	10	10	10	10	10	10	10	10	10
F_j	99	99	179	179	179	249	339	339	339	339
δC_{ij}	0	0	0	0	0	0	0	0	0	0

[a]When (1) $P_j = P_{j+1}$ and (2) $C_{1, j+1}$ is consecutive with $C_{N_j j}$, columns j and $j + 1$ may be collapsed into a single column. This condition occurs for $j = 1, 7,$ and 9.

It was shown in SPS 37-57 that publication of the νth high-deck channel, say K_ν, will begin at the following times:

$$t_P(K_\nu) = t_M + (K_\nu - 1)\, T_c - mT_F, \qquad \begin{cases} m = 0, 1, \cdots \\ K_\nu \le NH \end{cases}$$

(8)

Moreover, the publication time of the first high-deck channel in the integration interval $[t_L, t_R]$, say K_L, is related to t_L by

$$t_P(K_L - 1) \le t_L < t_P(K_L)$$

(9)

Taking $\nu = L$ and substituting Eq. (8) into Eq. (9), there results the index number of the earliest high-deck channel to be published, relative to $[t_L, t_R]$:

$$K_L = 2 + \left\lfloor \frac{t_L - (t_M + m_L T_F)}{T_c} \right\rfloor \pmod{NH}$$

(10)

where the auxiliary m_L is given by

$$m_L = \left\lfloor \frac{t_L - t_M}{T_F} \right\rfloor$$

(11)

The index number of the last high-deck channel to be published, relative to $[t_L, t_R]$, is then given by

$$K_R = K_L + \left\lfloor \frac{t_R - t_P(K_L)}{T_c} \right\rfloor \pmod{NH}$$

(12)

Corresponding, therefore, to $[t_L, t_R]$, the index numbers of the high-deck channels to be published are those indexes K_ν such that

$$K_L \le K_\nu \le K_R$$

(13)

Recognizing that in the instance of a subcommutated channel, the high-deck channel is merely an alias of the true channel, it is the responsibility of the locator algorithm to thread through any depth of subcommutation to find the actual channel to be published. A description of this algorithm refers to the array DK of Table 15, which is shown as it appears just after reading the DECK and SUBCOM inputs, i.e., in terms of channel names. (See also Tables 13 and 14.) Internally, channel names

are inconvenient to use because they do not form a consecutive sequence. For this reason, the program logic is carried out in terms of channel index numbers. Before the information in DK is useful, therefore, the channel names C_{1j}, $C_{N_j j}$, and P_j must be transformed by Eq. (3) into channel index numbers, K_{1j}, $K_{N_j j}$, and P_j^K. Subsequent references to DK or Table 15 assume this transformation.

Row 6 of Table 15 contains the quantity δC_{ij}, which, for the channel named C_{ij}, is defined by

$$\delta C_{ij} = C_{ij} - C_{1j}$$

(14)

Converting names to index numbers by Eq. (3), it is apparent also that

$$\delta C_{ij} = K_{ij} - K_{1j}$$

(15)

These equations are useful in the subcommutation process.

The locator algorithm may now be given. The notation employed is essentially that developed in Ref. 2:

(1) $\alpha \leftarrow K_\nu$

(2) $(\exists j \ni \alpha = P_j^K); \quad (T, F) \to (3, 5)$

(3) $\alpha \leftarrow K_{1j} + \delta C_{ij}$

(4) $\delta C_{ij} \leftarrow \delta C_{ij} + 1 \pmod{N_j}; \quad \to 2$

(5) $K_{ij} \leftarrow \alpha; \quad \to$ return

Fundamentally, the algorithm states that, if K_ν is *not* a subcommutated channel, then K_ν is the desired index. This is the *false* exit of step 2. If it *is* subcommutated (the *true* exit of step 2), obtain the index of the channel pointed to (step 3: Eq. 15). Since *that* channel may be subcommutated also, the process is iterated until no further subcommutation is detected.

Once the true channel index has been found (i.e., K_ν has been mapped into K_{ij}), the telemetry value for that channel at $t_P(K_\nu)$ can be obtained. The mode of determination depends on whether the simulation function for the channel in question depends explicitly on time. If so, its name will be among the CHANT inputs. The only channels of this class encountered thus far belong to the

temperature subsystem. For such a channel, the supervisor executes the following code:

$$\text{IE} \leftarrow C_{ij}$$

$$\text{KSECT} = 3$$

$$\text{KSUB} = 1$$

$$\text{KCOM} = 60$$

$$\text{GO TO 3000}$$

The result will be the telemetry value of channel C_{ij} at time $t_P(K_v)$, stored in $ZL(K_{ij})$.

If the channel is not found in the CHANT set, its value is obtained by interpolation: $ZL(K_{ij})$ and $ZR(K_{ij})$ contain the telemetry values of C_{ij} at t_L and t_R, respectively; hence,

$$ZL(K_{ij}) \leftarrow \left[\frac{ZR(K_{ij}) - ZL(K_{ij})}{t_R - t_L} \right] [t_P(K_v) - t_L] \qquad (16)$$

If there is room in the telemetry output queue, the channel value is placed there to await bit-wise publication under control of the interval timer. If the queue is momentarily full, the supervisor attends to miscellaneous tasks and input/output interrupts that have been accumulated. A subsequent article will investigate the degradation in telemetry publication that may occur in certain critical situations.

e. Language descriptors. The symbols of the metalanguage used to describe the input syntax are defined as follows [after Lee (Ref. 1)]:

$<x>$ read, "the object named x."

$:=$ read, "is formed from."

$|$ exclusive *or*.

$\{z\}_i^{j/\sigma}$ z is to be repeated *in situ* at least i times and not more than j times. Consecutive instances of z are separated by the contents of the field "σ." If i is omitted, its value is assumed to be 1. If j is omitted, its value is assumed to be infinity. If "$/\sigma$"

is omitted, σ is assumed to be the null character.

$[R]$ R is a reducing set, defined as follows: Let N denote the full set of elements under consideration. Let A denote the set of elements of N already used, and, therefore, no longer available for use. Let R denote the set of elements of N not yet used, and, therefore, available for use. Then $R = N - A$.

To illustrate the repetition operator, consider $\{A \mid B\}_0^2$. Here, $i = 0$, $j = 2$, $\sigma = $ null. Any of the following constructs is a legitimate production:

null	A	AA
	B	AB
		BA
		BB

By way of contrast, consider also $\{A \mid B\}_0^{2/'}$. In this instance, $i = 0$, $j = 2$, and σ is the symbol ",". Any of the following constructs is legitimate

null	A	A, B
	B	A, A
		B, A
		B, B

To illustrate the reducing set, consider the options field of the IBJOB Fortran compiler control card (Ref. 3) (i.e., the $IBFTC card). This field begins in column 16. It may be null, or it may contain up to five subfields in any order, without repetition, separated by commas. The available options are suitably abbreviated as follows:

Symbol	Option
$<L>$	List
$<D>$	Debug
$<P>$	Punch
$<I>$	Instruction set
$<R>$	Index register

The syntax of the options field may, therefore, be written as

$$<\text{options field}> := $$
$$\{[<L> \mid <D> \mid <P> \mid <I> \mid <R>]\}_0^{5/,}$$

References

1. Lee, J. A. N., *The Anatomy of a Compiler*. Reinhold Book Corp., New York, N. Y., 1967.

2. Iverson, K. E., *A Programming Language*. John Wiley & Sons, Inc., New York, N. Y., 1962.

3. *IBM 7090/7094 IBSYS Operating System, Version 13, FORTRAN IV Language*, Form C 28-6390. IBM Systems Reference Library.

2. Modifications to the Syntax of TMG for Purposes of Spacecraft Telemetry Simulation, R. I. Scibor-Marchocki

a. Introduction. The first three articles in this series on spacecraft telemetry simulation discussed certain aspects of the supervisory program (SPS 37-57, Vol. II, pp. 117–121), the user-oriented source language (SPS 37-58, Vol. II, pp. 87–97), and the lines of communication created among various program components (SPS 37-59, Vol. II, pp. 74–78). These articles mentioned that the source code would be translated by a special-purpose compiler.

b. Spacecraft simulation. The transmogrification (TMG) compiler is employed to compile the simulation compiler which translates from the user-oriented spacecraft-simulation language to Fortran IV. The syntax portion of TMG, known as TMGL, has been modified to improve the performance of both the TMGL compiler itself and, indirectly, the simulation compiler.

Of the various compilers, for compiling a compiler, which have been reported (Ref. 1), the TMG compiler, invented and coded by Robert McClure (Ref. 2), possesses these advantages: (1) it is versatile, (2) its parser is capable of backing up, (3) its syntax TMGL is written in its own language and thus can grow easily by a recompilation performed by its previous generation, and (4) the TMG compiler exists, works, and is available (SPS 37-44, Vol. IV, pp. 17–22).

Like most other compiler-compilers, TMG had its problems—incomplete documentation, inadequate diagnostics, lack of or incorrect error recovery, and erratic behavior. As a result, it was difficult to write the source for a compiler. A run frequently terminated unsuccessfully in a meaningless dump or a report by IBLDR of the presence of obscure undefined virtuals. The compilation often yielded a wrong translation. Checkouts were inconclusive because subsequent runs again were subject to the foregoing problems; i.e., the target compiler was unreliable.

The motivation for the work reported herein has been to help TMG realize its potential by improving TMGL— optimization of the source coding and correction of coding errors has benefited the *first* generation of TMGL itself. Optimization of the target coding, expansion of diagnostics, introduction of error recovery, improvement of existing features, introduction of new features, and the addition to the documentation benefited the *second* generation of TMGL itself.

c. TMG compiler. The TMG compiler employs a top-down left-to-right parser with backup. A typical colon-type sentence

$$A..B/C \quad D = E$$

consists of a label A followed by a colon, zero or more components with optional alternates, and an optional subject E preceded by an equal sign. The left part of a component may be simple or compound, e. g.,

$$B1'B2'B3$$

The alternate of a component may be either a name of a colon-type sentence exclusive or a similar sentence, without a label and colon, but enclosed in parentheses, e. g.,

$$(C1 \; C2 = C3)$$

A component that does not possess an alternate may be enclosed in parentheses, and if it is either a name of a character-class exclusive or is enclosed in parentheses, then it may be followed by a star, e. g.,

$$(D1 \; D2)$$

$$(D)*$$

$$D*$$

The subject may be a name of a definition or a definition, separated by another equal sign if both a name and a definition are present. The subject, at its end, may possess an alternate consisting of the name of a colon-type sentence.

The TMGL compiler parses the source code and translates it into a suitable sequence of assembly language cards. A listing of this intermediate assembly language code is instructive both as an educational aid and as a check upon the compiler coding under whose guidance the translation was accomplished.

d. ✳✳✳ *Functions.* Each component which does not possess parentheses or the BNF| compiles into one computer word consisting of: an operation code, an address indicating the name of the left part, and the decrement either indicating the name of the alternate by an address exclusive or the absence of an alternate by a value of zero. For example,

$$\text{LP/IMAC LS}$$

compiles into

C	LP,,IMAC
C	LS,,0

where, for easier readability, we write the assembly language target code, substituting the real names whenever they are available.

The left part of the component may be a function without arguments. Such a function is called a single-star function because it is declared by an equal-sign-type sentence like

$$\text{TYPVAR} = \text{✳TYPVAR}$$

A component consisting of this function

$$\text{TYPVAR}$$

compiles into

M	TYPVAR,,0

A function with an argument

$$\text{CHKFLG} = \text{✳✳CHKFLG}$$

presents a problem of where to indicate the address of the argument. The solution adopted for such double-star functions is to place the address of the argument in the decrement and to omit any indication of the alternate. The alternate is placed into the preceding word which is

inserted and possesses the function ALEX as its left part. For example,

$$\text{CHKFLG(DEF-FL)/(FV1 RSETKY(FAIL)} = \text{R2)}$$

compiles into

F4960X	C	FV1,,0
	MS	RSETKY,,FAIL
	S	R2,,0
	M	ALEX,,F4960X
	MS	CHKFLG,,DEF-FL

The function ALEX is a complicated time-consuming function but essential in the execution of a two-star function.

Certain functions with an argument can never fail because they just perform a specific arithmetical, logical, or housekeeping operation which is defined for all values of the argument. For such a function, the use of ALEX is wasteful of execution storage and especially time, but is not wrong. Such a function now is indicated by a triple star, e. g.,

$$\text{RSETKY} = \text{✳✳✳RSETKY}$$

and compiled without the use of ALEX, as already illustrated in the foregoing example.

e. *Dictionary.* All of the coding involved has been rewritten to increase the use of the dictionary and to provide error recovery and better diagnostics. Extensive use is made of the dictionary to obviate the necessity of detailed parsing and subsequent translation of recurrences of a common expression. The argument of each of the functions

$$\text{COMPUTE}$$
$$\text{IF}$$
$$\text{NOT}$$

is parsed quickly by the sentence BALSTG which looks for strings with balanced, i.e., paired, parentheses. Literal strings are parsed quickly by the sentence DDNDS which looks for strings with balanced, i.e., paired, dollar signs. Such a quick parse hopefully delimits a given entity, which then is entered into the dictionary and checked to see whether it has been parsed in detail and

translated previously. For the same reasons, the definitions now are entered into the dictionary.

A named literal or definition is not entered into the dictionary because a new copy of the coding of the literal or definition is required each time that it is named differently. Therefore, one should make certain that a given literal *or* definition is designated by a unique name, which may be itself.

A set of flags is associated with each word entered into the dictionary. A flag is a binary variable, initialized at false 0. Each time a word is parsed, its flags are interrogated to ascertain compatibility with prior use of the word or are set to indicate present use. Since the compiler performs most of its work on the second pass, each sentence which has an equal sign = rather than a colon .. immediately following the name of the sentence now has to be placed ahead of where that name is used. The only exception is that a definition may be placed either in conformity with the foregoing exclusive or anywhere in the .DEFINITION. section. Suitable diagnostics now are issued if a name is used without being designated, is misused, or is used in non-compatible ways.

Since, at present, the definition is not parsed by TMGL, the semantics of the definition are not checked. For example, no check is made to ascertain whether the argument(s) of a $Pn or $Fn function have been designated already. If anything except an integer constant or a name of a colon-type sentence is used as such an argument without prior designation or without a definition in the .DEFINITION. section, then the *real* name of that argument will become an undefined virtual symbol during the subsequent IBLDR pass.

In the past, if a name were not designated at all or early enough, diagnostics would be unlikely, but, at best, only an obscure alias of the name would appear as an undefined virtual during the subsequent IBLDR pass. At worst, a meaningless dump would result during an execution which invoked that alias.

f. Alternate. Each component may possess an alternate, to be attempted upon the failure of either the next component(s) or the left part of the given component. The alternate has been improved by the introduction of the diagnostics, the error recovery, and the following documentation.

* + I. The alternate of a component may be indicated in the style of the assembler as * + I, where the star

means here and the integer constant indicates how many words hence. This construction is especially popular to indicate an optional item. For example, the sentence

$$OPTC.. \$,\$/* + 1 = RO$$

compiles into

ZZ101 OCT	730000000000
OPTCT RACE	584,,22360
X	ZZ101,,* + 1
S	= 0,,0

To remind the programmer that a double-star function compiles into two words and thus the component count does not equal the word count, four warning messages are available now. For example, the sentence

$$X.. COMPUTE(J1 = 0) IF(I-KEY)/* + 2$$

COMPUTE (J1 = 1)

CVTD(J1) COMPUTE(J1 = 0)

CHKFLG(ARRAY)/* + 3

COMPUTE(J1 = 1) CVTD(J1) = Y

compiles into

(1211X NULL	
CLA	= 1
STO	J1
TRA	ALEX
(0211X TSX	PACK,1
CLA	I-KEY
TZE	NOGO
TRA	EXIT
(9111X NULL	
CLA	= 0
STO	J1
TRA	ALEX

X	TRACE	463,,22360
	M	(9111X,,0
	M	(0211X,,* + 2
	M	(1211X,,0
	MS	CVTD,,J1
	M	(9111X,,0
	M	ALEX,,* + 3
	MS	CHKFLG,,ARRAY
	M	(1211X,,0
	MS	CVTD,,J1
	S	Y,,0

and causes the warning message

$$*****THIS\ *+I\ MAY\ NOT\ WORK$$

to be written with a pointer to the $*+3$. The $*-I$ is used too rarely to justify any checking to be performed by the compiler.

SCAN. The SCAN parser, which is employed by default at each level below the top level, is a left-to-right parser with backup. This backup capability is both useful and dangerous. Consider the fragment of a colon-type sentence

$$A/C\ B$$

If the left part A of the first component fails, then control passes to its alternate C. If A succeeds, control passes to the second component B. Thereupon, if the component B fails, then control reverts, i.e., backs up, to C, the alternate of the successful A. For example, the construction

$$A/*+1\ B$$

makes A optional but usually will waste execution time whenever B fails, after a successful A, because then control will back up to the alternate $*+I$ which redirects control to B. Thereupon, B will fail again every time unless the intersection of A and B is non-null. The more complicated construction

$$(A)\ B$$

makes A optional and not subject to backup from B

because A is placed one level down. The related construction

$$(A)*\ B$$

makes one or more occurrences of A optional and for the same reason is not subject to backup from B. In each of these last two cases, output, perhaps null, will be produced by the parenthesized expression. This output will correspond to the last output-producing component of A, if any.

Another example, the construction

$$A/*+2\ B\ C$$

will cause control to skip past B directly to C if A fails, but control also will pass to C if B fails after a successful A. The more complicated construction

$$D/(B)\ C$$

where D is the complement of A, solves the problem but creates a new one if C is subject to failure. This new problem is apparent in the resulting target code:

D1X	C	B,,0
	C	0,,B2X
	C	D,,D1X
B2X	NULL	
	C	C,,0

which is equivalent to the source

$$D/(B\ GO\text{-}TO\text{-}C)\ C$$

except that the syntax has no provision for the component go-to-C.

Because the .OR. compiles into a construction involving alternates, it has a backup problem. For example, the construction

$$A\ .OR.\ B/C\ D$$

compiles into

	C	A,,A1X
	C	0,,A2X

```
        A1X  NULL

             C        B,,C

        A2X  NULL

             C        D,,0
```

which is equivalent to the source

$$A/* + 2 \; **/* + 2 \; B/C \; D$$

If A succeeds and then D fails, control reverts to B *via* the alternate of A.

g. Termination. A colon-type sentence may be either terminated by an equal sign = followed by a subject exclusive or left unterminated but followed by another colon-type sentence.

SUBJECT. The SUBJECT has been rewritten completely to treat each of the eight syntactical situations exemplified by

P1

$($P1/PZE/0//$)

ARDEF = (4)$($P1(ARBNOP)/S/XP21,,$Q4//
   $Q1/C/$Q3,,O//$)

ARDEF

P1/TMA

 = $($P1/CHS//$)/TMA

R321 = $($P3$P2$P1$)/AP1

R321/AS1

in a systematic manner and to improve the readability of the source code. As a result, each of the eight choices now is permitted and in each case the same, more extensive, diagnostics are available.

External bypass. For the occasional colon-type sentence that does not end with a subject, the following sentence, which then must be of colon-type, has to provide a bypass around its subsidiary text to cause control to transfer to its beginning from the end of the previous sentence. For example, the typical left-recursive construction consisting of a pair of sentences

LS1.. LP/IMAC

LS2.. V/(= R1) LP/IMAC = $($P2+$P1)/LS2

compiles into

```
LS1  TRACE      173,,22360

     C          LP,,IMAC

     C          ,,L4360X

(3360X  OCT     007502002000

     OCT        750100000000

L5360X  S       =O007501000000,,0

LS2  TRACE      174,,22360

L4360X  X       V$,,L5360X

     C          LP,,IMAC

     S          (3360X,,LS2
```

Now an average of almost a word of storage per colon-type sentence is saved by the avoidance of the unnecessary use of this bypass, consisting of

```
     C          ,,created-name
```

and the same created-name on the card immediately following the starting card

```
label  TRACE   line-number,,22360
```

If a colon-type sentence that does not end with a subject is not followed by another colon-type sentence, an error message is written now.

h. Recovery from warning errors. A colon-type sentence whose name has been employed as an alternate imposes a different requirement upon its subject than does a colon-type sentence whose name has been employed as a left part of a component; therefore, seldom is it possible to use the name of the same colon-type sentence in both syntactical positions. A warning message is printed when such a second use is encountered by the compiler. A similar warning message results if a name of a definition is present as the left part or alternate of a component or as the alternate of a subject. The compilation now is performed suitably for the actual entity which is present. An intentional example of the recoverable errors has been coded:

NM8.. $,$/(NM9/R1 R2C1/REQN) NM6/IMAC
   R2C1/RFUN

prints the error messages

*****ALTERNATE FIELD NAME HAS BEEN
USED AS A DEF NAME

*****R1

*****NAME USED AS A COMP HAS ALSO
BEEN USED AS A DEFINITION

*****R2C1

*****ALTERNATE FIELD NAME HAS BEEN
USED AS A DEF NAME

*****REQN

*****NAME USED AS A COMP HAS ALSO
BEEN USED AS A DEFINITION

*****R2C1

*****ALTERNATE FIELD NAME HAS BEEN
USED AS A DEF NAME

*****RFUN

with pointers to the items involved and compiles into

	C	,,R4580X
R5580X	S	RFUN,,0
ZZ45	OCT	730000000000
R8580X	S	REQN,,0
R9580X	S	R1,,0
R6580X	C	NM9,,R9580X
	S	R2C1,,R8580X
	C	0,,R7580X
NM8	TRACE	318,,22360
R4580X	X	ZZ45,,R6580X
R7580X	NULL	
	C	NM6,,IMAC
	S	R2C1,,R5580X

i. Macros. Since the TMGL compiler yields an assembly target code, the TMGL compiler has at its disposal all of the features of the following IBMAP assembler, e. g., macro instructions. Each name stored in the dictionary has associated with it a set of binary variables, called flags. The flags are designated by the compiler using the MFLG macro, which now permits up to 18 inclusive flags to be designated. This macro is invoked by, e. g., the source code

.FLAGS. ARRAY,DEF-FL,G-FLAG,L-FLAG

which compiles into

MFLG	ARRAY
MFLG	DEF-FL
MFLG	G-FLAG
MFLG	L-FLAG

A new macro has been introduced to permit the declaration of arrays for use by the compilers. This macro is invoked by, e. g., the source code

.PTRS. PTR1(10),PTRA1(50),PTRB1(10)

which compiles into

PRTS	PTR1,10
PRTS	PTRA1,50
PRTS	PTRB1,10

The value of the name is the location of the first word of the array, while the size of the array is enclosed by the pair of parentheses. The elements of the array are indirectly addressed, using any variable whose value is the address of the desired element. For example, the component

COMPUTE($J2$ = PTRA1,($J2$) = EQUADR)

compiles into

ZZ85	NULL	
	CLA	PTRA1
	STO	J2
	CLA	EQUADR
	STO*	J2
	TRA	ALEX

and stores the name just parsed into the first element of the array PTRA1. The apparently redundant pair of parentheses around J2 compiles as the star—indicating indirect addressing to the subsequent assembler.

j. Linkage. The necessary communication among routines is accomplished *via* the linkage from a virtual name to an entry name.

Entry. Specific allowance now is made for naming any label, i. e., the name of a colon-type sentence or of a definition, as an entry. Each syntax has to have a main-link entry, called PROGRM, which points to the top-level sentence. For example,

PROGRAM = PROGRM

PROGRAM.. FORTIO INITIALIZE HEADER

PR1.. TRAILER/PR2 TERMINATE
   DICT/* + 1 **

PR2.. CA EOLMRK/(GLOT EOLMRK **/PR1)
   **/PR1

compiles into

PROGRM	ENTRY	P1840X
P1840X	TRACE	115,,22360
	C	FORTIO,,0
	C	INITIALIZE,,0
	etc.	

Since the PARSDO parser, which automatically is employed at the top level, by itself is a left-to-right parser *without* backup, the top-level sentences have to be written as a loop with a suitable entry and exit(s). Each exit terminates at the null component **. If there is more than one entry pointing to the same label, then the entry (if any) which is named the same as the label must be indicated last.

Virtual. A call to an overlay *via* the virtual OV now could be coded as

OVER = *OV..

A.. PARSDO(OVER) = NULL

which would compile into

A	TRACE	211,22360X
	M	ALEX,,0
	MS	PARSDO,,OV
	S	= 0,,0

The corresponding entry in the overlay could be coded as

PROGRAM = OV

PROGRAM.. A

B.. C D/B **

which would compile into

OV	ENTRY	P1200X
P1200X	TRACE	17,,22360
	C	A
	C	,,B2700X
B	TRACE	18,,22360
B2700X	C	C,,0
	C	D,,B
	C	0,,0

A virtual name F of a definition E now is indicated by a trailing equal sign, e. g.,

$$E = *F =$$

When TMG operates in its two-pass mode, TMG cannot compile more than one deck. Since TMGL employs the two-pass mode, TMGL cannot compile more than one deck at a time. Therefore, neither the initial compilation nor any subsequent recompilation of more than one *segment* of an overlay compiler can be stacked with the execution of that compiler in a single computer run.

k. New features. The new features introduced into TMGL are summarized here for the convenience of a reader who already is familiar with TMG.[3]

Two options have been added:

NOT-size

PREDEFined

Each of the size options now defaults to the value 25. Each size indicates an upper bound on the length of the

_____

[3]Germann, D. A., *TMG, A Syntax-directed Compiler,* Sep. 23, 1967 (JPL internal document).

named expression which will be entered into the dictionary in the hope of eliminating a duplication(s). The names

R0 P0 NULL

R1 P1

for the definitions

$($)

$($P1$)

respectively, are known in most places as PREDEFined if the option is selected. The use of this option saves compilation time and dictionary space. Since there are a few places, e. g., error recovery and arguments of the $Pn function, where these names are unknown as PREDEFined, whichever of these names are used should be defined, e. g., in the .DEFINITION. section.

The triple star has been introduced as another *explicit* type for unknown functions. Thus, nothing was lost by dropping each of the triple-star functions from the known status.

A virtual name of a colon-type sentence or of a definition now may be designated by, e. g.,

A1 = *V1..

A2 = *V2 =

respectively.

A double-word octal constant now may be designated by, e. g.,

A = 123456,654321B

where the B indicates that the preceding one or two words are to be read by TMGL in "binary," i. e., octal. Such a double-word "character class" is required as the argument of each of the functions

**CHAR

***STRING

The macro .PTRS. now is part of the syntax. This macro is used to define arrays, e. g.,

.PTRS. PTR1(10),PTRA1(50)

Since the only functions which now remain known for use as a left-side of a component are

IF

COMPUTE

ARBNO

NOT

any other function has to be declared before it is employed as a left-side of a component. All other names now are available for free use by the programmer.

A definition now may be placed anywhere in the .SYNTAX. section, but ahead of its use as a left-part of a subject. The two other locations still are permissible for the definition.

The apostrophe ' now is available as a synonym for .OR. in a compound left-part of a component. For example, the construction

A'B/C

is much clearer than

A .OR. B/C

but yields the same target code.

A colon-type sentence, without the label and colon, now may be the argument of a double- or triple-star function. This new feature is required for certain uses of the

**LOCAL

**PARSDO

functions. For example,

COMPONENT-LIST.. LOCAL(SPI CLO SPI4 $

 = (1)$($P2(BV1)$)) = (1)$($P1(BV1)$)

compiles into

X2X	OCT	000001007501
	OCT	010000000000

```
        PTR      BV1
        OCT      000000000000
  X4X   OCT      000001007502
        OCT      010000000000
        PTR      BV1
        OCT      000000000000
  X1X   C        SPI,,0
        C        CLO,,0
        C        SPI4,,0
        S        X4X,,0
  CLST  TRACE    267,,22360
        M        ALEX,,0
        MS       LOCAL,,X1X
        S        X2X,,0
```

The default subject

$$= \$(\$P1\$)$$

would be unable to pass down the bound variable BV1.

The second arithmetic expression of the arithmetical relation now defaults to zero, e. g.

A.LT.

is a short form for

A.LT.0

l. Conclusion. The guiding principle has been to make both TMGL and the syntax as systematic as possible. That principle, together with attention to detail throughout, has resulted in greater compactness of the source code and in improved readability, reliability, diagnostics, and error recovery. In spite of the greater sophistication, a reduction in source and target coding of TMGL itself and of a typical compiler compiled by TMGL has been effected. Furthermore, any target coding not generated need not be assembled, stored, or executed afterwards; hence, a substantial savings in assembly, execution, and compile time results. The *second* generation of any of the few compilers that, like TMGL, is written in its own language benefits from its own improvements.

As a result, any compiler, e. g., TMGL or the simulation compiler, became easier to write and more likely to compile successfully, compiled and executed faster, used less storage for itself hence could translate larger pro-grams because more space was available for the dictionary, and provided more reliable performance.

References

1. Feldman, J. and Gries, D., "Translator Writing Systems," *Communications of the ACM,* Vol. 11, No. 2, pp. 77–113, Feb. 1968.

2. McClure, R. M., "TMG—A Syntax Directed Compiler," in *Proceedings of the 20th National Conference,* Cleveland, Ohio, August 24–26, 1965. Association for Computing Machinery, 1st edition, ACM Publication P-65, pp. 262–274. Lewis Winner, New York, N.Y., Aug. 1965.

3. A Formalism for Telemetry Decommutation, *J. Kulick*

a. Introduction. Telemetry decommutation is basically a problem in pattern recognition. Because of this, the various classical approaches to pattern recognition problems should be applied to this specific one. Two primary approaches to pattern recognition are statistical decision theory techniques (statistical pattern recognition) and linguistic techniques (linguistic pattern recognition). Statistical techniques are used primarily in cases where there is a classification task. That is, an unknown stimulus is to be classified into one of a pre-defined number of classes. Statistical techniques are also used where a great deal is known about the statistical structure to be encountered. Linguistic techniques are used primarily when the recognition task involves detecting structural relationships among entities. The primary goal here is to parse a given surface structure into its constituent elements and the relationships between these elements.

Telemetry decommutation represents a particularly interesting pattern recognition problem since aspects of both linguistic and statistical processing are inherent in it. In this article, both approaches are used in an integrated system. The linguistic part of the system generates alternative parses of the input telemetry string, and associates, with each alternative parse, values representing the difficulty of the parse, the "difficulty" being measured by heuristic techniques. Each of the alternative parses are then evaluated, using heuristic and statistical information to select the best one. Heuristic and statistical information is also used during the parsing process to reject uninteresting parses.

The approach taken here is based on previous work by Duda and Hart (Ref. 1). Their problem of recognizing handwritten Fortran is similar in structure to the telemetry decommutation problem.

b. The problem. The telemetry decommutation problem is basically one of taking a string of 1's and 0's, and reconstructing the original values that were associated with its construction. Telemetry streams are normally generated by taking the output of a shift register and transmitting it bit by bit. This shift register, or commutator, is broken up into a number of channels. Each channel is assigned a fixed number of bits. Each channel either represents a directly sampled measurement, such as a physical system state, or is subcommutated into a number of subchannels. The subchannels are, of course, sampled at a lower rate. Figure 26 shows a simple commutation with one subchannel. The basic problem, that of deconcatenating or decommutating the channels from the telemetry stream is complicated by the introduction of errors. Errors are introduced in the communication network. The goal now becomes one not only of deconcatenating the telemetry stream, but of choosing, from among the possible deconcatenations, the best one.

The problem can be thought of in linguistic terms. The data transmitted from each channel is considered to be a letter in an alphabet. A *word* in the language consists of the output of one pass through the high deck of the commutator. For example, in Fig. 26 a word would be either B1 N2 B2 H2 or B1 N2 Clock H2. The structure of each word is given by rules of grammar defined by the commutator structure. To *parse* the data is meant to identify the letters (or *terminals*) and deduce the value of identified terminals for each valid (conforming to the rules of grammar) word.

There are essentially two types of parse, top down and bottom up. The top-down parse assumes a structure, and searches for supporting terminals, while the bottom-up parse looks for terminals, and deduces the structure.

We are approaching the telemetry decommutation problem from a bottom-up parse point of view. Therefore, the terminals must be identifiable. We now come to the first statistical aspect of the problem. The various bits assoc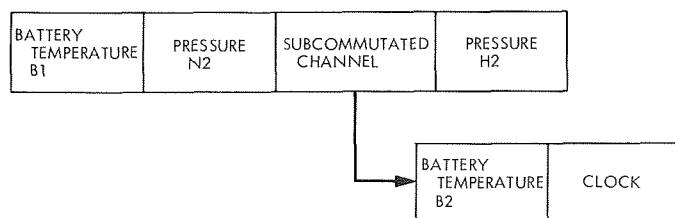iated with a channel are identifiable only with some statistical reliability that they are indeed the correct bits for the channel.

The statistical characteristic is caused by two distinct types of phenomena. Firstly, the physical phenomena being observed have probability distributions. For example, if the expected value of a battery temperature is 72°C, there is a non-zero probability that a measurement will yield 71, 73, 70, or 74°C. These distributions are caused by the physical process being observed. So, if we had located what we believed to be the correct set of bits for a particular channel, we could only say that with some probability that these were indeed the correct bits. Secondly, errors with known probabilities are introduced by the communications channel, e.g., bits are received incorrectly, bits are added or dropped, etc. During the parse, occurrences of these errors are hypothesized depending on the probabilities.

The parse will be accomplished by means of a heuristic tree search. The problem is represented by a decision tree where each node or position in the tree represents a particular step or subgoal in the process. Each arc represents a rule of the system that enables one to proceed from one subgoal to the next. There is an evaluation function that assigns a value to each node. The object of the search is to proceed from the root of the tree to the highest level of the tree (representing a complete parse), ending on the node with a maximum value.

The most difficult part of any heuristic system is to develop the evaluation functions to be used. If we were to pursue all nodes with all possible rules, we would have an inordinate number of nodes. What we want here is a way to tell us just how good a position is, and whether or not it is worthwhile pursuing in comparison with the other positions available. The goal of the evaluation function is to eliminate as many nodes as possible.

The specific features of a position that are used in the system will be discussed more fully in *Paragraph c.* In the proposed system, there will be two types of evaluation functions. One will be a position evaluation function, the other a rule evaluation function. The position evaluation will determine what positions to use as the next starting point, while the rule evaluation function will tell what rule to use once a starting position is chosen.

c. Formalization of the problem. In the heuristic tree-search formulation of the problem, we have positions or nodes representing alternative partial interpretations of the bit strings, and a set of rules such that when a rule

Fig. 26. A simple commutator

is applied to a position, a new position or positions are obtained.

$$\Pi = \text{a set of all positions}$$

$$\mathbb{R} = \text{a set of all rules}$$

$$\pi = \text{a single position} \in \Pi$$

$$R = \text{a single rule} \in \mathbb{R}$$

We must be able to calculate for every position π a value that tells us, relative to the other positions, how good a position it is:

$$V_\Pi (\pi) = \text{value of position } \pi$$

At the highest level, each rule is talking about one channel, and for each channel, there is one and only one rule. To determine whether a rule is applicable to a position, we have a rule–position evaluation function.

$$V_R(R,\pi) = \text{value of rule } R \text{ with respect to the position } \pi$$

Finally, again at the highest level, we have a transform map which applies a rule to a position. In general, a rule applied to a position yields many new positions, each with a different value, each due to a different hypothesis within the rule.

$$T_{PR} : \mathbb{R} \times \Pi \to \text{power set } (\Pi)$$

We have a transform axiom that tells us just when this transformation map is defined

$$(\forall \pi)\,(\forall R)\,[(R \in \mathbb{R}) \text{ and } (\pi \in \Pi)$$

$$\text{and } (V_\Pi (\pi) \geq \theta_1)$$

$$\text{and } (V_R (R,\pi) \geq \theta_2)]$$

$$\Longleftrightarrow (\exists x)\,[x \in T_{pr} (R,\pi)$$

$$\text{and } (x \neq \phi)], \qquad \phi = \text{empty set}$$

This simply says that for $T_{pr}(R,\pi)$ to be defined, the value of the position, and the value of the rule with respect to the position, must be sufficiently high, i.e., greater than θ_1 and θ_2, respectively.

A position in the tree represents a subgoal of the parse, i.e., some channels have been identified and others re-

main to be identified. A *position* is defined as a 6-tuple, containing the following information:

(1) *Bit string* being operated on.

(2) *Set of found channels* {<*name, value, confidence measure, position in bit string, hypothesis used*>}.

(3) *Synchronization descriptor.*

(4) *Value of this position* $V_\Pi (\pi)$.

(5) *List of rules used to get to this position.*

(6) Information about non-local hypotheses that affect adjacent channels.

The *bit string* is arbitrary length bit string being operated on (usually 1 or 2 "words" long). The *set of found channels* is a list of the channels that have been identified at this position. The *confidence measure* of a found channel is derived from the statistics of the terminals mentioned previously. The *hypothesis used* is part of a rule. It is described below. The *synchronization descriptor* gives the current synchronization of the subcommutated decks. It is described in *Paragraph d.* The *position evaluation* $V_\Pi(\pi)$ is heuristic. The position evaluation function will utilize:

(1) Confidence measure on found channels.

(2) Complexity of rules (the more complex the rules, the less confident the measure).

(3) Depth of the tree (the deeper in the tree, the better the position).

(4) Distance of this channel from other previously identified channels.

A rule description is similar in concept to a position description; i.e., it should describe the parameter to be searched for, and any transformations that may be used on the input data stream. A rule consists of the following:

(1) *Name* of channel affected.

(2) *Width* of channel (number of bits).

(3) *Location*, a number (not a bit position) indicating where in the high-deck this channel is normally found.

(4) *Hypothesis set*, a set of all possible alternative hypotheses to be used to find this channel. This will be discussed shortly.

(5) *Value* of the rule.

The value of the rule is obtained from the *sampling rate* and the *complexity index*. The sampling rate is simply an indicator of how often a given commutator structure will cause this parameter to appear in words. This is, in some sense, how often this rule should have been used. The complexity index is associated with each hypothesis, and is inversely proportional to the complexity of the hypothesis.

An individual rule represents all possible ways of locating a specific channel. Each rule R_i has a hypothesis set.

$$H = \{h_1^{R_i}, h_2^{R_i}, \cdots, h_j^{R_i}\}$$

Each hypothesis is based on the errors that have been introduced by the communication channel on the bits in question, i.e., bits have been added, dropped, complemented, etc. The confidence measure of the hypothesis is determined by the statistics of the errors.

Before applying a hypothesis, we must first calculate a location in the bit stream at which the hypothesis is applied. This is done as follows:

(1) Calculate *distance* (number of bits) between channel being hypothesized about and the *anchor* or sync channel being used.

(2) Obtain the location in the bit string of the anchor.

(3) Obtain the location where the hypothesis is to be applied as the location of the anchor plus the distance.

d. Linguistic representation of the commutator structure. There are two main reasons for desiring to define the commutator structure linguistically. Firstly, it establishes the grammar rules that are to be used in the parsing process. Secondly, it supplies a suggested representation system for synchronization information. (The *synchronization descriptor* mentioned earlier.)

For specifying the commutator structure, we will use a phrase structure grammar. The following special symbols are used:

V_{NN} non-terminal non-subcommutated channel names = {A, B, C $\cdots$}

V_{NA} non-terminal subcommutated channel names = {$\alpha \beta \gamma \delta \cdots$}

V_N non-terminals = $V_{NN} \cup V_{NA}$

V_T terminals = {a,b,c, $\cdots$}
  spatial concatenation

| temporal concatenation

Each deck of the commutator is represented by a grammar rule. Each subcommutated channel in a deck is represented by a non-terminal ϵ V_{NA}. Each non-subcommutated channel is represented by a non-terminal ϵ V_{NN}. Ad-hoc productions rewrite non-subcommutated non-terminals into terminals. A new production (not ad-hoc) is added for each subcommutated channel.

The following grammar rules describe the commutator shown in Fig. 27:

$$S \rightarrow A \alpha C D \beta E \delta F$$
$$\alpha \rightarrow G \mid \delta \mid H \mid I$$
$$\beta \rightarrow J \mid K \mid L \mid M$$
$$\gamma \rightarrow N \mid O$$
$$\delta \rightarrow P \mid Q$$
$$A \rightarrow a$$
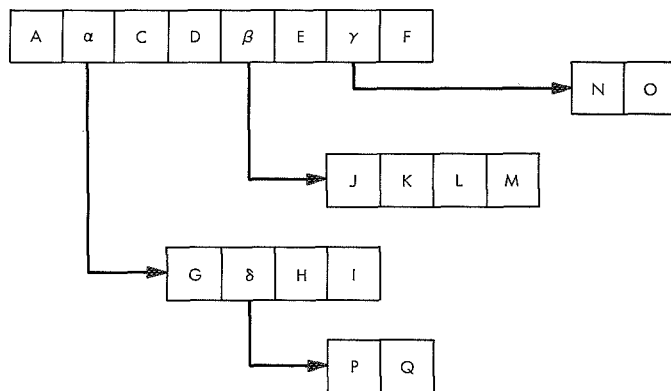
.

.

$$Q \rightarrow q$$

Fig. 27. A commutator structure

The interpretation of the linguistic representation of the commutator structure is straightforward. The linguistic representation also forms the basis for the representation of synchronization information. The synchronization descriptor could be given by a vector giving the position last recognized for each grammar rule with a member of V_{NA} on the left. In the example of Fig. 26, the vector

$$(3, 2, 1, 2)$$

would indicate that the last recognized channels in commutator positions α, β, γ, and δ were H, K, N, and Q, respectively. The next expected commutator words should then be

A I C D L E O F

A G C D M E N F

A P C D J E O F

etc.

Reference

1. Duda, R. and Hart, P., "Experiments in the Recognition of Handprinted Text," *AFIPS Proceedings Fall Joint Computer Conference*, pp. 1139–1150, 1968.

4. A Comparison of Methods for Synthesis of Correlated Noise, C. Travis

a. Introduction. This article compares two methods of generating a stationary time series with a prescribed spectral density function. Each method generates a sequence of numbers x_k which can be regarded as having been derived from a continuous time series $x(t)$ by sampling the values of the signal at spacing Δt, i.e., $x_k = x(t_k) = x(k\Delta t)$.

b. Theory.

Method I. In method I (Ref. 1), a sequence of independent normal random numbers with zero expectation and unit variance is passed through a linear filter to obtain the desired time series. Linear filtering is the process by which a set of input data y_k is transformed into a set of output data x_k by means of the relationship

$$x_k = \sum_{n=-L}^{L} c_n \, y_{n+k} \tag{1}$$

where the c_n are suitably chosen weights. The spectrum of the output of a linear filter, when the input is a stationary process, is

$$\Gamma_x(w) = R(w)^2 \, \Gamma_y(w) \tag{2}$$

where $\Gamma_x(w)$ and $\Gamma_y(w)$ represent the spectrum of the output and input, respectively (Ref. 2). The c_n in Eq. (1) and the $R(w)$ in Eq. (2) are related by the following formulas:

$$c_n = \frac{1}{w_0} \int_0^{w_0} R(w) \cos \left(\frac{n \pi w}{w_0} \right) dw \tag{3}$$

$$R(w) = \sum_{n=-\infty}^{\infty} c_n \cos \left(\frac{n \pi w}{w_0} \right) \tag{4}$$

where $R(w)$ is a symmetric periodic function with period $2w_0$, and the c_n can be considered as having been sampled from a continuous time series $c(t)$ at a spacing of $\Delta T = 1/2w_0$. It is only necessary to use a finite number of c_n in Eq. (4) to approximate $R(w)$ quite accurately. This corresponds to replacing $c(t)$ by

$$c^*(t) = \begin{cases} c(t) & \text{if } |t| \le T^* \\ 0 & \text{if } |t| > T^* \end{cases}$$

The degree of accuracy obtained in approximating $R(w)$ depends only on where $c(t)$ is truncated. Once the desired degree of accuracy has been decided upon and a step size Δt has been chosen, the L in Eq. (1) can be determined by $L \, \Delta t = T^*$. Thus, for a given degree of accuracy, the smaller Δt, the more c_n are required.

Now, suppose it is desired to generate a sequence of numbers with spectral density function $F(w)$, $0 \le w \le w^*$, where this sequence is considered as having been derived from a continuous signal $x(T)$ by sampling at a spacing of Δt.

In Ref. 2, it is shown that white noise which has been sampled at a spacing of Δt has spectral density function

$$\Gamma_y(w) = \Delta t, \qquad -w_0 \le w \le w_0$$

where $w_0 = 1/2\Delta t$. The input data y_k can be considered as such a sampling. Using the above formula, Eq. (2) becomes

$$\Gamma_x(w) = \Delta t \, R(w)^2$$

Thus, if the c_n in Eq. (1) are obtained from Eq. (3) using

$$R(w) = \begin{cases} \left[\dfrac{1}{\Delta T} F(w)\right]^{1/2} & \text{if } 0 \leq |w| \leq w^* \\ 0 & \text{if } w^* < |w| \leq w_0 \end{cases} \quad (5)$$

the sequence x_k will have spectral density function

$$\Gamma_x(w) = \Delta t \, R(w)^2 = \begin{cases} F(w) & \text{if } 0 \leq |w| \leq w^* \\ 0 & \text{if } w^* < |w| \end{cases}$$

(Note that the requirement $w^* \leq w_0$ imposes a maximum on the step size Δt.)

Method II. The technique of method II is similar to that given in Ref. 3. Suppose $F(w), 0 \leq w \leq w^*$ is the prescribed spectral density function. This function will be approximated with spikes of power at frequencies chosen uniformly, but randomly, in the interval $[0, w^*]$. Let this interval be divided into N equal parts, and $w_k, k = 1, \cdots, N$, be chosen from a sequence of independent random numbers with a uniform distribution over the interval

$$\left[(k-1)\frac{w^*}{n}, k\frac{w^*}{n}\right], \qquad k = 1, \cdots, N.$$

The power in each of these intervals will be approximately $F(w_k)$ multiplied by the length of the interval, or $F(w_k) w^*/n$. Let $\phi_1, \cdots, \phi_2$ be a sequence of independent random numbers with a uniform distribution over $[0, 2\pi]$. Then, if

$$A_k = \left[2 \frac{w^*}{n} F(w_k)\right]^{1/2}$$

the time series

$$x(T) = \sum_{k=1}^{n} A_k \cos\left(2\pi w_k T + \phi_k\right) \quad (6)$$

will have power $F(w_k) w^*/n$ at the frequencies w_k and zero power elsewhere. As n is increased, the spectral density function of Eq. (6) will approach $F(w)$.

c. Programming techniques.

Method I. $F(w)$, Δt, and L (the number of c_n to be used) were inputs to the program. $F(w)$ was given in the form of a table of equally spaced values. $w_0 = 1/2\Delta t$ and $R(w)$ was calculated using Eq. (5). The c_n were obtained from Eq. (3) using the trapezoidal rule for numerical

integration, and unknown values of $R(w)$ were found by linear interpolation. Then, a sequence (the sequence y_k) of independent normal random numbers was developed on the computer. This sequence was converted into the desired sequence by the sliding summation Eq. (1).

Method II. $F(w)$, Δt, and ND (defined below) were inputs to the program. $F(w)$ was given as a table of equally spaced values $F(f_J)$, $J = 1, 2, \cdots, M$. ND was the number of random frequencies $w_k^{(J)}$, $k = 1, \cdots, ND$, to be chosen in each of the intervals $[f_J, f_{J+1}]$. The value of F at $w_k^{(J)}$ was found by linear interpolation.

To make what follows simpler, it will be assumed that only two values of F were given, its values at f_1 and f_2. Let $[f_1, f_2]$ be divided into ND equal parts, and $w_k, k = 1, \cdots, ND$, be a random frequency chosen in each of these subdivisions. The power in each subdivision is approximately

$$F(w_k) \frac{(f_2 - f_1)}{ND}$$

Let

$$A_k = \left[2 F(w_k) \frac{(f_2 - f_1)}{ND}\right]^{1/2}$$

Then, by Eq. (6)

$$x_J = \sum_{k=1}^{n} A_k \cos\left(2\pi w_k J \Delta T + \phi_k\right)$$

is the sequence of numbers to be generated. The cosines on this equation were calculated using a recursion formula. A flow chart in Fortran notation for the process is shown in Fig. 28.

d. Comparison of methods.

Dependence on step size. Method I is very dependent on step size. As an example, consider the function

$$F(w) = \begin{cases} 0 \text{ if } 0 \leq w < 2 \\ 1 \text{ if } 2 \leq w \leq 3 \\ 0 \text{ if } 3 < w \end{cases} \quad (7)$$

Suppose it is desired to approximate this function to within 0.05 except at points of discontinuity where the error is allowed to exceed this value only in an interval
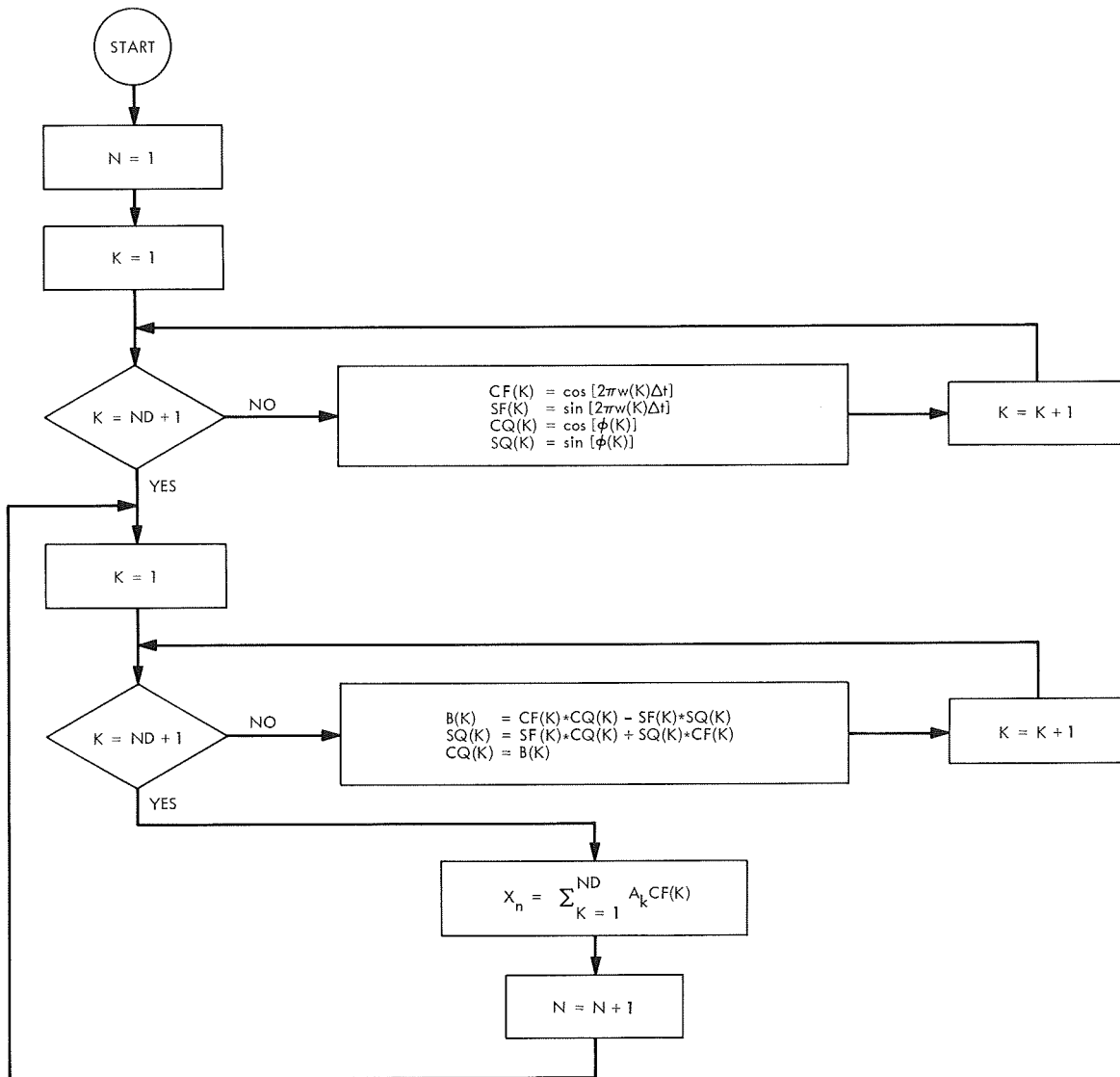
Fig. 28. Flow chart in Fortran notation for method II

of length 1/16 on either side of the points of discontinuity. The following table shows the relationship between Δt, w_0, and L (the number of c_n taken) when the above degree of accuracy is maintained.

Δt	w_0	L
0.166	3	15
0.04	12.5	60
0.01	50	240

Note this table is consistent with the relationship $L \Delta t = T^*$ which was stated earlier.

Method II is not dependent on step size.

Accuracy. The retrieval of the spectrum of a time series $x(t)$ is accomplished with two formulas:

$$0(T) = \frac{1}{T} \int_0^T x(t)\, x(t + T)\, dt \qquad (8)$$

$$\int (w) = 2 \int_0^S \phi(T) \cos(2 \pi w T)\, dt \qquad (9)$$

However, the choice of T and S in these two formulas is critical. T and S determine how long the time series, $x(t)$ and the autocorrelation Function (8) are sampled. To understand the problems involved, one must realize that Eq. (9) does not give the "true spectrum" of $x(t)$, but rather a statistical estimation of it. As with most statistical estimators, in using Eq. (9) one is forced to compromise between variance and bias. Increasing S decreases the bias but increases the variance. Decreasing S produces the opposite effect. The extent to which fine detail can be detected in the spectrum of a time series is influenced by both the variance and the bias. Both should be made as small as possible. This can be accomplished by increasing the time T that the time series is sampled. Thus, it is possible to estimate the "true spectrum" to as much accuracy as desired if T is made large enough. However, for a fixed T, there must be a trade-off between variance and bias.

In discussing the accuracy of the two methods, the above considerations must be kept in mind. There are actually two types of accuracy involved. One is how close is the actual spectrum of the time series generated to the prescribed spectrum. The other is how close is the statistical estimation of the actual spectrum to the prescribed spectrum.

It is possible to determine what the actual spectrum of the two methods should be. As can be seen from Eq. (5), the prescribed spectrum of method I is $F(w) = \Delta t\, R(w)^2$ where $R(w)$ is defined by Eq. (4). The time series actually generated will have spectrum Δt at $R^*(w)^2$ where

$$R^*(w) = \sum_{N=-L}^{L} c_n \cos\left(N\, \frac{\pi\, w}{w_0}\right) \qquad (10)$$

Thus, to determine how the actual spectrum of method I deviates from the prescribed one, Eq. (10) must be compared with Eq. (4).

In method II, the actual spectrum of the time series generated is a series of spikes at the random frequencies and zero power elsewhere. However, if one is not interested in resolving these spikes, and chooses T and S accordingly, the statistical estimation of the actual spectrum can come quite close to the prescribed spectrum. It was found that if 16 random frequencies were used in the interval (Refs. 2 and 3) that Function (7) could be reproduced to within an accuracy of 0.05.

Speed. Both methods were programmed in Fortran IV and run on a Univac 1108. Method I takes an average of $31*L + 38$ μs per generated point, where L is the number of c_n taken in Eq. (1). Method II takes an average of $31*ND + 5$ μs per generated point, where ND is the number of random frequencies used in Eq. (6). For a given degree of accuracy, the running time for method I will vary with step size, whereas method II will not. Demanding the same degree of accuracy for both methods, the following table shows how running time in μs varies with step size for spectral density Function (7).

Δt	Method I	Method II
0.166	503	501
0.04	1898	501
0.01	7478	501

Storage. Method I requires 256 locations for the subroutine with 61,228,902 locations for data when $L = 15$,

60, and 240. Method II requires 213 locations for the subroutine with 118 locations for data when $ND = 16$.

e. Conclusions. Method I compares favorably with method II only when using the maximum step size possible. In all other cases method II is superior.

References

1. Bykov, V. V., *A Method of Modeling Stationary Normal Noise on a Digital Computer.*

2. Jenkins, C. M., and Watts, D. C., *Spectral Analysis and Its Applications.* Holden-Day, Inc., San Francisco, Calif., 1968.

3. Peabody, P. R., and Adorno, D. S., "Digital Synthesis of Correlated Stationary Noise," *Communs. Assoc. Comput. Mach.,* Vol. 5, No. 7, Jul. 1962.

5. A Switch Controller for the SCU Cone, R. B. Kolbly

a. Introduction. This article describes a prototype microwave switch controller for use with the DSS 14 S-band cassegrain ultra (SCU) cone. This switch controller provides control of three microwave switches, prohibits selection of an improper transmitter load, and protects against microwave switch failure. Provision is made for remote operation, and a pictorial switch position display is provided.
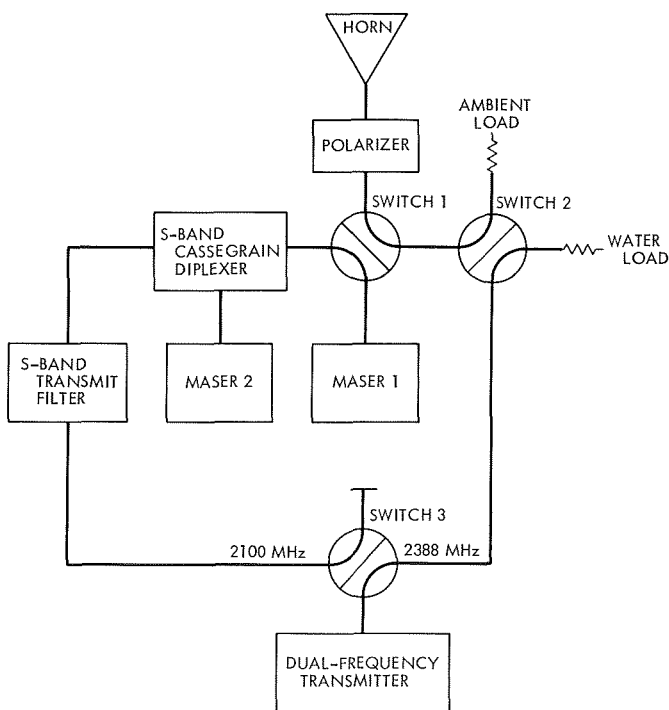

Fig. 29. SCU feedcone modification 2

b. Design. Figure 29 is a block diagram of the SCU feedcone and related microwave equipment. Inspection will show that there are certain switch combinations which could result in the transmitter being connected to a low-power termination or into a traveling-wave maser. To guard against any unfortunate incidents, the switch position information is applied to a relay-logic circuit which, through the external beam interlock circuit, will not allow the transmitter to operate unless all waveguide switches are in an acceptable configuration.

Individual control of each waveguide switch is available on the switch controller panel (Fig. 30). Also, any one of four operational modes (maser I, radar transmit, diplex and water load) may be selected either locally by push buttons on the front panel or remotely by contact closures. This allows remote control of a planetary radar mission.

Display of switch position is provided by panel lamps on the controller and also by projection-type displays in a block diagram of the microwave system on the front panel of the controller. These projections are visible in Fig. 30, along the upper edge of the panel.

c. Waveguide switch protection. Failure of a waveguide switch is usually caused by one of the control relays internal to the switch failing to disable the motor at the travel limit or a rotor "frozen" between positions. In either case, power remains applied to the stalled switch motor until either a fuse blows or the motor destroys itself.

To prevent these failures, a circuit is provided which senses the length of time power has been applied to the switch, and if it is excessive, power is removed and a fault is signaled to the operator.

Figure 31 is a schematic diagram of the switch protective circuitry. A small current transformer T1 senses the current to the waveguide switches. This 60-Hz ac voltage is rectified and clipped (so the output voltage is essentially independent of the number of switches drawing current) and used to charge a capacitor C1 through resistor R3. When capacitor C1 is charged to a set value, it operates a Schmitt trigger and relay K1. Relay K1 is in a latching circuit so the power remains off the waveguide switches until the current is manually reset. Provision is made for testing by applying a small dc input signal, which will check for satisfactory operation.
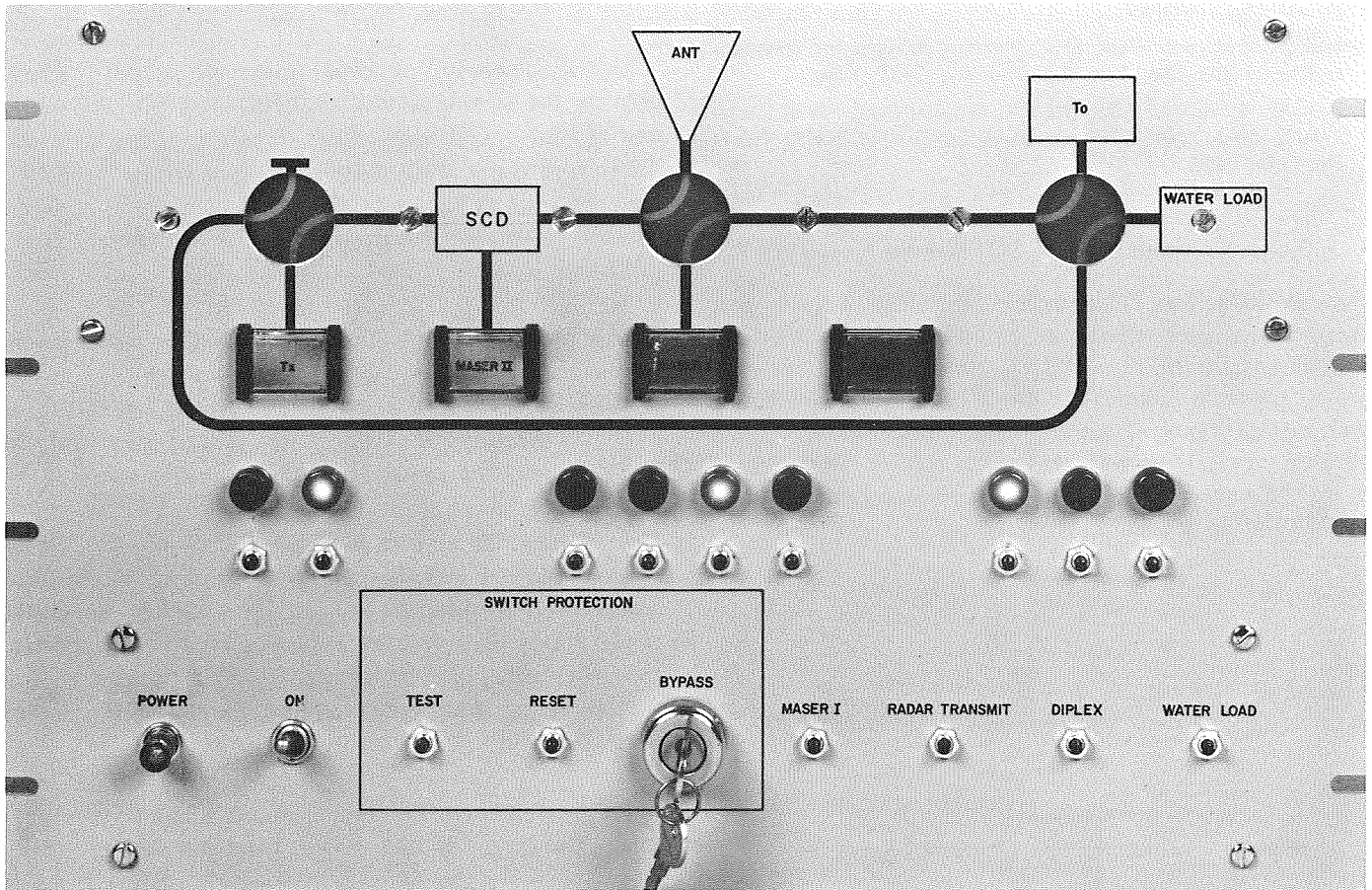
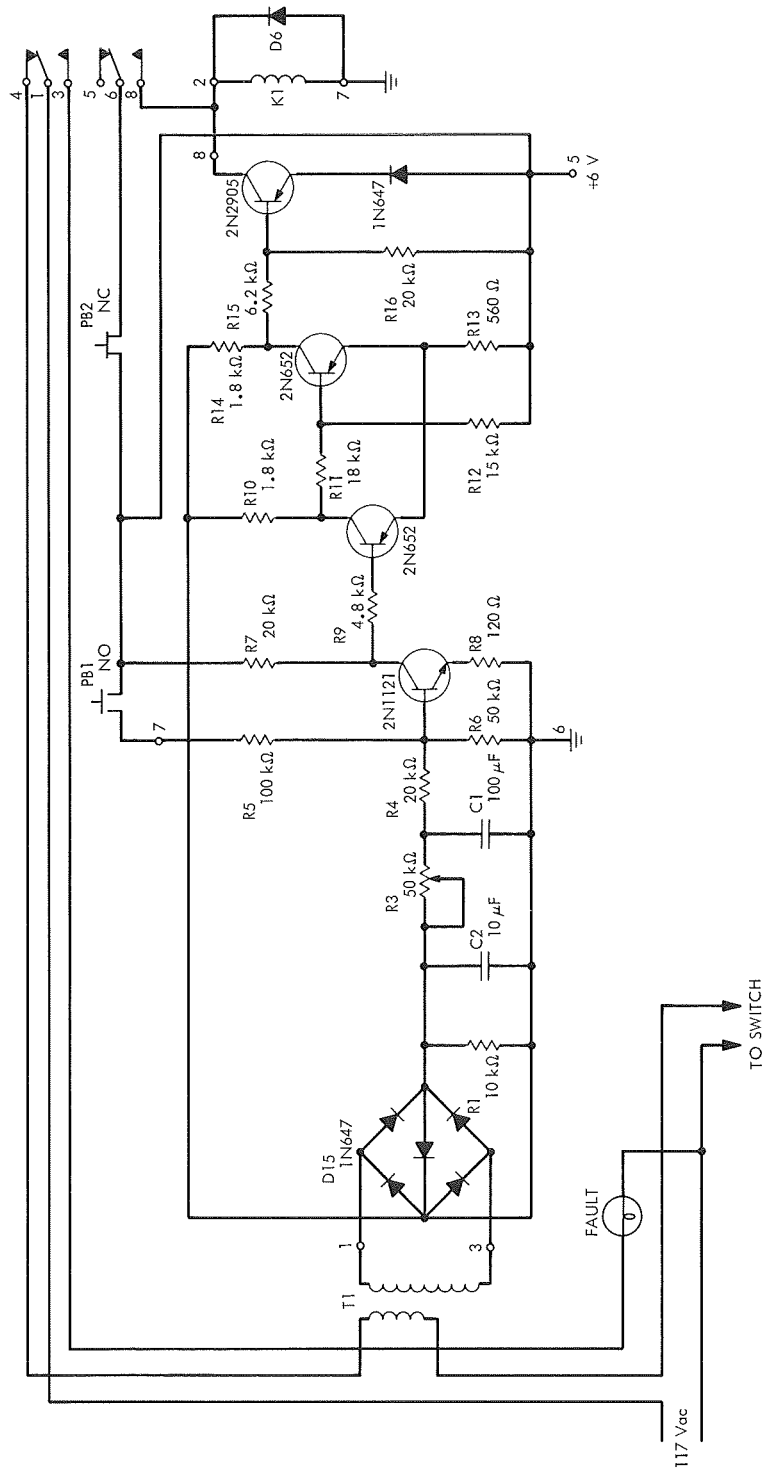Fig. 30. Front view of SCU feedcone microwave switch controller

Fig. 31. Schematic diagram—microwave switch protection circuit

6. Automatic (Computer-Controlled) Ephemeris Update Tracking, R. M. Gosline

Automatic boresighting of antennas on coherent or noncoherent sources would be of benefit in DSIF operations, and would offer the possibility of automatic tracking of spacecraft, with only a small amount of signal degradation, without the use of monopulse feed systems. Previous testing at DSS 13 has indicated that the approach initially chosen was not optimum.

Considerable analysis of an ephemeris update tracking scheme has been made and will be summarized here, although experimental verification has not yet been attempted.

The method is to offset the ephemeris angles of a source with time-varying constant amplitude sinusoids that are shifted 90 deg in each axis. The antenna beam will, thus, trace a conical scan around the source, and if the sinusoids are correlated with a voltage proportional to the received noise (for radio sources) after suitable filtering, the boresight error may be determined and used to modify the ephemeris angles in near real-time.

The offset function is characterized by

$$X = r \cos wt, \qquad y = r \sin wt \qquad (1)$$

The angular distance from the source to the center of the beam is

$$\phi(t) = [(r \cos wt - E_x)^2 + (r \sin wt - E_y)^2]^{1/2}$$

where E_x, E_y are the angular boresight errors. Solving for wt yields

$$wt = \sin^{-1} \left[\frac{r^2 + E_x^2 + E_y^2 - \phi^2(t)}{2r(E_x^2 + E_y^2)^{1/2}} \right] - \tan^{-1} \frac{E_x}{E_y} \qquad (2)$$

The received noise is a function $N(\phi)$ of this distance and could be characterized by $| \sin A\phi(t)/A\phi(t) |$. With an appropriate digital filter, analysis is simplified and the system behavior made more predictable. Consider then

$$N(\phi) = 1, \qquad \phi(t) \leq \phi \atop N(\phi) = 0, \qquad \phi(t) > \phi \qquad (3)$$

where ϕ is the 3-dB point. The correlation coefficients are

$$C_x = \int_0^{2\pi/w} N(\phi) \cos wt \, dt, \qquad C_y = \int_0^{2\pi/w} N(\phi) \sin wt \, dt \qquad (4)$$

and, using Eq. (3), become

$$C_x = \sin \theta_B - \sin \theta_S, \qquad C_y = \cos \theta_S - \cos \theta_B \qquad (5)$$

where θ_B is the scan angle where the source enters the beam and θ_S is the scan angle when the source leaves the beam.

If $r \neq \phi$, a dead zone will exist at the center where the source will either be always in the beam ($r < \phi$) or always outside the beam ($r > \phi$), yielding no boresight information. It is reasonable then to choose $r = \phi$, and from Eq. (2)

$$\theta = \sin^{-1} \frac{(E_x^2 + E_y^2)^{1/2}}{2r} - \tan^{-1} \frac{E_x}{E_y}$$

so that

$$\left. \begin{array}{l} \theta_S = \sin^{-1} \dfrac{d}{2r} - \tan^{-1} \dfrac{E_x}{E_y} \\[2mm] \theta_B = \pi - \sin^{-1} \dfrac{d}{2r} - \tan^{-1} \dfrac{E_x}{E_y} \end{array} \right\} \qquad (6)$$

with

$$d = (E_x^2 + E_y^2)^{1/2}$$

Combining Eqs. (5) and (6), it can be shown that

$$C_x = E_x \left(\frac{4}{E_x^2 + E_y^2} - \frac{1}{r^2} \right)^{1/2}, \qquad C_y = E_y \left(\frac{4}{E_x^2 + E_y^2} - \frac{1}{r^2} \right)^{1/2} \qquad (7)$$

and

$$E_x = FC_x, \qquad E_y = FC_y \qquad (8)$$

with

$$F = r \left(\frac{4}{C_x^2 + C_y^2} - 1 \right)^{1/2} \qquad (9)$$

The sign of E_x and E_y may be resolved by assigning the sign of C_x and C_y, respectively. Thus, the boresight error may be found by equating Eqs. (8) and (9), using the correlation coefficients C_x and C_y.

For the unlikely case where $E_x = E_y = 0$ exactly, then $C_x = C_y = 0$ and special provisions must be provided because F becomes infinite. It may be advantageous to choose r slightly greater than ϕ to avoid this point of instability at the price of a small dead zone.

7. DSS 13 Operations, E. B. Jackson and R. M. Gosline

a. Experimental activities. From August 16 through October 15, 1969, DSS 13 conducted monostatic and bistatic planetary radar experiments with the planet Venus serving as a target. During bistatic experiments, the system was configured in a total spectrum, cross-polarized mode, while during monostatic experiments, the system was configured in a ranging and total spectrum, matched polarization mode. During this period, the range to Venus increased to 223.5×10^6 km and is still increasing.

Clock synchronization transmissions expanded to include DSSs 14, 41, 42, 51, and 62, with all stations reporting successful data reception, particularly during the period immediately succeeding the *Mariner* Mars 1969 encounter. A transient-induced failure in the programmed oscillator caused extensive lost time; however, full operation was restored on October 7, 1969, with a new transmitting coder being placed into service to correct some irregularities in correlated time at the receiving station.

In preparation for more extensive OSS antenna tests during later missions, the *Apollo 11* lunar surface experiments package was monitored for several days, with signals as strong as -119 dBm being measured.

The asteroid Geographos made its closest approach to the earth (9×10^6 km) on August 27, and an attempt was made to receive signals reflected from it after being transmitted, using the 450-kW R&D transmitter, from the 85-ft-diam antenna at DSS 13. However, due to a number of equipment failures, including the 450-kW klystron and elements of the water cooling system, insufficient integration time was obtained for signals to be detected. Geographos' next close approach will be in 1983.

During testing of a new spacecraft spectrum analysis computer program and associated hardware, observation of several radio sources, among them W3A, VYCMA,

W49, and Orion, was made in an effort to detect an emission line for HDO, a form of heavy water where one hydrogen atom has been replaced by a deuterium atom. On-site data reduction did not disclose this line, and it is felt considerably longer observation times will be necessary if this line is to be observed at Venus.

Among the other effects predicted by the general relativity theorem is bending of electromagnetic waves during passage through a gravitational field. Although very slight, it should be possible to observe this predicted effect under appropriate conditions for waves which pass close by the sun. Utilizing DSSs 13 and 14 as a special long baseline interferometer, experimenters from California Institute of Technology carefully measured the position of quasars 3C273 and 3C279 for several days during the period when 3C279 was occulted by the sun. A position offset on the order of 1.25 arc secs is predicted for 3C279 by the general relativity theorem, although observation of this apparent offset may be masked by system instabilities and the effects of the sun's plasma field. Although some system problems were encountered, between 25 and 30 h of observing were performed over the period September 29 through October 14, with occultation of 3C279 taking place on October 8. Extensive data analysis will be necessary before system performance can be specified and conclusions drawn.

b. System performance.

Digital systems. A major system failure of the SDS 910, antenna positioning subsystem, programmed oscillator, and clock synchronization coders occurred as a result of a momentary short circuit of the 110-Vac line in the SDS 910, inadvertently caused by an operator performing routine maintenance. Forty-two integrated circuits were replaced in the interface logic between the above subsystems. Investigation is being conducted toward providing additional circuit protection. All other digital subsystems performed satisfactorily.

Antenna (electromagnetic). A new, wideband cassegrain feed cone with which the 85-ft-diam antenna has been equipped was described in SPS 37-59, Vol. II, pp. 93–95. Additional measurements of radio sources have been made to evaluate antenna efficiency with this new cone. Measurements of the apparent source temperature of Cygnus A indicate efficiencies of 61% at 2295 MHz and 57% at 2388 MHz. Data analysis indicates that mismatch between the feedhorn and the subreflector may be contributing to the low efficiency at 2388 MHz, but further tests are necessary to isolate the difficulty.

Transmitter (S-band). The 450-kW klystron sprang a leak in the drift tube coolant circuit. The leak was caused by a crack in the klystron coolant fitting, which was located in such a position that local repair was not practical. The tube was returned to the manufacturer for repair and the spare klystron, which had been previously repaired by the manufacturer, was installed. Unfortunately, it also failed (vacuum leak) after a short period of service, leaving an inoperative transmitter with which to conduct the Geographos experiment. Although expedited return and installation of the first klystron was performed, insufficient time remained during which Geographos was close enough for the experiment to be attempted. The already short operating time was further reduced by a failure of a pump which circulates the transmitter coolant, and the experiment was unsuccessful.

c. *System improvements.*

Digital Systems. Software capability of the station control and monitor (SCAM) subsystem was expanded with the addition of a SCAM program tape editing program written for the SDS 930. Means are provided to automatically shorten a SCAM program tape by removal of corrected corrections, inserting only the latest corrections and punching out only non-zero words. With this capability, the fast and slow coder programs were combined (under breakpoint selection) with SCAM internal checkout routines on a program tape one-half the length of either of the original coder programs.

The radiometer program used at DSS 14 with gas-tube noise sources was modified to run on the DSS 13 SDS 930 with solid-state noise diodes. The SDS 930 has been interfaced with binary-coded decimal time, and binary angles from the angle readout subsystem have been connected for use in the servo automation program.

8. Hi-Rel Module Development, D. W. *Slaughter*

a. Low-level interface module. A low-level interface module has been designed in the format of the family of Hi-Rel digital modules (SPS 37-46, Vol. III, pp. 159–161), and provides four identical interface circuits. Each circuit has two inputs. One input is compatible with most integrated circuits. The other input detects signal zero-crossings and provides an interface with certain DSIF RF systems which present a binary signal with levels of +2 and −2 V across 50 Ω. The circuit output has the same characteristics as the Hi-Rel *nand* gate.

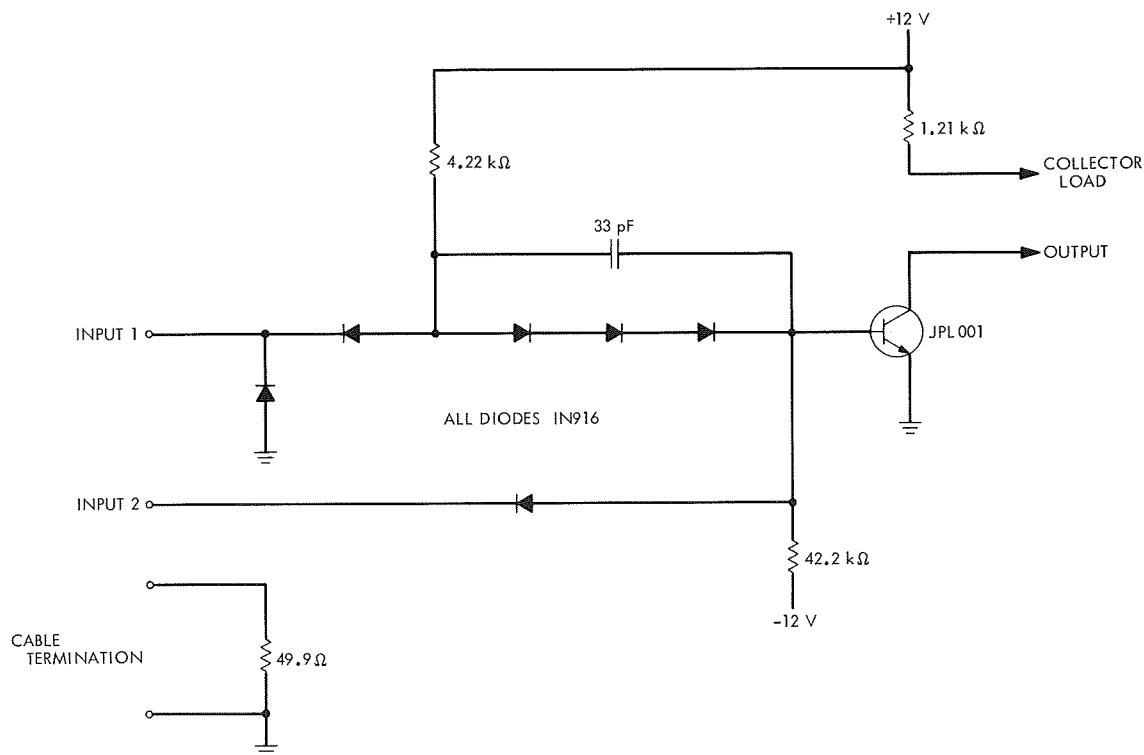Figure 32 is a circuit diagram. Input 1 has a logic threshold in the range of 1.2 to 2.1 V (worst-case), which

Fig. 32. Low-level interface circuit

is compatible with diode–transistor logic and transistor–transistor logic integrated circuits using 5-V power supplies. The input circuit is diode back-clamped to prevent ringing on the interface wiring, which could otherwise result in spurious output responses. Input 2 has a logic threshold in the range of 0 to 0.2 V. A 50-Ω resistor is available for terminating 50-Ω coaxial cables. The circuit output will be the *nand* function of the two inputs, if both are used.

b. Integrated circuit applications. As reported in SPS 37-57, Vol. II, pp. 121–123, a project is underway which will qualify integrated circuit (IC) devices for use in DSIF mission-independent digital equipment.

The DSIF Hi-Rel digital modules program (SPS 37-46, Vol. III, and later issues) provided the DSIF with a standardized approach to the construction of digital equipment. The benefits of this program have been listed as an input to our IC program.

·(1) Standardization permits much of the time-consuming portion of the total manufacturing effort to be performed prior to the final completion of the logic design. Basic logic circuits are pre-wired into a module whose size is identical for all circuits. Connections between modules are made by taper-pin wiring. Assembly hardware is also standardized and prototype equipment can be rapidly assembled after the logic design is complete.

(2) The use of the same module types on several different equipments in various stages of design and construction allows for the modest stocking of these modules. Original estimates of module quantity or mix may be adjusted between projects.

(3) Costs are reduced. The number of DSIF stations (requiring copies of a given equipment) is modest; however, there are a broad spectrum of system functions to be mechanized. Thus, considerable cost savings accrue when it is possible to use the same logic devices to implement various system functions.

(4) Compatible logic modules are available for future activity, including equipment modification, additional spares, and new station equipment.

The benefits of standardization will accrue for ICs only if the chosen family is continuously available. JPL ownership of the design is not in itself sufficient to ensure availability. If the basic approach does not have widespread usage and quickly becomes obsolete, production

facilities will be shut down. Maintenance of these facilities under sustaining contract from JPL could be costly. Therefore, an attempt is being made to identify a family of ICs which has achieved wide-spread acceptance, is manufactured by several competent companies, and is likely to experience graceful obsolescence. It appears possible to make a choice from one of the currently available transistor–transistor logic families which meet the above criteria. The remaining effort consists of:

(1) Selecting and qualifying preferred circuits.

(2) Deciding on the degree of control which JPL must exercise over the manufacturing process to ensure reliability.

(3) Developing procurement and test specifications.

(4) Selecting and certifying vendors from those available and interested.

The following is a discussion of the packaging problems being evaluated: Connections to the Hi-Rel logic modules were made through a taper-pin connector block integral to each module. The additional series connections of a plug and socket were not necessary since the equipment repair philosophy called for the replacement of functional assemblies (which contain a number of modules and do have a quick disconnect plug) at the individual stations. Replacement of modules by pulling taper pins is readily accomplished at the class A repair depot. Unfortunately, the taper-pin block, if used as the connector for IC standard logic modules, would not provide adequate logic density for many of our future equipments. The required logic density is a function of limitations on the length of the wires connecting the logic elements. These limitations derive from the speed capability of the chosen logic family, noise thresholds which are lower than those of our discrete component circuits, and the system logic complexity. A search is underway for a logic packaging scheme which will yield the required density while retaining the benefits of standardization which have accrued from our existing Hi-Rel modules.

The IC packages themselves may represent the smallest number of logic module types available in a form which can be pretested and stocked. Unit logic modules carrying several IC packages (unit logic brings all logic element inputs and outputs to the module connector pins) may be an archaic carry-over from a package form used with discrete components. Furthermore, the unit logic module packaging format tends to be incompatible with

medium-scale integrated (MSI) and large-scale integrated (LSI) circuits which are a form of functional (special-purpose) packaging.

The following general outlines describe a packaging scheme which may meet our objectives. Plugable functional subassemblies carry a significant number of IC packages. These subassemblies accept IC packages on standard grid dimensions. The standard grid dimensioning permits the blank subassembly to be pre-manufactured, and after mounting the IC packages, to be quickly intraconnected by a tape-controlled automatic machine. Special-purpose modules carrying discrete components, hybrid microelectronics, or LSI will fit the standard grid pattern being constrained to some multiple of the standard dimensions. The key to the acceptability of the whole packaging scheme just described is the technology and methodology for attaching the IC packages.

D. Tracking and Navigational Accuracy Analysis

1. Introduction, T. W. Hamilton and D. W. Trask

The DSN Inherent Accuracy Project was formally established by the DSN Executive Committee in July 1965. The objectives of the project are:

(1) Determination (and verification) of the inherent accuracy of the DSN as a radio navigation instrument for lunar and planetary missions.

(2) Formulation of designs and plans for refining this accuracy to its practical limits.

Achievement of these goals is the joint responsibility of the Telecommunications and Mission Analysis Divisions of JPL. To this end, regular monthly meetings are held to coordinate and initiate relevant activities. The project leader and his assistant (from the Mission Analysis and Telecommunications Divisions, respectively) report to the DSN Executive Committee, and are authorized to task project members to (1) conduct analyses of proposed experiments, (2) prepare reports on current work, and (3) write descriptions of proposed experiments. The project is further authorized to deal directly with those flight projects using the DSN regarding data-gathering procedures that bear on inherent accuracy.

The various data types and tracking modes provided by the DSIF in support of lunar and planetary missions are discussed in SPS 37-39, Vol. III, pp. 6–8. Technical work directly related to the Inherent Accuracy Project is

presented in SPS 37-38, Vol. III, and in subsequent *Deep Space Network* SPS volumes, and is continued in the following subsections of this volume.

The first five articles (*Subsections 2–6*) of this section report on work carried out under the Tracking System Analytical Calibration (TSAC) activity. The TSAC activity provides calibration of tracking data and estimates of DSN parameters whose uncertainties represent limitations to navigational accuracy. In addition to the generation of analytic calibration coefficients, TSAC validates their proper transmission/utilization during a mission and performs detailed post-flight analysis of the DSN tracking data to uncover/resolve any anomalies which may exist. Further, this activity is concerned with defining the present inherent limitations to navigational accuracy and recommending feasible improvements which will reduce these limitations to meet future navigational accuracy requirements. This information is presented for the consideration of the DSN and flight projects in negotiating error levels for these parameters consistent with the navigational requirements of the projects and economical constraints.

The major guideline for TSAC in the formulation of an error budget is to maintain a balanced system of error sources. That is, the system is balanced such that a given expenditure of resources is budgeted to minimize the rss of the resultant navigational errors. In general, this necessitates advancing the state-of-the-art for the most critical error sources and, within the above constraints, reducing the effects of other error sources to a level which is negligible when compared to the most critical error source.

For a mission such as *Mariner* Mars 1969, the tightest bounds on the allowable errors for a number of parameters arise from the navigational accuracy requirements during encounter support. In particular, encounter navigational accuracy is most sensitive to error sources, which cause a diurnal signature on the radio tracking data (see Hamilton and Melbourne, SPS 37-39, Vol. III, pp. 18–23). These sources of error are of two classes: (1) those parameters which define the location of the DSS in inertial space, and (2) those phenomena which directly affect the DSS tracking data. The first category includes the location of the DSS with respect to the earth's crust, Universal Time (UT1), polar motion (the motion of the earth's crust with respect to the spin axis), precession and nutation (orientation of the earth's spin axis with respect to inertial space), and the ephemerides of the earth, moon, and target body. Of these, uncertainties in the first three are currently the major limitations to encounter support navigational accuracy. Utilizing the information on UT1 supplied by the

U. S. Naval Observatory (USNO) and the Bureau International L'Heure (BIH) and information on polar motion supplied by the BIH and the International Polar Motion Service (IPMS), the DSN has actively supported efforts to reduce the operational uncertainties of these three parameters. Improvements for the remaining ephemeris-related parameters have been primarily supported by non-DSN efforts.

The dominant sources of error in the second category, those affecting the tracking data directly, include charged particles (ionosphere and space plasma), troposphere, frequency system instability, and electrical phase path variations (through both the spacecraft and the DSS). Reducing the effect of all these error sources is directly supported by the DSN. In SPS 37-59, Vol. II, the real-time TSAC support of *Mariner* Mars 1969 encounter was described for two of these error sources, namely, UT1 (pp. 110–114) and the ionospheric calibration of radio tracking data (pp. 97–110). The latter article concentrated on the effect of calibrating the data for the southern hemisphere stations; the first article (*Subsection 2*) in this section extends this work to include the calibration of tracking data for the entire net. *Subsection 3* describes the effect of using the new and more accurate orbit determination program (DPODP) and also the effect of applying ionospheric corrections to the tracking data of past flights in obtaining the DSS locations utilized for the *Mariner* Mars 1969 mission. Our goals on *Mariner* Mars 1969 were to obtain spin axis (r_s) solutions good to 1.5 m and longitude (λ) solutions good to 3 m. Present indications are that these goals were met, although further analysis is required. The spread of Goldstone r_s solutions was 2 m about the average before the ionospheric corrections were applied. The application of the ionospheric corrections caused the average to move by 4 m, but the spread reduced to 1 m. This spread may be even further reduced when corrections for the charged particles in the space plasma (not available for all missions) are applied to the tracking data. These corrections are discussed for the cases of *Mariner V* and *Pioneer IX* in *Subsection 4*, where it is shown that the effects of the charged particles in the space plasma typically affect the DSS location solutions on the order of 1 m.

The tracking data corrections due to the ionosphere and the troposphere are functions of the path (elevation angle) through which the radio wave transverses the atmosphere. For the case of the ionospheric corrections, the program ION (SPS 37-58, Vol. II, pp. 66–73) computes the required elevation angles using the round-trip flight time and an algorithm permitting the facile computation

of view periods for a distant spacecraft, as presented in *Subsection 5*. This algorithm requires a knowledge of the right ascension and the declination of the probe within a few days of the time of interest. Although the use of this simple algorithm saves computing time, the algorithm is not exact. The size of the error is analyzed in the following article (*Subsection 6*), where it is found that an error of less than 0.03 m is introduced into the ionospheric calibration process using tabulated values of right ascension and declination 5 days apart. These errors are small compared to the calibration goals for the *Mariner* Mars 1969 Project.

Subsection 7 describes the use of sequential estimation on the orbit determination problem for a planetary orbiter. The sensitivity of estimation accuracy to placement of the data span was studied for an idealized case of a spherical central body and it was found that the tracking of the probe over a span which is centered about, or at least includes, the periapsis time is the most efficient strategy.

The following three articles (*Subsections 8–10*) discuss recent work on the lunar surface mass distribution. For over one year, JPL and the Aerospace Corporation have been cooperating in an effort to determine the lunar gravimetric data from a dynamic fit of the *Lunar Orbiter* doppler tracking data, using a dense grid of discrete mass points on the lunar surface. *Subsection 8* presents the surface (earth side) mass distribution obtained to date from this work, while *Subsection 9* presents a representation of these local gravity features in terms of accelerations at a 100-km altitude (representative of the altitude at which the data most critical to the construction of this model was obtained) and expands on the work presented in *Subsection 8* by using the residual accelerations to estimate additional masses. Because of the success of utilizing the *Lunar Orbiter* tracking data, which has a periapsis altitude of 50 to 100 km, it was felt that the data from the *Apollo 10* and *11* missions, which were tracked within 11 km of the lunar surface, may provide even more information. Unfortunately, as reported in *Subsection 10*, there seems to be a sufficient number of anomalies in the *Apollo* tracking data to preclude its usefulness for this type of analysis.

The landed *Surveyor* two-way doppler "observe minus computed" residuals have systematic structures as shown in SPS 37-50, Vol. II, pp. 110–125, and SPS 37-51, Vol. II, pp. 42–50. The long-term periodocities are lunar ephemeris-dependent while the diurnal signature has a number of suspected causes, among which are the imperfections in the tropospheric refraction corrections applied to the

doppler and ionospheric charged-particles effects which have been discussed in previous issues. The tracking data from the *Surveyor* spacecraft, while they were resting on the lunar surface, represents an excellent source of accurate DSS location solutions providing certain problems such as the above can be surmounted.

An additional corrupting influence associated with the lunar landed *Surveyor* tracking data that prevents the determination of absolute DSS longitude is the physical libration of the lunar figure, which is the topic of the next article (*Subsection 11*). In SPS 37-56, Vol. II, pp. 74–80, the effect of the Heyn physical libration model was compared against a later model (Eckhardt's libration coefficients) as well as against no model. It was surprising that no single model was best for all *Surveyors* utilized in this study and that, in fact, one case was best with no model. However, the libration models utilized in this study were truncated; therefore, the article in this issue investigates the effect of this truncation. It is found that the failure of the model to properly fit the *Surveyor* data does not result from the truncation of the libration series. However, some of the truncated terms are significant.

Generally, reductions from earth–satellite tracking data result in a high correlation between the gravitational mass of the earth ($GM_\oplus$) and the scale of the coordinate system (i.e., linear coordinates of the tracking station). This is especially true in the case of optical data that relies on an independent determination of $GM_\oplus$. To provide the scale for quantities that involve linear dimensions, the most accurate $GM_\oplus$ determinations have been provided from the radio tracking data of deep space probes, such as those reported in SPS 37-43, Vol. III, pp. 3–18, and SPS 37-44, Vol. III, pp. 11–28. At present, these $GM_\oplus$ determinations from deep space probe data have no close competitors in that their claimed uncertainty is an order of magnitude less than provided by other techniques. In previous SPS articles (SPS 37-53, Vol. II, pp. 16–20; SPS 37-56, Vol. II, pp. 80–85), the ability to determine $GM_\oplus$ from a moderate-altitude satellite and from a family of three high-altitude satellites (including *Syncom II*) was analyzed. In *Subsection 12*, this analysis is extended to reveal the relative quality of $GM_\oplus$ solutions obtainable as a function of the elements of the earth-orbiting spacecraft. This analysis was accomplished by the use of the Multiple-Link Satellite Program (MLSP) discussed in *Subsection 13*. MLSP was developed as a tool to study the statistics of satellite orbit determination using data types involving several satellites. In particular, the MLSP assumes that the orbit determination process will be done with radio ranging and/or doppler data; however, unlike

current orbit determination programs, the MLSP does not confine the signal path to direct ground station–satellite measurements, but allows the signal to be relayed many times, including relays between satellites.

The last article (*Subsection 14*) in this section demonstrates the feasibility of computing doppler observables from differenced-range observables. Changes are specified for the DPODP which should produce differenced-range doppler accurate to 10^{-5} m/s or better for all count times above 0.2 s. This is compatible with the design goal of being able to compute range differences accumulated over 10^4 s to 0.1 m or better.

2. Results of *Mariner* Mars 1969 In-Flight Ionospheric Calibration of Radio Tracking Data,

B. D. Mulhall, V. J. Ondrasik, and N. A. Mottinger[4]

Using the procedures described by Mulhall in SPS 37-57, Vol. II, pp. 24–29, the authors processed the ionospheric measurements obtained from the Faraday rotation polarimeters at the Venus site and at the University of New England, Armidale, Australia, and from ionosonde vertical sounding stations at Tortosa, Spain, Mount Stromlo and Woomera, Australia, and Johannesburg, South Africa. These measurements were converted to total electron content and mapped to the *Mariner* ray path; range and doppler corrections were computed and applied to *Mariner VI* and *VII* radio tracking data. The results of the calibrations are shown in Table 16.

The recommended changes listed in Table 16 were determined by differencing the results of Double Precision Orbit Determination Program (DPODP) solutions using in-flight data which had not been calibrated for the ionosphere with station location based on post-flight solutions using uncalibrated data versus DPODP runs using ionospherically calibrated data and station location based on post-flight calibrated data (see Mottinger, *Subsection 3*). These differences are not necessarily the actual ionospheric effect on the orbit determination since the error introduced by the ionosphere into the in-flight data might be masked in part by the uncalibrated station location.

For example, the ionosphere caused an error which consistently increased the apparent station spin radius r_s.

Table 16. Recommended changes due to ionospheric effect, Mariner Mars 1969 mission

Mission	B · R, km	B · T, km
Mariner VI	−53	48
Mariner VII	−40	20

It is very likely that the ionosphere had a similar effect for *Mariner* Mars 1969. Consequently, station locations based on uncalibrated *Mariner V* data would compensate in part for the ionospheric error in *Mariner* Mars 1969 data.

The ionospheric effect on navigation shown in Table 16 is measured in terms of the **B** vector, a vector perpendicular to the incoming asymptote, from the center of the planet Mars to the probe's aiming point. **B · T** is the component of the **B** vector in the ecliptic plane and **B · R** is the component perpendicular to **B · T**.

The ionospheric effects shown in Table 16 are different from the effects shown by Ondrasik in SPS 37-59, Vol. II, pp. 97–110, because Table 16 shows the results obtained by calibrating the entire net (not just the southern hemisphere stations) and does not include certain days with ionospheric measurements that could not be reduced prior to encounter.

The ionospheric effect was considerably lower than anticipated. Although 1969 has been a year of high ionospheric concentrations due to solar flare activity, the ionosphere was relatively inactive during the period when the calibration was performed (July 1 to August 5, 1969). This low activity was particularly noticeable in the southern hemisphere where the total columnar electron ionospheric content was typically less than half of the content in the northern hemisphere. Due to the southerly declination of the *Mariner* spacecraft, most of the radio tracking data were obtained from southern latitude stations. Consequently, the smaller effect of the southern ionosphere outweighed the effect in the northern ionosphere and reduced the magnitude of the calibration for the entire net.

Future plans include converting the ionospheric calibration programs from a power series to a Chebychev series. The power series proved to be an inferior smoothing technique for the ionospheric range calibration prior to differentiation into a doppler calibration. Occasionally, the power series fit was so noisy that the calibration for

that day could not be used. The deficiency was recognized prior to encounter but could not be incorporated in the software system without jeopardizing the calibration effort. The software is presently being revised to incorporate the Chebychev series and the ionospheric effect will be recomputed for the *Mariner* Mars 1969 data.

Measurement mapping techniques will also be studied for possible improvement as well as techniques for resolving ambiguities in Faraday rotation measurements.

3. Status of DSS Location Solutions for Deep Space Probe Missions: Third-Generation Orbit Determination Program Solutions for Mariner Mars 1969 Mission, N. A. Mottinger

a. Introduction. As discussed by Mottinger and Trask in SPS 37-48, Vol. II, pp. 12–22, the uncertainties in DSS locations can become limiting factors to the navigational accuracy obtainable with earth-based radio tracking data. To meet the navigational goals under consideration for some planetary projects, the uncertainties in the DSS longitude σ_λ and the distance off the earth's spin axis[5] σ_{r_s} must be known on the order of 1 m. In an earlier article, Hamilton, Grimes, and Trask (SPS 37-44, Vol. III, pp. 4–11) presented an approximate method for determining the navigational accuracy obtainable during the encounter phase of a mission and discussed the dependence of this accuracy on station location uncertainties.

A general discussion of DSS location solutions obtained from postflight analyses is presented in SPS 37-48, Vol. II. SPS 37-49, Vol. II, pp. 10–23, gives the solutions for DSS locations obtained in processing the *Mariner V* data at about the same time the mission was in progress.

The third article in the series (SPS 37-56, Vol. II, pp. 45–58) discussed solutions obtained which were considered accurate at the 5-m level in r_s and λ. The results presented in this article are location solutions obtained with a third-generation orbit determination program, the double-precision orbit determination program (DPODP)[6]. Ionospheric corrections have been included in the reductions and have reduced the scatter to about 2 m in r_s and 2.5 m in λ. Uncertainties for these solutions are about 3 m.

b. Discussion. The reduction of earth-based radio tracking data done in the last year, using the single-precision orbit determination program (SPODP) (Ref. 1)

---

[5]r_s = geocentric radius times the cosine of the geocentric latitude.
[6]See SPS 37-47, Vol. II, pp. 35–41, SPS 37-38, Vol. III, pp. 24–26, and successive articles in the DSN Volume III series.

and more recently the DPODP, has produced station location solutions that are consistent at and below the 5-m level. The 10-m level was broken with the SPODP by processing the planetary zero declination and encounter two-way doppler data. These results are discussed in SPS 37-56, Vol. II, pp. 45–58, and were also presented at the American Geophysical Union Meeting in April 1969 (Ref. 2). In the early part of the year, reductions with essentially the same data were initiated using the DPODP and employing simple averaging techniques to create a best estimate. Maximum disagreement between the two sets of solutions (SPODP vs DPODP) was 3.3 m in spin axis r_s and 4.2 m in longitude, with the average difference of 1 m in r_s and 1.6 m in longitude. The implied quality of the SPODP results was extremely encouraging, considering the vast improvements and changes in the DPODP over the SPODP. Following these reductions, changes were made in the timing and polar motion polynomials provided by Muller and Chao (SPS 37-57, Vol. II, pp. 42–51). The new polynomials incorporated the changes in UT1 made by the U.S. Naval Observatory (USNO) after switching to the Bureau International L'Heure (BIH) polar motion as well as the processing and data selection choices made by Muller and Chao. Succeeding reductions using the new timing and polar motion coefficients were performed exclusively with the DPODP. A program was developed to combine the estimates obtained from each reduction in the same manner as were the *Ranger* Block III station location and other common parameter estimates (SPS 37-43, Vol. III, pp. 3–18).

Breaking the 5-m level was made possible by the ionosphere corrections produced by Mulhall, Ondrasik, and Thuleen as discussed in a JPL internal document.[7] As will be shown, the scatter in location estimates was reduced with the application of the ionosphere corrections. The most significant reduction was 50% for r_s at Goldstone. The absolute longitude solutions from the planetary encounter solutions, *Mariners IV* and *V*, diverge by 2.9 m following the application of the ionosphere corrections. The exact agreement noted in SPS 37-56, Vol. II, pp. 45–58, appears to have been coincidental. Possible explanations for this scatter lie in the ephemeris, precession rates, or a secular rate in UT1, which would be associated with proper motion of the stars used to determine UT1. A half meter of the spread is due to the specific ephemeris developed for the *Mariner* Mars 1969 encounter activities. Using the current recommended ephemeris of the solar system reduces the spread to 2.4 m.

Priority was given to processing the *Mariner IV* and *V* data near zero declination to obtain r_s and $\Delta\lambda$ (relative longitude) and encounter for r_s and λ. Although some *Pioneer* zero declination cases were analyzed, the analyses are neither as complete as for the *Mariner* cases nor were charged-particle calibrations available. The locations obtained with the ionosphere corrections appear to be reliable at the 3-m level.

c. DPODP vs SPODP station locations. The decisions which led to the reduction of solely planetary data to support the *Mariner* Mars 1969 mission have been discussed in SPS 37-56, Vol. II, pp. 45–58, and Ref. 2. Basically, the problem is that the lunar and planetary ephemerides are not compatible at the level desired in terms of the DSS locations obtained from these two mission types.

The *Mariner* reductions listed in Table 17 are very nearly identical to those listed in a similar table in SPS 37-56, Vol. II, p. 50. Since these earlier reductions had been performed with the SPODP, it was attempted to reduce the same data with the DPODP to test the agreement in station locations obtained by these two programs. In addition to the numerical accuracy of 16 digits instead of 8 for the SPODP, other improvements such as the employment of a polar motion model[8] in the DPODP will cause the SPODP and DPODP location solutions to differ. The agreement noted with initial reductions from the DPODP were very encouraging.

Location set (LS) 14, the best SPODP set, is compared with the first DPODP set, LS 17, in Table 18. Average disagreement was 1 m in r_s and 1.6 m in λ, with worst case of 4.2 m occurring in λ. The uncertainty expressed with the locations, both SPODP and DPODP, was about 5 m. The important item, however, was the overall general consistency obtained between programs.

d. Location combination techniques. A combination technique developed by J. D. Anderson and used by Trask and Vegos to combine the *Ranger* Block III missions (SPS 37-43, Vol. III, pp. 3–18) was also used to combine these DPODP estimates. The technique uses the normal equations matrix from the orbit determination program and condenses the information, producing a new information matrix on those parameters that are common to several missions and whose combined estimate is desired. The problem present with the station location solutions obtained from the zero-declination

---

[7]Mulhall, B. D., *In Flight Ionospheric Calibration Procedures for Mariner Mars 1969 Radio Tracking Data*, June 26, 1969.

[8]A polar motion model was nonexistent in the SPODP. Polar motion had to be applied after the reduction assuming a mean pole position over the time interval in question.

reductions is that statistical significance is attached to the absolute station longitudes by the program when it is not clear where this information comes from. Relative longitudes are well determined, however, and it is this information that must be brought out in the normal matrix. A technique adopted was to invert the matrix, corrupt the absolute longitude uncertainties by an arbitrary factor, generally 1 km, and reinvert to obtain the new normal matrix. This preserves the information on relative longitudes by increasing the correlation between stations (longitude), while destroying information on absolute. It may not be the most desirable technique to use, however, because of the double inversion required. Satisfactory results appear to have been obtained with this method. Other techniques will be investigated which may lead to abandonment of this procedure.

Similar techniques were developed for use as an information matrix in preserving relative locations at the Goldstone and Madrid DSCCs where these are accurately known from geodetic surveys. The Australian stations are too far apart to be able to rely upon the geodetic relative locations.

e. Advanced station location solutions using the DPODP. As mentioned earlier, Table 17 is essentially a duplicate of the *Mariner* missions listed in SPS 37-56, Vol. II, p. 50, Table 1. Summarized are the flights analyzed, the time span of each, number of doppler points fit, ephemeris, and other items pertinent to the reduction. One of the most interesting items is the new timing polynomials which have been used. The difference, UT1 − UTC, is presented in each table; that in SPS 37-56, Vol. II, is for the system as it existed then and that in Table 17 of this article as it stands now. Pole positions are also shown. Although they are applied for each data point in the program, an average value was calculated for the time span of the flight for inclusion in this table. For the *Mariner IV* and *V* encounter cases, it is possible to note very good agreement between the changes in UT1 − UTC for the old and new timing systems and the shift in DSS longitude.

This table also lists five different *Pioneer* reductions which have been performed with these probes in the zero-declination configuration. To distinguish between different zero-declination passages for the same spacecraft, the letters A and B have been added. If the spacecraft is near the threshold of the 85-ft antenna, as was *Pioneer IX* in this case, the data is quite noisy (~0.1 cycle). The 210-ft antenna data is not as noisy (~0.03 cycle).

The table concludes with the declination of the probe and the sun–earth–probe (SEP) angle. The latter is useful for comparing possible ionospheric and space plasma effects on the data from different missions.

As was mentioned earlier, problems did exist with some of the *Pioneer* zero-declination reductions. Specifically, the *Pioneer VIIA, VIIIB,* and *IX* reductions had occasional solutions which disagreed significantly with the existing *Mariner* solutions. For these reasons they were never included in a combination. These can be seen in Tables 19 and 20.

Table 17 also summarizes the data spans of the *Mariners* used with ionospheric corrections.[9] In some cases these represent a significant reduction in the number of points or even stations due to a lack of ionospheric calibration data. Because of the long lead time required to obtain ionospheric total electron content from ionosonde data, only the spans listed in Table 17 could be calibrated prior to *Mariner* Mars 1969 encounter.

Additional data have been obtained and are awaiting the conclusion of this report and other *Mariner* Mars 1969 summaries before they can be applied to the data. Figures 33 and 34 show what the application of the ionospheric corrections (discussed in Footnote 7) did to the r_s and longitude solutions, respectively, at the Goldstone DSCC. However, it should be noted that, due to the times at which the particular missions occurred and the particular stations tracking, the northern hemisphere stations received the largest corrections. Southern hemisphere stations, as may be noted in Table 21, did not show the scatter that the northern hemisphere did. In Figs. 33 and 34 are the combined solution, no ionosphere (LS 24), and solutions from constituent runs and those with the ionosphere corrections (LS 25). Absolute and relative locations for all stations are listed in Tables 22 and 23. In some cases it was necessary to transfer a solution from DSS 11 or DSS 14 to DSS 12 using the geodetic survey relative locations. These relative locations are given in Table 24. In other cases, solutions for DSS 12 were available directly and indirectly in the same reduction. Most significant is the reduction of the 4.9-m scatter in the left side (non-ionosphere) to 2.3 m on the right side of Fig. 33, r_s solutions. The combined solutions

---

[9]In the course of compiling this table a mistake was uncovered. For *Mariner V* cruise, the data from DSS 62 was left in the fit but the station location was not estimated. This was corrected by eliminating the DSS 62 data. The combination has not been redone. The spin axis of DSS 14 changed ~0.1 m. In future reductions, with more ionospheric data available, this will be corrected.

Table 17. Flight analysis summary

Flight	Doppler points	Doppler count time, s	Tracking span, days	Ephemeris		DPODP		ET − UTC, s	UT1 − UTC ms	Effective data weights (60-s count time), mm/s	Instantaneous pole position (BIH)[a]				Probe declination, deg	SEP angle, deg	Location set
				DE	LE	Mod	Lock file				X, m	Y, m	ΔX, m	ΔY, m			
Non-ionosphere reductions																	
Mariner IV Encounter	419	600[b]	15 (Jul 7–21, 1965)	69	16	5.0	5A	36.178	19	3.3	−2.9	13.9	1.3	0.6	−3	77	24
Mariner V Cruise	616	600	58 (Jul 21– Sep 16, 1967)	69	16	4.3	5A	Start 37.965 End 38.113	66 94	3.3	−0.2	6.5	0.5	0.4	−8 to 8	35–20–35	24
Encounter	561	600[b]	11 (Oct 14–24, 1967)	69	16	5.0	5A	38.198	107	3.3	−0.5	6.5	0.1	0.1	6	45	24
Post- encounter	665	600	15 (Oct 29– Nov 12, 1967)	69	16	5.0	5A	38.240	100	3.3	−0.6	6.7	0.03	0.4	2 to −2	43	24
Pioneer VIIA	1392	600	43 (Aug 19– Sep 30, 1966)	69	16	5.0	5A	Start 37.095 End 37.204	13 30	3.3 3.3	0.8	10.9	2.4	0.4	−1.4 to 0.8	150	—
Pioneer VIIB	75	60	8 (Jul 27– Aug 3, 1968)	69	16	5.0	5A	38.837	36	3.3	2.6	5.2	0.06	0.1	3 to −2	54	—
Pioneer VIIIA	370	300	9 (Jun 3–11, 1968)	69	16	5.0	5A	38.699	−4	3.3	1.5	6.7	0.2	0.2	1.3 to −1.3	102–105	—

[a]Although a polar motion model is present in the DPODP, these values were computed at the midpoint of the tracking span primarily for comparison with previous articles.
[b]Count time reduced to 60 s during encounter.

Table 17 (contd)

Flight	Doppler points	Doppler count time, s	Tracking span, days	Ephemeris DE	Ephemeris LE	DPODP Mod	DPODP Lock file	ET − UTC, s	UT1 − UTC ms	Effective data weights (60-s count time), mm/s	Instantaneous pole position (BIH)[a] X, m	Y, m	ΔX, m	ΔY, m	Probe declination, deg	SEP angle, deg	Location set
Non-ionosphere reductions																	
Pioneer VIIIB	520	600	19 (Dec 25, 1968–Jan 12, 1969)	69	16	5.0	5A	39.244	30	3.3	−4.6	7.6	0.5	1.2	−2.8 to 5.0	80	—
Pioneer IX	309	600	6 (May 8–13, 1969)	69	16	5.0	5A	39.573	−1	3.3	1.0	11.4	0.3	0.06	−3 to 3	50	—
Ionosphere reductions																	—
Mariner IV Encounter	373		12 (Jul 10–21, 1967)	71	16	5.0	5A			3.3							25
Mariner V Cruise	364		58 (Jul 21–Sep 16, 1967)	69	16	5.0	5A			3.3							25
Encounter	561		11 (Oct 14–24, 1967)	69	16	5.0	5A			3.3							25
Post-encounter	411		15 (Oct 29–Nov 12, 1967)	69	16	5.2	5A			3.3							25

Table 18. First DPODP estimates compared with best SPODP

DSS	DPODP (LS 17) − SPODP (LS 14)	
	Δr_s, m	$\Delta_{\Delta\lambda}{}^{\mathrm{a}}$ from DSS 12, m
12	0.1	1.0
41	0.5	0.7
42	0.8	1.3
51	3.0	4.2
61	3.3	1.5
62	0.4	2.2
Average	1.0	1.6

$^{\mathrm{a}}(\lambda_i - \lambda_{12})_{\mathrm{LS}\,17} - (\lambda_i - \lambda_{12})_{\mathrm{LS}\,14}$

also differ by about 4 m. The changes noted all agree well with those anticipated by Mulhall et al. In these figures the standard deviations are not shown since the reduction of scatter and the change in absolute value is of primary importance. Figure 34 shows the ionosphere effects on the absolute longitude solutions obtained in the *Mariner IV* and *V* encounter reductions. Unlike the previous figure showing the spin axis solutions, the addition of the ionosphere has disrupted the previous continuity in absolute longitude solutions. This earlier agreement appears to have been coincidental, since portions of the disagreement may be explained in terms of possible ephemeris inconsistencies [*Mariner IV* (Mars) vs *Mariner V* (Venus)], or more realistically in terms of precession errors which could account for 0.3 m, or a secular drift in UT1 which could result from proper motions of stars used by the USNO to determine UT1.

Location set 24 was produced using solutions obtained with Development Ephemeris (DE) 69. Just before the ionosphere corrections for *Mariner IV* were obtained, a special ephemeris (DE 71) was issued to support the *Mariner* Mars 1969 encounter activities. DE 71 was intended only for use during the encounter phase of *Mariner* Mars 1969 to facilitate the fitting of doppler and range data during this critical phase of the mission.[10] In order to support the station location effort, the *Mariner IV* data were refitted to DE 71, corrected for ionosphere, and used in the combination program along with other ionosphere-corrected station locations. The changes observed in the *Mariner IV* longitude solutions

---

[10]O'Handley, D. A., *Ephemeris of Mars for Mariners 6 and 7*, Aug. 15, 1969 (JPL internal document).

using DE 71 were the predicted 0.5 m. The solutions corrected for ionosphere appear in Figs. 33 and 34. The combination with this ephemeris produced insignificant changes in λ because the *Mariner V* solution dominated the weighted solution due to its smaller uncertainties. For purposes of general comparison, 0.5 m should be subtracted from the *Mariner IV* longitude plotted in the right-hand side of Fig. 34 to obtain the correct indication of the agreement with *Mariner V*. Spin axis was not significantly affected by the change in ephemeris. DE 69 will be used for all station location reductions until a different ephemeris is recommended.

New ionosphere corrections will be computed for these missions since Mulhall et al have more data for them and better ideas and programs for preparing the corrections. Efforts are also underway to provide space plasma corrections.

Improvements have also been made in Z, the component along the earth's spin axis. Values prepared by Lambeck (Ref. 3) at the Smithsonian Astrophysical Observatory (SAO) were incorporated in LSs 24 and 25. The changes made in Z vary from 4 to 55 m, when compared with the previous sets. Although these changes have imperceptible effects on doppler tracking, they can have quite an effect on range data, particularly at extremely high or low declinations. When they were incorporated into the *Mariner* Mars 1969 reductions, a low-declination case, using the DPODP, approximately 30- to 40-m reductions occurred in the range biases, confirming that they represented an improvement. Confidence at the 15-m level was expressed by SAO for these Z values as computed using dynamical and geometrical fits to Baker–Nunn and other earth–satellite data.

Although there have been significant advances in station locations obtained using the ionosphere corrections, the troposphere model used in the SPODP and the DPODP has come under examination. In consideration of goals of the *Mariner* Mars 1969 mission and future missions, studies have been made of the tropospheric refraction effects on the doppler signal and how this affects determination of station locations. Balloon measurements of pressure, temperature, and humidity are being analyzed to see which measurements will be necessary to calibrate these effects out of the tracking data.

During the *Mariner* Mars 1969 mission, changes were made in the existing refraction model. The troposphere model represents a least-squares fit from the horizon to the zenith to a ray trace model based upon a standard

Table 19. Absolute station locations and statistics[a]

DSS	Data source	Distance off spin axis, km	1-σ standard deviation, m	Geocentric longitude,[b] deg	1-σ standard deviation,[b] 10^{-5} deg	Distance along spin axis,[c] km
		Non-ionosphere reductions—DPODP				
11		5206.3xxx		243.15xxxx		3676.xxx
	Mariner IV encounter	40.8	2.9	063.3	5.6	759
	Pioneer VIIA	40.8	1.6	045.4	17.0	759
	Pioneer VIIIA	38.2	1.9	068.6	109.0	759
12		5212.0xxx		243.19xxxx		3665.xxx
	Mariner V encounter	47.5	2.1	456.0	3.6	624
	Mariner V postencounter	50.9	1.9	458.8	9.8	624
	Pioneer VIIA	50.8	1.2	438.2	16.5	624
	Pioneer VIIIB	48.4	3.6	431.8	77.4	624
	Pioneer IX	46.9	5.8	449.8	61.0	624
14		5203.9xxx		243.11xxxx		3677.xxx
	Mariner V cruise	96.4	2.4	053.1	9.2	048
	Mariner V encounter	94.2	1.7	052.8	3.6	048
	Mariner V postencounter	93.6	3.0	052.3	9.8	048
	Pioneer VIIB	95.7	2.5			
	Pioneer IX	99.2	5.7	043.8	62.0	048
41		5450.xxxx		136.88xxxx		−3302.xxx
	Mariner V encounter	197.5	2.1	753.1	3.0	238
	Mariner V postencounter	200.0	2.4	757.8	9.7	238
	Pioneer VIIA	200.6	8.0	736.5	17.6	238
42		5205.3xxx		148.98xxxx		−3674.xxx
	Mariner IV encounter	49.4	2.9	128.8	5.0	628
	Mariner V cruise	50.3	1.4	131.1	9.3	628
	Pioneer VIIA	51.9	1.6	112.9	16.5	628
	Pioneer VIIIA	47.8	1.6	137.8	108.0	628
	Pioneer VIIIB	47.5	2.1	100.4	75.7	628
	Pioneer IX	42.4	7.8	126.8	62.0	628
51		5742.9xxx		27.68xxxx		−2768.xxx
	Mariner IV encounter	40.8	2.6	543.2	4.5	760
	Pioneer VIIIB	37.0	2.4	519.2	75.7	760
	Pioneer IX	39.7	9.1	539.6	62.0	760
61		4862.6xxx		355.75xxxx		4114.xxx
	Mariner V cruise	03.7	1.4	101.9	9.3	829
	Mariner V postencounter	05.6	5.5	103.3	10.4	829
	Pioneer VIIIA	12.0	1.9	107.4	109.0	829
62		4860.8xxx		355.63xxxx		4116.xxx
	Mariner V cruise	14.9	2.1	221.9	9.8	950
	Mariner V encounter	15.1	2.0	222.1	3.3	950
	Mariner V postencounter	15.5	2.4	223.4	10.0	950
	Pioneer IX	12.7	8.1	207.5	69.0	950

[a]These are formal uncertainties computed by the DPODP based on data weights listed in Table 17. They do not include uncertainties in Universal Time, polar motion, ephemeris, ionosphere, or space plasma, but are about 1.5 times the visible noise on the data.

[b]The minor part may be assumed to be tabulated in meters, where the equivalence of 10^{-5} deg at: DSSs 11, 12, 14 = 0.91 m, DSSs 61, 62 = 0.85 m, DSS 51 = 1.00 m, DSS 41 = 0.95 m, and DSS 42 = 0.91 m.

[c]This component was not estimated, but is included for completeness.

Table 19 (contd)

DSS	Data source	Distance off spin axis, km	1-σ standard deviation, m	Geocentric longitude,[b] deg	1-σ standard deviation,[b] 10^{-5} deg	Distance along spin axis,[c] km
			Ionosphere reductions			
11		5206.3xxx		243.15xxxx		3676.xxx
	Mariner IV encounter	41.8	2.9	065.3	6.2	763
12		5212.0xxx		243.19xxxx		3665.xxx
	Mariner V encounter	52.3	2.1	455.5	3.6	628
	Mariner V postencounter	54.5	2.0	459.4	10.8	628
14		5203.9xxx		243.11xxxx		3677.xxx
	Mariner V cruise	98.6	2.7	057.7	4.9	052
	Mariner V encounter	99.6	1.7	051.9	3.6	052
	Mariner V postencounter	97.5	3.0	052.6	10.8	052
41		5450.xxxx		136.88xxxx		−3302.xxx
	Mariner V encounter	198.0	2.1	749.7	3.0	243
	Mariner V postencounter	200.3	3.0	756.8	10.7	243
42		5205.3xxx		148.98xxxx		−3674.xxx
	Mariner IV encounter	50.1	3.3	130.3	5.8	646
	Mariner V cruise	50.5	2.0	136.8	6.0	646
51		5742.9xxx		27.68xxxx		−2768.xxx
	Mariner IV encounter	42.1	3.2	544.1	5.0	744
61		4862.6xxx		355.75xxxx		4114.xxx
	Mariner V cruise	06.9	1.6	107.0	6.0	
62		4860.8xxx		355.63xxxx		4116.xxx
	Mariner V encounter	17.9	2.0	219.8	3.3	908
	Mariner V postencounter	20.1	3.0	224.3	11.0	908

Table 20. Relative longitude solutions—nonionosphere[a]

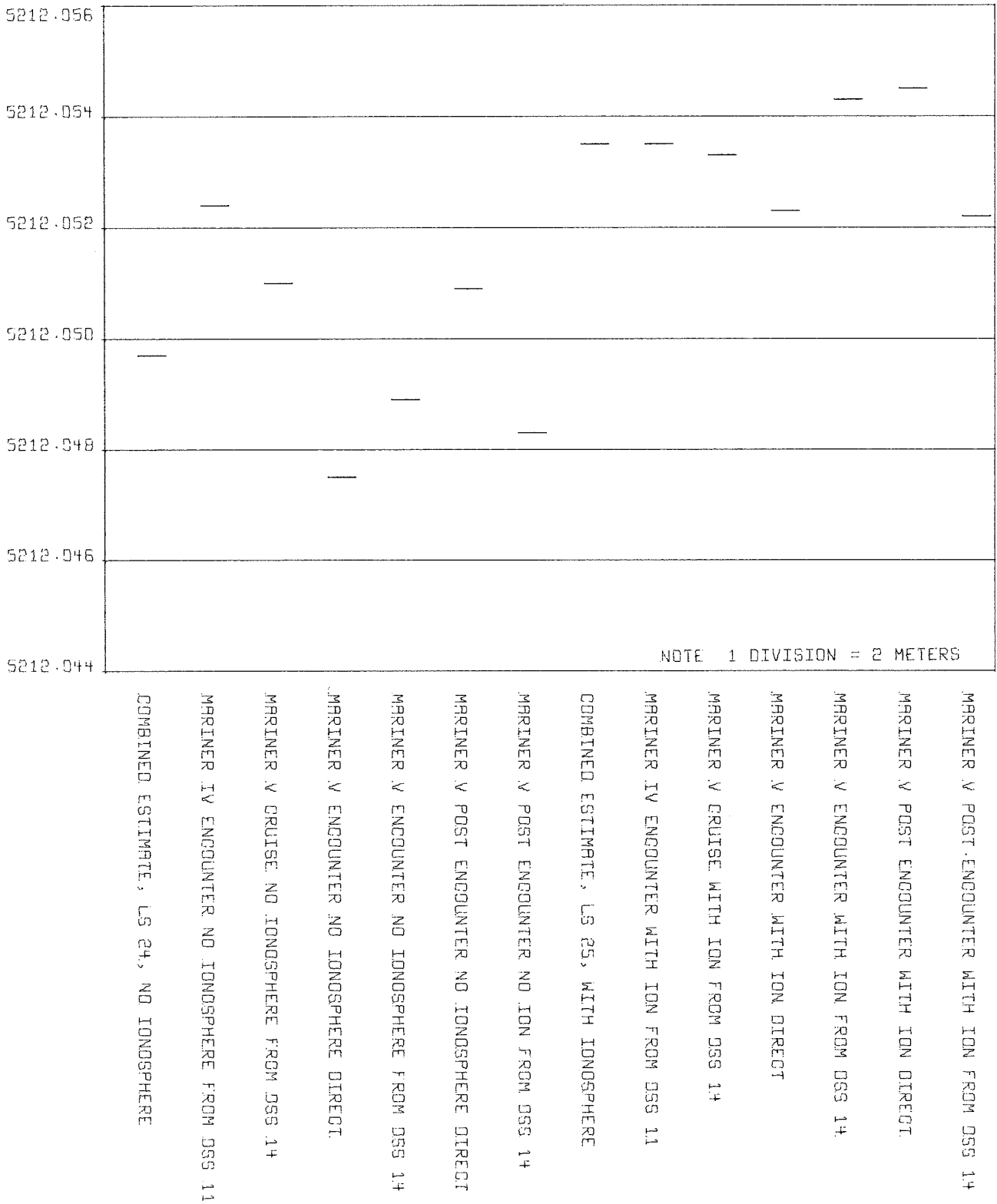| Source	$\Delta\lambda_{12-41}$	$\Delta\lambda_{12-42}$	$\Delta\lambda_{12-51}$	$\Delta\lambda_{12-61}$	$\Delta\lambda_{12-62}$
	906.30xxxx	94.21xxxx	215.50xxxx	−112.55xxxx	−112.43xxxx
Mariner IV encounter	—	327.6	913.3	—	—
Mariner V cruise	—	326.6	—	644.3	764.3
Mariner V encounter	702.9	—	—	—	766.1
Mariner V postencounter	701.0	—	—	644.5	764.6
Pioneer VIIA	701.7	325.3	—	—	—
Pioneer VIIIA	—	323.9	—	645.7	—
Pioneer VIIIB	—	331.4	912.6	—	—
Pioneer IX	—	323.0	910.2	—	757.7

[a]See Footnote b, Table 19.

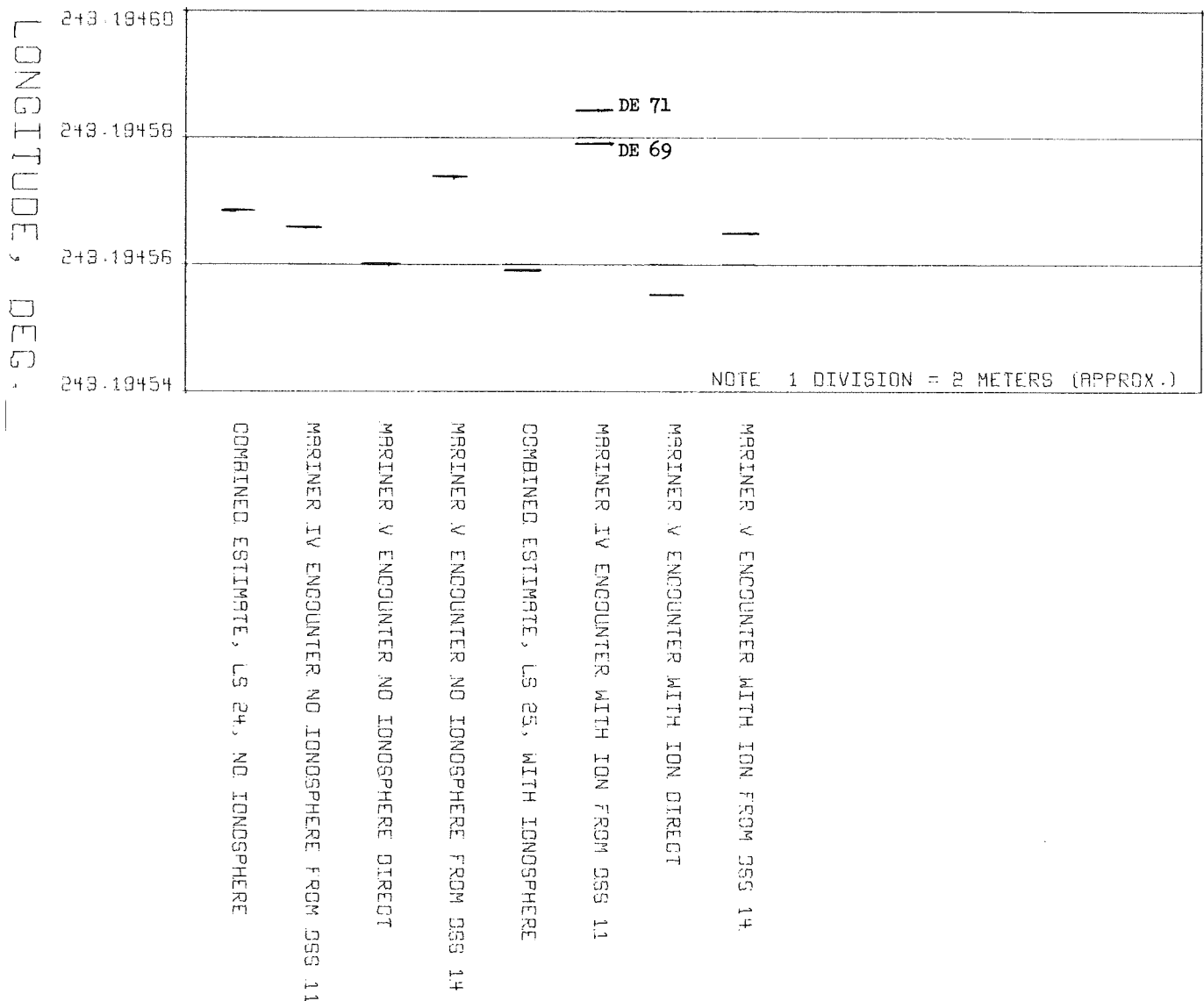**Fig. 33. Distance off spin axis, earth-fixed system (1903.0 pole), DSS 12**

Fig. 34. Geocentric longitude, earth-fixed system (1903.0 pole), DSS 12

Table 21. Difference in station locations, LS 25 (ionosphere) − LS 24 (no ionosphere)

DSS	Δr_s, m	$\Delta\lambda$, 10^{-5} deg[a]	Δ relative longitude (DSS 12 − DSS --)
11	3.8	−0.94	—
12	3.8	−0.94	—
14	3.8	−0.96	—
41	0.26	−3.24	2.3
42	−0.28	−0.32	−0.62
51	−0.61	−0.84	−0.1
61	3.47	−1.04	0.1
62	3.45	−1.08	0.14

[a]See Footnote b, Table 19.

atmosphere. A new fit was made from 15 deg to the zenith for use by *Mariner* Mars 1969 in the DPODP. To check the effects of this new model on the existing station locations, only the *Mariner* V zero-declination cruise case was refitted due to time limitations. The corrections were made in r_s only and range from 0.5 to 0.8 m. They were applied to the spin axis values in LSs 24 and 25 to create sets 27 and 26, respectively. Their general usage is not recommended until the current investigations are completed.

f. Location set uncertainties. The formal statistics produced by the combination program may not be realistic in view of known contributing error sources. An attempt will be made to expand the existing normal matrix from each DPODP reduction by scaling the station location rows and columns by factors to represent different error

Table 22. Absolute locations[a]

DSS	RI, km	ϕ, deg	λ, deg	r_s, km	Z, km	UC, km[b]	VC, km[c]
				LS 24[d]			
11	6372.0084	35.208049	243.150637	5206.3381	3673.763	−2351.4238	−4645.0794
12	6371.9927	35.118672	243.194568	5212.0497	3665.628	−2350.4372	−4651.9789
14	6371.9915	35.244360	243.110523	5203.9951	3677.052	−2353.6156	−4641.3423
41	6372.5561	−31.211425	136.887540	5450.1984	−3302.243	−3978.7193	3724.8430
42	6371.7103	−35.219659	148.981300	5205.3501	−3674.646	−4460.9808	2682.4093
51	6375.5247	−25.739300	27.685441	5742.9410	−2768.744	5085.4416	2668.2683
61	6370.0235	40.238924	355.751018	4862.6043	4114.885	4849.2395	− 360.27414
62	6369.9643	40.263216	355.632211	4860.8141	4116.908	4846.6970	− 370.19224
				LS 25[e]			
11	6372.0115	35.208029	243.150627	5206.3419	3673.763	−2351.4263	−4645.0824
12	6371.9958	35.118652	243.194559	5212.0535	3665.628	−2350.4397	−4651.9819
14	6371.9946	35.244340	243.110513	5203.9989	3677.052	−2353.6181	−4641.3453
41	6372.5563	−31.211423	136.887507	5450.1986	−3302.243	−3978.7174	3724.8454
42	6371.7106	−35.219658	148.981301	5205.3504	−3674.646	−4460.9809	2682.4097
51	6375.5252	−25.739297	27.685432	5742.9417	−2768.744	5085.4425	2668.2678
61	6370.0262	40.238904	355.751007	4862.6078	4114.885	4849.2429	− 360.27527
62	6369.9670	40.263196	355.632200	4860.8176	4116.908	4846.7004	− 370.19342

[a]All location sets at 1903.0 pole. Survey constraints used at Goldstone and Madrid DSCCs.
[b]UC = $r_s \cos\lambda$.
[c]VC = $r_s \sin\lambda$.
[d]*Mariners* IV and V with no ionosphere.
[e]*Mariners* IV and V with ionosphere.

Table 23. Relative locations

DSS parameter[a]	LS 24		LS 25	
	$\Delta\lambda$	Δr_s	$\Delta\lambda$	Δr_s
DSS 12 — 41	106.307029	−238.1487	106.307052	−238.1451
DSS 12 — 42	94.213264	6.6996	94.213258	6.7032
DSS 12 — 51	215.509128	−530.8913	215.509127	−530.8881
DSS 12 — 61	−112.556449	349.4454	−112.556448	349.4457
DSS 12 — 62	−112.437643	351.2356	−112.437641	351.2359
DSS 41 — 42	− 12.093764	244.8483	− 12.093794	244.8483
DSS 41 — 51	109.202099	−292.7427	109.202075	−292.7430
DSS 41 — 61	−218.863478	587.5940	−218.863500	587.5908
DSS 41 — 62	−218.744671	589.3842	−218.744693	589.3811
DSS 51 — 61	−328.065577	880.3367	−328.065575	880.3339
DSS 51 — 62	−327.946770	882.1269	−327.946768	882.1241

[a]Relative locations for DSS 11 — 12, DSS 12 — 14, and DSS 61 — 62 are listed in Table 24.

Table 24. Relative locations at Goldstone and Madrid tracking complexes[a]

DSS parameters	Δr_s, km	$\Delta\lambda$, deg	ΔZ, km
Goldstone DSCC			
DSS 11 — 12	−5.7117	−0.043931	8.1353
DSS 11 — 14	2.3430	0.040114	− 3.288
DSS 12 — 14	8.0547	0.084046	−11.42364
Madrid DSCC			
DSS 61 — 62	1.7902	0.118807	− 2.0232

[a]Computed from geodetic survey reductions.

sources and adding them to the matrix. All the location sets discussed in this article have had formal statistics of 0.9 to 2.5 m in r_s and 2.5 to 3.0 m in longitude. Using the distribution of the components of the combination as a guide to the uncertainty, one would say that LS 24, the no ionosphere set, should have an uncertainty in r_s of about 5 m based on the worst-case scatter found in the solutions for DSS 12. The longitude solutions only show a scatter of about 1 m. To quote this as an uncertainty for the combined longitude value would not be realistic considering possible ionosphere, ephemeris, and timing effects. Upon examining the ionosphere-corrected reductions and the resulting combination, the shift from LS 24 in r_s at the Goldstone and Madrid DSCCs and the reduction in the scatter show that 5 m may have been a realistic

uncertainty in r_s for the non-ionosphere set and, similarly, 2.4×10^{-5} deg in longitude for DE 69. Given a number of solutions in the combination, a reasonable estimate of the uncertainty for the combination appears to be obtainable by observing the worst-case distribution of the constituents. The criteria of the total scatter at Goldstone DSCC would have appeared to produce acceptable uncertainties for LS 24 in view of the results noted when applying the ionosphere to produce LS 25. For the ionosphere-corrected set, uncertainties of about 2.25 m would appear reasonable for r_s based on the scatter at DSS 12. Considering that space plasma and troposphere might still be adversely affecting the solutions, an estimate of 3 m might be more applicable. The longitude would be at about the same level.

The location set recommended for a specific task will depend upon many things. As has been indicated in the text of this article, the timing system, choice of ephemeris, polar motion, troposphere model, and ionosphere corrections are very important parts of the overall earth–solar system model, which strongly influences the derived station location solutions. Of greatest importance are the timing, polar motion, and ephemeris systems used. Before a given location set can be recommended for usage or comparison with other results, an understanding of these systems as they exist is necessary. Differences in certain lunar and planetary ephemeris systems at JPL are one indication of how station locations (longitude) would have to be modified before use.

g. Concluding remarks. It has been demonstrated that an accuracy of 5 m or better was obtained in estimating station locations using the SPODP. The DPODP has been required, though, to carry the solutions below the 5-m level, with its improved data reduction capability and application of the ionosphere corrections. Improved techniques in combining the estimates obtained are helpful in using the output of the DPODP to provide more meaningful location estimates. This same program will also be used as a part of the process to improve the credibility of the uncertainties calculated. There are still areas to be investigated. The lunar-derived locations can hopefully be joined with the planetary, but first the differences appearing in the planetary encounter longitude solutions need to be clearly understood. Improved ionosphere, space plasma, and troposphere corrections are being investigated and will hopefully trim even more of the scatter and uncertainty off the existing solutions.

References

1. Warner, M. R., and Nead, M. W., *SPODP—Single Precision Orbit Determination Program*, Technical Memorandum 33-204. Jet Propulsion Laboratory, Pasadena, Calif., Feb. 15, 1965.

2. Mottinger, N. A., "Breaking the 10 Meter Level in Obtaining Consistent Station Location Solutions From the Reduction of Deep Space Probe Data," presented at the American Geophysical Union Meeting, Washington, D.C., Apr. 23, 1969.

3. Lambeck, K., "Comparisons and Combinations of Geodetic Parameters Estimated From Dynamic and Geometric Satellite Solutions and From Mariner Flights," prepared for XII Plenary Meeting of COSPAR, Prague, May 1969, Smithsonian Institution Astrophysical Observatory, Cambridge, Mass.

4. A Cursory Examination of the Effect of Space Plasma on *Mariner V* and *Pioneer IX* Navigation With Implications for *Mariner* Mars 1971 TSAC,

V. J. Ondrasik, B. D. Mulhall, and N. A. Mottinger

a. Introduction. The tracking system analytical calibration (TSAC) effort is concerned with reducing the effect of various error sources that limit the ability to determine the orbit of a spacecraft using earth-based radio tracking data. One of these error sources is the change in the phase and group velocities of the radio signal as it passes through the charged particles in the earth's ionosphere and the interplanetary medium, the space plasma. Although an intensive effort is in progress to calibrate radio tracking data for the effects of charged particles in the ionosphere, relatively little attention has been paid to the effect of the charged particles in the space plasma. This is due primarily to the extreme scarcity of space plasma data. Two missions that did carry dual frequency experiments, which enable space plasma calibrations to be made, were *Mariner V* and *Pioneer IX*. Selected portions of the tracking data from these two missions have been calibrated and the effects of the space plasma are illustrated in terms of the apparent daily changes in station locations. These results are then used to draw implications concerning the navigational capabilities of *Mariner* Mars 1971 TSAC.

b. Space plasma total electron content. Before space plasma corrections to range and doppler measurements can be made, it is necessary to determine the number of charged particles, and their time rate of change, that the signal encounters along its ray path in the interplanetary medium. This quantity, called the space plasma electron content E_s, may be found very simply from Eq. (1), under the following assumptions:

(1) Any time variations occurring in the time span of the round-trip light time between the earth and the spacecraft are negligible. Note that for typical Venus missions the round-trip light time is less than 10 min.

(2) The difference in path lengths outside the ionosphere between the spacecraft and the various earth-based tracking stations is negligible.

Since the purpose of this article is to determine the magnitude of the effects of space plasma and not to calibrate the tracking data, these assumptions are justified.

$$E_s(t) = E_T(t) - E_I(t) \qquad (1)$$

where

$E_T(t)$ = total electron content along the entire ray path, determined from Stanford University dual frequency measurements[11] (SPS 37-58, Vol. II, pp. 66–73) for the *Mariner V* and *Pioneer IX* missions.

$E_I(t)$ = ionospheric electron content along the portion of the ray path in the earth's ionosphere. This quantity may in this case be most conveniently determined by mapping (SPS 37-57,

---

[11]The principle investigator of the Stanford University dual frequency is Prof. V. R. Eshleman. Members of his team include Drs. T. Howard and T. Croft. The total electron content determined from this experiment was supplied to Dr. L. Efron of JPL, who made it available to the authors.

Vol. II, pp. 38–42) Faraday rotation measurements made at Stanford University to the spacecraft's ray path. This mapping process contains some errors (which will be discussed in a forthcoming article) that will allow E_s to be determined to an accuracy of about 5×10^{16} electrons/m², which corresponds to approximately one-half meter in path length change for S-band frequencies.

The small circles in Figs. 35–38 show the space plasma electron content as determined from Eq. (1) along with the corresponding S-band range errors for data acquired from

(1) *Pioneer IX* near zero declination in May 1969.

(2) *Mariner V* in July, August, and September 1967 when there were at least 8 h of data per pass.
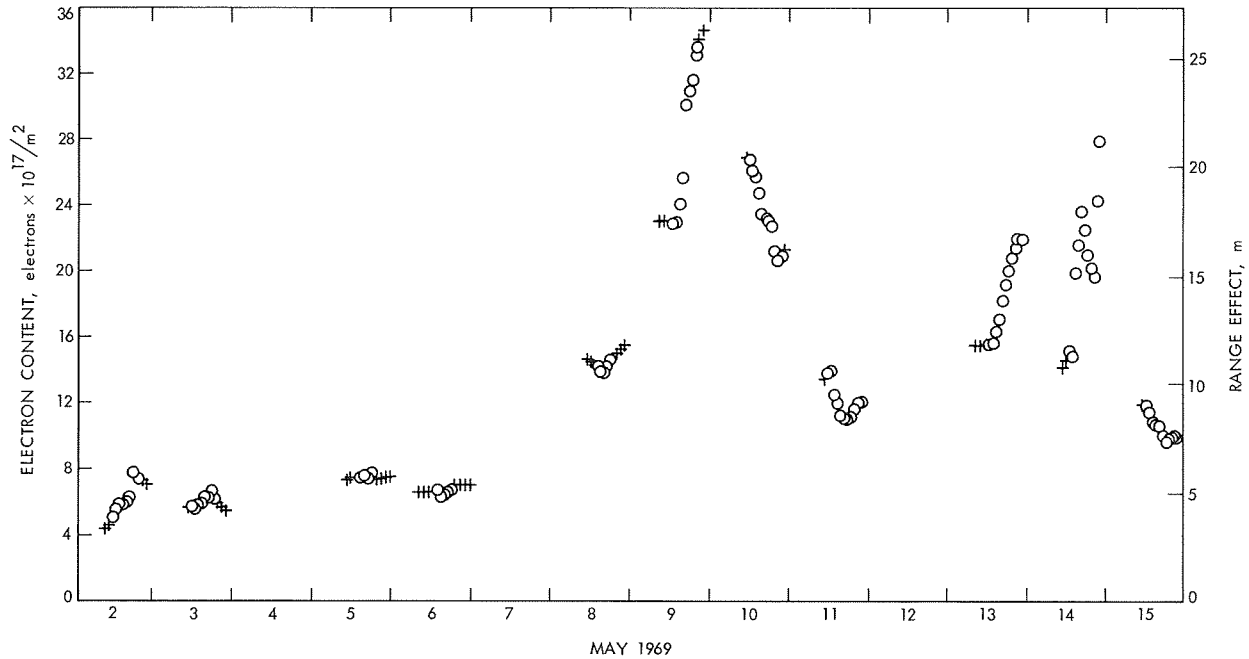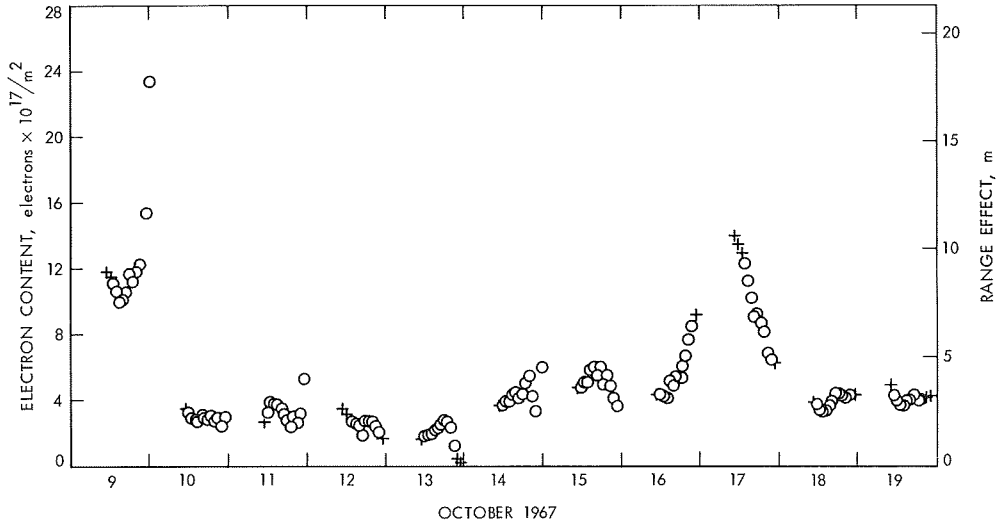

Fig. 35. *Pioneer IX* space plasma electron content and range effect in May 1969
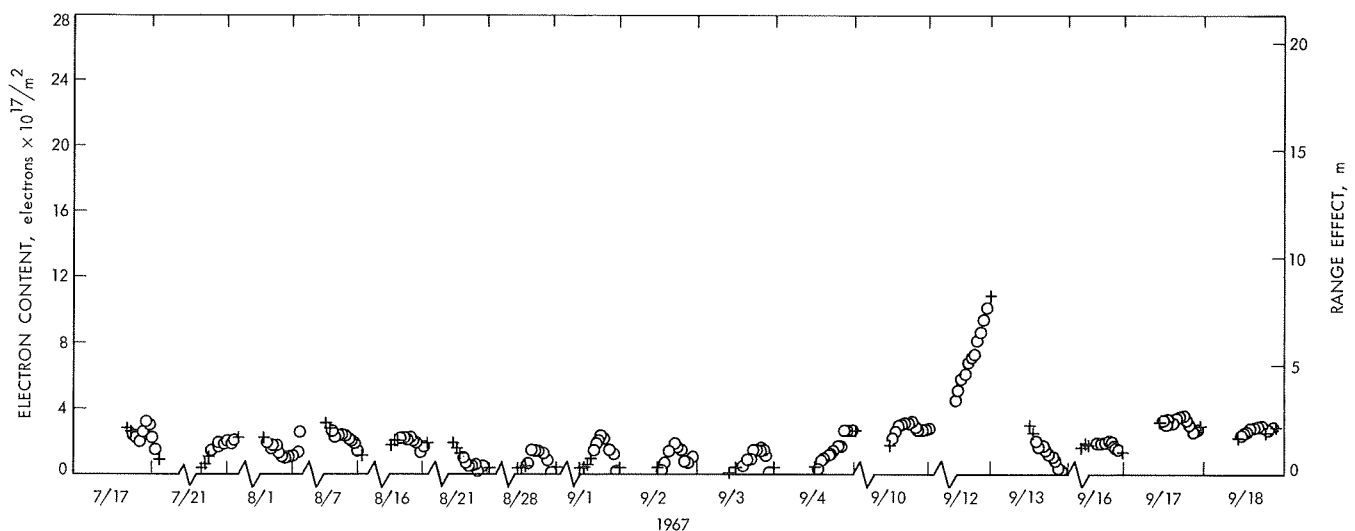
Fig. 36. *Mariner V* space plasma electron content and range effect in Jul, Aug, and Sep 1967

(3) *Mariner V* for the Venus encounter on October 19, 1967 and the surrounding days.

(4) *Mariner V* near zero declination in October and November 1967.

The data from (1), (3), and (4) are particularly useful in determining the tracking station locations, and the data

from (3) may be used to determine the encounter trajectory.

Figures 35, 37, and 38 have a continuous time scale and indicate that trying to interpolate the space plasma electron content for approximately half of every day, when the spacecraft is not in view by Stanford University, would often be impossible. This is particularly true during periods of high solar activity, such as occurred

Fig. 37. *Mariner V* space plasma electron content and range effect in Oct 1967
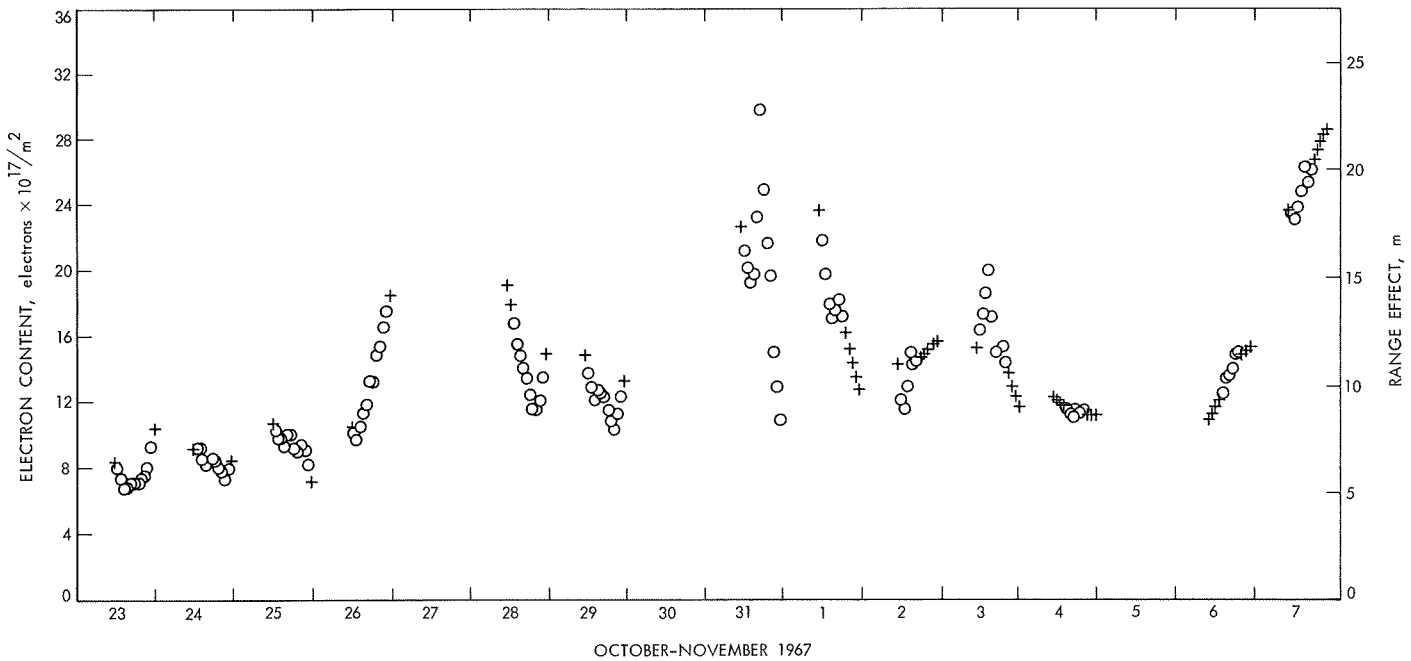

Fig. 38. *Mariner V* space plasma electron content and range effect in Oct and Nov 1967
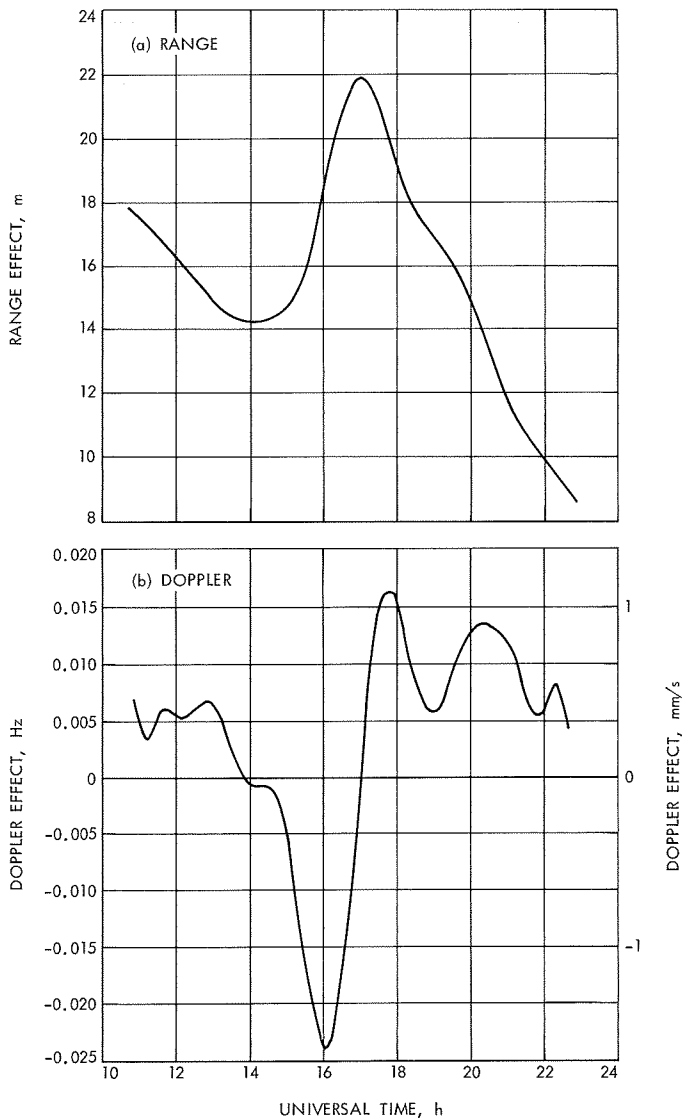
Fig. 39. Mariner V space plasma range and doppler effects on Oct 31, 1967

as crosses in Figs. 35–38. This combination of real and simulated data may be substituted into ION (with the mapping operations peculiar to the ionosphere deleted) to produce range and doppler corrections. Figure 39 shows the computed range and doppler space plasma effects for *Mariner V* on October 31, 1967, which was a day of very high solar activity. It should be noted that the peak values of 22 m in range and -1.6 mm/s in doppler are twice as large as produced by an active ionosphere (SPS 37-57, Vol. II, p. 42).

d. Apparent changes in station locations produced by the space plasma. A useful artifice for investigating the navigational errors is to describe them in terms of errors in tracking station location. As described in SPS 37-57, Vol. II, pp. 24–29, an effect which corrupts tracking data can be decomposed into parameters, one of which is the apparent change in the station distance off the spin axis, Δr_s, and another is the apparent change in the station's longitude, $\Delta\lambda$. The program HAMMEL (SPS 37-57, Vol. II, pp. 24–29) has been developed to obtain these apparent daily changes in station location using the doppler corrections produced by ION.

The apparent daily changes in station locations obtained from HAMMEL for the *Mariner V* and *Pioneer IX* space plasma illustrated in Figs. 35–38 are given in Table 25 and Figs. 40 and 41. Although the *Mariner V* results are generally significantly lower than the ionospheric changes in apparent station locations computed for the same days, of approximately Δr_s (ion) $\sim$5 m and $\Delta\lambda$ (ion) $\sim$3 m (SPS 37-57, Vol. II, p. 34), these numbers were sometimes exceeded as on October 31, 1967. Table 26 gives the percentage of days when the apparent station location changes were above a certain limit, and, in particular for *Mariner V*, shows that for more than 60% of the days either Δr_s or $\Delta\lambda$ is larger than 0.5 m.

Table 27 shows that although the standard deviations of Δr_s and $\Delta\lambda$ are fairly large (1.7 and 3.1 m, respectively, for *Mariner V*), the averages are almost zero. This indicates that over a long period of time the space plasma change in station locations is random, unlike the ionospheric corrections which are usually biased in one direction (SPS 37-57, Vol. II, p. 34). To see if the random character of the change in station locations is maintained over a 10-day period, running averages were calculated for this time scale. The results are given in Fig. 42 and show that a high solar activity, as occurred in late October and early November 1967, can bias the 10-day averages by 1 m. Even deleting the abnormally high days of

during October–November 1967 and May 1969, when there are many peaks and valleys.

c. Range and doppler space plasma corrections. The software used for this analysis (ION) (SPS 37-58, Vol. II, p. 73) was designed to produce ionospheric range and doppler corrections using measured values of the ionospheric electron content. ION may give inferior results if the electron content measurements do not cover the entire pass. For this reason it was sometimes desirable to extend the real data by estimating the space plasma total electron content at the beginning and end of the tracking pass. These estimated values are shown

Table 25. *Mariner V* apparent station location changes in July, August, and September 1967

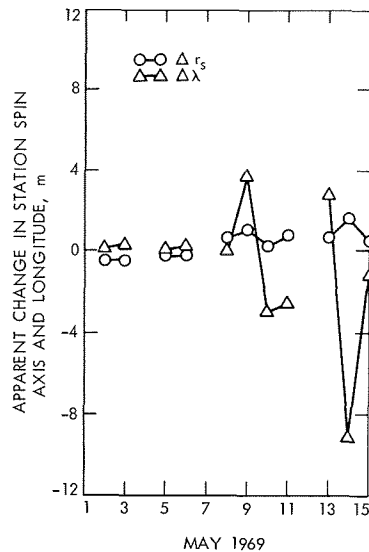| Date, 1967	Δr_s, m	$\Delta\lambda$, m
7/17	−1.0	−0.5
7/21	−0.4	−0.5
8/1	1.2	−1.6
8/7	−0.1	1.0
8/16	0	−1.1
8/21	0.4	0.3
8/28	−0.9	0.5
9/1	−1.4	0.5
9/2	−1.2	0
9/3	−0.8	−0.8
9/4	−0.2	0.5
9/10	−0.7	−0.9
9/12	0.3	−0.5
9/13	0.3	0
9/16	−0.3	0
9/17	−0.2	−0.5
9/18	−0.3	−0.2
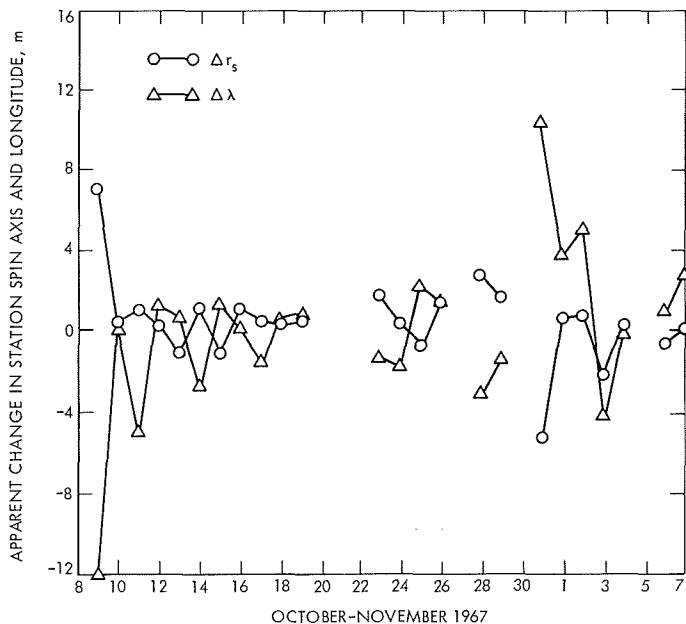
Fig. 41. Apparent changes in station locations for *Pioneer IX*

Table 26. Percentage of days when apparent change in station locations exceeds a certain limit

Limit, m	*Mariner V*[a]		*Pioneer IX*[b]	
	$\|\Delta r_s\| >$ limit, %	$\|\Delta\lambda\| >$ limit, %	$\|\Delta r_s\| >$ limit, %	$\|\Delta\lambda\| >$ limit, %
0.5	61	68	45	55
1.0	29	52	18	55
1.5	16	35	9	45
2.0	6	23	0	45
3.0	3	13	0	18
5.0	3	6	0	9

[a]For 41 days during July–November 1967.
[b]For 11 days in May 1969.

Fig. 40. Apparent changes in station locations for *Mariner V*

Table 27. *Mariner V* and *Pioneer IX* average and standard deviations for apparent changes in station locations

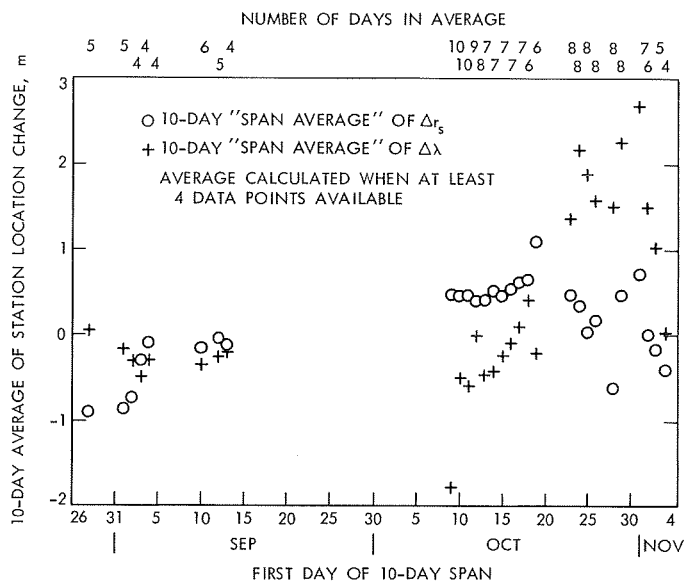| Spacecraft	Number of days	Time span	Average		Standard deviation	
			Δr_s, m	$\Delta\lambda$, m	Δr_s, m	$\Delta\lambda$, m
Mariner V	41	Jul 17 to Nov 7, 1967	0	0	1.7	3.1
Pioneer IX	11	May 2 to 15, 1969	0.41	−0.8	0.62	3.2

Fig. 42. Ten-day running averages for apparent changes in station locations for *Mariner V* in Jul–Nov 1967

October 9 and 31, 1967, does not significantly improve the averages.

The results of this section may be related to the *Mariner* Mars 1971 mission by using Efron's steady-state model of the solar wind (SPS 37-56, Vol. II, pp. 61–69). This model predicts that a solar activity that produced the apparent changes in station locations shown in Fig. 40 would give changes of a similar size for a *Mariner* Mars 1971 encounter.

e. Summary and implications for Mariner Mars 1971. Although only a cursory examination has been made of a portion of the Stanford space plasma data available from *Mariner V* and *Pioneer IX*, it demonstrates that the space plasma is a potentially limiting effect with regard to the navigational requirements for future missions. For example, the navigational goals for *Mariner* Mars 1971 encounter minus 30 days are to know the effective tracking station locations within 0.8 and 1.6 m in spin axis and longitude, respectively. Assuming there are no other errors, the randomness of the space plasma apparent changes in station locations may allow these goals to be approached without making space plasma corrections, if the sun is not unusually active and a method of determining which data should be deleted is developed. However, for a situation such as a planetary encounter, which has a span of only a few days, so that none of the data may be deleted and the randomness does not help, the data may easily contain a bias on the order of 1 m in

effective tracking station locations. Thus, to meet the Mariner Mars 1971 navigational goals, near-real-time space plasma corrections will probably have to be made. This article has shown that simulation runs of the *Mariner* Mars 1971 mission, particularly the encounter sequence, with the data suitably corrupted by a simulated space plasma are certainly justified.

5. An Algorithm for Calculating the View Periods of a Distant Spacecraft, G. A. Madrid

a. Introduction. There are many applications that require an analytical method for determining the time that a distant spacecraft will appear over an observer's horizon and the extent of time that it will remain in view. This type of application often requires that the algorithm employed be embedded in a computer program thereby imposing certain constraints. These are that the algorithm be convenient to use and efficient in operation.

No algorithm permitting such a facile computation of view periods is currently in use. Existing systems that can provide such information are integral parts of large computer programs and therefore could not be suitably implemented for the purposes being considered here. Furthermore, the interface and format requirements are usually sufficiently distinct from those provided by existing systems that information from them must be transcribed onto cards before it can be utilized.

The method presented here exhibits all of the features desired of such an algorithm and, notwithstanding certain simplifying assumptions, produces a remarkably accurate representation of the view periods of a *distant* spacecraft.

b. Method. It is required that the time of rise, time of set, and maximum elevation of a distant probe be calculated analytically, knowing the right ascension α and declination δ of the probe at any time. Assuming that the declination remains fairly constant over the view period[12] and overlooking any correction due to land mask and atmospheric refraction, we can calculate the rise time t_r as

$$t_r = \frac{\alpha + \theta_r - \lambda - p(d)}{\omega}$$

---

[12]For deep space probes this is practically true after 5 days from launch. For terrestrial or lunar orbiting vehicles this assumption fails, thereby restricting the use of this method.

where

d = number of days from 1950.0

t_r = number of seconds past beginning of day d

α = right ascension of probe on day d, deg

θ_r = hour angle of probe at time of rise, deg

λ = east longitude of observing station, deg

$p(d) = [100°\ 0.0755426 + 0.9856473d + 2.9015 \times 10^{-3}d^2]_{\text{mod 360}}$

ω = rotation rate of earth, deg/day

Values for all of these parameters are known except for θ_r. This parameter can be evaluated by

$$\theta_r = 360° - \cos^{-1}(-\tan\phi\tan\delta)$$

where

ϕ = latitude of observing station

δ = declination of probe on day d

The set time t_s can be readily computed by

$$t_s = t_r + (480)\cos^{-1}(-\tan\phi\tan\delta)$$

and the maximum elevation of the pass γ_{max} can be determined by the well-known relationship

$$\gamma_{\text{max}} = 90° - |\phi - \delta|$$

c. *Applications.* A program called LOOK, which utilizes this algorithm, has been coded and has successfully produced view periods for *Mariner V* and *Pioneer VII* for use by the program ION[13]. In this application ION required elevation angles for the upleg and downleg of both the first and last radio tracking antenna transmissions. This information was provided by using this algorithm to obtain the geometric view period relationships, then using the distance to the spacecraft to correct for

the elapsed light time. In tests the geometric rise and set times computed were within 30 s of the times computed for angular observations by the single-precision orbit determination program (SPODP) (Ref. 1). The maximum elevation was never more than 0.1 deg from the SPODP value and the hour angle and declination at rise were never more than 0.125 deg from the reference values. The SPODP values were, of course, obtained without reference to a land mask (i.e., at the observer's geometric horizon). If land mask is taken into consideration, there would be a difference of about 10 to 15 deg in elevation at rise. Such corrections could easily be incorporated into the algorithm if a closer correspondence to the real world were desired.

Reference

1. Warner, M. R., Nead, M. W., and Hudson, R. H., *The Orbit Determination Program of the Jet Propulsion Laboratory*, Technical Memorandum 33-168. Jet Propulsion Laboratory, Pasadena, Calif., Mar. 18, 1964.

6. The Effect of Interpolation on Ionospheric Calibration, G. A. Madrid

a. Introduction. One of the aims of the Precision Navigation Project (PNP) was to improve the estimates of the DSN station locations for the *Mariner* Mars 1969 mission. In accordance with this aim, Mulhall has developed several techniques to calibrate the radio tracking data so as to remove the effects of charged particles in the ionosphere. One of these methods is embodied in the computer program ION developed by Mulhall and Thuleen (SPS 37-58, Vol. II, pp. 66–73). This method requires as inputs the hour angle and declination[14] of the spacecraft at the beginning of each pass in order to map the ionospheric data to the spacecraft ray path. The correction to the ray path used by this program was derived from a relationship developed by Cain and Liu[15] relating range corrections as a function of the elevation angle. Since the hour angle and declination are obtained by interpolation, any error will be propagated into the calculation of the elevation angle and therefore into the range correction.[16]

---

[13]The program ION (Mulhall, SPS 37-58, Vol. II, pp. 66–73), which provides the capability to calibrate tracking data for ionospheric effect based on either ionosonde data, Faraday rotation measurements or model of the ionosphere, requires the calculation of view periods. An analysis of the errors introduced in ION through the use of this algorithm is presented in the following article (*Subsection 6*).

[14]The program LOOK, which uses a simplified view period calculation developed by the author, provides these inputs to ION. A description of the view period algorithm is described in the previous article, *Subsection 5.*

[15]Cain, D., and Liu, A., *Ionospheric Range and Angular Correction*, Mar. 23, 1966 (JPL internal document).

[16]It is assumed that a light time correction has been applied to obtain the correct elevation angles and that any errors from this process are negligible.

b. Effects. For a Chapman ionosphere, the elevation angle effect can be expressed as

$$\Delta\rho_I = G_1 + G_2 Z + G_3 Z^2 + G_4 Z^3 + G_5 Z^4 \qquad (1)$$

where

$$\Delta\rho_I = \text{range correction, m}$$

$$Z = (\pi/2 - \gamma)$$

$$\gamma = \text{elevation, rad}$$

The error in the slant range correction is related to an error in the elevation angle by

$$\epsilon_{\Delta\rho} = (G_2 + 2G_3 Z + 3G_4 Z^2 + 4G_5 Z^3)\epsilon_Z \qquad (2)$$

where $\epsilon_Z = -\epsilon_\gamma =$ an error in the elevation angle.

Selecting the coefficients G_1 through G_5 to represent a "heavy" electron situation (i.e., 5.0×10^{17} electrons/m^2) and finding that the range correction reaches a maximum at $\gamma = 0$ deg, it can be stated that

$$\left| \epsilon_{\Delta\rho} \right|_{max} \leq \left| G_2 + 2G_3 Z + 3G_4 Z^2 + 4G_5 Z^3 \right|_{max} \left| \epsilon_Z \right|_{max}$$

$$\leq 28.625 \left| \epsilon_Z \right|_{max} \qquad (3)$$

The error in elevation ϵ_Z is related to errors in hour angle and declination. An error in hour angle is directly related to an error in right ascension:

$$\theta = \alpha_G - \alpha + \lambda$$

where

$$\alpha_G = \text{right ascension Greenwich}$$

$$\alpha = \text{right ascension probe}$$

$$\lambda = \text{longitude of observer}$$

Thus,

$$\left| \epsilon_\theta \right| = \left| \epsilon_\alpha \right|$$

The relationship between the elevation parameter Z, the right ascension of the probe α, and the declination of the probe δ is such that

$$\epsilon_Z^2 = \epsilon_\alpha^2 + \epsilon_\delta^2$$

From this it follows that

$$\left| \epsilon_Z \right|_{max} = \left[(\epsilon_\alpha^2)_{max} + (\epsilon_\delta^2)_{max} \right]^{1/2} \qquad (4)$$

Now $(\epsilon_\alpha)_{max}$ and $(\epsilon_\delta)_{max}$, the interpolation errors in right ascension and declination, can be determined directly from numerical relationships to be

$$(\epsilon_\alpha)_{max} = \frac{(t_1 - t_0)^2}{8} K_\alpha$$

$$(\epsilon_\delta)_{max} = \frac{(t_1 - t_0)^2}{8} K_\delta$$

where K is the curvature at a local maximum or minimum point along the locus of the function of right ascension or declination with respect to time, and $t_1 - t_0$ is the interpolation interval.

Figure 43 shows the locus of the right ascension and declination histories for *Mariner V*. Table 28 lists the maximum interpolation errors at the critical segments of these curves. These segments are numbered 1, 2, 3, and 4. At 5-day intervals, the largest of these maximum values are $(\epsilon_\alpha)_{max} = 0.09$ deg and $(\epsilon_\delta)_{max} = 0.07$ deg.
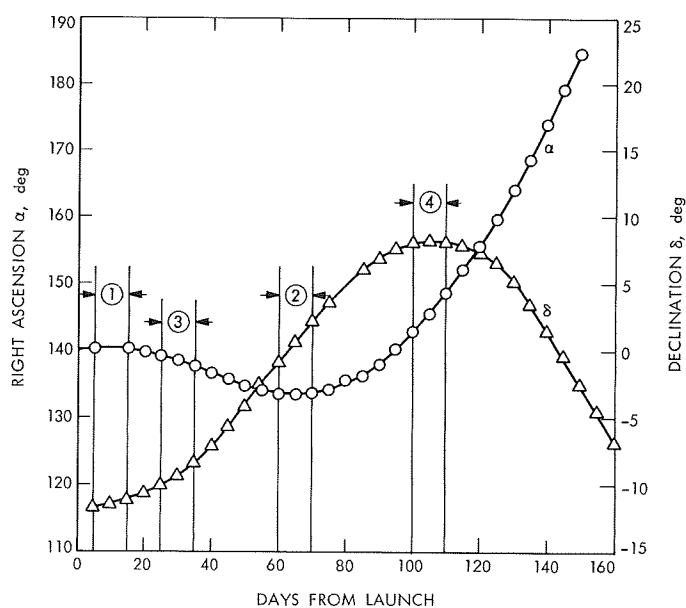

Fig. 43. *Mariner V* right ascension–declination plotted from post-flight trajectory characteristics

Table 28. Interpolated errors in right ascension and declination at critical positions in Mariner V trajectory

Interval, days	Days from launch	Position	Parameter	Maximum interpolation error, deg
10	10	1	α	0.220
	65	2	α	0.170
	30	3	δ	0.100
	105	4	δ	0.120
5	7	1	α	0.090
	12	1	α	0.001
	67	2	α	0.040
	72	2	α	0.060
	27	3	δ	0.030
	32	3	δ	0.070
	102	4	δ	0.030
	107	4	δ	0.030
2	9	1	α	0.010
	11	1	α	0.006
	64	2	α	0.009
	66	2	α	0.017
	29	3	δ	0.004
	31	3	δ	0.004
	104	4	δ	0.005
	106	4	δ	0.004

By substituting these values in Eq. (4) and then using this result in Eq. (3), a bound for the error in the range correction can be determined to be

$$\left| \epsilon_{\Delta\rho} \right|_{\max} \leq 0.06 \text{ meters}$$

Utilizing the same procedure, the corresponding result for *Mariner VII* is

$$\left| \epsilon_{\Delta\rho} \right|_{\max} \leq 0.0012 \text{ meters}$$

Figure 44 illustrates the right ascension and declination history for *Mariner VII*. Because the curves are smoother (curvature is smaller) than the *Mariner V* data, it is to be expected that the latter will exhibit larger interpolation errors than the former. This is borne out by the results stated above.

c. Conclusions. The PNP goals for 1969 call for a range resolution capability of 0.1 m in the calibration of the ionospheric effect. According to this criterion, the maximum interpolation error at 5-day intervals of 0.06 m
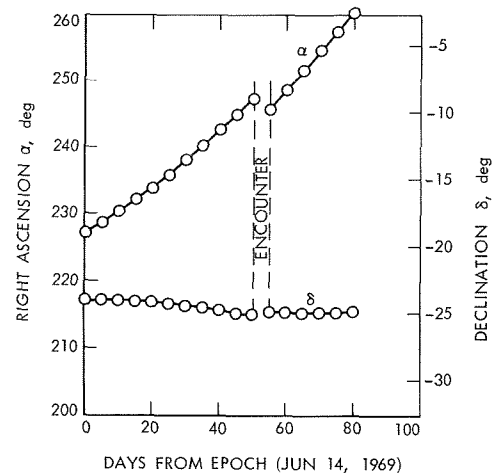

DAYS FROM EPOCH (JUN 14, 1969)

Fig. 44. *Mariner VII* right ascension–declination plotted from post-flight trajectory characteristics

introduced in calibrating the *Mariner V* tracking data falls within these requirements and can therefore be considered an acceptable error. The *Mariner VII* 5-day interpolation error of 0.0012 m is clearly acceptable.

7. The Use of Sequential Estimation With DSN Tracking Data for a Planetary Orbiter, *J. F. Jordan and R. K. Russell*

a. Introduction. With the advent of technical studies on the feasibility of planetary orbiter missions, such as the *Mariner* Mars 1971 orbiter mission and the *Viking* 1973 Mars orbiter/lander mission, JPL has become increasingly aware of the difficulties of determining accurately the orbit of a spacecraft placed as an artificial satellite of a distant planet from DSN range-rate and ranging data.

Some of the unique features of this orbit-determination problem which contribute to the difficulty are: (1) the nonlinearity of the equations of motion of the probe in orbit; (2) the lack of complete knowledge of the physical model involved, e.g., the planet's gravitational model and surface features, atmospheric drag effects, and nongravitational spacecraft-generated forces; and (3) the absence of appreciable position parallax due to the distance from which measurements are made.

For the past year, JPL has been engaged in research directed at developing a sufficient planetary orbiter navigation capability. The research has included the investigation of the feasibility of using current software tools for the task, defining the problem areas resulting from

their use, and the investigation of new state estimation techniques which may circumvent these problems.

One such technique is the sequential data filtering concept. In order to investigate the possibilities of this technique, the sequential orbit determination (SOD) program has been developed. The program is designed primarily for sequential state estimation of a planetary satellite using earth-based range and range-rate observations. The primary goals of the program production results will be aimed at (1) making recommendations (using the results of simulation studies) for the formulation of the sequential filter option to be implemented into the double-precision orbit determination program (DPODP), and (2) influencing (using the results of inherent accuracy studies) the trajectory and guidance maneuver planning in future planetary satellite missions.

The immediate tasks to be performed with the program are as follows:

(1) Conduct a tracking strategy study to determine the most favorable time during the orbit to take data if a given tracking time is alloted.

(2) Perform a definitive study on the sensitivity of the inherent estimation accuracies to the values of the orbital parameters, i.e., the orbit shape and position relative to earth.

(3) Investigate the effects of the nonlinearity of the equations of motion of the orbiting spacecraft on the linear estimation scheme and note the sensitivities of the effects to the orbit parameters.

(4) Investigate the effects of uncertainties in the gravitational model of the planet on the accuracy of the filtering procedure. Look at both harmonic uncertainties and surface anomalies (mascons). Note the sensitivities of the effects to the orbit parameters.

(5) Attempt simple methods for adjusting the filtering routine to accommodate the errors due to the effects investigated in tasks (3) and (4). Examine the use of the process noise concept and the feeding of uncertainty into the planetary mass for keeping the filter gain large.

(6) Attempt more sophisticated methods for adjusting the filtering algorithm. Examine and compare the suitability of several methods, including the limited memory filter concept and the adaptive filter concept, for the planetary orbiter problem.

(7) Examine the suitability of nonlinear extensions to the filtering routine.

(8) Investigate the advantages of increasing the dimension of the estimated state vector to include uncertain model parameters.

The purpose of this and subsequent articles is to report the progress made while carrying out the tasks listed above. Included here is a discussion of the program structure, the coordinate systems and input–output options, and the filtering equations. Results of the first task, the tracking strategy study, are presented for both the 12- and 33-h orbits of the *Mariner* Mars 1971 mission.

b. SOD program structure and description. A description of the input–output options and major functions of the program (see Fig. 45) is as follows:

(1) The initial simulated and estimated spacecraft states and *a priori* covariance matrix of the error in the estimated state can be introduced in the following systems:

(a) Cartesian, earth equatorial.

(b) Cartesian, plane-of-the-sky (see Fig. 46).

(c) Orbital elements, earth equatorial.

(d) Orbital elements, plane-of-the-sky (see Fig. 46).

The position and velocity of the target body relative to the earth in cartesian coordinates can be stated in plane-of-the-sky or earth equatorial systems. The position of the earth tracking station is an input to the program in cylindrical, earth equatorial coordinates.

(2) The program maps the simulated state $(\bar{x}_a, \bar{v}_a)$ and estimated state $(\bar{x}, \bar{v})$ of the spacecraft between points in time in target-centered, plane-of-the-sky cartesian coordinates. The vector equations of motion are

$$\dot{\vec{v}} = -\frac{\mu}{r}\mathbf{x}$$

$$\dot{\mathbf{x}} = \mathbf{v}$$

where μ is the mass of the central body. (Note that the simulated state is mapped with the simulated μ, while the estimated state is mapped with the estimated μ.)

(3) The covariance matrix, Λ, of errors in the estimated state and gravitational mass μ is mapped by

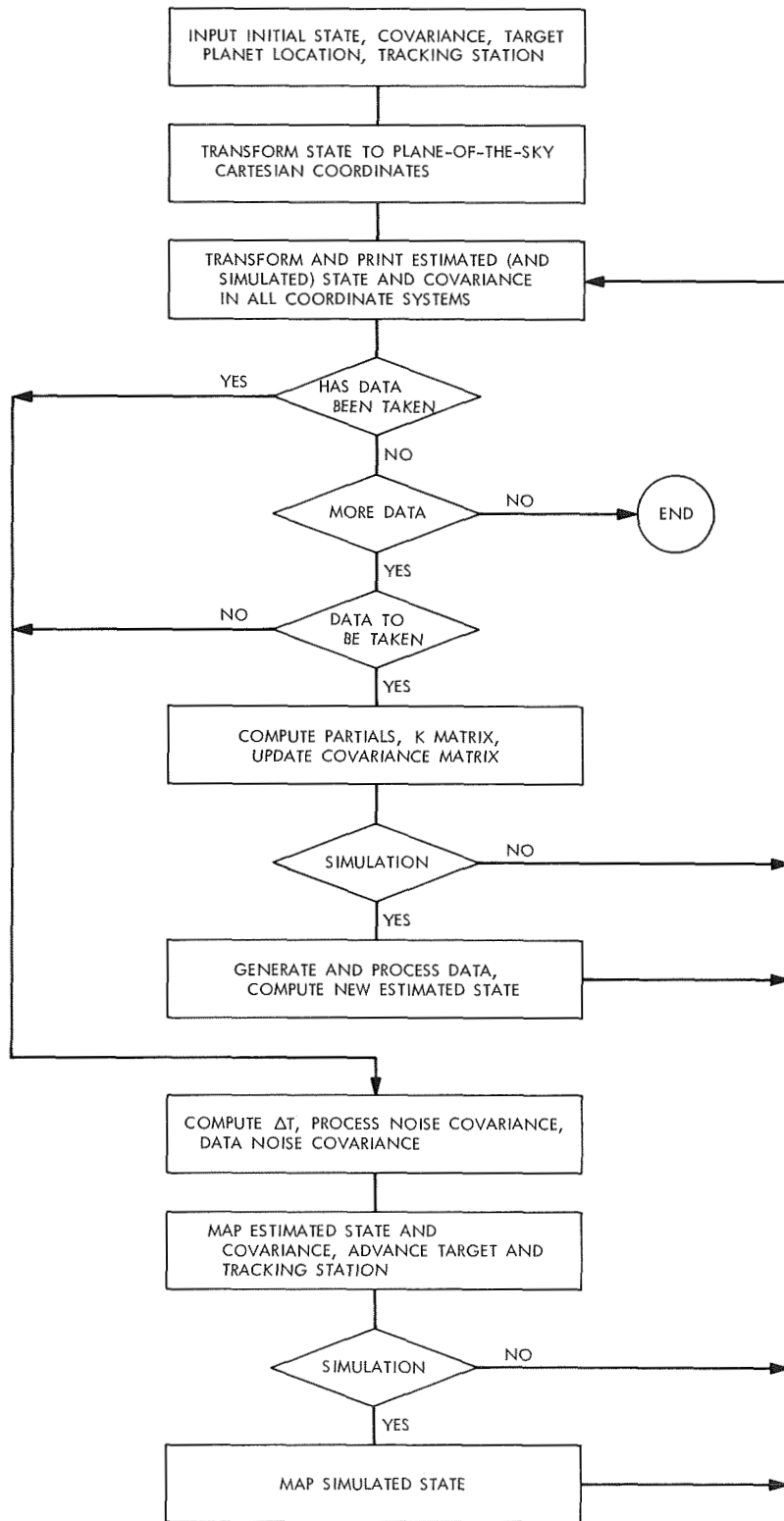$$\frac{d\Lambda}{dt} = F\Lambda + \Lambda F^T + Q$$
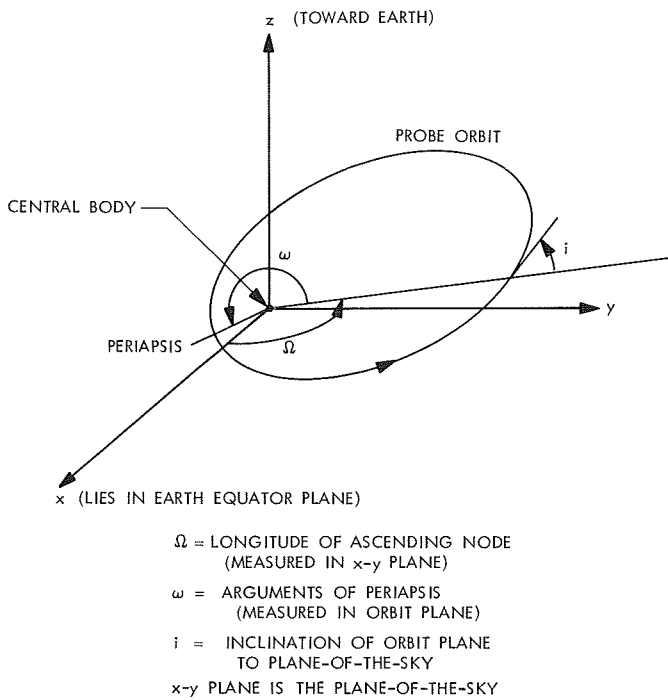
Fig. 45. SOD program flow chart

Fig. 46. Orbit configuration referenced to plane-of-the-sky

z (TOWARD EARTH)

PROBE ORBIT

CENTRAL BODY

PERIAPSIS

ω

Ω

i

y

x (LIES IN EARTH EQUATOR PLANE)

Ω = LONGITUDE OF ASCENDING NODE
(MEASURED IN x-y PLANE)

ω = ARGUMENTS OF PERIAPSIS
(MEASURED IN ORBIT PLANE)

i = INCLINATION OF ORBIT PLANE
TO PLANE-OF-THE-SKY

x-y PLANE IS THE PLANE-OF-THE-SKY

where

$$F = \frac{\partial\left(-\frac{\mu}{r^3}\mathbf{x}, \mathbf{v}, 0\right)}{\partial(\mathbf{v}, \mathbf{x}, \mu)}$$

and Q is a symmetric matrix representative of the covariance of any assumed "white noise" type of accelerations on the probe (including both gravitational and nongravitational accelerations).

(4) The tracking observables $\dot{\rho}_a$ (range rate) and ρ_a (range) are generated directly from the simulated state. The observables are assumed corrupted by independent gaussian noise increments, and the observable vector z_a becomes

$$z_a = \begin{bmatrix} \dot{\rho}_a \\ \rho_a \end{bmatrix} + \begin{bmatrix} \eta_1 \\ \eta_2 \end{bmatrix}$$

η_1 and η_2 are simulated by a random number generator which yields the following statistics:

$$E[\eta_1] = E[\eta_2] = 0$$

$$E[\eta_1(t_i)\eta_1(t_j)] = \sigma_{\eta_1}^2 \, \delta_{ij}$$

$$E[\eta_2(t_i)\eta_2(t_j)] = \sigma_{\eta_2}^2 \, \delta_{ij}$$

$$E[\eta_1(t_i)\eta_2(t_j)] = 0$$

The estimated tracking observables $\dot{\rho}$ and ρ are computed directly from the estimated state.

(5) A new state estimate is formed at each point of observation, which can be as often as desired. The new state estimate X_+, where

$$X = \begin{bmatrix} \mathbf{x} \\ \mathbf{v} \end{bmatrix}$$

is computed from the old estimate X_- by the equation

$$X_+ = X_- + K[z_a - z]$$

where z is the estimated observable vector

$$z = \begin{bmatrix} \dot{\rho} \\ \rho \end{bmatrix}$$

and K, the gain matrix, is given by

$$K = \Lambda_- H^T [H\Lambda_- H^T + R]^{-1}$$

with

$$\Lambda_- = E[(X_a - X_-)(X_a - X_-)^T]$$

$$H = \frac{\partial z}{\partial X_-}$$

$$R = \begin{bmatrix} \sigma_{\eta_1}^2 & 0 \\ 0 & \sigma_{\eta_2}^2 \end{bmatrix}$$

The updated covariance matrix Λ_+, defined as

$$\Lambda_+ = E[(X_a - X_+)(X_a - X_+)^T]$$

is then computed from the old covariance matrix by

$$\Lambda_+ = (I - KH)\Lambda_- (I - KH)^T + KRK^T$$

(6) The output from the program consists of the simulated and estimated states, the matrix of the partials of the observables, the mapping matrix, and the covariance of the error in the estimated state before and after each data point, or as often as specified. In addition these quantities are also mapped and displayed in all coordinate systems referenced in subparagraph (1).

c. Mariner Mars 1971 tracking strategy study. In line with the tasks mentioned above for this program, a tracking data strategy study has been performed that examines questions relating to the orbiter portion of the *Mariner* Mars 1971 mission.

The purposes of this study are:

(1) To determine the relative importance of data spans taken at different intervals of an eccentric orbit.

(2) To recommend a suitable tracking strategy contingent upon requirements of a limited amount of available tracking time.

To study the first problem, two orbits typical of those being considered for the *Mariner* Mars 1971 orbiter were chosen for investigation. Their characteristics in plane-of-the-sky orbital elements follow:

Parameter	Orbit 1	Orbit 2
Period p, h	12	33
Semi-major axis a, km	12651	24862
Eccentricity e	0.58	0.8
Inclination to plane-of-the-sky i, deg	69	85
Argument of periapsis ω, deg	200	220
Longitude of ascending node Ω, deg	111	136

The assumptions of the program's operation are:

(1) Range rate data only, with a noise of 10^{-3} m/s.

(2) A sample interval of 60 s.

(3) Sphericity of Mars is assumed, and accordingly no process noise perturbing the estimated state.

(4) Six probe-state parameters and the mass of the central body are estimated.

(5) The *a priori* covariance of the errors in the state are

$$\sigma_a = 100 \text{ km}$$

$$\sigma_e = 0.1$$

$$\sigma_{T_p} = 100 \text{ s}$$

$$\sigma_\Omega = 1 \text{ deg}$$

$$\sigma_\omega = 1 \text{ deg}$$

$$\sigma_i = 1 \text{ deg}$$

$$\sigma_\mu = 10 \text{ km}^3/\text{s}^2$$

where T_p is the time of periapsis passage.

(6) The earth station is assumed to be at the center of the earth. During the course of this study, it was ascertained that station location and station motion had no effect on the subsequent results, since estimated state was target-centered.

Sensitivity of estimation accuracies to placement of the data span. In order to investigate the tracking strategy problem, it was decided to take a fixed amount of data in the orbit and observe the influence on the estimation capability of varying the portion of the orbit where these data were taken. In addition it should be mentioned that two successive orbit passes of data are used instead of one pass, since the estimation capability is significantly improved by using the additional pass of data. In the following results, the length of the data span is fixed at 4 h.

The plots in Fig. 47 display respectively, in polar form, the uncertainty in the estimates of the semi-major axis and eccentricity as a function of the time of the center of the data span from periapsis for Orbit 1.

It is easily seen that data spans including periapsis offer the best determination of the parameters. For example, for a span taken about periapsis, $\sigma_a = 0.036$ km, while for a span centered about a time 4 h before periapsis, $\sigma_a = 0.26$ km; an order of magnitude difference exists between the two results although the same tracking time span was employed.

Figure 48 illustrates the tracking accuracies of a and e for Orbit 2. The same conclusions can be drawn from the Orbit 2 results, namely, that data spans including periapsis provide the best determination of a and e. In Orbit 2 it is seen that the data spans at periapsis provide a relatively greater determination of the estimated parameters than in Orbit 1. This is due to the higher eccentricity of Orbit 2.

It should be noted that the remaining orbital elements exhibit similar behavior to the semi-major axis.

Sensitivity to variation in the tracking span. Since it has been concluded that tracking centered about the periapsis time is the most efficient general tracking strategy, it would be interesting to note the sensitivity of the parameter estimate uncertainties to the width of the pass.
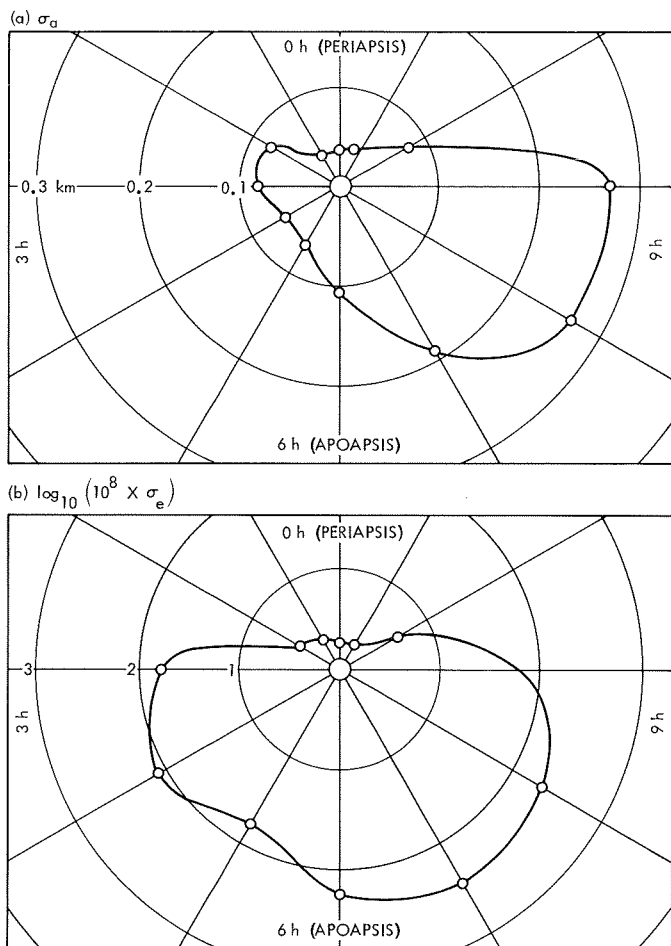
(a) σ_a

0 h (PERIAPSIS)

0.3 km — 0.2 — 0.1

3 h

9 h

6 h (APOAPSIS)

(b) $\log_{10}\left(10^8 \times \sigma_e\right)$

0 h (PERIAPSIS)

-3 — 2 — 1

3 h

9 h

6 h (APOAPSIS)

Fig. 47. Uncertainties of semi-major axis and eccentricity for Orbit 1

(a) $\log_{10}\left(10^2 \times \sigma_a\right)$; σ_a, km

0 h (PERIAPSIS)

-3 — 2 — 1

8.25 h

24.75 h

16.5 h (APOAPSIS)

(b) $\log_{10}\left(10^9 \times \sigma_e\right)$

0 h (PERIAPSIS)

-6 — 4 — 2

8.25 h

24.75 h

16.5 h (APOAPSIS)
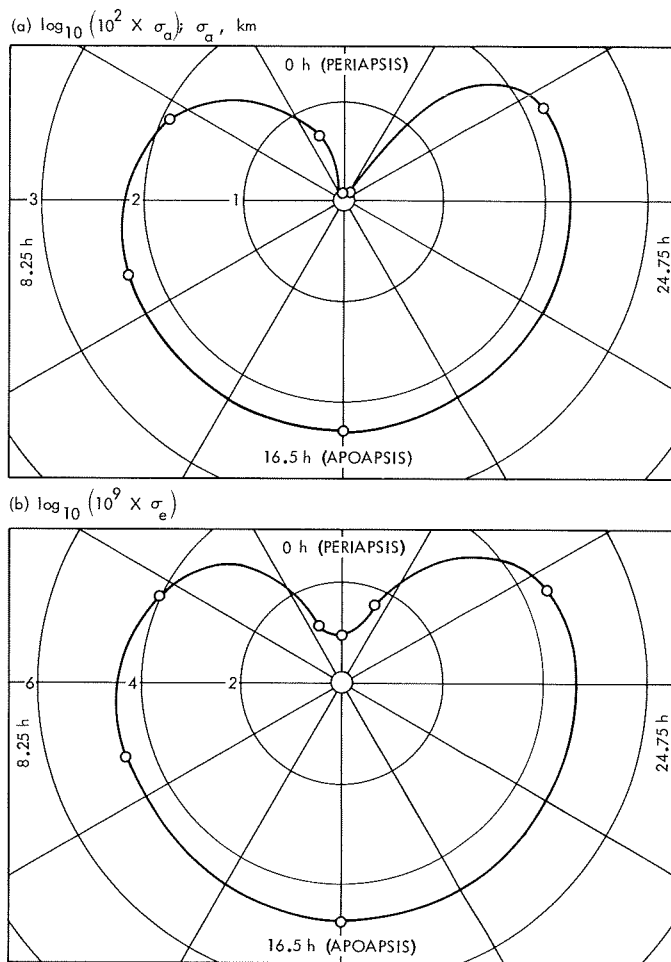
Fig. 48. Uncertainties of semi-major axis and eccentricity for Orbit 2

Plots of the uncertainties in a and e versus the pass width time are presented for Orbit 1 in Fig. 49, with curves shown for both one and two passes. The uncertainty in the semi-major axis appears to level off at a value of 35 m, while the eccentricity has an uncertainty of 0.18×10^{-7}. Plots of the same parameters for Orbit 2 are presented in Fig. 50. σ_a reaches a value of 10 m, while σ_e is just under 10^{-8}. The uncertainties in the other orbital elements behave similarly to those shown and reach the following values:

Parameter	Orbit 1	Orbit 2
σ_{T_p}, s	0.21×10^{-3}	0.16×10^{-3}
σ_Ω, rad	0.9×10^{-5}	0.66×10^{-5}
σ_ω, rad	0.7×10^{-7}	0.5×10^{-7}
σ_i, rad	0.57×10^{-5}	0.42×10^{-5}

Conclusions of the tracking strategy study. The results indicate that the most efficient tracking strategy is the tracking of the probe over spans that are centered about or at least include the periapsis time. It also appears that if more than 1 pass is taken, the parameter uncertainties are not very sensitive to the span width when it is wider than about 4 h.

It should be cautioned that the results presented in this article are idealized in the sense that a spherical central body was assumed with no effects of oblateness considered. The consideration of oblateness effects and harmonic uncertainties will no doubt affect the numerical results presented here, but it is doubtful if the presence of these and other error sources will affect the tracking strategy conclusions stated above, if the orbit determination process effectively accounts for the error sources. As nonlinear and gravitation model error effects are investigated in future work, the results of these investi-
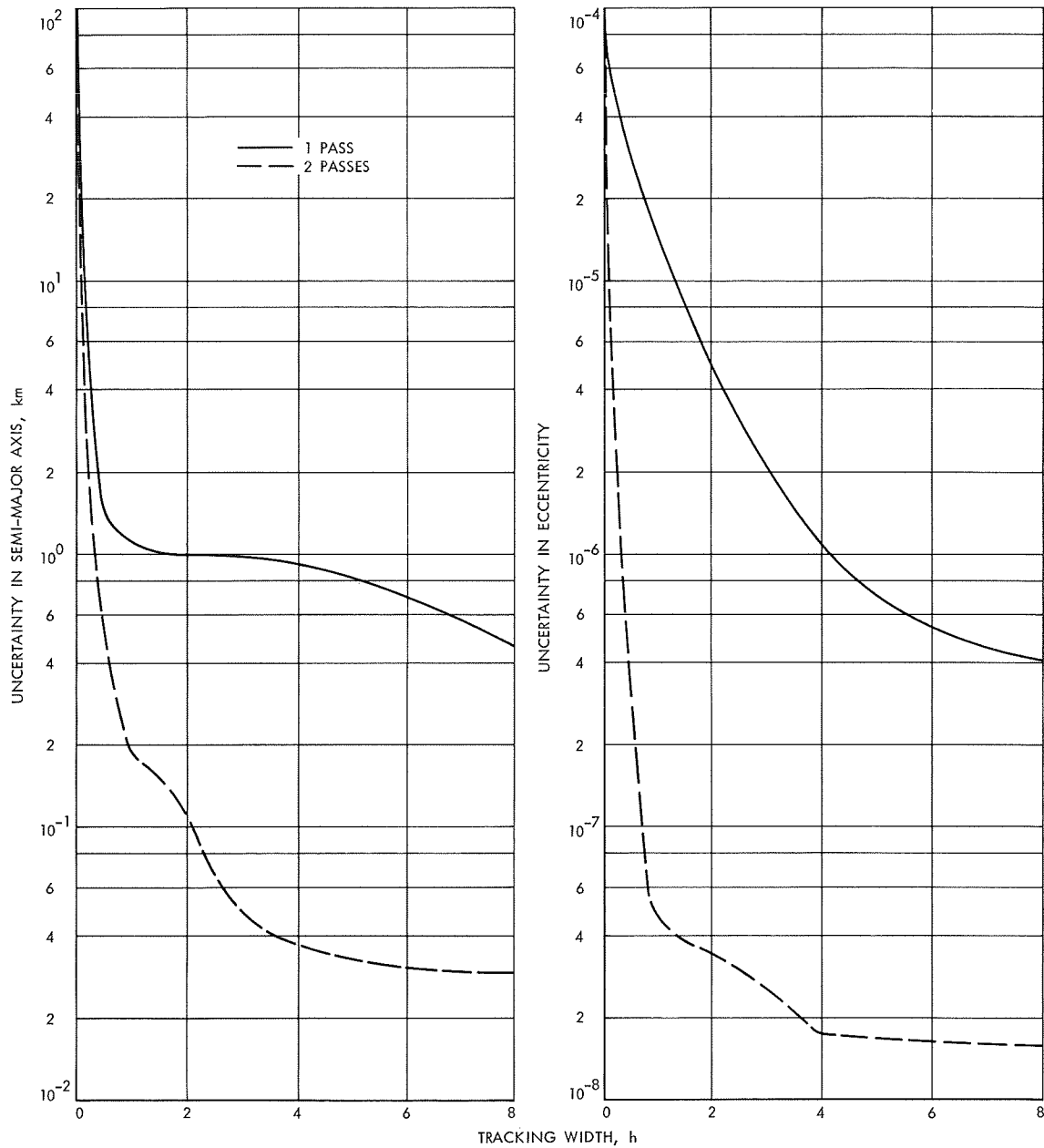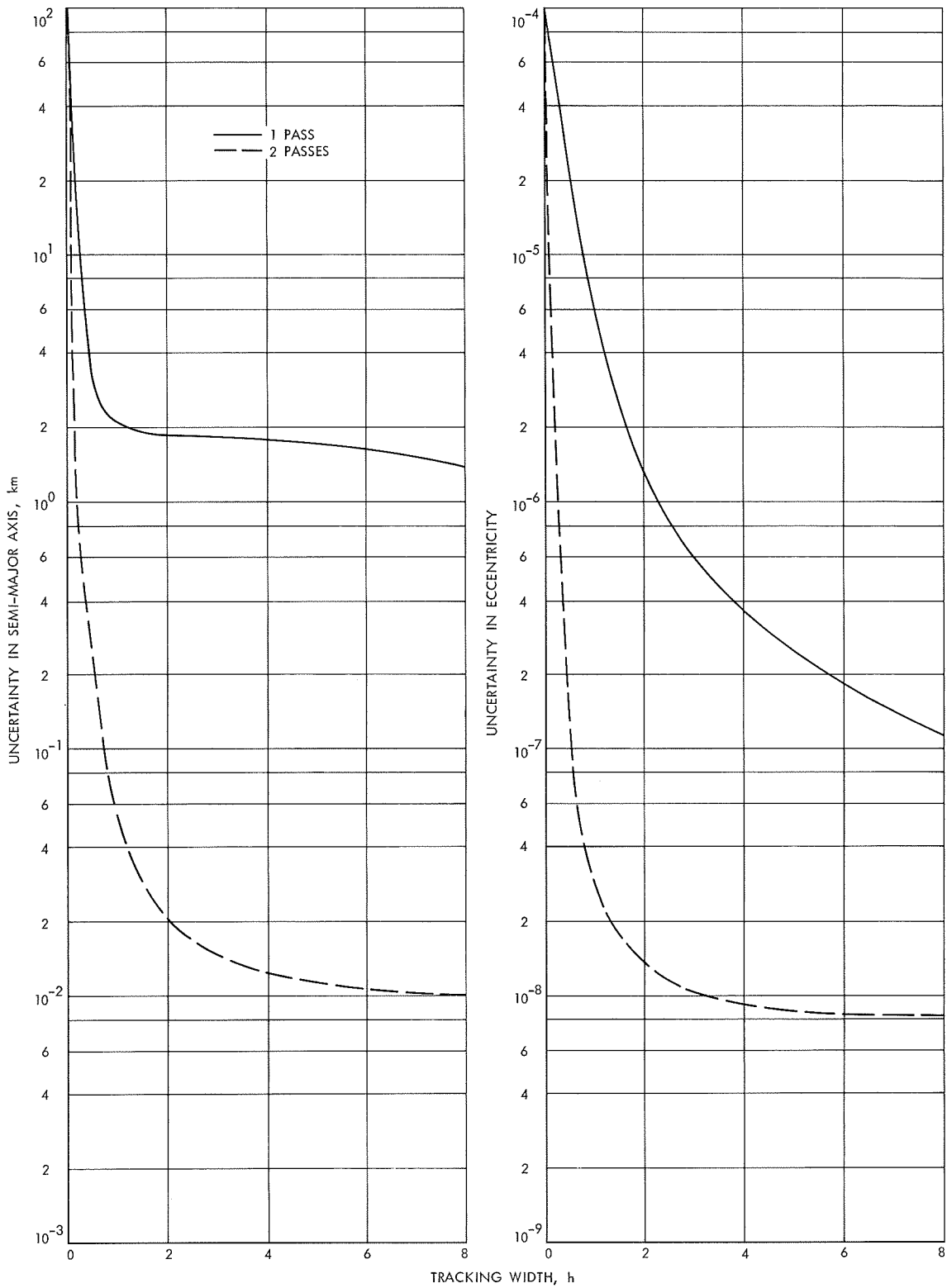
Fig. 49. Uncertainties of semi-major axis and eccentricity as a function of tracking interval width for Orbit 1

gations and their bearing on the conclusions of this article will be published.

8. Lunar Surface Mass Distribution Map From Dynamic Point-Mass Solution, *P. M. Muller and W. L. Sjogren*

a. Introduction. For over one year, JPL and the Aerospace Corporation of El Segundo, California, have been cooperating in an effort to determine lunar gravimetry from a dynamic fit of the *Lunar Orbiter* doppler tracking data, using a dense grid of discrete mass points on the lunar surface. This method differs in fundamental respects from that used in the previous analysis (Ref. 1).

In the original reductions of *Lunar Orbiter* data (Ref. 1 and SPS 37-53, Vol. II, pp. 10–15), the line-of-sight accelerations were inferred by differentiating the residuals after the fit to the doppler tracking data. The many simplifications necessary to this method were stated in Ref. 1. While the data reduced in this way had a high degree of qualitative information, it was always suspected

Fig. 50. Uncertainties of semi-major axis and eccentricity as a function of tracking interval width for Orbit 2

that a dynamic determination (either via harmonic expansions, point masses, or a combination) would eventually supersede the initial results. The Aerospace team, direct by L. Wong, and in cooperation with the authors and P. Gottlieb of JPL, has completed the determination[17] using over 100 orbits of *Lunar Orbiter IV* and *V* polar-orbit data. While it is expected that the inclusion of a like amount of equatorial orbit data (*Lunar Orbiters I, II, and III*) in subsequent work will change the results slightly, it is deemed appropriate to present the new map at this time.

b. Method. A brief description of the method is presented here. Some 580 discrete mass points were set at the lunar surface, spanning ±90° in longitude and ±55° in latitude. The separation of individual points at the equator was 5°, increasing to 10° in latitude at 55°N lat, such that correlation between the "solved-for" masses at adjacent points were approximately 0.8[18] given the geometry of *Lunar Orbiter V* polar orbits. These orbits reach perilune at the equator with an altitude of approximately 100 km, increasing with increasing latitude (eccentricity = 0.27). This results in the spacecraft traveling over the surface of the moon (within the region where the doppler tracking data is sensitive to the local lunar surface mass distribution) for 55 min out of each orbital period of 220 min.

A total of 121 orbits was processed individually, solving for the spacecraft state associated with each 55-min data arc centered on the equator. The program was capable of solving 100 parameters, which were usually apportioned to 8 spacecraft data arcs (48 state parameters) and approximately 50 mass points falling under the selected family of data arcs. Groups of orbits processed in this way were overlapped, with the families of mass points in the solve-for set similarly shifted. The solution converged after some 50 computer runs, in which previously solved mass points (not in the solution set of a given run) were included in the trajectory integration. This "bootstrapping" system was the result of an extensive correlation and sensitivity analysis carried out by the Aerospace team.

c. Results. The 580 mass points were plotted on the ACIC mercator earthside hemisphere lunar map. They were then contoured at intervals of 1×10^{-6} lunar masses (Fig. 51). This method of presentation is a surface mass

distribution, and can be converted to units of mass/deg² by multiplying the map value by the factor $0.04 \cos^2$ (lat). This relates the mass per square equatorial degree (approximately 1000 km²) and the latitude on the map for the contoured levels in units of 1×10^{-6} lunar masses.

Preliminary examination of independent comparison with the quasi-static model (next article, *Subsection 9*) and other data such as equatorial orbits, plus the statistical output of the computer program after the fit, led us to believe that the standard deviation of error is 0.5×10^{-6} lunar masses for a typical individual point. This may be somewhat larger at the limbs, and the effective averaging implied in the contouring may have somewhat reduced the apparent errors. The error limits will be further reduced when the equatorial data set is added to the solution.

d. Interpretation. The most significant observation would seem to be confirmation of the negative ring surrounding Mare Orientale as speculated in Ref. 3 from interpretation of the line-of-sight acceleration. In fact, it can be noted that all the ringed seas seem to have negative areas, particularly Imbrium, Nectaris, and Serenitatis, with Nectaris and Crisium having less pronounced relative lows.

The central-eastern highlands are generally slightly positive, with an interesting field of discrete highs around Mare Nectaris. These include the new mascon area (with our proposed name Lacus Gravitatis) northwest of Nectaris. In addition, there is a diffuse but definite high southeast of Nectaris, one in Mare Fecunditatis and two more highs over Petavius and Furnerius. No speculation is offered regarding whether these last two areas are physically related to the large named craters.

Sinus Aestuum, Grimaldi, and the newly discovered mascon area near the crater Balmer do not show up well on this map. The latter two may just not be quite resolved, and the former is probably coming out with an amplitude that is too low. Equatorial data should refine these regions, since the mass-point spacing will be closer (2.5°) and lower perilune data will have more information content.

It has generally been agreed (Refs. 4 and 5) by selenologists that the Oceanus Procellarum and Mare Tranquillitatis areas are among the most recent lunar surfaces, are most likely to be lava flows, and have a thin regolith. It is interesting to note that these are gravimetric lows, an observation which casts some doubt on

---

[17]A detailed description of the method employed and the results are presented in Ref. 2.

[18] Although additional useful results can still be obtained by allowing closer mass spacing and still higher correlations (see following article, *Subsection 9*).

the suggestion that the mascons are themselves lava flows which built up the extra mass that we now observe.

References

1. Muller, P. M., and Sjogren, W. L., "Mascons: Lunar Mass Concentrations," *Science*, Vol. 161, No. 3842, pp. 680–684, Aug. 16, 1968.

2. *Dynamic Determination of Mascons on the Moon*, Report No. ATR-69(7140)-1. Aerospace Corp., El Segundo, Calif., Apr. 29, 1969.

3. Muller, P. M., and Sjogren, W. L., "Lunar Gravimetrics," *Proceedings of COSPAR*, 1969.

4. Oberbeck, V. R., and Quaide, W. L., "Genetic Implications of Lunar Regolith Thickness Variations," *Icarus*, Vol. 9, pp. 446–465, 1968.

5. Tyler, G. L., "Oblique-Scattering Radar Reflectivity of the Lunar Surface: Preliminary Results from Explorer 35," *J. Geophys. Res.*, Vol. 73, No. 24, Dec. 1968.

9. Lunar Gravimetric Maps, P. Gottlieb

Most of the information on local lunar gravity features has been obtained from doppler tracking of *Lunar Orbiter* spacecraft at altitudes near 100 km. A representation of the local gravity features (such as mascons) in terms of accelerations at 100 km altitude would, therefore, be quite representative of the data most critical to the construction of the model. The present article provides representations of two models in terms of the resulting radial (directed toward the center of the moon) acceleration expressed in earth milligals (10^{-6} of the gravitational acceleration at the surface of the earth). (Line-of-sight accelerations would be more representative of the actual data, but would greatly distort the field at points more than 20° distant from the sub-earth point.)

The model represented in Fig. 52 was obtained by dynamically estimating the values of 580 point masses on a regular grid across most of the earthside lunar hemisphere. This is called a dynamic model because the values of the masses are estimated in the orbit determination run to estimate the spacecraft state. A description of the actual procedure used to obtain this dynamic model is given in the preceding article (*Subsection 8*).

The model represented in Fig. 53 was obtained by an open loop iteration procedure using 35 orbits (25 nearly polar and 10 nearly equatorial) spaced to cover the earthside lunar hemisphere. At each iteration the model was updated by adding masses whose values were estimated from residual accelerations remaining after orbit determination estimation of the spacecraft state, using the

gravitational model updated at the previous iteration. The locations and depths of each new set of masses were chosen according to a reasonable physical interpretation of the residual accelerations. Many masses obtained in this manner had strongly overlapping spheres of influence, and, consequently, had little *individual* physical significance. It was, therefore, physically reasonable to smooth the mass distribution by expanding the field of the point masses in a set of twentieth-degree spherical harmonics. (Further details on the construction of this model are given in SPS 37-57, Vol. II, pp. 68–70.)

The contours of Figs. 52 and 53 were drawn by a program utilizing a two-dimensional interpolation subroutine (described in SPS 37-32, Vol. IV, pp. 18–22). The interpolations were based on numerical evaluations of the acceleration at 2.5° intervals.

A summary of the distinctions in the two model constructing procedures is provided by Table 29. The agreement between Figs. 52 and 53 is somewhat remarkable in view of these distinctions, and should be taken as a confirmation of the results. One difference between the two maps is that the positive acceleration above Sinus Aestuum (lat 10°, lon −10°) is very weak in Fig. 52 (as is mentioned in the preceding article, *Subsection 8*). From the residuals remaining after application of these models, probable errors are estimated to be less than 20 milligals.

Table 29. Comparison of model constructing procedures

Parameter	Dynamic model (Fig. 52)	Quasi-static model (Fig. 53)
Number of orbits	100 polar	25 polar 10 equatorial
Depth of masses	Surface	50–150 km
Spacing of masses	Regular grid	As needed
Smoothing of discrete masses	None	Twentieth-degree spherical harmonics
Arc length	55 min	90 min

The features of these maps are also comparable to the least squares filtered line-of-sight accelerations originally found by Muller and Sjogren (Ref. 1). One new feature of interest is the relative positive acceleration over Mare Fecunditatis (lat −4°, lon 48°).

Reference

1. Muller, P. M., and Sjogren, W. L., "Mascons: Lunar Mass Concentrations," *Science*, Vol. 161, No. 3842, pp. 680–684, Aug. 16, 1968.
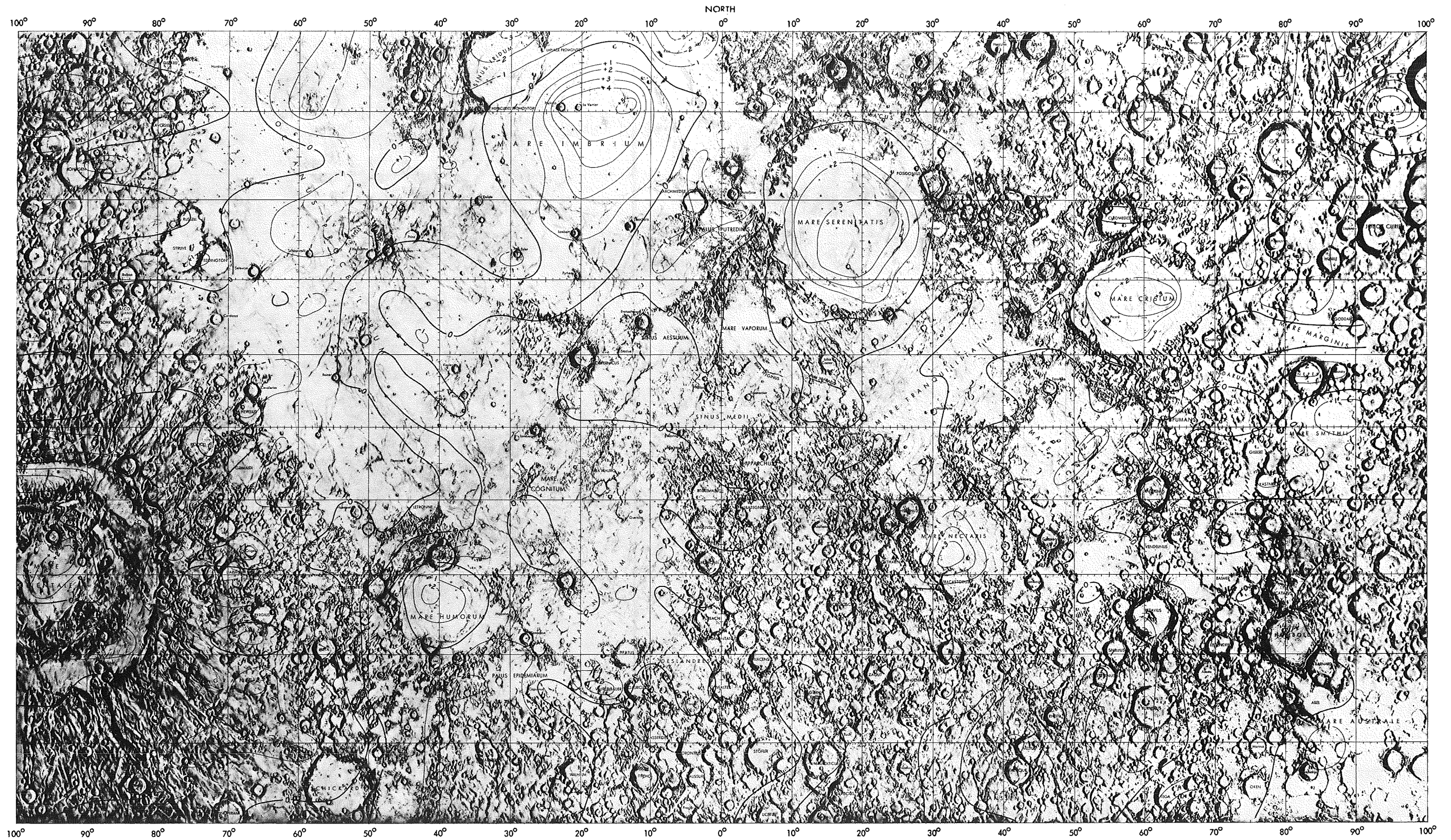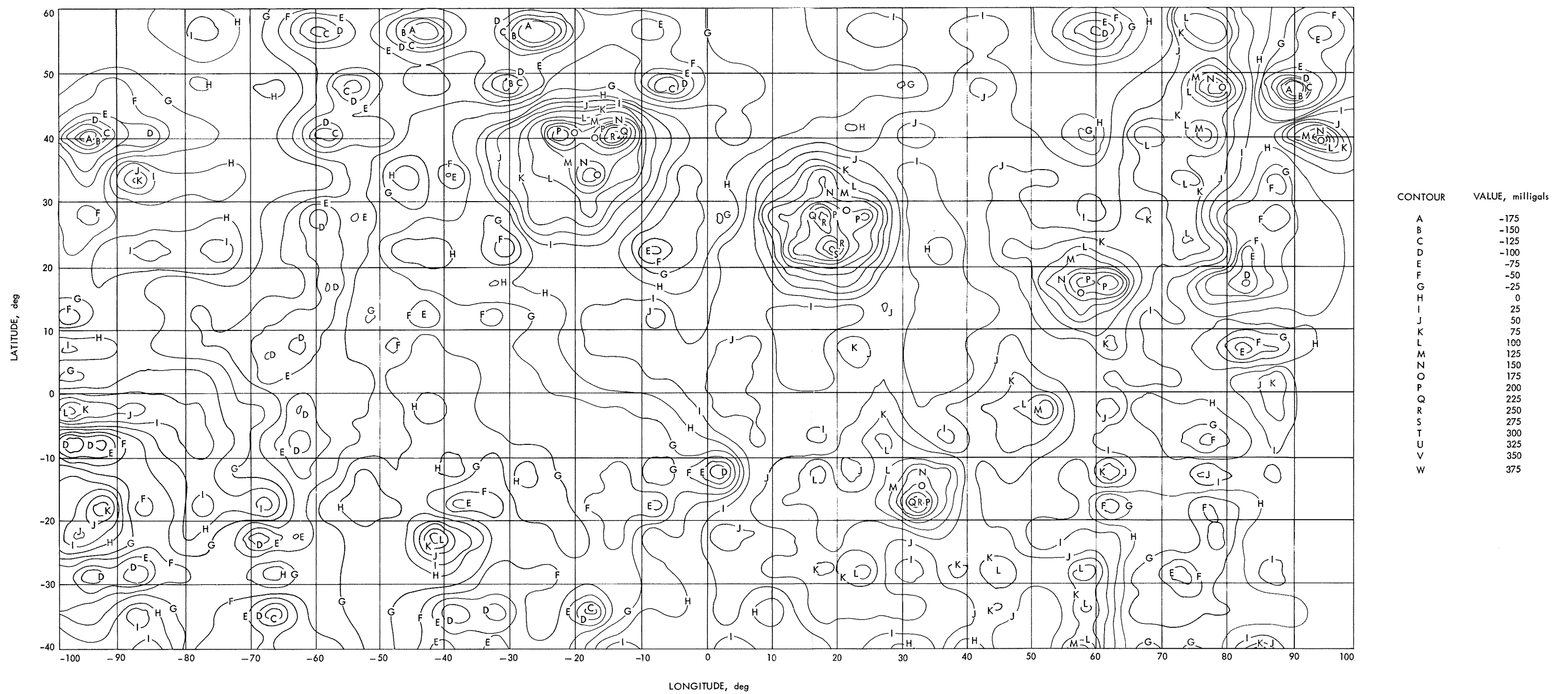
Fig. 51. A surface mass distribution

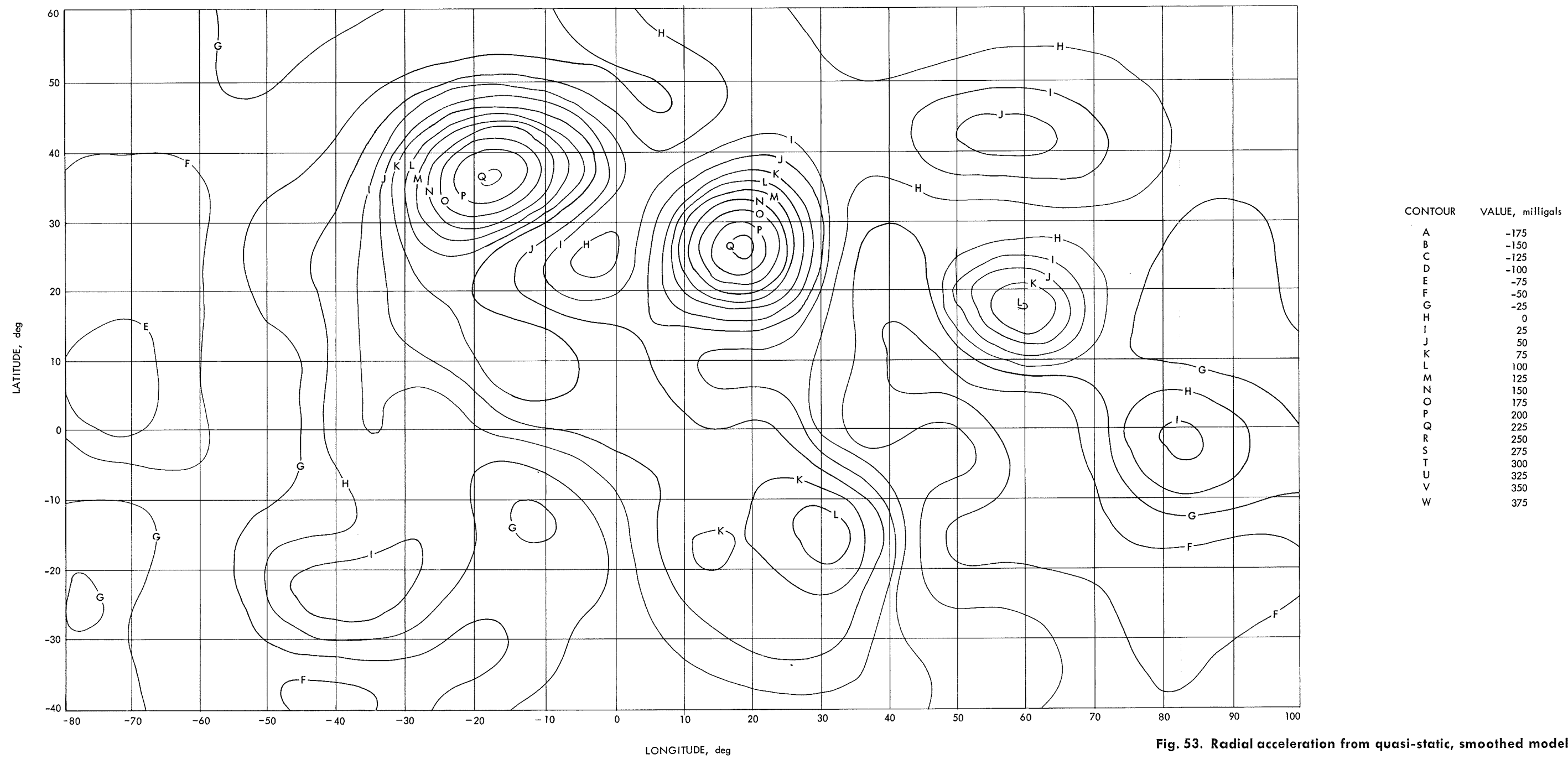**Fig. 52. Radial acceleration of discrete points mass from dynamic model**

The contour legend reads:

CONTOUR	VALUE, milligals
A	−175
B	−150
C	−125
D	−100
E	−75
F	−50
G	−25
H	0
I	25
J	50
K	75
L	100
M	125
N	150
O	175
P	200
Q	225
R	250
S	275
T	300
U	325
V	350
W	375

Fig. 53. Radial acceleration from quasi-static, smoothed model

CONTOUR	VALUE, milligals
A	−175
B	−150
C	−125
D	−100
E	−75
F	−50
G	−25
H	0
I	25
J	50
K	75
L	100
M	125
N	150
O	175
P	200
Q	225
R	250
S	275
T	300
U	325
V	350
W	375

Page intentionally left blank

10. The Paucity of Gravimetric Information Due to Spurious Anomalies in *Apollo 10* and *11* LM Tracking Data, *P. Gottlieb and W. L. Sjogren*

Recent progress in the estimation of local lunar gravity features based on doppler tracking data from *Lunar Orbiter* spacecraft (see the two preceding articles, *Subsections 8 and 9*) has encouraged the belief that still more gravitational information should be obtainable from lower altitude spacecraft. An attempt was made on the *Apollo 10* and *11* missions where the lunar module (LM) was tracked in a ballistic orbit to within 11 km of the lunar surface. This compares with a 50- to 100-km periapsis altitude for the *Lunar Orbiter* spacecraft. Unfortunately, the receiver seems to have been poorly locked-up during much of the tracking time (i.e., there were 10 bad gaps in the 30 min of *Apollo 10* LM data). Perhaps there were antenna pointing problems, for there were some large doppler anomalies on *Apollo 10* for which there seems to be no physical explanation and which were not observed on *Apollo 11* when overflying the same area. Even the smaller doppler anomalies of *Apollo 10*, which could have been due to the surface mass distributions, were not confirmed in the *Apollo 11* tracking data. These smaller scale doppler anomalies were probably caused by spurious oscillation of the spacecraft leading to small, but rapid, motions of the antenna. The spacecraft attitude control logs were insufficient to either confirm or contradict this hypothesis.

The DSS 14 antenna (Goldstone, 210 ft) was used to receive the 3-way S-band signal and the doppler was computed at 1-s intervals using the fractional cycle resolver to overcome the quantization error caused by the small counting time. The minimum spacecraft altitude of 11 km allowed resolution (minimum observable horizontal dimension of a well-distinguished feature) to approximately 10 km. This resolution is at least a factor of 10 better than the *Lunar Orbiter* data. The sample rate of 1-per-second provided 6 samples over 10 km of path length, giving some redundancy and smoothing capability.

The *Apollo 10* and *11* orbits were almost equatorial and essentially had the same lunar track, so that they provide a direct check on each other's acceleration patterns. The 20–25 min arc of 1-s tracking data was fit using a simple triaxial model for the lunar gravitational field.

There were three large anomalies (Fig. 54) in the resulting doppler residuals from *Apollo 10*. The first two were positive peaks at longitudes of 85°E and 78°E,
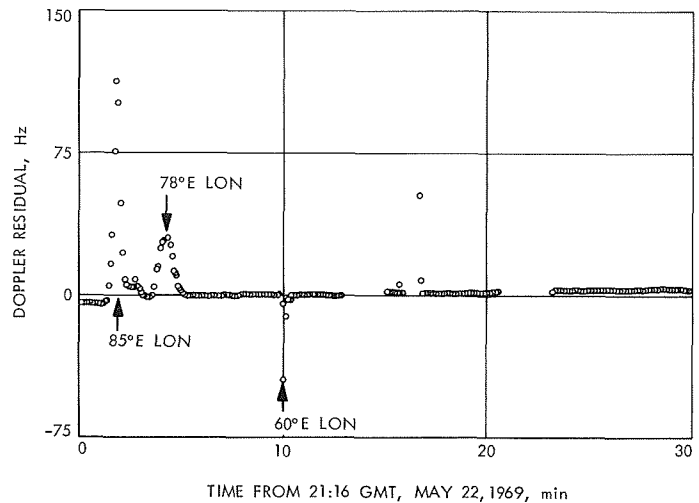

Fig. 54. *Apollo 10* LM descent residuals

respectively. The third was a negative peak at longitude 60°E. Examples of positive masses which could produce such positive peaks are hemispherical lumps of material of density 12 g/cm^3, 68 and 50 km deep, respectively. The negative peak is so sharp that it would have to be produced by a 10-km-diameter mass of 10 g/cm^3. These large residuals occurred shortly after initial acquisition of signal from exit occultation and during times of loss of voice communication. It is believed that antenna pointing problems caused the difficulty in signal lock-up.

The *Apollo 10* LM tracking data also shows three less spectacular features. One of the features is the sharp negative slope at 23.5 min (68°E lon) shown in Fig. 55. The extreme sharpness of this acceleration indicates a hole 25 km in diameter which would have to be more than 20 km deep to provide the required negative mass. However, when this same longitude is examined in *Apollo 11* data (Fig. 56), there is no indication of any negative slope in the residuals. Also visible here is the
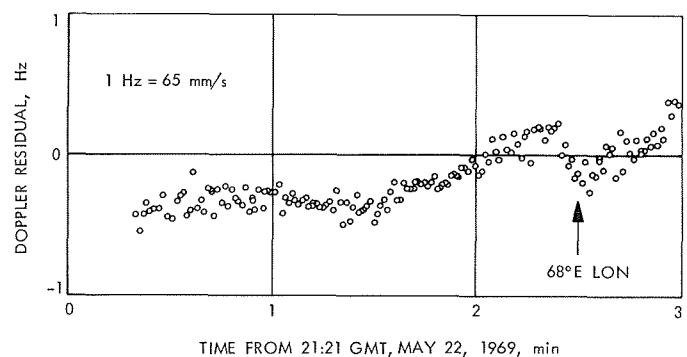

Fig. 55. Detail of *Apollo 10* LM descent residuals

1 Hz = 65 mm/s
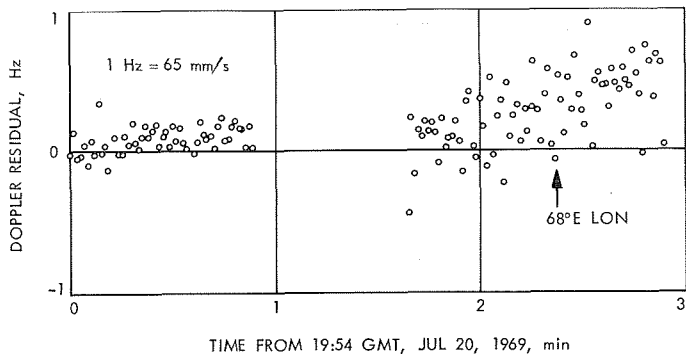
68°E LON

TIME FROM 19:54 GMT, JUL 20, 1969, min

Fig. 56. Detail of Apollo 11 LM descent residuals

fact that *Apollo 11* data was somewhat noisier than *Apollo 10*. This was the same situation with the other possible gravity anomalies, that each data block contradicted the other and no two anomalies are correlated.

If significant information from the low-altitude LM tracking data is to be obtained, both the receiver lock-up (spacecraft antenna pointing?) problem and spacecraft spurious motions from maneuvers and venting must be eliminated.

11. Use of Lunar Transponders to Obtain DSS Locations: Lunar Physical Libration Analysis,
F. B. Winn and G. Dvornychenko

Planetary and lunar spacecraft tracking data have been used to determine the absolute longitudes of Deep Space Stations (DSSs), as discussed by Mottinger in *Subsection 3* of this chapter. At present only two data spans are available which result in absolute longitude solutions of the desired accuracy, namely, the encounter phases of the *Mariner IV* (Mars, 1964) and *Mariner V* (Venus, 1967) missions. Additional solutions are needed and the tracking data from the *Surveyor* spacecraft, while they were resting on the lunar surface, represent an excellent source of accurate DSS location solutions, providing certain problems can be surmounted.

One of the corrupting influences associated with the lunar landed *Surveyor* tracking data, which prevents the determination of absolute DSS longitude, is the physical libration of the lunar figure.

In the first article of this series (SPS 37-56, Vol. II, pp. 74–80), Winn, employing the single-precision orbit determination program (SPODP) (Ref. 1), showed that the SPODP lunar physical libration model (Refs. 2 and 3) does not model the lunar landed *Surveyor I*, two-way doppler

tracking data. Furthermore, the replacement of Heyn's coefficients with Eckhardt's (Ref. 4) did not improve the performance of the libration algorithm.

This article, the second of this series on lunar physical librations, will show that:

(1) The omission of some of the libration terms from the SPODP libration model does induce detectable range-rate errors in the *Surveyor I* topocentric doppler calculations.

(2) All libration terms of this study should be incorporated into the double-precision orbit determination program (DPODP)[19] libration model (Ref. 4).

(3) The preponderance of the SPODP libration modeling error does not stem from libration series truncation errors.

The SPODP and DPODP physical libration models utilize only the three terms of largest amplitude for each physical libration series:

$$\sigma = [-109'' \sin(g) + 37'' \sin(g + 2\omega) - 11'' \sin(2g + 2\omega)]/I$$

(1)

$$\rho = -107'' \cos(g) + 37'' \cos(g + 2\omega) - 11'' \cos(2g + 2\omega)$$

(2)

$$\tau = -12'' \sin(g) + 59'' \sin(g') + 18'' \sin(2\omega) \qquad (3)$$

where

σ = total physical libration in the longitude of the mean ascending node of the lunar orbit on the ecliptic

ρ = total physical libration of the mean inclination of the lunar equator relative to the ecliptic

τ = total physical libration in the mean lunar longitude measured along the ecliptic

$g = \mathbb{C} - \Gamma'$ = mean anomaly of the moon

$g' = \odot - \Gamma$ = mean anomaly of the sun

$\omega = \Gamma - \Omega$ = argument of perigee of the moon

I = inclination of lunar equator relative to the ecliptic

---

[19]Warner, M., *Double Precision Orbit Determination Program*, June 15, 1967 (JPL internal document).

The truncation error associated with the σ, ρ, and τ series due to the omission of eight smaller amplitude terms are formulated in Eqs. (4), (5), and (6) (Ref. 5):

$$\Delta\sigma = [-3''2 \sin(2g' + 2\omega') -2''5 \\ \sin(g - 2g' + 2\omega - 2\omega')]/I \qquad (4)$$

$$\Delta\rho = -3''2 \cos(2g' + 2\omega') -1''9 \\ \cos(g - 2g' + 2\omega - 2\omega') \qquad (5)$$

$$\Delta\tau = -10'' \sin(-2g' + 2\omega - 2\omega') \\ -4''2 \sin(g - 2g' + 2\omega - 2\omega') \\ + 3''5 \sin(\omega - g' - \omega') \\ + 1''7 \sin(2g' + 2\omega') \qquad (6)$$

where

$$\omega' = \odot\text{-}g' = \text{argument of perigee of the sun}$$

To ascertain unambiguously the contributions of each physical libration term (Eqs. 1 through 6), the spatial displacements and speeds and topocentric radial velocities of Surveyor I[20] due to each individual libration were determined.

The spatial displacement of Surveyor I due to the libration algorithm defined by Eqs. (1) through (6) was computed in the following manner:

$$\left| \sum_{i=1,17} \Delta r_i \right| = \left| \sum_{i=1,17} \Delta L_i \left[\frac{\partial [M]^T}{\partial L_i} \right] R \right| \qquad (7)$$

where

$|\Delta r_i|$ = spatial displacement of Surveyor I in selenocentric, earth-equatorial, coordinates due to the ith libration term

R = selenocentric, moon-fixed, coordinates of Surveyor I

ΔL_i = numerical value of the ith libration coefficient as reported by Eckhardt (Ref. 4)

$\dfrac{\partial [M]^T}{\partial L_i}$ = partial derivative of the selenocentric, moon-fixed, to selenocentric, earth-equatorial, coordinate transformation matrix with respect to the ith libration coefficient

[20]Surveyor I, because of its displacement in longitude from the center of the earth-viewable lunar disk, is more sensitive to the libration than any other Surveyor (that is, the line-of-sight projection of the total libration is the largest), and hence was used for this study.

$[M]^T$ = moon-centered, moon-fixed, to moon-centered, earth-equatorial, transformation matrix defined as

$$[M]^T = [R_{+x}(\bar{\epsilon})]^T [R_{+z'}(\bar{\Omega} + \sigma)]^T \\ [R_{-x}(\bar{I} + \rho)]^T [R_{+z}(\bar{\mathbb{C}} + \tau - \bar{\Omega} - \sigma + \pi)]^T \qquad (8)$$

$[R_{+x}(\bar{\epsilon})]^T$ = rotation about the earth-equatorial X axis through angle equal to the mean obliquity of the ecliptic

$[R_{+z'}(\bar{\Omega} + \sigma)]^T$ = rotation around the resulting Z' axis through an angle equal to the longitude of the true ascending node of the lunar orbit referenced to the mean ecliptic

$[R_{-x}(\bar{I} + \rho)]^T$ = rotation around the X' axis through an angle equal to the true inclination of the lunar equator with respect to the ecliptic (negative rotation)

$[R_{+z}(\bar{\mathbb{C}} + \tau - \bar{\Omega} - \sigma + \pi)]^T$ = rotation around the resulting Z'' axis through an angle equal to the true longitude of the moon minus the longitude of the true ascending node plus π radians

Similarly, the spatial displacement of Surveyor I, from a nonlibrated inertial position, due to the libration algorithm defined by Eqs. (1) through (3), was computed.

Figure 57 depicts the Surveyor I spatial displacement, from a nonlibrated inertial position, associated with both libration functions. The plots show that the two libration functions do significantly differ in their influences on the Surveyor I inertial position (at times, the separation is greater than 35 m).

Using a technique similar to Eq. (7), it is also simple to compute the spatial speed resulting from the two sets of libration series components:

$$\left| \sum_{i=1,17} \Delta \dot{r}_i \right| = \left| \sum_{i=1,17} \Delta L_i \left[\frac{\partial [\dot{M}]^T}{\partial L_i} \right] R \right| \qquad (9)$$
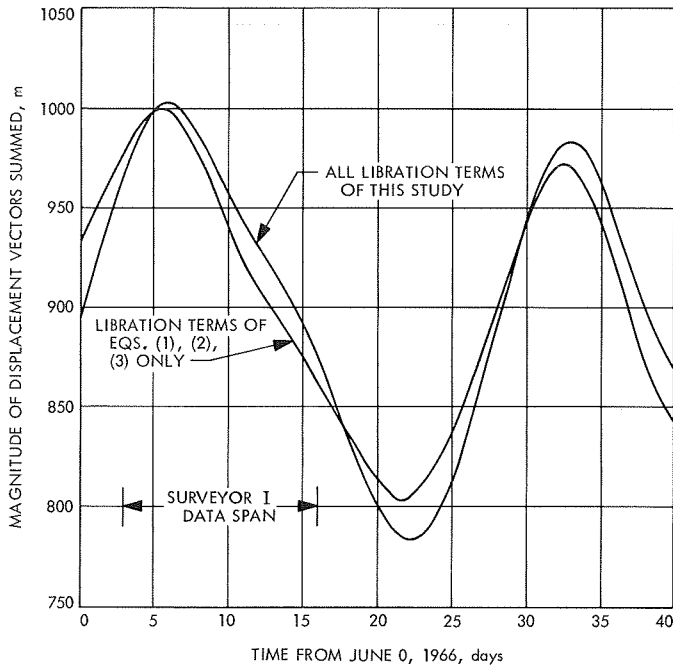
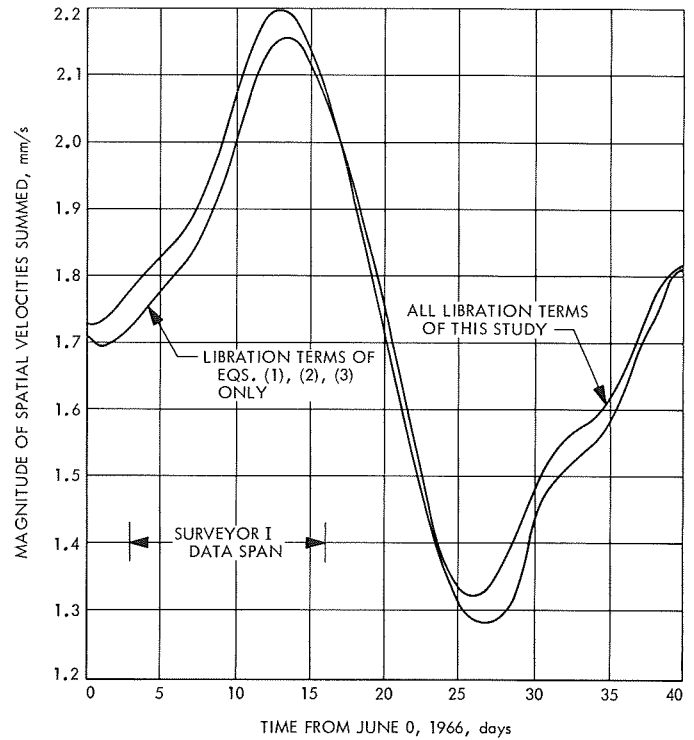**Fig. 57.** *Surveyor I* spatial displacement: total libration functions

Fig. 58. *Surveyor I* spatial velocity: total libration functions

where

$| \Delta \dot{\underline{r}}_i | = $ spatial speed of *Surveyor I* in selenocentric, earth-equatorial, coordinates due to the ith libration term

$\dfrac{\partial [\dot{M}]^T}{\partial L_i} = $ partial of the time rate of change of the selenocentric, moon-fixed, to selenocentric, space-fixed, coordinate transformation matrix with respect to the ith libration term

The magnitudes of $\Delta \dot{\underline{r}}_i$ are plotted in Fig. 58. The plotted spatial speeds of *Surveyor I* due to the libration functions reveal the upper limits of the libration series truncation influences upon the topocentric range-rate observations, for the induced spatial speeds are the induced range-rate upper limits.

Figure 58 shows a maximum spatial speed error of 0.56 mm/s (that is, a 5.6-m differenced range error per 10^4 s). This significantly exceeds the accuracy constraint placed upon the DPODP which is the ability to compute doppler integrated over 10^4 to an accuracy of better than 0.1 m.

A more detailed investigation of the libration series component terms is permitted in Figs. 59, 60, and 61. These figures depict the spatial speed of the *Surveyor I*

lunar site during a 40-day period due to each libration term independently.

The maximum differenced range error will be realized when the total spatial velocity is aligned with the observer-probe direction. Thus, by taking the maximum spatial velocities associated with each libration term as plotted in Figs. 59, 60, and 61, and assuming the velocities to be non-variant over 10^4 s, it is a simple operation to ascertain the maximum differenced range error that can result for a *Surveyor I* doppler observation due to individual libration term omissions. Table 30 tabulates the maximized differenced range error associated with each libration component of this study. The sum of the maximum differenced range errors which could result from truncated libration terms is 5.6 m/10^4 s.

Finally, the lunar physical libration model's modification of the *Surveyor I* topocentric radial velocity is examined. The projection of the spatial speed induced by the physical libration algorithm along an observer's line of sight is accomplished:

$$\sum_{i=1,\,17} \Delta \dot{\rho}_i = \sum_{i=1,\,17} \left[\Delta L_i \frac{\partial [\dot{M}]^T}{\partial L_i} \underline{R} \right] \cdot \underline{\rho} \qquad (10)$$
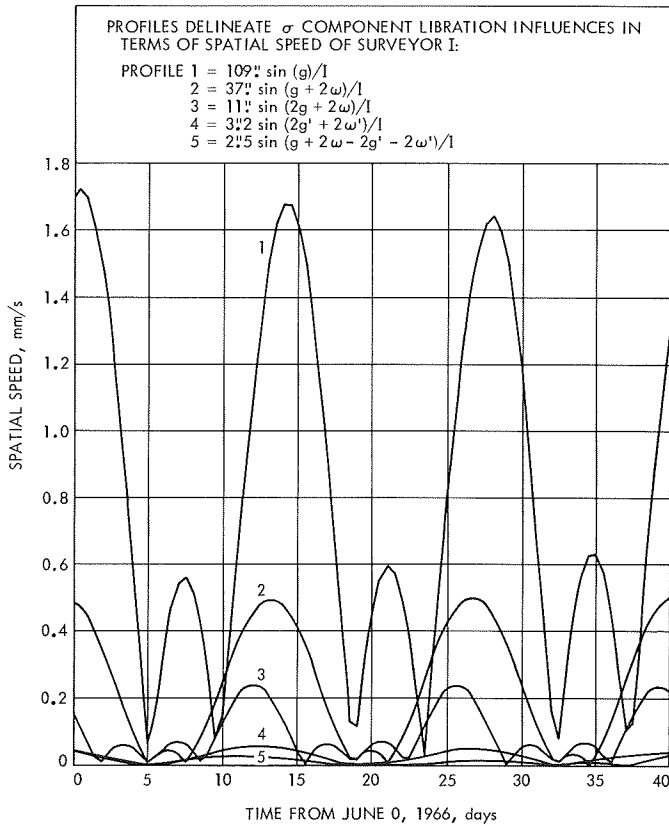
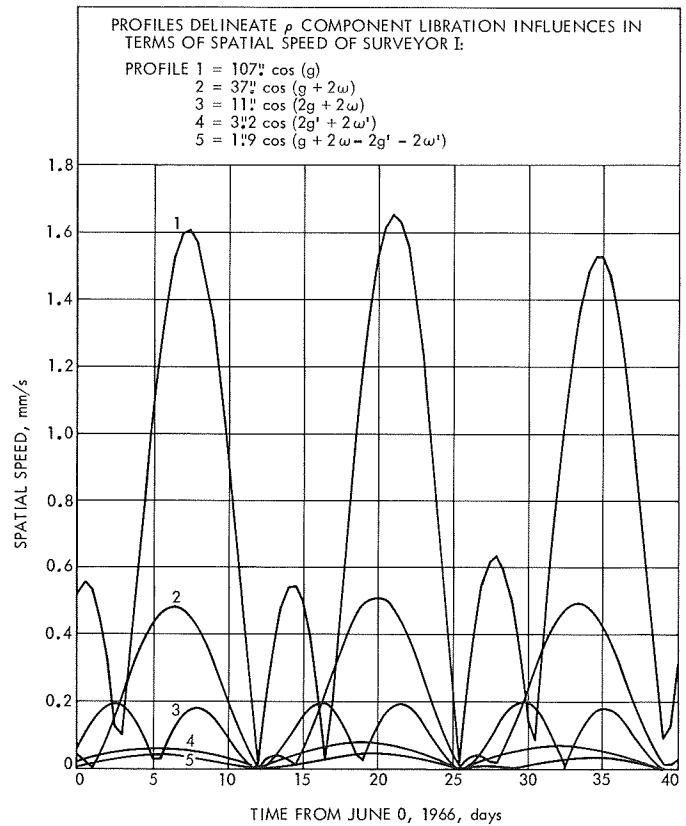Fig. 59. Spatial speed: σ libration series

Fig. 60. Spatial speed: ρ libration series

where

$\Delta \dot{\rho}_i$ = topocentric radial velocity of *Surveyor I* due to the *i*th component of the libration model

$\underline{\rho}$ = topocentric range vector of *Surveyor I* as viewed at Canberra

The accumulative error which can result due to libration series truncation is shown in Fig. 62. The figure also presents a comparison between the truncated and the complete libration model of this study as they influence the *Surveyor I*–Canberra range rate.

The maximum difference between the two range-rate profiles is only 0.11 mm/s (1.1 m/10⁴ s) or approximately 20% of the truncated libration models minimum value during the *Surveyor I* period.

As previously reported (SPS 37-56, Vol. II), the *Surveyor I* data was fit "best" when no libration modeling was attempted. Thus, it is apparent that the 20% range-rate error due to series truncation is not the primary cause of the algorithm's failure.
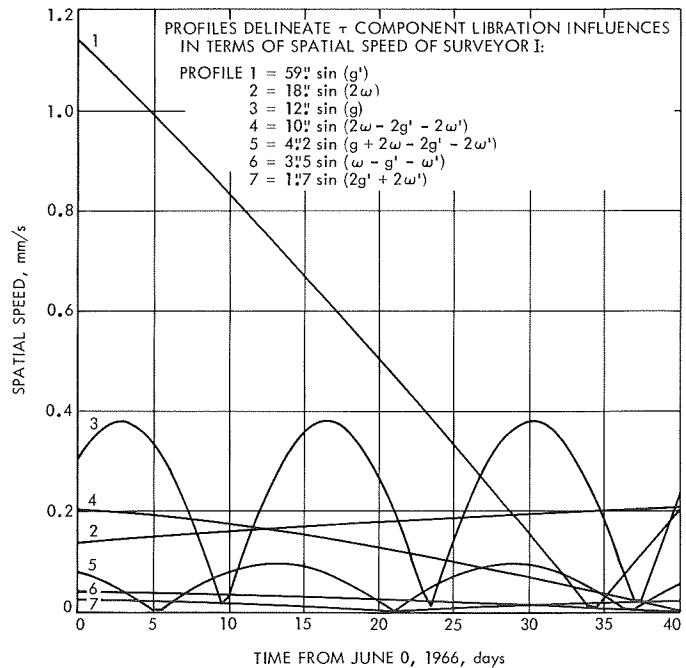

Fig. 61. Spatial speed: τ libration series

Table 30. Libration terms

Libration term argument	Period, days	Libration term amplitude, arc sec			$\left| \sum \underline{\Delta i} \right| \times 10^4$ s, meters			SPODP and DPODP retained
		σ^a	ρ^a	τ^a	σ	ρ	τ	
$2g + 2\omega$	14	11.0	11.0	—	2.3	2.0	—	✔
$g + 2\omega$	28	37.0	37.0	—	4.9	4.8	—	✔
g	28	109.0	107.0	12.0	17.0	16.0	3.7	✔
$g + 2\omega - 2g' - 2\omega'$	32	2.5	1.9	4.2	0.2	0.4	1.0	
$2g' + 2\omega'$	174	3.2	3.2	1.7	0.5	0.6	0.3	
$2\omega - 2g' - 2\omega'$	206	—	—	10.0	—	—	2.1	
g'	365	—	—	59.0	—	—	20.5	✔
$\omega - g' - \omega'$	418	—	—	3.5	—	—	0.5	
2ω	1100	—	—	18.0	—	—	3.9	✔
^{a}Lunar central angle.								

At this time, there is no confirmed explanation for the libration model's apparent failure. As a matter of course, the theory and computer algorithm are being investigated in detail; however, there are other possible error sources which remain to be studied. Such error sources are: tropospheric refraction, ionospheric charged-particle effects, lunar ephemeris, data selection effects, etc.

TIME FROM JUNE 0, 1966, days

Fig. 62. Surveyor I range rate: total libration functions

All libration terms of this study (17) should be included into the DPODP to meet the DPODP accuracy constraint of 0.1 m/10⁴ s. Not only are these libration terms of sufficient size to warrant DPODP inclusion, but their summed influences introduced a 0.1-mm/s error in the *Surveyor I* range-rate calculations (20% of the total libration algorithm influence). The preponderance of the SPODP libration model failure is not due to libration series truncation errors.

References

1. Warner, M. R., and Nead, M. W., *SPODP—Single Precision Orbit Determination Program*, Technical Memorandum 33-204. Jet Propulsion Laboratory, Pasadena, Calif., Feb. 15, 1965.
2. White, R. J., et al., *SPACE—Single Precision Cowell Trajectory Program*, Technical Memorandum 33-198. Jet Propulsion Laboratory, Pasadena, Calif., Jan. 15, 1965.
3. Hoffman, H. M., and Davies, J. R., *Landed Surveyor Modification for the Orbit Determination Program*, Design Document. Computer Applications, Inc., Glendale, Calif., Oct. 13, 1966.
4. *Measure of the Moon*. Edited by Z. Kopal and C. L. Goudas. D. Reidel Publishing Co., Dordrecht, Holland, 1967.
5. Melbourne, W. G., et al., *Constants and Related Information for Astrodynamic Calculations, 1968*, Technical Report 32-1306. Jet Propulsion Laboratory, Pasadena, Calif., July 15, 1968.

12. The Doppler Determination Accuracy of the Earth Gravitational Constant From Artificial Satellites as a Function of Orbital Elements,
G. E. Pease

a. Introduction. To date, it has been recognized that one of the most accurate values for $GM_\oplus$, the earth gravi-
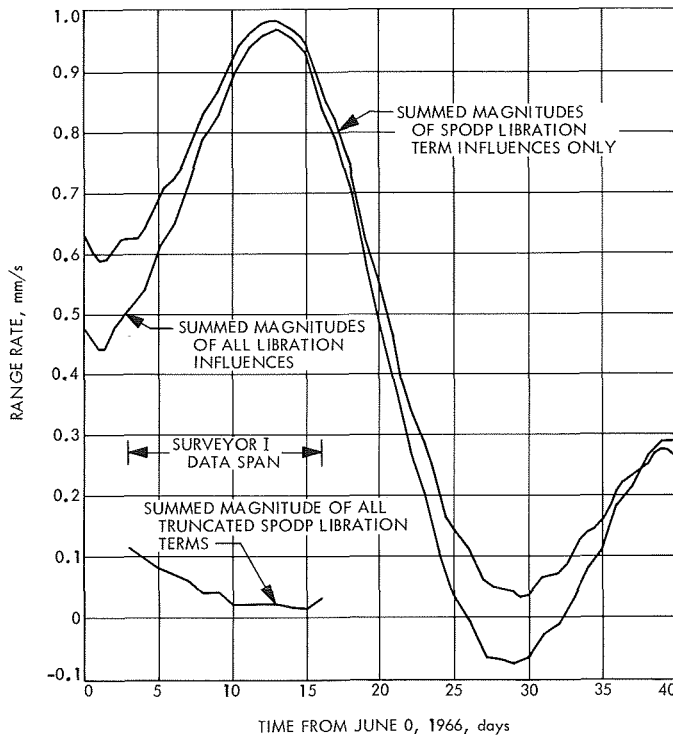
tational constant, has been obtained by combining the result of the *Ranger* lunar missions (Ref. 1). This has been widely used to represent the zero-order term of the earth's potential in geodetic satellite solutions for the harmonic coefficients of the potential expansion. Gravitational constant solutions competitive with the combined *Ranger* value may now exist based on the early phase of the *Mariner* planetary missions (Ref. 2) and the radio tracking of artificial satellites (SPS 37-53, Vol. II, pp. 16–20, and SPS 37-56, Vol. II, pp. 80–85). In the case of a satellite solution, it is of interest to discover which orbital characteristics are most favorable to a rapid solution for $GM_\oplus$.

This article examines the doppler solution for $GM_\oplus$ as the conic elements of the satellite orbit are varied. Two classes of effects are involved here: (1) gravitational effects, primarily involving the distance of the satellite from earth (these are predominant in varying a and e); and (2) tracking geometry effects, primarily involving the length of time the satellite is tracked by each tracking station (predominant orbital elements here are i and Ω). In this study we examine the effects of varying the orbital elements a, e, i, and Ω. Early tracking results from varying a and e in many respects reproduce the effects of varying ω, the argument of perigee, which was, therefore, not studied separately. The geometrical effect of varying the mean anomaly t_0 is slight with good tracking station coverage, and was also not considered of sufficient interest for inclusion. Here again, the gravitational effects of varying t_0 are identical to those in varying a and e for short initial tracking spans.

As with other data reduction tasks, there are inherent limitations on the ability to extract information, including $GM_\oplus$, from the analysis of radio tracking data. These limitations include the degree to which both the noise on the observations and the physical system are properly represented in the regression model.

The noise on each data point was assumed independent of that on any other tracking data point, while in reality correlations do exist (this assumption greatly simplifies the analysis). However, the data weights are increased as a function of known correlated error on the tracking data to compensate for this assumption.

The fitter's model of the universe (physical system) may differ from the real universe either because of a simplified dynamical model (a conic spacecraft orbit is assumed, i.e., all gravitational forces are ignored except that due to $GM_\oplus$) or because random disturbances to the
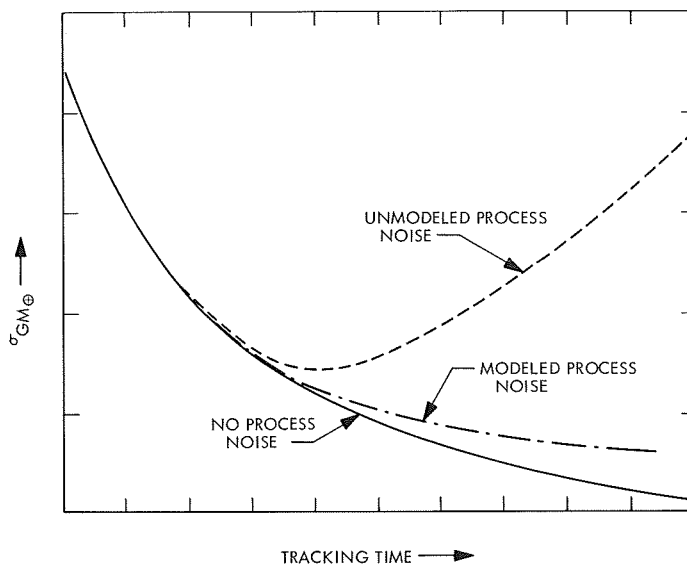

Fig. 63. Illustration of role of process noise in obtaining $GM_\oplus$ solutions

spacecraft motion are not properly taken into account. This latter category is known as process noise and includes such items as attitude-control forces (i.e., valves seating differently after each use thus causing a variable leak rate) and fluctuations in drag or solar radiation forces. Some model errors can be treated as correlated noise on the tracking data and thus contribute to the data weight used for this study.

For the case of process noise, previous investigators have shown[21] effects analogous to those illustrated in Fig. 63, when cases containing unmodeled, modeled, and no process noise are compared. Notice that if process noise exists and is ignored (either not practical to model or not known well enough), the $GM_\oplus$ solution can actually be degraded by the addition of more tracking data. Also, if the process noise is properly modeled, the accuracy of the $GM_\oplus$ solution approaches a lower bound asymptotically as more data is added, thereby putting a practical limit on the length of data arc which need be processed.

Uncorrelated data noise, a conic spacecraft orbit, and the absence of process noise were assumed for this study. Although such a technique can reveal the relative quality of $GM_\oplus$ solutions obtainable as a function of the elements of an earth-orbiting spacecraft, care must be used in determining the region of validity. That is, while the

[21]Nishimura, T., *Evaluation of the Error Caused by Application of Non-optimal Estimators to the Orbit Determination of Low-Thrusted Spacecraft*, Apr. 21, 1966 (JPL internal document).

weight assigned the tracking data was adjusted to compensate for the first two assumptions, the fact that process noise is ignored causes the comparisons of the ability to determine $GM_\oplus$ among various orbital geometries presented in this article to lose their validity as the tracking data span increases. The analysis of process noise and its effects on the ability to determine $GM_\oplus$ from radio tracking of earth orbiters will constitute the next phase of this study.

b. Tracking model. As in Refs. 1 and 2, simulated range-rate tracking data were utilized, with a 1-σ weight of 2.23 mm/s per 300-s data sample except for the runs with small a ($a = 800$ km), where an equivalent 1-σ weight of 5 mm/s was used per 60-s sample. These data weights are roughly an order of magnitude higher than correlated data noise of observed S-band high-frequency data in order that unmodeled error sources such as the non-spherical earth gravitational potential can be represented. Three tracking stations were simulated 120° from each other in longitude and latitudes of 0°, +45°, and −45° (in order of increasing east longitude). The mean anomaly and argument of perigee were selected to place the satellite at perigee and on the meridian of the 0° latitude tracking station at the start of simulated tracking. Simulated tracking data were not taken below 10-deg satellite elevation angle.

c. Statistical model. The statistical computations were performed by the JPL Multiple-Link Satellite Program (MLSP) described in the following article, *Subsection 13.* This computer program utilizes elliptical orbital elements to define the satellite state vector, which makes it extremely fast and efficient for statistical computations. A simple two-body representation such as this does, however, ignore effects such as lunisolar and planetary perturbations, solar radiation pressure, atmospheric drag, and non-spherical gravitational potential of the central body. Although MLSP may be used for analyzing simultaneous tracking of more than one satellite, only one satellite at a time was simulated in this study. The program was used to compute a covariance matrix

$$\Gamma = \left(\sum_{i=1}^{N} \phi_i \, w_i^{-1} \, \phi_i^T + \widetilde{\Gamma}^{-1} \right)^{-1}$$

where, for the ith observation, ϕ_i is the vector of partial derivatives of range rate with respect to the parameters for which we desire statistics, w_i the variance of the data point, and $\widetilde{\Gamma}$ a diagonal *a priori* covariance matrix.

The topocentric range vector of the satellite at each data point is computed as

$$\rho = \mathbf{R}_G - \mathbf{R}_{GS}$$

where $\mathbf{R}_G$ is the geocentric range vector of the satellite and $\mathbf{R}_{GS}$ is the geocentric station vector, and

$$\mathbf{R}_G = f(a, e, i, \Omega, \omega, GM_\oplus, t_0, t) = f(Q_G, t)$$

$$\mathbf{R}_{GS} = f(\lambda, \phi, R_{GS}, t) = f(Q_{GS}, t)$$

In this formulation, t is the independent time argument and λ, ϕ, R_{GS} are the respective station coordinates of longitude, latitude, and geocentric radius. The range rate is computed as

$$\dot{\rho} = \frac{\dot{\rho} \cdot \rho}{\rho}$$

and the partial derivatives are

$$\frac{\partial \dot{\rho}}{\partial Q} = \frac{\dfrac{\partial \dot{\rho}}{\partial Q} \cdot \rho + \dot{\rho} \cdot \dfrac{\partial \rho}{\partial Q} - \dfrac{\partial \rho}{\partial Q} \cdot \dfrac{\dot{\rho}}{\rho}}{\rho}$$

For this study, the full set of $Q = Q_G$, Q_{GS} was represented in the covariance matrices from which standard deviations of $GM_\oplus$ were obtained.

d. Parametric analysis. No *a priori* information was input except on tracking station coordinates. These were assumed known to 20 m in λ and ϕ and 10 m in R_{GS}.[22] In each of the runs, a covariance matrix is computed every 3 h from the start of tracking up to 36 h. A standard orbit was adopted and a, e, i, Ω were varied one at a time, holding the others fixed at the standard values. The standard elements and the variations on them are listed in Table 31.

It may be seen that a very wide range of satellite orbits is represented in the table. Figure 64 shows $GM_\oplus$ accuracy as a function of tracking time for the standard orbit. The tracking stations which are in view (satellite above 10-deg elevation angle) are identified on the horizontal bar by their latitude.

---

[22]Although tracking stations with a capability comparable to a DSS were assumed, it was not assumed that their locations are known to 3 m in λ and 1.5 m in r_s as is the case for the DSS.

Table 31. Standard and varied orbital elements

Element	Standard value	Varied values
a, km	24000	8000, 16000, 32000, 40000
e	0.1	0.3, 0.5, 0.7
i, deg	45	5, 25, 65, 85
Ω (measured from t_0), deg	0	90, 180, 270
ω, deg	0	Not varied
t_0	(see *Tracking model*, Paragraph b)	Not varied

This plot indicates that doppler tracking of a satellite in the standard orbit is not sufficient to determine $GM_\oplus$ to the combined *Ranger* accuracy, at least for only 36 h of tracking data. This conclusion was also reached for somewhat lower orbits in SPS 37-53, Vol. II. In that study the addition of ranging data was found to significantly lower $\sigma_{GM_\oplus}$.

Figure 65 shows the behavior of the standard orbit solution as the semimajor axis of the orbit is varied. Each curve represents a different amount of tracking time. The plateau between $a = 24{,}000$ km and $a = 32{,}000$ km for the 6-h tracking interval plot is caused by the existence of more tracking station view overlap for the higher satellite. This is because the first station tracking the

lower satellite is lost from view more quickly due to the greater angular velocity of this satellite. The lower-altitude orbits show an astonishingly rapid and accurate ability to estimate $GM_\oplus$. In reality, these orbits would be somewhat corrupted by atmospheric drag and high-order earth gravitational potential effects. Because of this, the plotted numbers at $a = 8000$ km should not be taken too literally. An effect that was noticed in SPS 37-56, Vol. II, is also present. This is the tendency for the higher-altitude orbits to become comparatively more suitable for determining $GM_\oplus$ with long tracking times. This is seen in the flattening of the curves towards the horizontal at longer tracking times. On the other hand, absolute accuracies at the higher altitudes are in substantial disagreement with the results of SPS 37-56, Vol. II, which utilized a much more sophisticated mathematical model, including a numerical integration of the satellite orbits which represented perturbations of the sun, moon and planets. Nevertheless, the results of this study, using a simple conic model, appear to be a great deal more realistic. This may be due to a number of factors, such as the different tracking station geometry or the 10-deg elevation limit on data in this study (in SPS 37-56, Vol. II, data were taken from horizon to horizon, but low-elevation data were weighted in a way that accounted for uncertainties in the refraction model). The possibility also exists that the complex motion resulting from lunisolar and planetary perturbations on high-altitude satellites enhances the orbit determination process, as reflected in the results
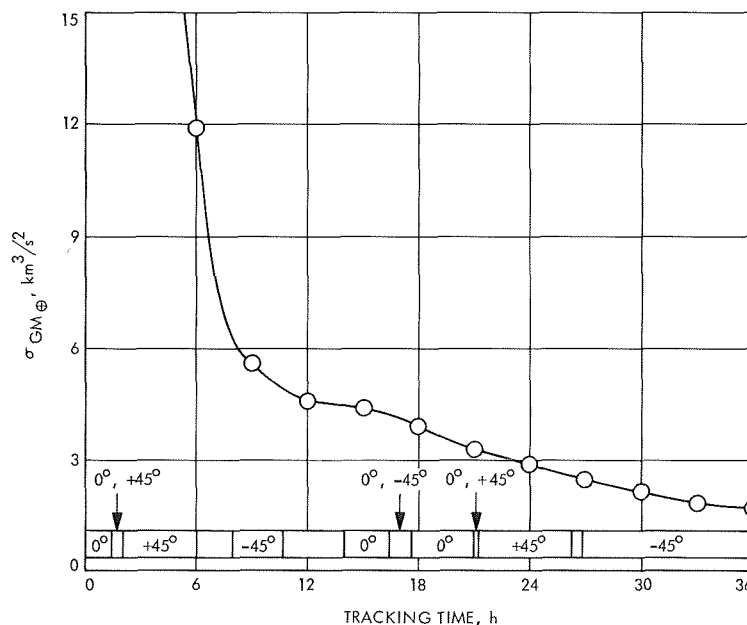

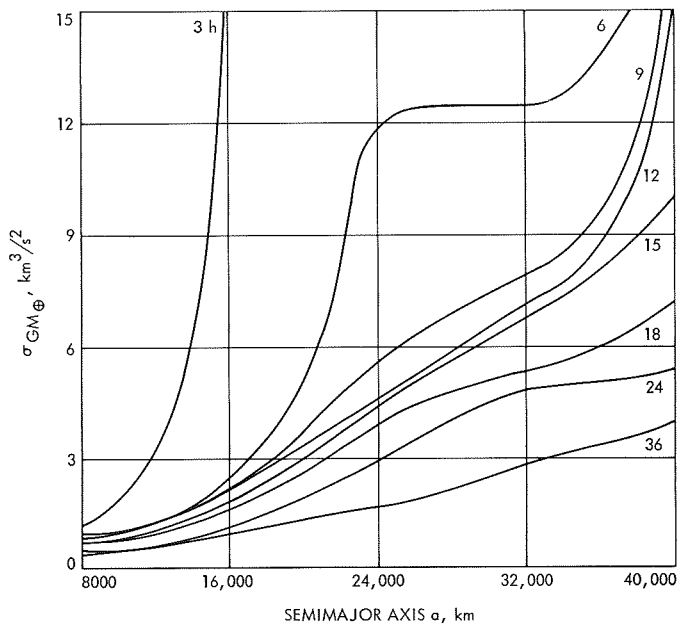**Fig. 64. $GM_\oplus$ standard deviation as a function of tracking time**

Fig. 65. $GM_\oplus$ standard deviation as a function of orbital semimajor axis for various tracking intervals

Fig. 66. $GM_\oplus$ standard deviation as a function of orbital eccentricity for various tracking intervals

of SPS 37-56, Vol. II. At any rate, it seems clear that high-altitude orbits require substantially longer tracking times and/or the addition of ranging data to equal the results from low orbits.

Figure 66 illustrates the improvement available to the 24,000-km standard orbit at higher orbital eccentricities. At an eccentricity of 0.5, the $GM_\oplus$ accuracy is dramatic. This is because tracking has been set up to start at perigee, so that the first data points are similar to those in a lower orbit. Apparently the increased radial velocity of the high-eccentricity satellites is an important factor, since these orbits yield an even lower 36-h value for $\sigma_{GM_\oplus}$ than a near-circular low-orbit satellite ($\sigma_{GM_\oplus} = 0.1$ km³/s² compared with 0.4 km³/s² for the 8000-km low-eccentricity orbit). Such a high-eccentricity, high-altitude satellite is therefore more than competitive with *Ranger* or *Mariner* for determining $GM_\oplus$, provided that earth gravitational harmonics can be well-modeled near perigee. Figure 66 indicates that for short tracking times the determination of $GM_\oplus$ becomes worse above an eccentricity of 0.5. This is because at perigee the angular velocity of these satellites is so high as to cause large gaps between acquisition by the various tracking stations. The longer tracking interval or the addition of extra tracking stations will remedy this situation.

Figure 67 illustrates the effect of altering tracking geometry by varying the orbital inclination of the stan-
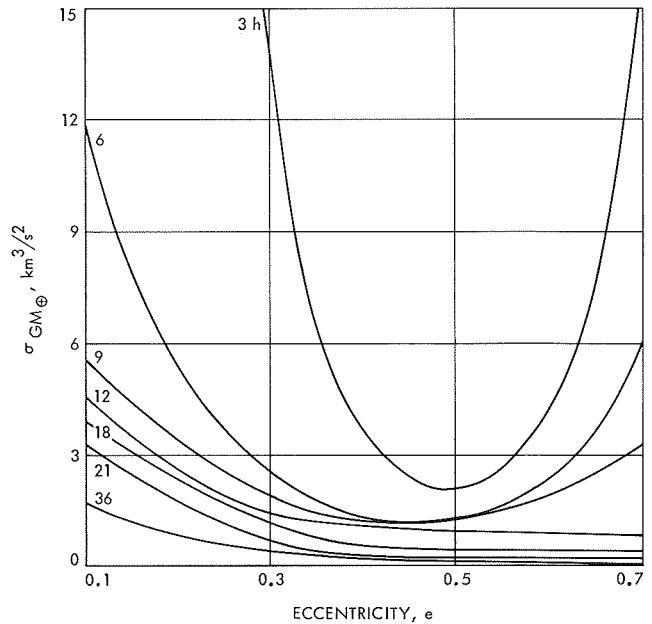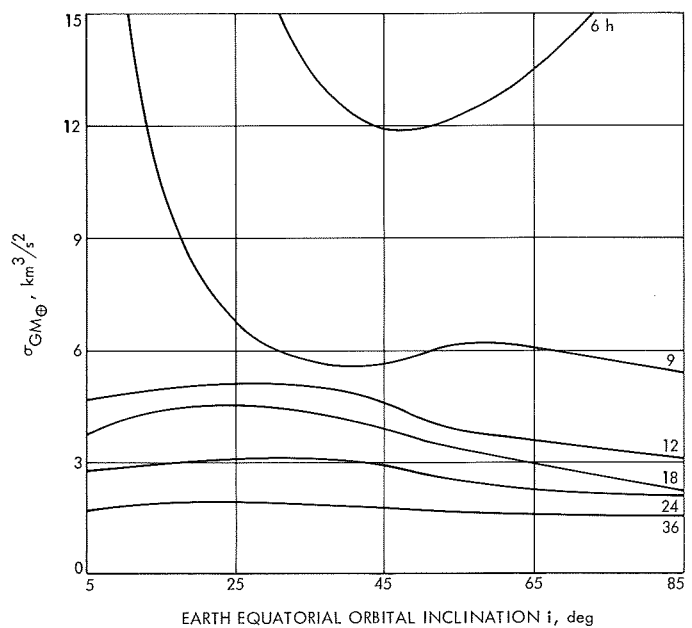

Fig. 67. $GM_\oplus$ standard deviation as a function of orbital inclination for various tracking intervals

dard satellite with respect to the earth equatorial plane. It appears that at high inclinations some advantage is taken of earth rotation rate in determining $GM_\oplus$. Since this is a geometrical effect, it does not have very much significance for long tracking intervals.

The effect of varying the longitude of the ascending node of the standard orbit is shown in Fig. 68. For this particular tracking station configuration, the primary effect is a degradation in the early determination of $GM_\oplus$ in the vicinity of $\Omega = 250°$. As the plot shows, this geometrical effect can be quite important for the first 9 h of tracking. Presumably, however, in actually attempting to determine $GM_\oplus$ from satellite tracking, one would be free to choose a data block containing favorable tracking geometry. This may be an important advantage of an orbiter as opposed to a lunar or planetary probe.

e. Conclusions. The primary desirable orbital characteristic for accurately determining $GM_\oplus$ from the doppler tracking of a satellite appears to be a low perigee altitude. In this class, satellites having a large semimajor axis and high eccentricity seem to be more suitable than those with a small semimajor axis and low eccentricity. The closeness of perigee is limited, of course, by the height of the atmosphere. Since it is not possible to accurately model atmospheric drag, perigee must be substantially above the atmosphere if the satellite is to be used for determining $GM_\oplus$. In such a determination, a very careful modeling of earth gravitational harmonics is also necessary. In addition, the data span must be limited to prevent the solution from being corrupted by process noise resulting from solar radiation pressure uncertainty and attitude-control accelerations. This is why this study

was restricted to data spans of 36 h or less. If these conditions are fulfilled, it appears that $GM_\oplus$ standard deviations of the order of 0.2 km³/s² are obtainable from doppler tracking of earth satellites, which is comparable to the accuracy obtainable from the *Ranger* lunar missions or the *Mariner* planetary missions.

References

1. Sjogren, W. L., et al., *Physical Constants as Determined from Radio Tracking of the Ranger Lunar Probes.* Technical Report 32-1057, p. 11. Jet Propulsion Laboratory, Pasadena, Calif., Dec. 30, 1966.

2. Pease, G., et al., *The Mariner V Flight Path and its Determination from Tracking Data,* Technical Report 32-1363, p. 7. Jet Propulsion Laboratory, Pasadena, Calif., July 1, 1969.

13. MLSP—The Multiple-Link Satellite Program,
D. W. Green

a. Introduction. In connection with recent JPL studies of a Tracking and Data Relay Satellite Network, a need became apparent for a computer program to study the statistics of satellite orbit determinations using data types involving several satellites. As the current JPL orbit determination programs generate data for only a single satellite at a time, a program was necessary either to combine the output of present JPL programs or to generate data for multiple satellites simultaneously. For
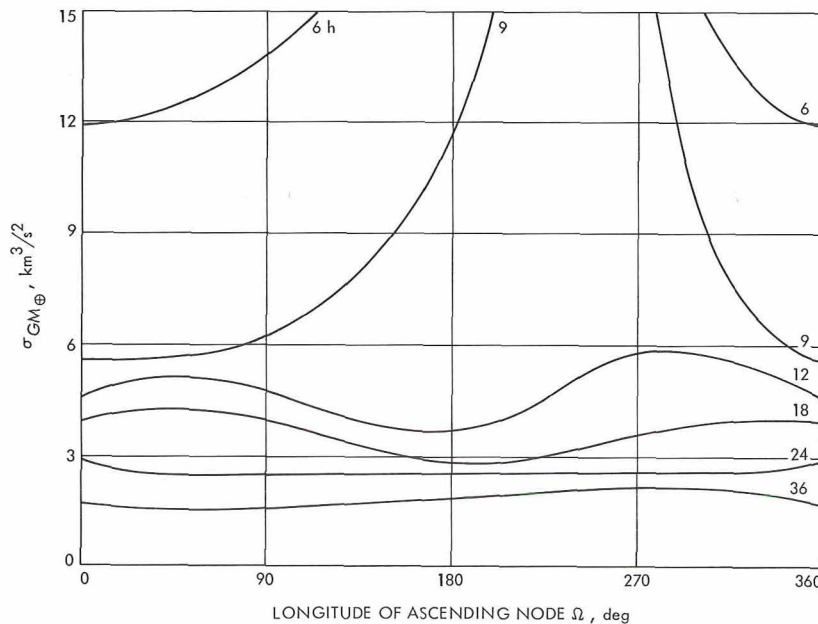

Fig. 68. $GM_\oplus$ standard deviation as a function of longitude of ascending orbital node for various tracking intervals

various reasons, the latter approach was chosen. The resulting program is called the Multiple-Link Satellite Program (MLSP).

The MLSP assumes that the orbit determination process will be done with radio ranging and/or doppler data. Unlike current orbit determination programs, however, the MLSP does not confine the signal path to direct ground station-to-satellite measurements but allows the signal to be relayed many times, including relays between satellites. In particular, the program accepts any sequence of ground stations and satellites as a path for a radio signal with two exceptions. Paths which contain two consecutive ground stations and paths for which a proper subset forms a closed loop are not allowed.

b. Satellite and ground station dynamic model. For reasons of economy both in programming and operating time, very simple dynamic models are used in the MLSP. The satellites move in strict two-body Keplerian orbits. The ground stations move on an earth which is rotating at an exactly uniform rate about a fixed axis. Specifically, the system takes no account of irregularities in the earth's geopotential, perturbations due to moon, sun, and other planets, irregularities in the earth's rotation and polar motion, solar pressure and spacecraft attitude-control effects, atmospheric drag, or atmospheric and ionospheric effects on signal propagation.

c. Mathematical formulation. The MLSP assumes that the satellite orbit determination process will be performed using a linearized, weighted, least-squares solution for the satellites' classical orbital elements. If an observable quantity O depends on a set of parameters q_i and time, we can write

$$O = F(q_1, q_2, \cdots, q_I, t)$$

and, if an initial guess q_{i0} is made, O can be expressed as a series expansion

$$O = F(q_{10}, q_{20}, \cdots, q_{I0}, t)$$
$$+ \sum_{i=1}^{I} \frac{\partial F(q_{10}, q_{20}, \cdots, q_{I0}, t)}{\partial q_i} (q_i - q_{i0})$$
$$+ \text{terms of order } (q_i - q_{i0})^2$$

Any real observation will be contaminated with measurement noise, and repeated observations will be required in order to solve for all of the required parameters and to

reduce the effects of the observational noise. If a set of observations are made at times t_j, we may write

$$\mathbf{y} = A\mathbf{x} + \boldsymbol{\varepsilon} \tag{1}$$

where

$\mathbf{y}$ = column vector of dimension J, the number of observations taken, and

$$y_j = O(t_j) - F(q_{10}, q_{20}, \cdots, q_{I0}, t_j)$$

that is, y is the actual observed value at each time minus the expected value of the quantity based on an initial guess for the parameters upon which it depends

A = matrix of the partial derivatives of the observable quantity evaluated at the nominal values of each parameter and at each observation time, i.e.,

$$a_{ij} = \frac{\partial F(q_{10}, q_{20}, \cdots, q_{I0}, t_j)}{\partial q_i}$$

$\mathbf{x}$ = column vector of differences between the nominal values of the parameters q_i and their true values

$\boldsymbol{\varepsilon}$ = vector of the noise on each measurement

Terms of order $\mathbf{x}^T \mathbf{x}$ have been ignored.

It will be stated here without proof that a minimum variance solution to such a system of equations is

$$\widehat{\mathbf{x}} = (A^T \Lambda_\varepsilon^{-1} A)^{-1} A^T \Lambda_\varepsilon^{-1} \mathbf{y} \tag{2}$$

where A and $\mathbf{y}$ are as defined above and Λ_ε is the covariance matrix of noise on observations.

The resulting covariance matrix on the solution is

$$\Lambda_x = (A^T \Lambda_\varepsilon A)^{-1} \tag{3}$$

If more than one observable is used in a solution and if an *a priori* covariance matrix Γ_0 exists for the solution,

$$\Lambda_x = \left(\Gamma_0^{-1} + \sum_{k=1}^{K} A_k^T \Lambda_{\varepsilon k}^{-1} A_k \right)^{-1} \tag{4}$$

where A_k and $\Lambda_{\varepsilon k}$ are the quantities A and Λ_ε defined in Eqs. (1) and (2) for the kth observable.

In particular, if the noise on each observable is uncorrelated in time,

$$A_k^T \Lambda_{\varepsilon k}^{-1} A_k = \frac{1}{\sigma_{\varepsilon k}^2} \sum_{j=1}^{J} a_{jk}^T a_{jk}$$

where

$\sigma_{\varepsilon k}^2 =$ variance of noise on each observation of the kth observable

$\mathbf{a}_{jk} =$ vector of partials of the kth data type at time t_j with respect to the parameters q_i

This allows the matrix Λ_x to be written

$$\Lambda_x = \left(\Gamma_0^{-1} + \sum_{j=1}^{J} \sum_{k=1}^{K} \frac{1}{\sigma_{\varepsilon k}^2} a_{jk}^T a_{jk} \right)^{-1} \tag{5}$$

and hence to be accumulated serially in time.

If the observables depend on parameters which are known imprecisely and it is desired to determine the effect of the uncertainty in those parameters (the so-called considered parameters), the covariance matrix of the solution is given by

$$\overline{\Lambda}_x = \Lambda_x + \Lambda_x M \Lambda_p M^T \Lambda_x^T \tag{6}$$

where

$$M = \sum_k A_k^T \Lambda_{\varepsilon k}^{-1} B_k$$

and

$B_k =$ matrix of partials of kth observable with respect to uncertain parameters

$\Lambda_p =$ covariance matrix of *a priori* uncertainties of uncertain parameters

$\overline{\Lambda}_x =$ total covariance matrix

The observables in the MLSP consist of range and range rate along a path connecting a series of ground stations and satellites. These observables are computed as

$$\rho_{123\cdots n-1\,n} = \rho_{12} + \rho_{23} + \cdots + \rho_{n-1\,n}$$

$$\dot{\rho}_{123\cdots n-1\,n} = \dot{\rho}_{12} + \dot{\rho}_{23} + \cdots + \dot{\rho}_{n-1\,n}$$

The partial derivatives are

$$\frac{\partial \rho_{123\cdots n-1\,n}}{\partial q} = \frac{\partial \rho_{12}}{\partial q} + \frac{\partial \rho_{23}}{\partial q} + \cdots + \frac{\partial \rho_{n-1\,n}}{\partial q}$$

$$\frac{\partial \dot{\rho}_{123\cdots n-1\,n}}{\partial q} = \frac{\partial \dot{\rho}_{12}}{\partial q} + \frac{\partial \dot{\rho}_{23}}{\partial q} + \cdots + \frac{\partial \dot{\rho}_{n-1\,n}}{\partial q}$$

i.e., range and/or range rate along a total path equals the sum of range and/or range rate between each sequential pair of vertices along that path.

For any sequential pair of points,

$$\rho_{12} = (\mathbf{R}_{12} \cdot \mathbf{R}_{12})^{1/2}$$

$$\dot{\rho}_{12} = (\dot{\mathbf{R}}_{12} \cdot \mathbf{R}_{12})/\rho_{12}$$

$$\frac{\partial \rho_{12}}{\partial q} = \left(\frac{\partial \mathbf{R}_{12}}{\partial q} \cdot \mathbf{R}_{12} \right)/\rho_{12}$$

$$\frac{\partial \dot{\rho}_{12}}{\partial q} = \left(\frac{\partial \dot{\mathbf{R}}_{12}}{\partial q} \cdot \mathbf{R}_{12} + \dot{\mathbf{R}}_{12} \cdot \frac{\partial \mathbf{R}_{12}}{\partial q} - \frac{\partial \rho_{12}}{\partial q} \cdot \rho_{12} \right)/\dot{\rho}_{12}$$

where

$$\mathbf{R}_{12} = \mathbf{x}_2 - \mathbf{x}_1$$

$$\dot{\mathbf{R}}_{12} = \dot{\mathbf{x}}_2 - \dot{\mathbf{x}}_1$$

$$\frac{\partial \mathbf{R}_{12}}{\partial q} = \frac{\partial \mathbf{x}_2}{\partial q} - \frac{\partial \mathbf{x}_1}{\partial q}$$

$$\frac{\partial \dot{\mathbf{R}}_{12}}{\partial q} = \frac{\partial \dot{\mathbf{x}}_2}{\partial q} - \frac{\partial \dot{\mathbf{x}}_1}{\partial q}$$

and

$\rho_{12} =$ range from point 1 to 2

$\dot{\rho}_{12} =$ range rate from point 1 to 2

$\mathbf{R}_{12} =$ vector from point 1 to 2

$\dot{\mathbf{R}}_{12} =$ time derivative of vector from point 1 to 2

$\mathbf{x}_2, \mathbf{x}_1 =$ cartesian coordinates of points 1 and 2, respectively

$q =$ parameter on which position 1 and/or 2 depends

For satellites, the parameters upon which position depends are:

a the semimajor axis

e the eccentricity

t_0 time of first perifocal passage

θ the longitude of the node

ϕ the argument of perigee

i the equatorial inclination

---

where M is the matrix

$$
\begin{pmatrix}
\cos\theta\cos\phi - \sin\theta\sin\phi\cos i \\
\sin\theta\cos\phi + \cos\theta\sin\phi\cos i \\
\sin i \sin\phi
\end{pmatrix}
$$

and $\mathbf{u}$ is the two-vector

$$
\mathbf{u} = \begin{pmatrix} u \\ v \end{pmatrix} = \begin{pmatrix} a\cos E - e \\ a(1 - e^2)^{1/2}\sin E \end{pmatrix}
$$

The quantity E is the solution to Kepler's equation

$$
(GM_e)^{1/2} a^{-3/2}(t - t_0) = E - e\sin E
$$

The matrix M is not time dependent so

$$
\dot{\mathbf{x}} = M\,\dot{\mathbf{u}}
$$

and

$$
\frac{\partial x}{\partial q} = \frac{\partial M}{\partial q}\,\mathbf{u}, \qquad q = \theta, \phi, i
$$

$$
\frac{\partial \mathbf{x}}{\partial q} = M\frac{\partial \mathbf{u}}{\partial q}, \qquad q = a, e, t_0, GM_e
$$

$$
\frac{\partial \dot{x}}{\partial q} = \frac{\partial M}{\partial q}\,\dot{\mathbf{u}}, \qquad q = \theta, \phi, i
$$

$$
\frac{\partial \dot{\mathbf{x}}}{\partial q} = M\frac{\partial \dot{\mathbf{u}}}{\partial q}, \qquad q = a, e, t_0, GM_e
$$

Finally, due to the introduction of the parameter E,

$$
\frac{\partial u}{\partial q} = \frac{\partial u}{\partial q} + \frac{\partial u}{\partial E}\cdot\frac{\partial E}{\partial q}
$$

$$
\frac{\partial \dot{u}}{\partial q} = \frac{\partial \dot{u}}{\partial q} + \frac{\partial \dot{u}}{\partial E}\cdot\frac{\partial E}{\partial q} + \frac{\partial \dot{u}}{\partial \dot{E}}\left(\frac{\partial \dot{E}}{\partial q} + \frac{\partial \dot{E}}{\partial E}\cdot\frac{\partial E}{\partial q}\right)
$$

$$
q = a, e, t_0, GM_e
$$

$$
\dot{E} = \frac{(GM_e)^{1/2} a^{-3/2}(t - t_0)}{1 - e\cos E}
$$

GM_e the gravitational mass constant of the earth

The position is given by

$$
\mathbf{x} = M\mathbf{u}
$$

$$
\begin{pmatrix}
-\cos\theta\sin\phi - \sin\theta\cos\phi\cos i \\
-\sin\theta\sin\phi + \cos\theta\cos\phi\cos i \\
\sin i \cos\phi
\end{pmatrix}
$$

For ground stations, the position depends on the parameters

R radius from center of earth
L latitude
λ longitude

Thus,

$$
\mathbf{x} = \begin{pmatrix}
R\cos L\cos(\omega t + \lambda) \\
R\cos L\sin(\omega t + \lambda) \\
R\sin L
\end{pmatrix}
$$

where ω is the rotation rate of earth.

A particular data type is occulted if the ray path between any pair of sequential points along the path intersects the surface of the earth. For satellite-to-ground station links, the occultation formula is

$$
A = (\mathbf{x}_s - \mathbf{x}_G)\cdot(\mathbf{x}_s - \mathbf{x}_G)
$$

$$
Q = \sin^2(E) - \frac{1}{4}\frac{A}{|\mathbf{x}_s|^2}\cdot\frac{A}{|\mathbf{x}_G|^2}
$$

where $\mathbf{x}_s$ is the satellite position, $\mathbf{x}_G$ the ground station position, and E the minimum elevation angle for station. Occultation occurs if $Q \leq 0$.

For satellite-to-satellite links

$$
Q = [\mathbf{x}_2\cdot(\mathbf{x}_2 - \mathbf{x}_1)]^2 - |\mathbf{x}_2 - \mathbf{x}_1|^2\cdot(|\mathbf{x}_2|^2 - R_e^2)
$$

where $\mathbf{x}_1$, $\mathbf{x}_2$ are satellite positions and R_e is the radius of the earth. Occultation occurs if $Q > 0$.

In addition to the covariance matrix of the classical Keplerian elements, the MLSP will produce a covariance

matrix on the instantaneous cartesian coordinate position at time x_j via the transformation

$$\Lambda_x = \frac{\partial x(t_j)^T}{\partial a} \Lambda_a \frac{\partial x(t_j)}{\partial a}$$

where a is the set of parameters a, e, t_0, θ, ϕ, i, GM_e.

d. Capacity and limitations. The current capacities and limitations of the MLSP include:

Parameter	Maximum number
Satellites	20
Ground stations	10
Links per data type	15
Data types	24
Solve-for parameters	24
Consider parameters	24

e. Applications. The MLSP has thus far been used for two applications, a study of the accuracy with which the gravitational mass constant of the earth can be determined (see previous article, *Subsection 12*, and a study of the accuracy with which a target satellite can be tracked via an orbiting tracking relay.[23]

14. Differenced-Range Doppler Versus Integrated Doppler, T. D. Moyer

a. Introduction. This study demonstrates the feasibility of computing doppler observables from differenced-range observables divided by the count time. The changes specified for the Univac 1108 version of the double-precision orbit determination program (DPODP) should produce "differenced-range" doppler (DRD) accurate to 10^{-5} m/s or better for all count times above 0.2 s. The primary analytical change is a more accurate expression for the relativistic transformation from coordinate time (ephemeris time, ET) to proper time (atomic time, A1). Specifically, the coefficient of one of the two existing terms has been changed and six new terms have been added (see Eq. 16). The increase in numerical precision from the 16-decimal digits of the IBM 7094 to the 18-decimal digits of the Univac 1108 is required; also, the precision of representation of time must be increased

from double- to triple-precision seconds past 1950.[24] It is also recommended that the current type 50 n-body ephemeris be replaced by the more accurate type 66 ephemeris or equivalent.

The doppler observables are currently computed by expanding the frequency shift in a Taylor series and averaging over the count time. The primary advantage of DRD is that there is no upper limit to the count interval, whereas with the current "integrated" doppler (ID) formulation, count times are limited to approximately 1000 s in heliocentric cruise due to truncation of the fourth and higher derivatives of the frequency shift in the Taylor series expansion. The partial derivatives of the DRD observables with respect to the estimated parameters $\mathbf{q}$ will be computed from differences of the partial derivatives of the two range observables (used to compute DRD) with respect to $\mathbf{q}$. The use of DRD will reduce running time since the formulation is simpler and because fewer observables will be computed (since larger count times will be used). Furthermore, the coding will be simplified and reduced in volume since the DRD formulation draws heavily upon the existing range observable formulation.

It is recommended that the DRD formulation be incorporated into the forthcoming Univac 1108 version of the DPODP as an alternate option to the existing ID formulation. This will allow a direct comparison of fits to real data with the two different formulations. If the DRD formulation proves itself, the ID formulation will be removed from the program.

Starting with the definitions of range and doppler observables, it is shown in *Paragraph b* that two-way doppler may be computed from differenced round-trip range observables divided by the count time. The DPODP runs, which produced range and doppler observables, and program DRDVID,[25] which used these observables to compute DRDVID residuals, are described in *Paragraph c*. Residuals were obtained for the *Mariner V* mission and for the first leg of a grand tour mission at 1, 2, 3, 4, and 5 AU and at encounter with Jupiter. The new expression for the ET$-$A1 time transformation is given in *Paragraph d*. In *Paragraph e*, the error sources affecting DRD and ID are discussed and are related to the DRD$-$ID residual versus count time plots.

[23]*Tracking and Data Relay Satellite Network (TDRSN) Final Study Report*, Chap. II, Section 4, Sept. 30, 1969 (JPL internal document).

[24]Alternately, time could be represented as one-single-precision word (8-decimal digits) for the Julian day number plus one double-precision word (18-decimal digits) for seconds past the beginning of the day.

[25]DRDVID = differenced-range doppler versus integrated doppler.

The range observables computed by the IBM 7094 version of the DPODP contain a random error of a few millimeters due to truncation of time (seconds past 1950) beyond 16-decimal digits.[26] The corresponding error in DRD is a maximum of 3×10^{-3} m divided by the count time. For DRD accurate to 10^{-5} m/s, the minimum allowable count time is 300 s. If the representation of time is changed from double precision to triple precision, the random error in the computed range observable is reduced to the smaller error due to truncation of position beyond double precision. On the forthcoming Univac 1108 version of the DPODP, which has a word length of 18-decimal digits, the position truncation error will be 10^{-6} m for range up to 7 AU. The corresponding error in DRD is 2×10^{-6} m divided by the count time, or 10^{-5} m/s or less for count times of 0.2 s or greater.

In the computation of the range observables used to compute DRD, the new terms of the ET−A1 time transformation are required to accurately transform round-trip ephemeris time from the light time solution to observed round-trip station time. The effect on the range observables is less than 2 m/AU. However, the corrections vary rapidly (with periods of 1 day or 1 mo) and the effect on the DRD observables of this study is as large as 3×10^{-4} m/s. The maximum effect of a periodic term of ET−A1 on DRD is the second time derivative of the term multiplied by the probe range. In the derivation of the new terms of ET−A1, all terms affecting DRD by more than 2×10^{-7} m/s per AU of distance to the spacecraft were retained. Several terms of this magnitude were neglected and the resulting error in DRD has a maximum value of about 10^{-6} m/s/AU or 10^{-5} m/s for a range of 10 AU. No correction is required to the ID observable formulation since it contains the exact differential equation relating proper time to coordinate time.

The pre-computed n-body ephemeris tapes used by the DPODP are of the so-called type 50 format. They contain modified second and fourth central differences of position and velocity. Interpolation is obtained by the fifth-order Everett's formula. Both the velocity interpolation error, which affects ID, and the differenced position interpolation error divided by the count time, which

affects DRD, can approach 10^{-5} m/s. This small error could be eliminated by converting to the type 66 n-body ephemeris tape format, which contains the full sum and difference array (on acceleration) used to generate the ephemeris. The heliocentric velocity of the spacecraft is affected by errors in interpolation of the heliocentric ephemeris of the center of integration for the probe trajectory, while errors in interpolation of the heliocentric ephemeris of the earth–moon barycenter affect the heliocentric velocity of the tracking station.

b. Equivalence of differenced-range and integrated two-way doppler. From SPS 37-42, Vol. III, pp. 15–21, the output from the electronic equipment at the tracking station is a signal whose frequency f in cycles per second of station time is

$$f = C_3 \left[f_q(t_3) - f_q(t_1) \left(\frac{f_R}{f_T} \right) \right] + C_4 \qquad (1)$$

where

$f_q(t_3), f_q(t_1)$ = transmitter reference oscillator frequency at reception time t_3 and transmission time t_1, respectively (generally identical unless f_q has been changed between t_1 and t_3)

f_R/f_T = ratio of received to transmitted frequency for unity frequency multiplication at spacecraft

$$C_3 = \begin{cases} 30 \left(\dfrac{96}{89} \right), & \text{L-band} \\[2mm] 96 \left(\dfrac{240}{221} \right), & \text{S-band} \end{cases}$$

$$C_4 = \begin{cases} 10^5, & \text{L-band} \\ 10^6, & \text{S-band} \end{cases}$$

The transmitted frequency is 30 or 96 times the reference oscillator frequency for L- or S-band operation. The spacecraft transponder multiplies the frequency of the received signal by 96/89 or 240/221 for L- or S-band operation before retransmitting. The expression for f may be written as

$$f = C_3 f_q(t_1) \left(1 - \frac{f_R}{f_T} \right) + f_{\text{bias}} \qquad (2)$$

where

$$f_{\text{bias}} = C_3 \left[f_q(t_3) - f_q(t_1) \right] + C_4 \qquad (3)$$

Note that the first term of f_{bias} normally is zero.

---

[26]Time is represented as double-precision (54 bits on the IBM 7094 computer) seconds past January 1, 1950,0^h. From 1967 to 1984, the value of the last bit is 0.6×10^{-7} s. The transmission time, reflection time at the spacecraft, and reception time (in ephemeris time) obtained from the light time solution may be in error by about this amount. Hence, for a probe range rate of 30 km/s, the error in computed range will be about 30 km/s $\times 10^6$ mm/km $\times 0.6 \times 10^{-7}$ s = 1.8 mm.

The signal with frequency f is fed into an electronic counter whose register is incremented by 1 each time the amplitude of the signal changes from minus to plus. N cycles are counted during the count time T_c. The two-way doppler observable which the data editing program passes on to the orbit determination program is

$$F2 = \frac{N}{T_c} - f_{\text{bias}} \qquad (4)$$

Since N is the integral of f over the count time,

$$F2 = \frac{1}{T_c} \int_{t_3 - \frac{1}{2}T_c}^{t_3 + \frac{1}{2}T_c} f d\tau - f_{\text{bias}} \qquad (5)$$

where

$\tau = $ station time (proper time) at tracking station, from station atomic clock

$t_3 = $ epoch at midpoint of count interval T_c

Substituting Eq. (2) into Eq. (5) gives

$$F2 = \frac{C_3 f_q(t_1)}{T_c} \int_{t_3 - \frac{1}{2}T_c}^{t_3 + \frac{1}{2}T_c} \left(1 - \frac{f_R}{f_T}\right) d\tau \qquad (6)$$

"Integrated" two-way doppler may be obtained from Eq. (6) by expanding $1 - (f_R/f_T)$ in a Taylor series with coefficients evaluated at t_3. Equation (6) may then be integrated term by term. The odd derivatives vanish, and the fourth and higher derivatives are ignored. The resulting expression for $F2$ is

$$F2 = C_3 f_q(t_1) \left[\left(1 - \frac{f_R}{f_T}\right) + \frac{T_c^2}{24} \left(1 - \frac{f_R}{f_T}\right)^{\cdot\cdot} \right] \qquad (7)$$

where $1 - (f_R/f_T)$ and its second derivative with respect to station time $[1 - f_R/f_T)]^{\cdot\cdot}$ are evaluated at the midpoint of the count interval. The first term, which has been truncated in Eq. (7), is $(1/1920) (T_c^4) [1 - (f_R/f_T)]^{\text{iv}}$. In order to limit the truncation error in Eq. (7) to 10^{-5} m/s, the count time T_c must be limited to approximately 1 s for near-earth spacecraft, and to approximately 1000 s when the spacecraft is in heliocentric cruise.

The expression for "differenced-range" two-way doppler may also be obtained from Eq. (6). The ratio of received to transmitted frequency is

$$\frac{f_R}{f_T} = \frac{dn}{d\tau_3} \cdot \frac{d\tau_1}{dn} = \frac{d\tau_1}{d\tau_3} \qquad (8)$$

where

$dn = $ infinitesimal number of cycles transmitted and received

$d\tau_1 = $ infinitesimal period (of proper time τ) of transmission of dn cycles from tracking station at time t_1

$d\tau_3 = $ infinitesimal period (of proper time τ) of reception of dn cycles at tracking station at time t_3

Substituting Eq. (8) into Eq. (6) and denoting $d\tau$ in Eq. (6) as $d\tau_3$ gives

$$F2 = \frac{C_3 f_q(t_1)}{T_c} \int_{t_3 - \frac{1}{2}T_c}^{t_3 + \frac{1}{2}T_c} \left(1 - \frac{d\tau_1}{d\tau_3}\right) d\tau_3 \qquad (9)$$

The count time T_c is an interval of reception time; the corresponding transmission interval is denoted T'_c, and has midpoint t_1. Thus,

$$F2 = \frac{C_3 f_q(t_1)}{T_c} \left[\int_{t_3 - \frac{1}{2}T_c}^{t_3 + \frac{1}{2}T_c} d\tau_3 - \int_{t_1 - \frac{1}{2}T'_c}^{t_1 + \frac{1}{2}T'_c} d\tau_1 \right]$$
$$= \frac{C_3 f_q(t_1)}{T_c} (T_c - T'_c) \qquad (10)$$

The four station time epochs corresponding to the start and end of the transmission and reception intervals T'_c and T_c are denoted as

$\tau_{3_e} = $ end of reception interval T_c

$\tau_{3_s} = $ start of reception interval T_c

$\tau_{1_e} = $ end of transmission interval T'_c

$\tau_{1_s} = $ start of transmission interval T'_c

Also, "range" ρ corresponding to reception time τ_3 and transmission time τ_1 is defined as elapsed round-trip proper time:

$$\rho(\tau_3) \equiv \tau_3 - \tau_1$$

and

$$\rho_e \equiv \tau_{3_e} - \tau_{1_e}$$

$$\rho_s \equiv \tau_{3_s} - \tau_{1_s}$$

Thus,

$$T_c - T'_c = (\tau_{3_e} - \tau_{3_s}) - (\tau_{1_e} - \tau_{1_s}) = \rho_e - \rho_s$$

$$(11)$$

Substituting Eq. (11) into Eq. (10) gives

$$F2 = C_3 f_q(t_1) \left[\frac{\rho_e - \rho_s}{T_c} \right] \qquad (12)$$

The DPODP range observables R, RD, and RT are computed as round-trip station time ρ multiplied by a conversion factor F and modulated by modulo number M:

R (kilometers/2): $F = \dfrac{c}{2}$

M = no modulo number

RD (range units): $F = \dfrac{1440}{221} f_q(t_1)$

$M = 785{,}762{,}208$

RT (nanoseconds): $F = 10^9$

$M = 1.00947 \times 10^9/1.0002$

$= 1.009{,}268{,}146{,}370{,}725{,}8548 \times 10^9$

where c = speed of light = 299,792.5 km/s, and one range unit ≈ 1 m of distance to the spacecraft. The observable R is obtained from the AFETR pulse radar ranging system. The observables RD and RT are obtained from the DSIF Mark 1A and R&D planetary ranging systems, respectively.

The DRD observables of this study were computed from differenced round-trip range R (in units of kilometers divided by two):

$$F2 = \frac{2C_3 f_q(t_1)}{c} \left[\frac{R_e - R_s}{T_c} \right] \qquad (13)$$

The conversion factor CON between two-way doppler (integrated or differenced-range) in observed units of Hz and in units of one-way meters/s is

$$CON = \frac{F2\,(\mathrm{Hz})}{F2\,(1\text{-way meters/s})} = \frac{2C_3 f_q(t_1)(\mathrm{Hz})}{c\,(\mathrm{meters/s})} \qquad (14)$$

$$= 15.343{,}946{,}229{,}475{,}39\ \mathrm{Hz}/(1\text{-way meters/s})$$

since the observables of this study were computed with $C_3 f_q(t_1) = 2300 \times 10^6$ Hz exactly and $c = 2.997925 \times 10^8$ m/s.

c. Generation of differenced-range doppler minus integrated doppler residuals. The DPODP was used to compute the round-trip range observable R (round-trip time multiplied by one-half the speed of light c) and two-way doppler $F2$ at each of three successive observation times, with a data spacing equal to half of the count time T_c. Differenced-range doppler was computed from the range observables R_e and R_s at the third and first observation times, respectively, and compared to two-way doppler at the second observation time. The computations were performed by program DRDVID. The equivalence of integrated and differenced-range two-way doppler is given by Eq. (13). The residual RES in m/s computed by DRDVID is

$$RES = \frac{1000\,[R_e(\mathrm{km}) - R_s(\mathrm{km})]}{T_c} - \frac{F2(\mathrm{Hz})}{CON} \qquad (15)$$

where CON is given by Eq. (14).

The doppler corrections due to antenna motion, troposphere, and ionosphere are in the form of differenced-range corrections divided by the count time; hence, all observables were computed without applying these corrections. It is noted that the sign of the ionospheric range correction must be changed when the range observable is used to compute DRD.

d. New expression for ET − A1 time transformation. Given a system of synchronized (on the average) A1 atomic clocks, one at each tracking station, the new expression for ET minus A1 obtained from any of the clocks (in seconds) is

$$\mathrm{ET-A1} = \Delta T_{1958}$$
$$- (\mathrm{JD} - 2436204.5)\,(86400)\,\frac{\Delta f_{\text{cesium}}}{f_{\text{cesium}}}$$
$$+ 1.658 \times 10^{-3} \sin E \qquad\qquad \text{[AT]}$$
$$+ 0.317679 \times 10^{-9} r_s \sin(\mathrm{UT} + \lambda) \qquad\qquad \text{[DA1 + DP]}$$
$$+ 5.341 \times 10^{-12} r_s \sin(\mathrm{UT} + \lambda - M) \qquad\qquad \text{[DA1(e)]}$$
$$+ 1.01 \times 10^{-13} r_s \sin(\mathrm{UT} + \lambda - 2M) \qquad\qquad \text{[DA1(e^2)]}$$
$$- 1.3640 \times 10^{-11} r_s \sin(\mathrm{UT} + \lambda + 2L) \qquad\qquad \text{[DA2]}$$
$$- 2.27 \times 10^{-13} r_s \sin(\mathrm{UT} + \lambda + 2L + M) \qquad\qquad \text{[DA2(e)]}$$
$$+ 1.672 \times 10^{-6} \sin D \qquad\qquad \text{[AM]}$$
$$+ 1.38 \times 10^{-13} r_s \sin(\mathrm{UT} + \lambda - D) \qquad\qquad \text{[DM]} \qquad (16)$$

Term identification column shown at right: [AT], [DA1 + DP], [DA1(e)], [DA1(e^2)], [DA2], [DA2(e)], [AM], [DM].

The first and second terms account for the initial setting and rate of the A1 atomic time scale relative to ET; the remaining terms account for the periodic relativistic variations in A1 atomic time relative to uniform ET. The variables in Eq. (16) are defined as

ΔT_{1958} = ET − UT2 on January 1, 1958, $0^h\,0^m\,0^s$ UT2 minus the periodic terms of Eq. (16) evaluated at this epoch using r_s and λ of the master A1 clock. The master A1 clock was set equal to UT2 on this date. The parameter ΔT_{1958} may be estimated by the DPODP.

f_{cesium} = 9192631770 cycles of cesium atomic clock per second of A1 time (definition). This adopted length of the A1 second is the current experimentally determined average length of the ET second.

$f_{\text{cesium}} + \Delta f_{\text{cesium}}$ = cycles of cesium atomic clock per ephemeris second. The parameter Δf_{cesium} may be estimated by the DPODP; its current nominal value is zero.

2436204.5 = Julian date on January 1, 1958, 0^h.

JD = Julian date.

M = mean anomaly of heliocentric orbit of earth–moon barycenter.

E = eccentric anomaly of heliocentric orbit of earth–moon barycenter.

L = geometric mean longitude of the sun, referred to mean equinox and ecliptic of date.

$D = \mathbb{C} - L$ = mean elongation of the moon from the sun, where

$\mathbb{C}$ = mean longitude of the moon, measured in the ecliptic from the mean equinox of date to the mean ascending node of the lunar orbit, and then along the orbit.

r_s = distance of tracking station from earth's spin axis, km.

λ = east longitude of tracking station.

UT = universal time, hours past midnight, converted to radians. It is computed from

$$\mathrm{UT} = 2\pi \left[\frac{\mathrm{UT1}}{86400} \right]_{\text{decimal part}} \qquad (17)$$

where UT1 = seconds of UT1 time past January 1, 1950, 0^h UT1. The angles M, L, and D in radians are given by

$$M = 6.248{,}291 + 1.990{,}968{,}71 \times 10^{-7}\,t \qquad (18)$$

$$L = 4.888{,}339 + 1.991{,}063{,}83 \times 10^{-7}\,t \qquad (19)$$

$$D = 2.518{,}410 + 2.462{,}600{,}818 \times 10^{-6}\,t \qquad (20)$$

where $t =$ seconds past January 1, 1950, 0^h. To a sufficient degree of accuracy, the eccentric anomaly E is given by

$$E \approx M + e \sin M \qquad (21)$$

where $e =$ eccentricity of heliocentric orbit of earth–moon barycenter $= 0.01672$.

The eight periodic relativity terms in Eq. (16) were obtained by integrating Eq. (13) of SPS 37-42, Vol. III, pp. 15–21. The derivation will be included in a forthcoming JPL Technical Report on the DPODP formulation. Term AT arises from the annual variation in velocity and potential at the tracking station. The second term is the sum of terms DA1 and DP with coefficients of 0.318549 and -0.000870, respectively. Terms DA1, DA1(e), DA1(e²) DA2, DA2(e) arise from the product of the daily and annual components of the heliocentric station velocity in the expression for the station velocity squared ($\dot{s}^2$) in Eq. (13) of SPS 37-42, Vol. III. Terms DA1 and DA2 account for the mean motion of the earth–moon barycenter about the sun. Terms DA1(e) and DA2(e) are first-order eccentricity terms while term DA1(e²) is a second-order eccentricity term. Term DP accounts for the daily variation in potential at the station. Term AM stems from the product of the annual and monthly components of station velocity in $\dot{s}^2$, while term DM is due to the product of the daily and monthly components.

The expression for ET $-$ A1 currently used in the DPODP consists of the first three terms of Eq. (16) and the following term derived by Anderson (SPS 37-50, Vol. III, pp. 39–47):

$$2.03 \times 10^{-6} \cos \phi \sin (\text{UT} + \lambda) \qquad [\text{DT}]$$

where ϕ is the station latitude. Anderson's term is term DA1 of Eq. (16) (coefficient $= 0.318549$) with r_s set equal to 6372 km cos ϕ. Computation of the daily terms of Eq. (16) from the station's spin axis distance rather than latitude accounts for the effect of the earth's flattening. The increased accuracy is required for the computation of DRD.

e. Residual plots. Differenced-range doppler minus integrated doppler (DRD $-$ ID) residuals were obtained for the *Mariner* V trajectory early and late in heliocentric cruise, and at encounter with Venus (10,000-km radius of closest approach), and also on the first leg of a grand tour mission at 1, 2, 3, 4 and 5 AU and at encounter with Jupiter (125,000-km radius of closest approach). The DRD $-$ ID residuals are plotted as a function of count time T_c in

Figs. 69, 70, and 71. For each curve, the epoch at the midpoint of the count interval is held fixed.

Figure 69 shows DRD $-$ ID residuals for three different observation times on the *Mariner* V trajectory to Venus. Each observable is computed with 24 different count times ranging from 0.1 to 10,000 s. For count times below approximately 100 s, the residuals are random with an upper limit of about 3 mm/T_c. These residuals represent errors in the range observables used to compute DRD due to truncation of time (seconds past 1950) beyond double precision on the IBM 7094 computer (54 bits or approximately 16-decimal digits). The randomness of the residuals is expected since the range observables and hence their time truncation errors change with the count time. It can be shown that if each of several contributing time truncation errors were at their upper limits, DRD could be in error by as much as 10 mm/T_c. Figure 70 shows the variation in the *Mariner* V residuals with integration central body on October 6, 1967 at 16 h UTC. Figure 71 shows residuals for the first leg of a grand tour mission at 1, 2, 3, 4, and 5 AU and at encounter with Jupiter. These figures have a typical residual of 1 mm/T_c due to truncation of time beyond double precision.

Integrated two-way doppler is computed from Eq. (7), which was obtained from Eq. (6) by expanding the doppler frequency shift in a Taylor series (with coefficients evaluated at the midpoint of the count interval T_c) and integrating term by term. The odd derivatives of the frequency shift vanish and the fourth and higher derivatives are ignored. The first deleted term in Eq. (7) is

$$(1/1920)T_c^4 \left[1 - (f_R/f_T)\right]^{\text{iv}}$$

where iv represents the fourth derivative with respect to the reception time (station time). For an accuracy of 10^{-5} m/s, truncation of the fourth derivative of the frequency shift limits the count time to approximately 1000 s in heliocentric cruise and typically 1 to 60 s at planetary encounter depending upon the radius of closest approach. Thus, on the log residual versus log count time plots, the residuals should rise linearly with a slope of four at high count times. This is exactly what is obtained in Figs. 69, 70, and 71.

For heliocentric cruise on the *Mariner* V and Jupiter trajectories, the doppler truncation residuals rise above 10^{-5} m/s at count times ranging from 1200 to 3000 s. At Venus and Jupiter encounter, the corresponding figures are 70 and 60 s, respectively. Once the doppler truncation residuals have risen above 10^{-4} to 10^{-3} m/s, all
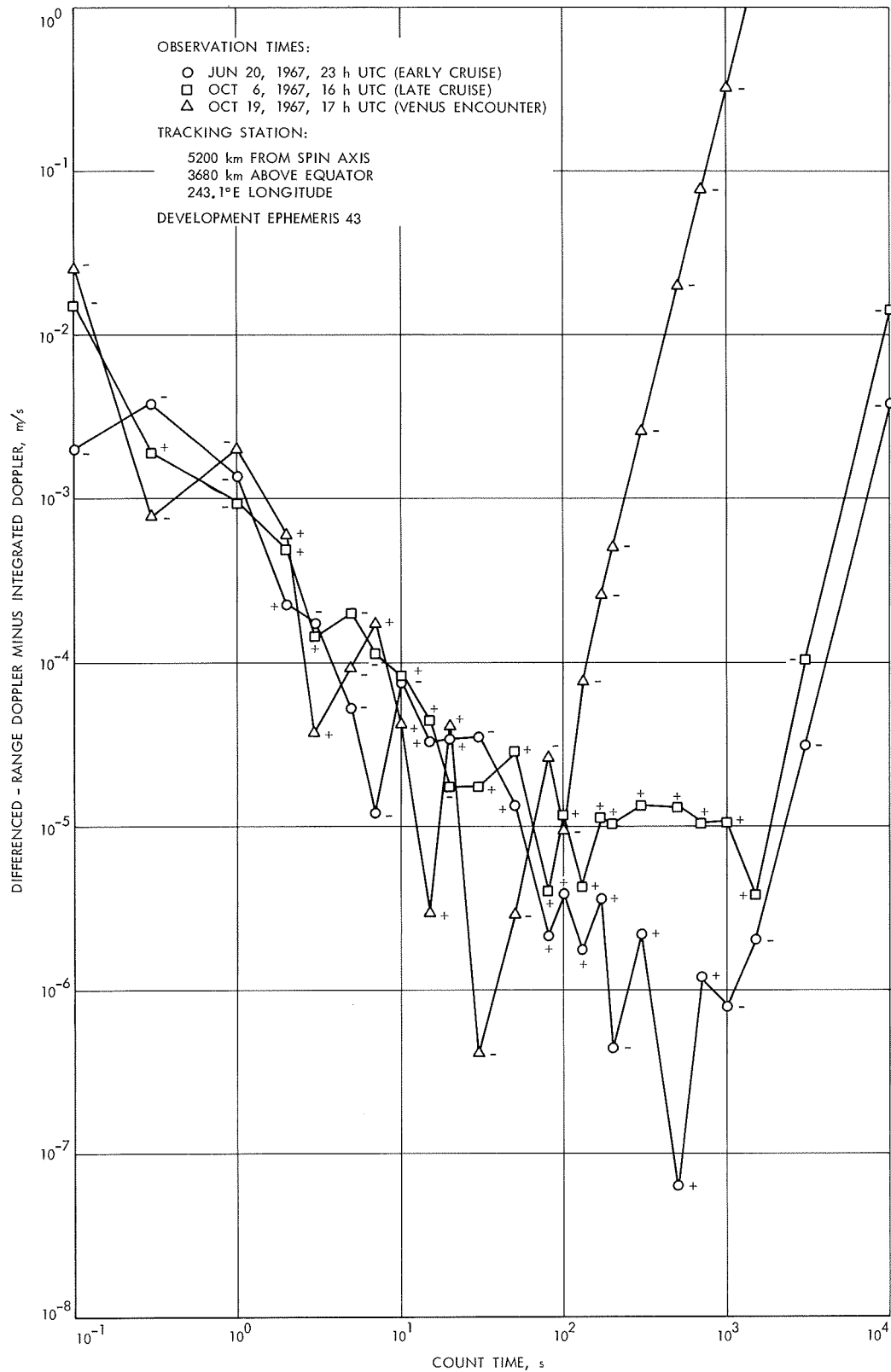
130

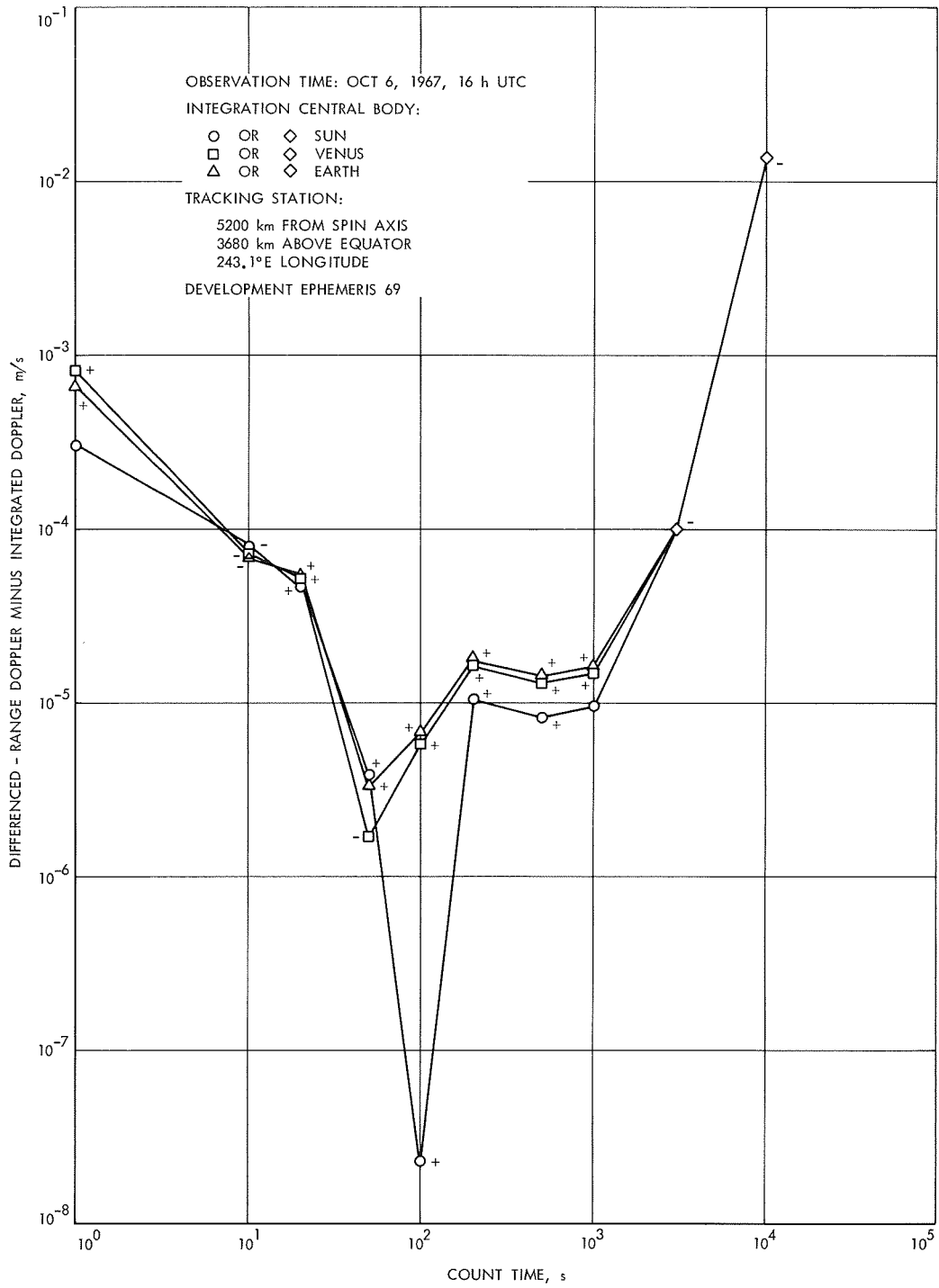**Fig. 69. *Mariner V* trajectory: Jun 20, Oct 6 and 19, 1967**

OBSERVATION TIME: OCT 6, 1967, 16 h UTC

INTEGRATION CENTRAL BODY:

○ OR ◇ SUN
□ OR ◇ VENUS
△ OR ◇ EARTH

TRACKING STATION:

5200 km FROM SPIN AXIS
3680 km ABOVE EQUATOR
243.1°E LONGITUDE

DEVELOPMENT EPHEMERIS 69

DIFFERENCED - RANGE DOPPLER MINUS INTEGRATED DOPPLER, m/s

COUNT TIME, s

Fig. 70. *Mariner V* **trajectory: variation in center of integration**
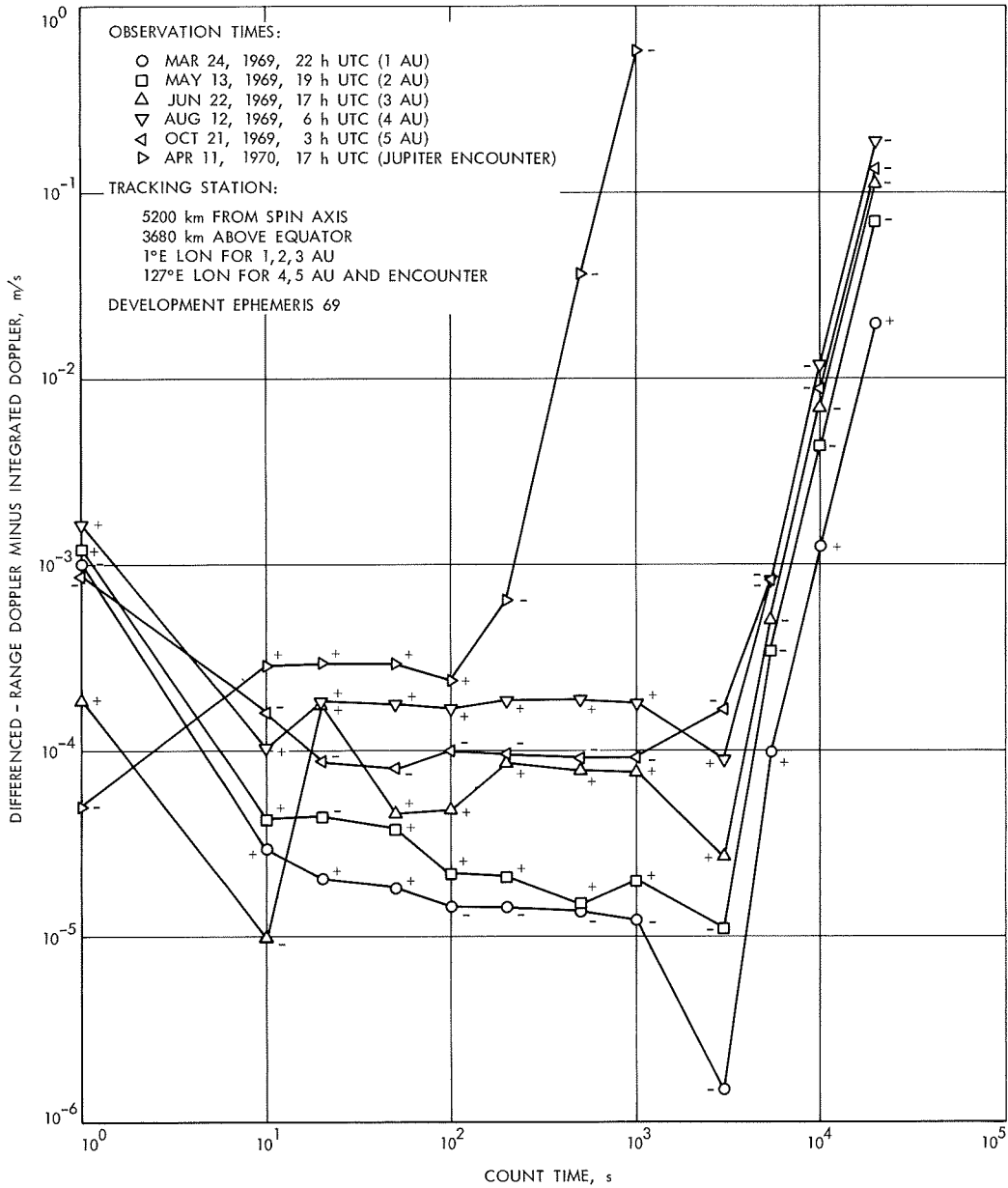
Fig. 71. Jupiter trajectory

points lie on a straight line with slope equal to four. All residuals on a given straight line have the same sign, namely, that of $[1 - (f_R/f_T)]^{iv}$. Thus, the residual versus count time curve is continuous for high count times since the doppler truncation error is continuous, whereas the residuals for moderate and particularly for low count times are discontinuous due to the random double-precision time truncation error.

If errors other than the time truncation error and the doppler truncation error were not present, minimum residuals of approximately 10^{-6} m/s would be obtained during heliocentric cruise at a count time of about 1000 s, as occurs on the *Mariner* V trajectory on June 20, 1967 (Fig. 69), where the probe range is 1.8×10^6 km. However, on October 6, 1967, where the probe range is 62×10^6 km (Figs. 69 and 70), and on the Jupiter trajectory with ranges of 1 to 5 AU (Fig. 71), the minimum residuals are 10^{-5} to 3×10^{-4} m/s with the larger values occurring for greater probe ranges. These residuals are due primarily to neglected relativity terms in the current expression for the ET $-$ A1 time transformation (*Paragraph d*) and will be reduced to less than 10^{-5} m/s by addition of the new terms of Eq. (16). The relativity terms of ET $-$ A1 represent the periodic variations in atomic time on earth relative to uniform ephemeris time ET (also denoted as coordinate time t in the heliocentric space-time frame of reference).

For each range observable used to compute DRD, the new terms of ET $-$ A1 are required to accurately transform round-trip ET obtained from the light time solution to observed round-trip station time ST. The terms in DRD and in ID which arise from the periodic variations in atomic time on earth due to general relativity will be referred to as Atomic Time Theory (ATT) terms. Integrated doppler is computed using the exact differential equation relating proper time τ and coordinate time t. The only error in the ATT contribution to ID is the neglect of the second derivative of $d\tau/dt$ in Eq. (7); for the observables of this study, the maximum error is 1.0×10^{-6} m/s.

A program was written to compute the residuals between the ATT terms of DRD and ID using both the current and new expressions for ET $-$ A1 to compute the ATT terms of DRD. Table 32 shows the DRD $-$ ID residuals of Fig. 70 (integration central body = sun) and Fig. 71 for intermediate count times, the contribution from the ATT residuals obtained from the current expression for ET $-$ A1, and the corrected residual with the ATT error removed. It is immediately evident that the larger residuals occurring at the larger probe ranges are due almost entirely to the ATT error. The corrected residuals

Table 32. Reduction in DRD — ID residuals with removal of ATT error[a]

Mission	$T_c = 100$	$T_c = 200$	$T_c = 500$	$T_c = 1000$
Mariner V	0.0	1.1	0.9	1.0
(Oct 6, 1967)	1.8	1.8	1.8	1.8
	−1.8	−0.7	−0.9	−0.8
Jupiter	−1.5	−1.5	−1.4	−1.3
1 AU	−1.1	−1.1	−1.1	−1.1
	−0.4	−0.4	−0.3	−0.2
2 AU	2.2	2.2	1.5	2.0
	2.1	2.1	2.1	2.2
	0.1	0.1	−0.6	−0.2
3 AU	4.9	8.6	7.9	7.9
	8.0	8.0	8.0	8.1
	−3.1	0.6	−0.1	−0.2
4 AU	17.3	18.9	19.0	18.5
	18.8	18.8	18.8	18.9
	−1.5	0.1	0.2	−0.4
5 AU	−10.1	−9.8	−9.2	−9.4
	−9.2	−9.2	−9.2	−9.2
	−0.9	−0.6	0.0	−0.2

Mission	$T_c = 10$		$T_c = 20$		$T_c = 50$
Encounter	29.2		30.0		29.5
	29.7		29.7		29.7
	−0.5		0.3		−0.2

[a]Units = 10^{-5} m/s.
xx = existing DRD — ID residual
xx = ATT error
xx = residual with ATT error removed

are as high as 3×10^{-5} m/s at a count time of 100 s; for count times of 200, 500, and 1000 s, they are less than 10^{-5} m/s. The higher corrected residuals at the lower count times represent the previously mentioned double-precision time truncation error. Using the new expression for ET $-$ A1, the ATT error in DRD is reduced to a maximum of 1.5×10^{-6} m/s and the ATT residuals are reduced to 2.3×10^{-6} m/s or less. Hence, Table 32 represents the approximate reduction in the DRD $-$ ID residuals of Figs. 70 and 71 due to addition of the new terms to ET $-$ A1.

Table 33 shows the DRD $-$ ID residuals corrected for the ATT error (obtained from Table 32), the contribution to the residuals from the n-body ephemeris interpolation errors, and the residuals corrected for both ATT and the n-body ephemeris interpolation errors. It is seen that the maximum contribution from the n-body ephemeris interpolation errors is 0.6×10^{-5} m/s. Removal of the

Table 33. Reduction in DRD — ID residuals with removal of ATT error and ephemeris interpolation error[a]

Mission	$T_c = 100$	$T_c = 200$	$T_c = 500$	$T_c = 1000$
Mariner V	−1.8	−0.7	−0.9	−0.8
(Oct 6, 1967)	−0.6	−0.6	−0.6	−0.6
	−1.2	−0.1	−0.3	−0.2
Jupiter	−0.4	−0.4	−0.3	−0.2
1 AU	−0.2	−0.2	−0.2	−0.2
	−0.2	−0.2	−0.1	−0.0
2 AU	0.1	0.1	−0.6	−0.2
	0.0	0.0	0.0	0.0
	0.1	0.1	−0.6	−0.2
3 AU	−3.1	0.6	−0.1	−0.2
	−0.2	−0.2	−0.2	−0.2
	−2.9	0.8	0.1	0.0
4 AU	−1.5	0.1	0.2	−0.4
	−0.2	−0.2	−0.2	−0.2
	−1.3	0.3	0.4	−0.2
5 AU	−0.9	−0.6	0.0	−0.2
	−0.3	−0.3	−0.3	−0.3
	−0.6	−0.3	0.3	0.1

	$T_c = 10$	$T_c = 20$	$T_c = 50$
	−0.5	+0.3	−0.2
Encounter	0.4	0.4	0.4
	−0.9	−0.1	−0.6

[a]Units = 10^{-5} m/s.
xx = existing DRD — ID residual with ATT error removed
xx = ephemeris interpolation error
$\overline{xx}$ = residual with ATT and ephemeris interpolation errors removed

ephemeris interpolation error greatly reduces the residuals for October 6 on the *Mariner* V trajectory and at a range of 1 AU on the Jupiter trajectory. For the remaining observation times, the residuals are changed but their average value is not. It is not possible to determine whether removal of the n-body ephemeris interpolation error is an improvement in all cases because of the presence of the random double-precision time truncation error. This error source has a typical value of 3 mm/T_c and the expected values at count times of 100, 200, 500, and 1000 s are 3, 1.5, 0.6 and 0.3×10^{-5} m/s, respectively. Thus, the remaining unaccounted for residuals of Table 33 may be due almost entirely to the double-precision time truncation error. If this is the case, the residuals will be considerably smaller on the Univac 1108 version of the DPODP. It should be noted that for a count time of 1000 s, where the time truncation error is small, removal of the n-body ephemeris interpolation error reduces the residual in every case.

Table 34 shows the DRD — ID residuals of Fig. 70 for the *Mariner* V trajectory on October 6, 1967, with the sun, Venus, and earth as integration central bodies. The uncorrected residuals vary with the center of integration. However, removal of the ATT error and different n-body ephemeris interpolation error for each center results in corrected residuals which are almost identical for each center of integration. This indicates that the double-precision time truncation error is the same for the different centers of integration. That is, changing the center of integration does not change the light time solutions for the range observables used to compute DRD. This is as expected since the variation in the heliocentric position of the probe with different centers and corresponding n-body ephemeris interpolation errors is only about 1 m, or 0.3×10^{-8} s of light time. This generally will not change the epochs of participation since the last bit of double-precision seconds past 1950 is 0.6×10^{-7} s.

The contributions to the DRD — ID residuals due to n-body ephemeris interpolation errors shown in Tables 33 and 34 are due primarily to differenced position interpretation errors divided by the count time. However, for the *Mariner* V observable of Table 33, with the sun as center of integration, the residual is almost entirely a velocity interpolation error. The upper limit for the error in either DRD or ID is probably about 10^{-5} m/s.

Table 34. Corrected *Mariner* V residuals with different integration central bodies[a]

Integration central body	$T_c = 200$	$T_c = 500$	$T_c = 1000$
Sun	1.1	0.9	1.0
	1.8	1.8	1.8
	−0.7	−0.9	−0.8
	−0.6	−0.6	−0.6
	−0.1	−0.3	−0.2
Venus	1.6	1.3	1.5
	1.8	1.8	1.8
	−0.2	−0.5	−0.3
	−0.1	−0.1	−0.1
	−0.1	−0.4	−0.2
Earth	1.7	1.4	1.6
	1.8	1.8	1.8
	−0.1	−0.4	−0.2
	0.0	0.0	0.0
	−0.1	−0.4	−0.2

[a]Units = 10^{-5} m/s; observation time = Oct 6, 1967, 16 h UTC.
xx = existing DRD — ID residual
xx = ATT error
$\overline{xx}$ = residual with ATT error removed
xx = ephemeris interpolation error
$\overline{xx}$ = residual with ATT and ephemeris interpolation errors removed

The position and velocity interpolation errors for the barycenter ephemeris are roughly sinusoidal with the vast majority of zero crossings occurring at the tabular points (four days apart). The position and velocity interpolation errors for the Venus ephemeris are zero at the tabular points and have typically 2–4 zero crossings in between. In all cases, the interpolation errors are extremely smooth functions.

Changing the representation of time from double- to triple-precision seconds past 1950 or equivalent and conversion of the DPODP to the Univac 1108 will reduce the random error of computed DRD from 3×10^{-3} m/T_c due to truncation of time beyond 16-decimal digits to 2×10^{-6} m/T_c due to truncation of position beyond 18-decimal digits. For an accuracy of 10^{-5} m/s, count times as low as

0.2 s may be used. Use of the new expression for ET − A1 (Eq. 16) will reduce the error in computed DRD to approximately 10^{-5} m/s. Use of the type 66 n-body ephemeris would reduce the error closer to 10^{-6} m/s. The growth of error in the probe ephemeris with time due to position interpolation error for the perturbing bodies would also be eliminated.

The new terms of ET − A1 affect the computed range observables by 0.01 to 1.0 m/AU. There is a monthly term of 0.05 m/AU not included in Eq. (16). In order to realize this increased accuracy, the type 66 n-body ephemeris or equivalent must be used since the current type 50 position interpolation errors are almost 1 m (or slightly larger for Mercury).

IV. Development and Implementation

A. DSIF Development

1. Antenna-Mechanical Subsystem Field Instrumentation—Modular Concept, J. A. Carpenter

a. Introduction. During erection of the antenna-mechanical subsystem, instrumentation (including strain gauges, accelerometers, fluid and gas-pressure-sensing devices, recording anemometers, force gauges, thermo-couples, and extensometers) is needed for installation, alignment, and performance evaluation.

During the early days of antenna installation, due to a lack of field housing facilities, instrumentation trailers were designed and built which housed not only the recording instrumentation needed in association with the above listed sensing devices, but also work and storage space. The subsequent history of utilization showed that the trailers spent from 40 to 75% of their life in transit and involved excessive handling, maintenance, and customs processing.

b. Design criteria. A re-evaluation of the utilization of this type of field instrumentation developed the following criteria:

(1) An instrumentation trailer embodying storage and work space was not needed, due to the on-location availability of such facilities.

(2) The instrumentation assemblies configuration should be as light and compact as reasonable and should lend itself to any mode of transport—air, sea, or land.

(3) The instrumentation assembly should be configured in discrete modules to support specific needs and avoid shipment of equipment not required for a specific task.

(4) The modular concept should allow for easy expansion of the assembly to the complexity required.

(5) The design of the instrumentation assembly should be simple enough to be able to be used at any skill level and to require minimum maintenance.

c. Final configuration. A modular instrumentation assembly concept was developed which affords the following:

(1) The basic equipment is resolved into two subunits: (a) an analog recording configuration with a strip

recorder for quick field looks and analyses; and
(b) a parallelable analog tape recording unit
(Fig. 1) for storing data from the strip recorder for
later more complex analysis or digital processing.

(2) The two instrumentation subunits are mounted permanently in shock-proof shipping containers.

(3) These containers are weatherproof for shipping and field housing.

(4) The shipping and housing containers are of dimensions acceptable for commercial air shipment, when necessary.

2. Damage Prevention System for 85-ft Antenna,
J. Carlucci

a. Introduction. As a result of operational experience
and an analysis of the safety needs of the DSIF antennas,
a system has been designed which will allow the servo
operator to monitor the antenna and surrounding area,
and to control or prevent vehicles, equipment, and personnel intrusion. Due to the layout of the servo console,
windows, hydromechanics building, cable trays and
associated antenna hardware, it is presently impossible
for the servo operator to perform control and monitoring
functions continuously.

b. Problem. The general problem was reduced to two
categories:

(1) Development of a barrier-alarm system that would
not only prevent movement of hardware or equipment on and off the antenna pad without the
servo operator's knowledge, but would have some
reasonable form of interaction with the antennas
drive system operation, and an alarm arrangement.

(2) Development of a surveillance system that would
give an acceptable picture both day and night, for
monitoring the antenna and surrounding area.

c. Solution.

Barrier-alarm system. Figure 2 shows a conceptual layout of the proposed barrier and safety alarm system (and
the surveillance system) at DSS 11. This concept will be
the basic one for all DSS alarm systems.

This system consists of a sectionalized chain link fence
around the circumference of the antenna at a 260-ft
diameter, with two 20-ft gates with locks and two 3-ft
gates for personnel. An integrity cable runs around the
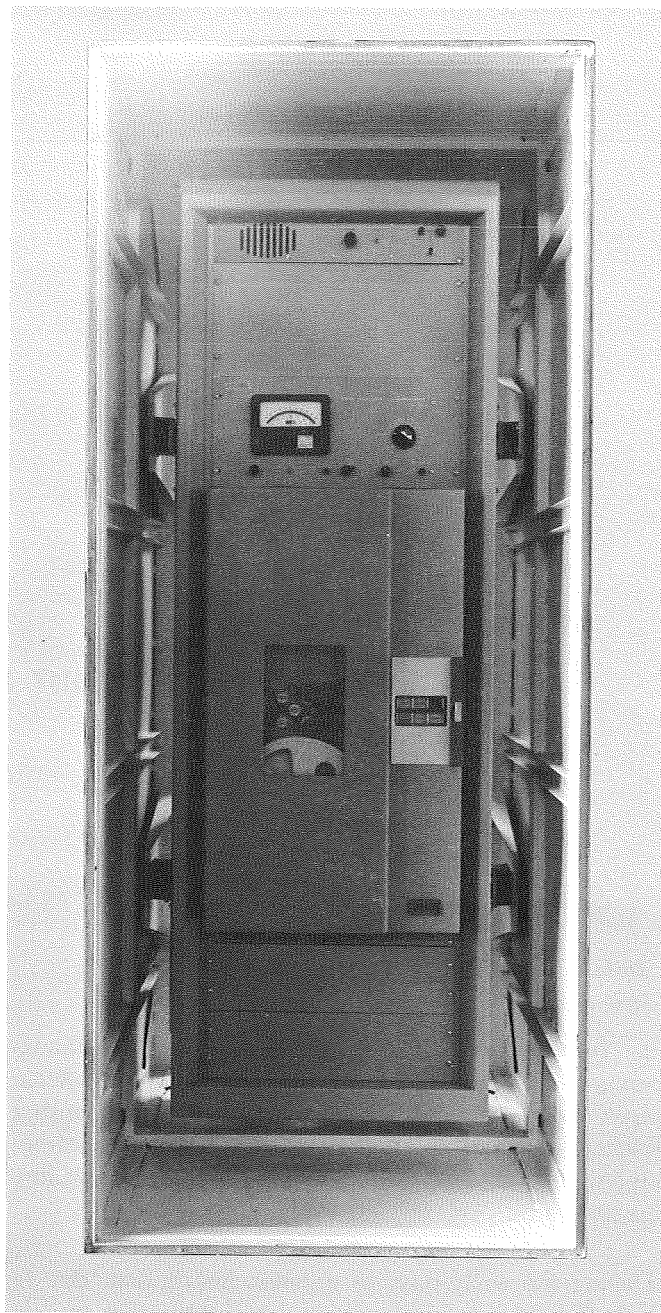top of the fence. The fence and integrity cable are made

**Fig. 1. Magnetic tape recording subunit in
shipping container**

up in 10-ft sections and are removable, if required, by
unbolting. The integrity cable is connected to the safety
alarm arrangement. The purpose of the integrity cable is
to provide the servo operator with an alarm indication
when the barrier is broken or all 20-ft gates are not closed.
The sectionalized chain link barrier acts as a personnel-control element.
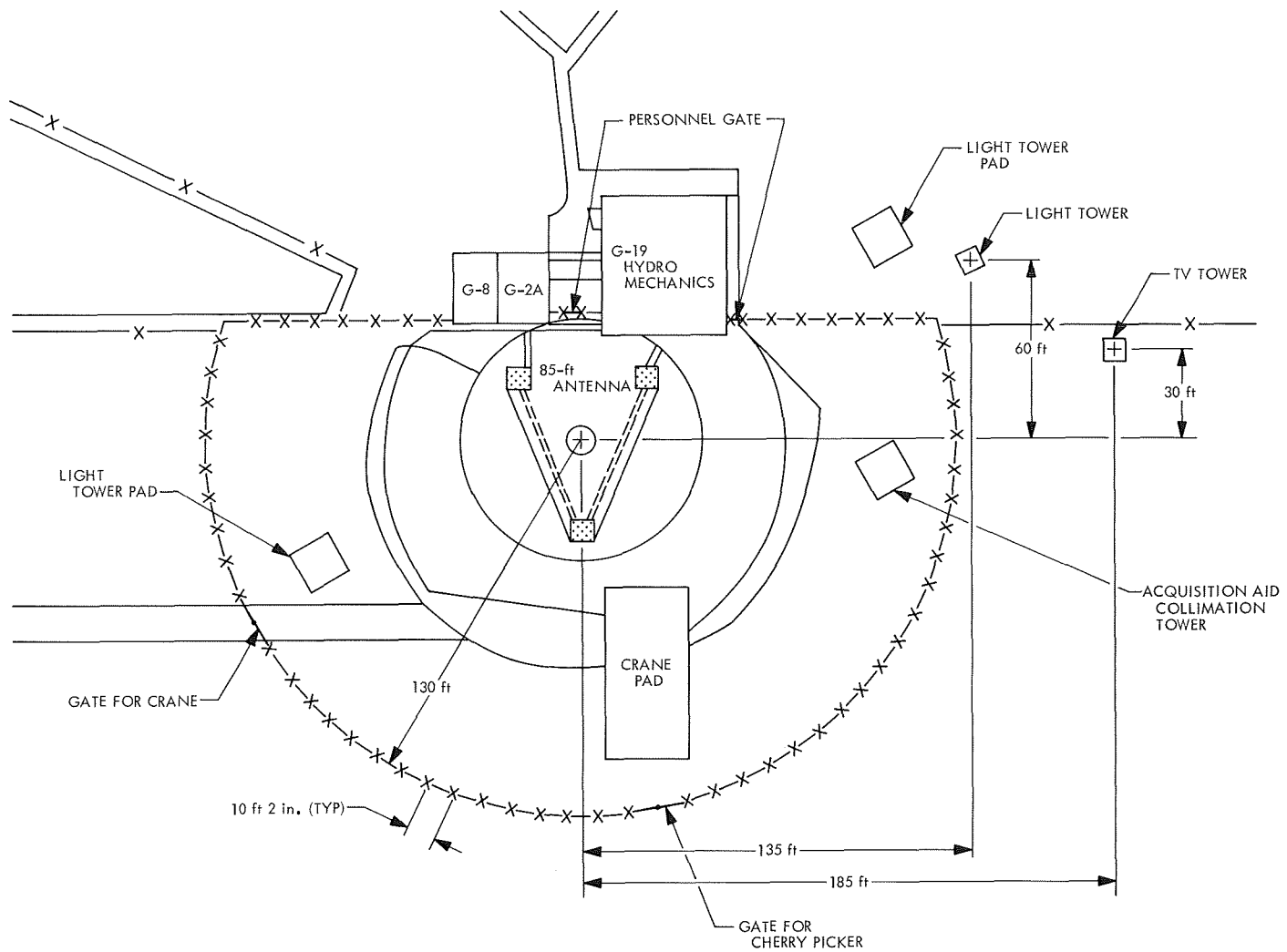
Fig. 2. Proposed barrier and safety alarm system

The safety alarm arrangement is a visual configuration which has a light bank reading "Hardware on Pad" when gates or fence sections are opened. In order to open the access gates a key must be removed from the servo console, which subsequently shuts down the servo. The shift supervisor also has a key which allows access to the antenna pad, on an emergency basis without disabling the servo, obtainable only with his approval.

Included in this system is a time delay which requires that the access key be in the switch and the TV system be operational for 5 min prior to servo power coming on. This is to make sure the servo operator surveys the antenna and area before operating the drive system.

Surveillance system. The resolved surveillance system is a TV system manufactured by Cohu Electronics, Inc.,

operating at 525 lines horizontal resolution with a 10,000/1 effective range for intensity variation. This range will produce a usable picture with light levels as low as 0.1 ft-cd on the face of the vidicon tube. The camera has a 10:1 zoom lens, mounted in an all-weather housing that is hermetically sealed, and all circuits are solid state.

Measurements made at DSS 11 indicated that existing area lighting was not sufficient to produce an acceptable picture at night. Therefore, the following requirements were adopted: the general scene area lighting, as measured at the TV camera, should be at least 0.1 ft-cd (preferably 1.0 ft-cd); the total distance from light source to antenna should be 140 ft and from antenna to camera 130 ft; for an emperically resolved actual reflection coefficient of about 0.20, there should be at least 1500-W
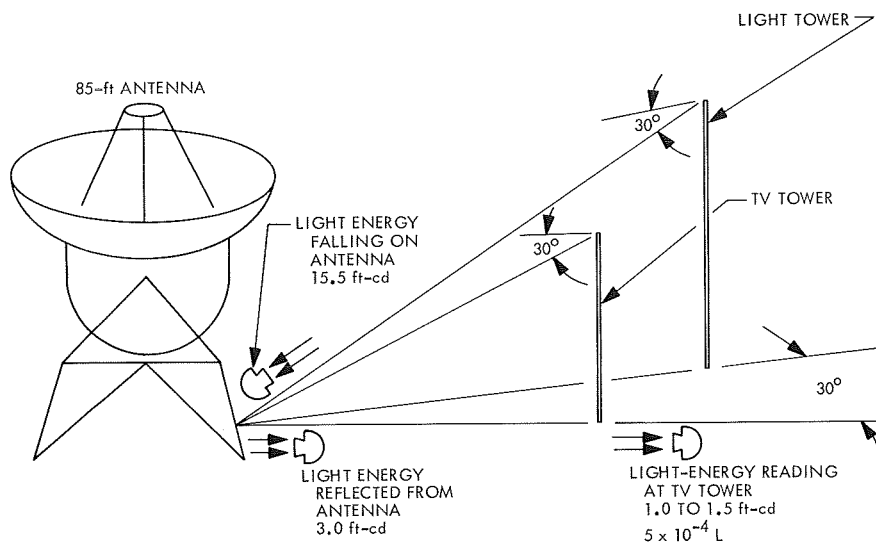
Fig. 3. Field test of surveillance system

lamps in banks of twelve, located on one of the present emergency light towers and directed at the center of the antenna with a maximum deviation from the normal of 30 deg or less, and having an initial rating of 33,000 lumens each.

Field test (Fig. 3) light readings at DSS 11 made at the base of the antenna, utilizing the θ and ϕ values of 30 deg each, confirmed the use of the 1500-W lamps. The results were:

Actual	Calculated
1 to 1.5 ft-cd	1.09 ft-cd
5×10^{-4} ft-L	5.55×10^{-4} ft-L

The number of lumens per unit area squared

$$E = \frac{I}{r^2} \cos \theta \cos \phi \text{ ft-cd}$$

where

I = light intensity, cd

r^2 = distance from light source, ft

θ = angle of incidence (zenith plane) to camera relative to reflecting surface

ϕ = angle of incidence (vertical plane) to camera relative to reflecting surface

3. $\times$3 Frequency Multiplier and Phase Modulator for Block IIIC S-Band Receiver—Exciter, C. E. Johns

a. Introduction. A new type of exciter phase modulator was developed to provide improved performance and the capability of setting modulation indices more precisely. The phase modulator presently used in the Block III C S-band receiver/exciter subsystem has a specified modulation linearity of ±5% over the range of indices from 0 to 2.4 rad at S-band. System measurements confirm that this is close to the limit of the capability of the present modulator design.

The present modulator design utilizes voltage-variable capacitors within a low-Q resonant circuit to achieve phase modulation. Due to the inherent nonlinear characteristic of capacitance variation versus applied voltage, voltage-variable capacitors are not suitable in a design requiring better than 5% linearity over large modulation indices. The design performance requirement of the new modulator is that the linearity be maintained within 1% for indices up to 2.4 rad at S-band.

b. Modulator design (ideal). A block diagram of the phase modulator module is shown in Fig. 4. The module being developed also contains a $\times$3 frequency multiplier ahead of the modulator. The 22-MHz input signal is amplified and amplitude-limited by amplifiers A1 and A2 and coupled to a wideband diode $\times$3 frequency multiplier. The multiplier output is filtered by a commercial filter centered at 66 MHz. The 66 MHz is then amplified (A3 and A4) and coupled to a 90-deg hybrid which provides two output ports, one having an in-phase signal
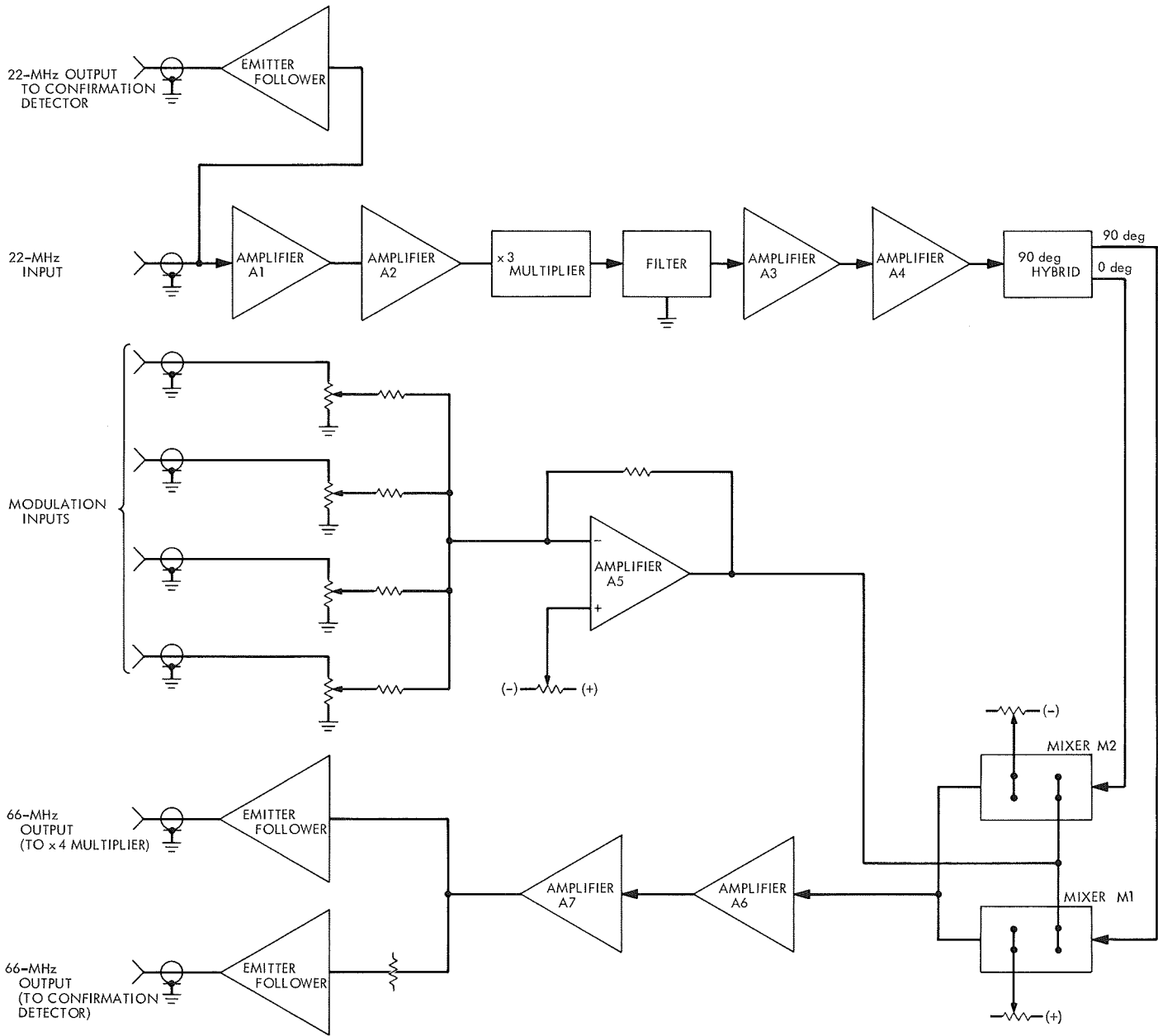
Fig. 4. × 3 frequency multiplier and phase modulator

and the second a quadrature signal. Each output port is then coupled to a commercial balanced mixer (M1 and M2) which is used as a voltage-variable attenuator. The control voltage on these mixers is the difference between the bias voltage and the voltage of the input modulation signal from the broadband video driver amplifier A5. Since the bias voltage on mixer M1 is positive and on mixer M2 is negative, the modulation signal will create control voltages that cause the attenuation of one mixer to increase while the attenuation of the other mixer decreases. These amplitude-modulated signals are then combined to produce a phase-modulated signal (discussed in more detail later). The combined carriers are subsequently amplified (A6 and A7) and applied to two isolated outputs through emitter followers.

The process of generating a phase-modulated carrier from amplitude modulation is not a new concept, but it was considered because of its capability of linear modulation over a large range of indices. The modulation process is best described in Fig. 5. Without the presence of modulation (assuming equal RF levels from each modulator, M1 and M2) the carrier vectors add as shown. When a positive modulating voltage is applied, the RF output amplitude of M1 increases linearly by the factor m and the output of M2 decreases linearly by m; a resultant carrier phase displacement (ϕ) occurs. Conversely, a negative modulation voltage results in a negative phase ($-\phi$) deviation. Figure 5 illustrates, then, an ideal situa-

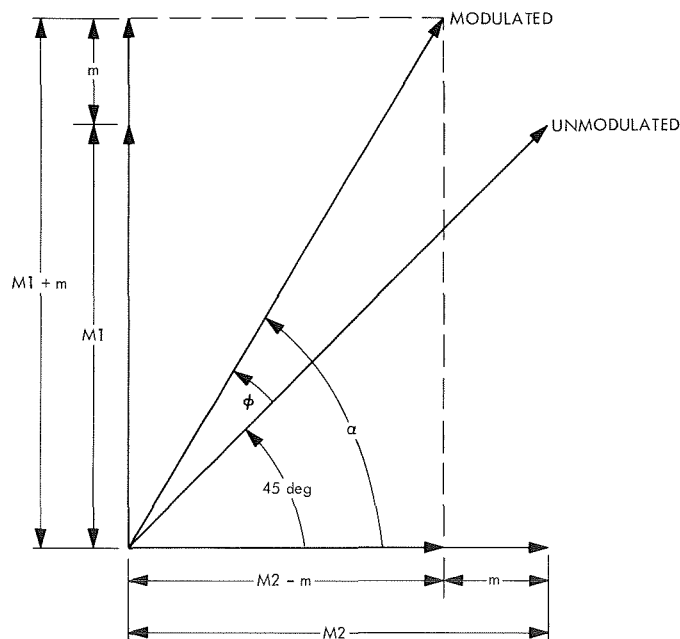tion where the unmodulated outputs of M1 and M2 are identical, and their output levels vary linearly with modulation voltage.

Assuming the ideal case and that M1 and M2 are normalized to a value of 1, then the maximum linear ($\pm 1\%$) range of modulation can be determined from Fig. 5, as follows:

$$\alpha = \tan^{-1} \frac{1 + m}{1 - m} \qquad (1)$$

and the phase deviation is

$$\phi = \alpha - 45 \deg = \tan^{-1} \frac{1 + m}{1 - m} - 45 \deg \qquad (2)$$

To obtain the modulation sensitivity for very low indices

$$S_0 = \frac{d\phi}{dm}\bigg|_{m=0} = \frac{d}{dm}\left[\tan^{-1}\frac{1 + m}{1 - m} - 45 \deg\right]\bigg|_{m=0}$$

$$= \frac{1}{1 + m^2}\bigg|_{m=0}$$

$$S_0 = 1 \text{ rad/modulation unit (peak)} \qquad (3)$$

Since the specified maximum modulation nonlinearity is 1%, then the sensitivity at the extreme of this linear range is

$$S_1 = S_0 - \frac{S_0}{100} = 1 - 0.01 = 0.99 \text{ rad/modulation unit (max)}$$

$$(4)$$

From Eqs. (3) and (4)

$$m_{\max} = \left(\frac{1 - S_1}{S_1}\right)^{1/2} = \left(\frac{1}{99}\right)^{1/2} = 0.10053 \text{ (max)}$$

$$(5)$$

From Eq. (2)

$$\phi_{\max} = \tan^{-1}\frac{1 + m_{\max}}{1 - m_{\max}} - 45 \deg$$

$$= \tan^{-1}\frac{1 + 0.100503}{1 - 0.100503} - 45 \deg = 5.7399 \deg \text{ (peak)}$$

$$(6)$$

For an ideal modulator, linearity within 1% can be attained to a peak phase deviation of ± 5.74 deg.

Fig. 5. Carrier vectors

In the S-band exciter subsystem a 5.74-deg phase deviation at the modulator output, due to subsequent frequency multiplication, corresponds to 32×5.74 or 183.7 deg at S-band. This is approximately 33% greater than is required for carrier suppression using a sine-wave modulation signal, and is more than twice that required with square waves.

The amplitude variation for the ideal case over the linear range of phase modulation index is less than 0.1 dB. However, any amplitude variation is removed by subsequent limiters in the multiplier chain.

c. Modulator design (actual). There are several factors that cause the actual design to deviate from the ideal case, such as:

(1) The modulator diodes may be biased at a point that does not provide linear level changes.

(2) RF delay changes occur in the modulator as a function of the modulation voltage.

(3) A pair of modulators may be unbalanced, causing unequal changes in level.

Consider first the bias of the modulators. Figure 6 shows a typical signal level versus modulation voltage for the amplitude modulator. Point A on the curve indicates the bias for linear modulation as described in the ideal case. B and C represent bias points that produce nonlinear amplitude variation with modulation voltage. Assume the modulators are biased at point B and that the modulation voltage increases the RF outputs of M1 and M2 by 1.1 but decreases them by only 0.9, causing a 10% amplitude linearity distortion. From Eq. (2)

$$\phi = \tan^{-1}\frac{1 + 1.1\,m}{1 - 0.9\,m} - 45 \deg \tag{7}$$

$$S_0 = \left.\frac{d\phi}{dm}\right|_{m=0} = \left.\frac{0.99009}{m^2 + 0.19802\,m + 0.99009}\right|_{m=0}$$
$$= 1 \text{ rad/modulation unit} \tag{8}$$

$$S_1 = S_0 - \frac{S_0}{100}$$
$$= 0.99 \text{ rad/modulation unit at 1\% nonlinearity} \tag{9}$$

Then from Eqs. (8) and (9)

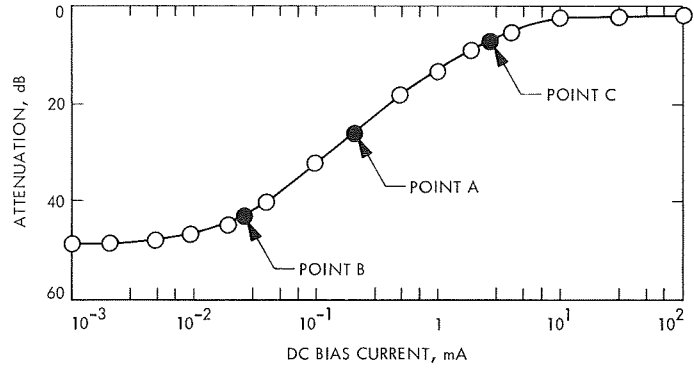$$m_{\max} = 0.0417131 \text{ modulation units} \tag{10}$$

Fig. 6. Characteristics of amplitude modulator

and from Eqs. (7) and (10)

$$\phi_{\max} = \tan^{-1}\frac{1 + 1.1\,m}{1 - 0.9\,m} - 45 \deg = 2.38131 \deg \tag{11}$$

Thus, biasing at point B on the curve shown in Fig. 6 greatly reduces the linear phase range.

If, on the other hand, the amplitude modulators are biased at point C of Fig. 6 where the modulation voltage increases the RF output by 0.9 but decreases them by 1.1, then

$$\phi = \tan^{-1}\frac{1 + 0.9\,m}{1 - 1.1\,m} - 45 \deg \tag{12}$$

$$S_0 = \left.\frac{d\phi}{dm}\right|_{m=0} = \left.\frac{0.990099}{m^2 - 0.19802\,m + 0.990099}\right|_{m=0}$$
$$= 1 \text{ rad/modulation unit} \tag{13}$$

$$S_1 = S_0 - \frac{S_0}{100} = 0.99 \text{ rad/modulation unit} \tag{14}$$

at 1% nonlinearity. Then from Eqs. (13) and (14)

$$m_{\max} = 0.198025 \text{ modulation units} \tag{15}$$

and from Eqs. (12) and (15)

$$\phi_{\max} = \tan^{-1}\frac{1 + 0.9\,m}{1 - 1.1\,m} - 45 \deg = 11.4215 \deg \tag{16}$$

at the negative 1% distortion point.

The region between the zero modulation and the negative 1% point was investigated. It was found that the phase slope is not monotonic; however, at no point in this region does the nonlinearity exceed ±1%. It can be shown that the same $(-\phi)$ linearity is obtained when a negative modulation voltage is applied.

Selecting a nonlinear bias point C has increased the linear range over the ideal case. This is a result of compensating the nonlinear arctan function with the nonlinear characteristics of the amplitude modulation.

Another contributing factor to nonideal performance is the carrier phase delay change versus attenuation of

Fig. 7. S-band modulation spectra: (a) ~ 2 dB carrier suppression; (b) carrier suppressed

each amplitude modulator, which constitutes approximately 15% of the total desired phase deviation. This phase shift is relatively linear over the operating amplitude range of the modulators of ±1 dB and does not contribute significantly to nonlinearity. The alignment procedure assures that both the phase delay characteristics and the differences between the characteristics of the modulators are compensated by selection of the proper bias.

The photographs in Fig. 7 show S-band phase-modulation spectra (2110 MHz) using the new phase modulator. In Fig. 7a the carrier has been suppressed approximately 2 dB, and in Fig. 7b the carrier has been nulled. In both cases the modulation signal was a 100-KHz square wave with a rise and decay time of 10 ns. The existence of even-order harmonics is partly due to the rise time of the modulating signal. To obtain the photographs, the 66-MHz output from the modulator module was frequency-multiplied ×32 using standard Block III C S-band exciter subassemblies.

d. Conclusion. The use of amplitude modulation techniques to obtain a linear phase modulator has been demonstrated. Nonlinearities of less than 1% up to an index of 2.4 rad at S-band have been attained. The modulator itself has a bandwidth greater than ±10 MHz and can handle square-wave modulation signals up to 1 MHz. However, in the present Block III C exciter, the bandwidth is limited by the frequency multiplier chain following the modulator.

4. 400-kW Transmitter Controls, R. L. Leu

a. Introduction. The size and complexity of the 400-kW transmitter system demands a larger and more reliable control system. The new system uses solid-state discrete logic and monitor circuits. The new control system for the DSN 400-kW transmitter is under test at DSS 13 and is being static-tested in the laboratory. Preliminary testing of these circuits at DSS 13 proved them to be very satisfactory.

b. Control system. The control system is made up of a master control and four auxiliary controls as shown in Fig. 8. The system controls, monitors, and protects the klystron amplifier. (The motor-generator controls are part of the 1-MW motor-generator and are not discussed in this article.)

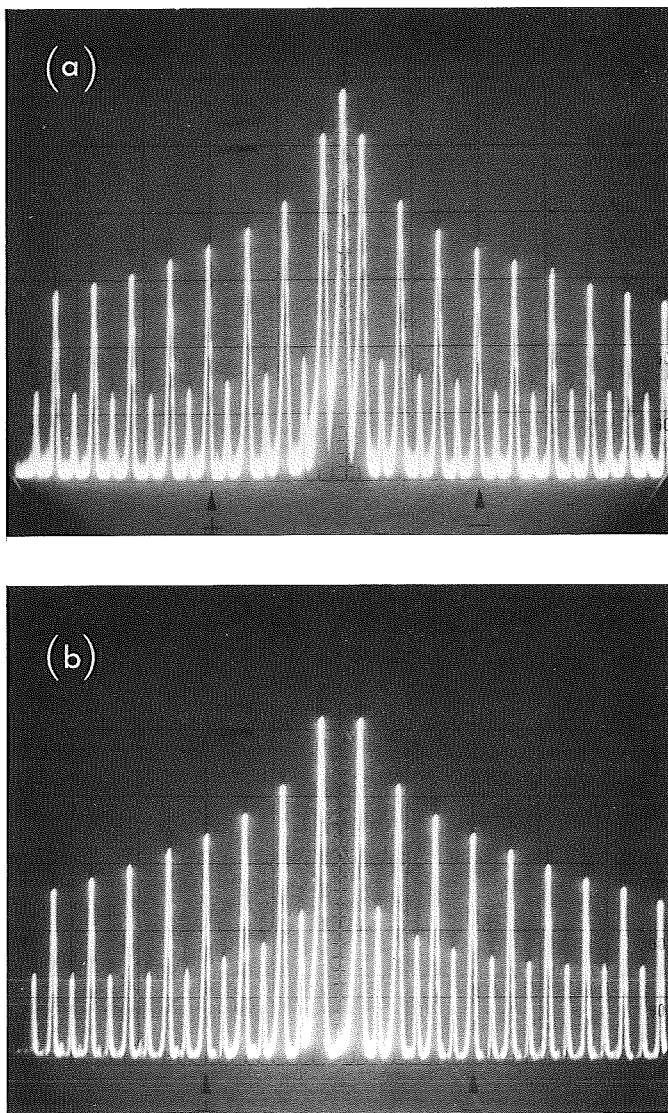*c. Local control console.* The local control console is the master control of the system. All system interlock,
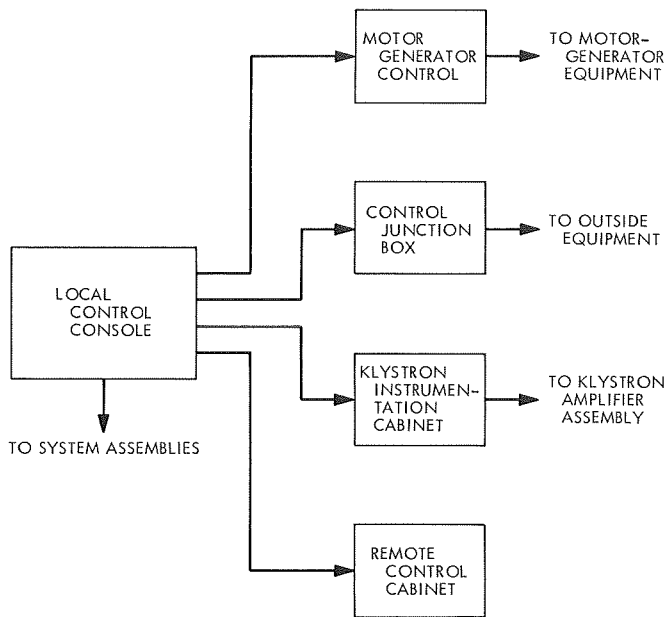
Fig. 8. 400-kW transmitter control system

monitor, and control functions are available on the terminal boards. This has been done to prepare for future computer control and monitor of the 400-kW transmitter. However, for complete computer control, additional functions will be required, and the termination bay is designed for the addition of more terminals.

To improve the system reliability and performance, solid-state logic has been designed for the interlock, control, and monitor functions. The relay interlock logic presently used in transmitter systems is being replaced by digital *and*-gate circuitry. The relay function used to illuminate fault and status lamps is being replaced by *lamp drivers*. The *on-off* control functions are being replaced by bistable circuitry. The logic units are designed to operate on an input signal between 15 and 30 Vdc. There are several additional advantages to using solid-state logic as opposed to relay logic. The size of the total logic chassis is about 1/10 the size of the existing relay assembly; power to energize the logic is 1/20 that required for relays; and the logic is more accessible for maintenance and trouble shooting.

Monitoring circuits to drive meters at remote locations have been designed, utilizing integrated differential amplifiers. These circuits are being used in the 450-kW transmitter at DSS 13 and have operated without failure or problems for the past 4 mo. The new design gives more reliable meter readings at the remote locations, decreased drift with temperature changes, and can be disconnected from the driving source without changing the local monitoring meter calibration.

d. Control junction box. This unit is located in the transformer/rectifier building north of the antenna. The control J-box is used as a control distribution and interlock status accumulation center for all outside equipment on the ground. The J-box contains a small logic chassis with summing logic, lamp driver, and bistable circuits. Interlock faults are summed into major fault categories and sent to the local control. The J-box has fault display lamps to indicate the precise fault of the local equipment. The lamp drivers are used for turning on and off the outside equipment on commands sent from the local control console.

e. Klystron instrumentation. The instrumentation cabinet will be located in the tri-cone with the klystron amplifier. This assembly is used for control and monitor of the 400-kW klystron amplifier. The control and interlock functions are: filament power, RF drive input, coolant flow, vacuum power, detection of waveguide arcs, and excessive reflected power. The instrumentation assembly monitors the klystron RF output power, RF reflected power, RF input power, and coolant flow.

f. Remote control. This unit is a transmitter system remote monitor with limited control. To operate the transmitter from the remote control requires that all auxiliary power supplies and motor–generators have been previously energized. The remote control design is such that it can be completely disconnected from the system without affecting the operation, with one exception: for safety purposes a *safe-run* key interlock is in series with the *beam voltage on* circuitry. The remote control is a self-contained unit and has a control logic assembly consisting of 15 lamp drivers, one bistable circuit, and a separate dc control power supply. This design then allows the remote cabinet to be placed several thousand feet from the local control and still function properly.

This unit has been tested at DSS 13 for 30 days in the R&D 450-kW transmitter system. Only two failures occurred during this period: one failure was not a design problem and the other failure was caused by the inductive kick of a relay in the old system with which it interfaced. The problem was corrected by adding damping diodes.

The local control console and the klystron instrumentation cabinet will be tested at DSS 13 prior to installation at DSS 14. Static tests only will be conducted on the

control J-box, and preliminary testing of the motor–generator controls will be started.

5. Installation of High-Voltage Power Supply and Cooling System at DSS 14, J. R. Paluka

a. High-voltage power supply components. The major components of the high-voltage power supply and cooling system for the Mark III 400-kW DSN transmitter have been placed on their various pads and in the vault room. In addition, the mechanical alignment and shimming of all the rotating machinery has been completed. Power wiring to the major components is now under way.

Figure 9 is an overall view of the major components of the high-voltage power supply. The top left unit in this view is the 3500-hp, 2400-V, 3-phase, 60-Hz synchronous motor of the main motor–generator set. To its immediate right is the 1300-kV-A, 400-Hz, 3-phase generator which powers the high-voltage power supply. The eddy current clutch and 300-hp cranking motor appear to the right of the generator.

The box-shaped unit in the left center of Fig. 9 is the drawout disconnect for the 3500-hp motor. To its right is the breakmaster for the 1300-kV-A generator and finally, to its right appears the starter for the 300-hp motor. In the left foreground is the high-voltage vault room and to the extreme right is the still and chiller pad. Installation has been partially accomplished.

Motor–generator set. Figure 10 is a view of the main motor–generator pad looking to the south. The pedestal of the 210-ft DSS 14 antenna appears in the background. Progress in the areas of conduit fitting and wire pulling is evident from this view. Conduit and power wires have been installed for the motor starter, breakmaster, and drawout units.

Still and chiller. Figure 11 is a view of the still and chiller pad. These units will be used to provide a ready means of replenishing pure cooling water for various components of the transmitter.

In the right background of Fig. 11 is the auxiliary heat exchanger. This heat exchanger will be used to cool the eddy current clutch and the high-voltage power supply. Power wire has been pulled to this unit.

High-voltage power supply. The high-voltage power supply is capable of a 1-MW output and will be operating at approximately 64 kV for the Mark III klystron.
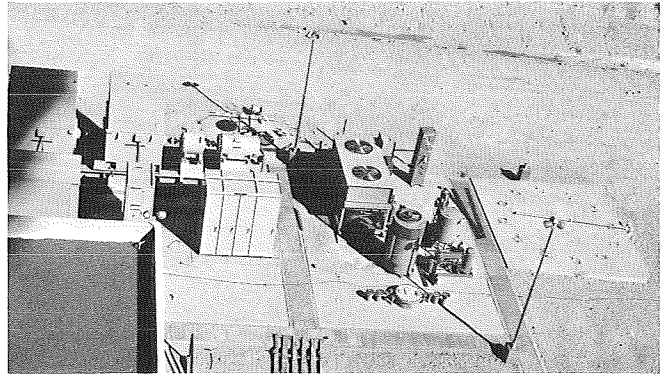

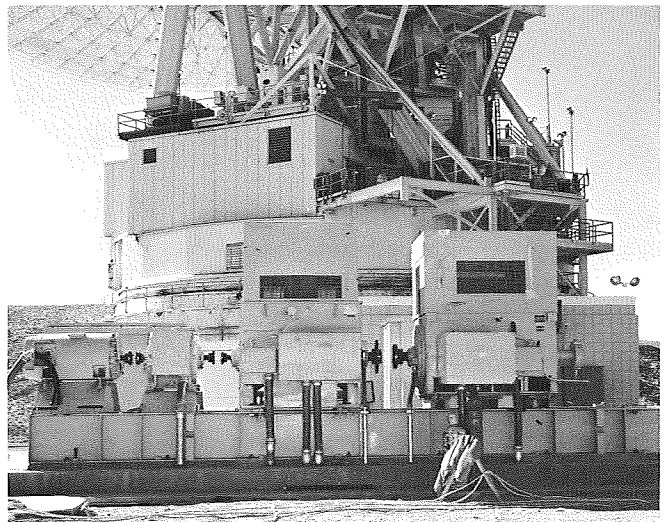Fig. 9. High-voltage power supply
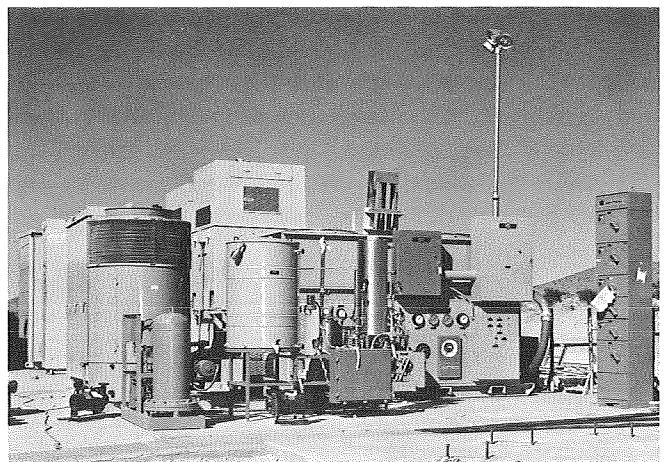

Fig. 10. Main motor–generator

Fig. 11. Still and chiller pad

Weight of this power supply is approximately 42,000 lb. Power wiring has been pulled to all components with the exception of the high-voltage output wiring.

Main heat exchanger pad. The main heat exchanger pad does not appear in Fig. 9, but is located about 350 ft east of the still and chiller pad. Major assemblies have been installed on this pad and power wiring has been pulled.

The main heat exchanger, which has five 10-hp fans and four 50-hp pumps, is capable of dissipating 1 MW of heat. Under normal operations at 400 kW, only two pumps will be used at one time.

This main water-to-air heat exchanger, which uses a water–glycol solution will operate into an antenna-mounted water-to-water heat exchanger (pure heated water) which, in turn, will be used to cool the klystron in the tri-cone base.

b. System testing. System testing should begin on December 1. Prior to that time the power-supply component wiring will be completed. A dummy load for the power supply will be installed. Control wiring, which is fabricated and on site, will be installed by the electrical contractor. The alidade (water-to-water) pumping unit will be mounted on the antenna. Subsystem level testing will be done.

6. DSIF Monitor System Phase I Development, R. Flanders

The DSIF Monitor System Phase I (DSIF MSØI) provides the DSSs in the DSIF with a capability for monitoring the performance and alarm status of the various subsystems within each station. A record is also maintained on magnetic tape for postmission analysis, and real-time status and alarm messages prepared for transmission to the SFOF via high-speed data line.

The DSIF MSØI consists of a hardware segment composed of the Digital Instrumentation Subsystem Phase II (DIS II) and the station monitor and control console (SMC), together with a software segment represented by the DSIF MSØI program running in the DIS II.

The current effort involves the update of both the hardware and software, in order to provide monitor support for *Mariner* Mars 1971 and subsequent missions. Hardware development has been initiated to implement six stations (DSSs 12, 14, 41, 51, 62, and the Cape Kennedy

Spacecraft Compatibility Station) with a capability for display of status and alarm data for station operational personnel. This equipment will typically consist of the following elements:

(1) Cathode ray tube (CRT) display.

(2) Image refreshing logic.

(3) Character generator.

(4) Addressable memory for data storage.

(5) High-speed data input/output registers.

(6) Control logic.

Data communication between the display equipment and the DIS II will be serial by bit via the high-speed data register and will be transmitted at rates of up to 50 kilobits/s. A keyboard on the terminal will provide for manual data entry and for addressing the display format of specific interest.

The principal effort in the software development involves the extension of the existing DSIF MSØI program. The present version was implemented on an interim basis for support of *Mariner* Mars 1969. As such, it offered considerably less than the full Phase I monitor capability. The version of the MSØI program to be implemented for *Mariner* Mars 1971 will contain routines for angle and range data processing, which were deleted from the present version due to core memory limitations. In addition, the program will provide for output to a graphical (X-Y) plotter for recording and displaying critical parameters. Typical parameters to be plotted as a function of time would include signal strength (AGC), static phase error, signal-to-noise ratio, transmitter power output, system temperature, and pseudoresiduals for doppler, angles, and range.

The program will also contain the capability to process data for display on the CRT and to output various display formats under operator control (addressable from the SMC display terminal keyboard). A revision of the present system for processing monitor criterion data (MCD) sets is also under consideration to reduce the volume and variations of MCD and provide for their definition at the individual DSS. The capacity for receiving and processing MCD, tracking, and RF predicts by way of high-speed data inbound to the station also offers a new capability.

The content of the high-speed data periodic and alarm messages to the SFOF is also under study, to investigate

the possibility of returning higher resolution data. The larger high-speed data block (1200 bits instead of 600 bits), together with a possibility for higher transmission rates may result in a redefinition of the DSN periodic and alarm messages.

The program will also be required to process monitor data from subsystems and equipment newly implemented for *Mariner* Mars 1971 support. This will include additional telemetry and command functions, and frequency and timing subsystem phase II (FTS II) monitor input parameters, when available.

The monitor functions within the DSS are also being redefined to be of greater value to station personnel for DSIF performance and alarm monitoring. The operational experience gained through use of the DSIF monitor system during the *Mariner* Mars 1969 missions will be reflected in these changes. Greater flexibility and control over alarm parameters to be displayed and the manner in which they are displayed will be provided at the station level. The means for calling up and displaying formats containing specific parameters will allow operational personnel to monitor critical parameters in greater detail than previously possible.

In summary, the DSIF monitor system phase I hardware is being extended, and the software is undergoing an extensive revision to process the new monitor functions to be implemented for *Mariner* Mars 1971 and increase the value of the monitor system to the DSIF by incorporating the experience gained in support of *Mariner* Mars 1969.

7. Frequency and Timing Subsystem, Phase II, M. Galitzen

For the past year the frequency and timing subsystem at DSSs 14, 41, 51, and 62 has been in a hybrid configuration referred to as FTS I/II. This configuration was necessary because of problems in the use of commercial equipment. The FTS II configuration required two commercially built isolation amplifiers for signal distribution. The digital isolation amplifier (DIA) exhibited bit pickup, bit dropout, and oscillation problems. The precision frequency isolation amplifier exhibited amplitude modulation, low isolation, spurious signals, and other lesser problems.

During the past months these problems have been under investigation, and steps have been taken to correct

them. The DIA design has been changed, and the first reworked unit has been returned from the vendor. This unit was tested at JPL by connecting the FTS II outputs to the DIA. The DIA outputs were then connected through an FTS junction module to a load bank. Through one of the junction modules parallel outputs, monitor points were connected. Data from the points was recorded on a strip chart recorder.

No failures of the DIA were detected during this testing. This unit is now at DSS 14 where it has been installed in the FTS racks. At this time preliminary tests have revealed no problems with the DIA. On three separate shifts the FTS II configuration was connected, and the DIA's performance was flawless. At the end of these test periods the station was restored to the FTS I/II configuration for operational use. Further FTS II testing at DSS 14 will be undertaken before an effort is made to convert to the FTS II system operation on a permanent basis.

The precision frequency isolation amplifiers have been under investigation at JPL and at the standards laboratory at the Goldstone DSCC. These performance tests have verified that the amplifiers under test have been improved by the vendor. One of the units has been tested at DSS 12. The tests were accomplished by observing the stations' operation with and without the amplifier in the operations loop. Future evaluations are necessary before these units can be used.

The auxiliary reference divider and its control panel have been installed at DSS 14. The auxiliary divider is a working spare to the FTS II reference timing pulse generator. In the present configuration the spare divider provides a 1-pulse/s back-up pulse to the FTS standard 1 pulse/s. The standard FTS 1-pulse/s signal is clocked from signals derived from the FTS primary frequency standard. The auxiliary divider now provides an additional 1 pulse/s which is clocked from a secondary frequency standard.

The control panel for the auxiliary divider provides a means of synchronizing the auxiliary divider's 1 pulse/s output to the FTS primary 1 pulse/s signal. In addition the auxiliary reference divider control panel provides status indications on the 1-MHz secondary signal used to drive the auxiliary reference divider. At present it is planned to install this auxiliary system as DSSs 12, 41, 51, and 62 when these stations are converted to the FTS II configuration.

8. Analog Recording Flutter Sensitivity Tests, J. P. Buffington

In SPS 37-58, Vol. II, pp. 127–129, it was shown that the primary source of the data degradation in the telemetry recording subsystem is time displacement error (TDE). This was deduced from the shape of the constant 1-dB data loss flutter amplitude FA versus flutter frequency curves. The relationship

$$\text{TDE} = (FA)/\omega \cos \omega T$$

(where ω is the angular velocity of the flutter component) was developed, and initial steps have been taken to optimize the recording subsystem.

That amount of TDE which results in a 1-dB data loss can be computed by taking values of FA and ω off the data curves in the referenced article and substituting them in the equation above. Table 1 gives the permissible TDE for three subcarriers and their corresponding data rates.

Table 1. Values of TDE for subcarriers

Subcarrier frequency, kHz	Data rate, bits/s	TDE for 1-dB data loss, μs
24	8 1/3	25
34	66 2/3	10
259	16,200	3

A survey was made of the recorder field to determine the industry capability in minimizing TDE, and the Ampex FR 1600 tape transport was selected for evaluation. An abbreviated table of specifications is shown in Table 2, together with specifications for the FR 1400 (presently used in the DSIF net telemetry recording subsystem).

Table 2. Comparison of FR 1400 and FR 1600 at 30 in./s

Specification	FR 1400	FR 1600
Capstan servo carrier frequency	60 Hz	50 kHz
TDE, μs	400	2
2-Sigma flutter, %	0.25	0.30
Servo crossover Frequency (12 dB per octave), Hz	2	80
Reproduce bandwidth, kHz	350	500

The very large improvement in TDE in the FR 1600 over the FR 1400 is due to a substantial improvement in

the bandwidth of the capstan servo and in the use of vacuum columns in the tape path to provide isolation from reel disturbances. The following schematic drawings illustrate the differences in the two mechanical tape transports. The relatively large diameter of the capstan on the FR 1600 facilitates reducing the length of magnetic tape between the capstan and the magnetic reproduce heads, which makes possible the relatively wide capstan servo bandwidth (Fig. 12).

The FR 1600 transport, when used as a subcarrier recorder–reproducer does, in fact, hold the TDE to a low enough value to allow the SDA to lock on to the reproduced data without any external flutter and/or TDE correction. The results (exclusive of conversion losses) are given in Table 3.

Table 3. TDE measurements for FR 1600 transport

Subcarrier frequency, kHz	Tape speed, in./s	ST_B/N_0 real-time	ST_B/N_0 after recording	Δ
259	30	3.5	2.4	1.1
34	15	5.6	4.7	0.9
24	15	5.8	5.0	0.8

These results were obtained with the capstan reference recorded on the adjacent track to the data in the same head stack. Tests indicate that the TDE of the FR 1600 is about four times as great under these conditions as it is between the local reference and the recorded reference track. A method of multiplexing the recorded reference in with the recorded subcarrier to take advantage of this improvement is being investigated in the laboratory at this time (Fig. 13).

It would appear that substantial improvements in the TDE of longitudinal recorders will be effected in the future, though in smaller increments and at great difficulty because of limitations in the supporting technology (e.g., grinding, machining, bearings, as well as the electromechanical components such as motors, etc.). As a result, electronic flutter and TDE correction methods are being studied in an effort to further optimize the recording subsystem. A block diagram of a TDE correction system that has been used with considerable success with rotary head transports is shown in Fig. 14.

In this system, a pilot tone from the local reference is multiplexed with the data and then separated out with comb filters and the reproduced pilot tone is again com-
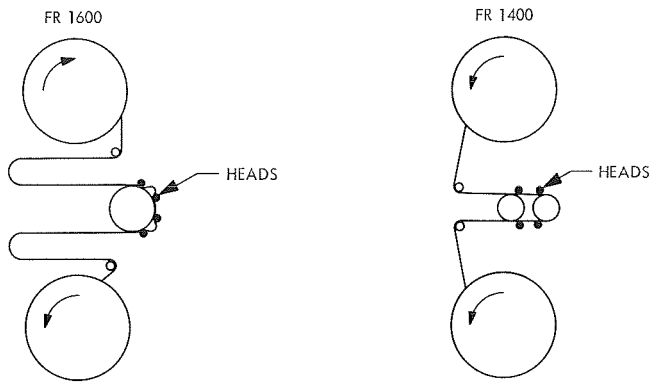
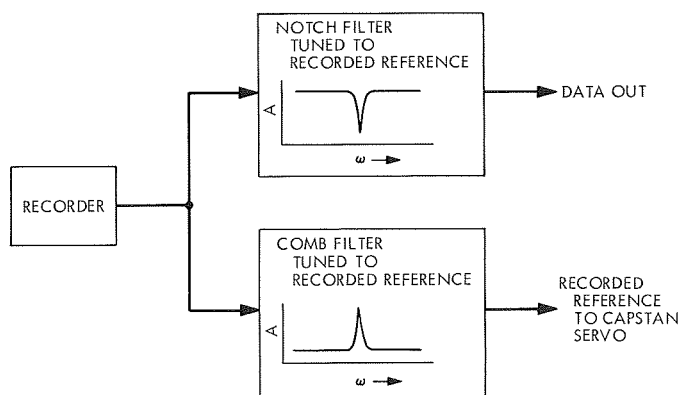**Fig. 12. Tape paths of FR 1400 and FR 1600 recorders**

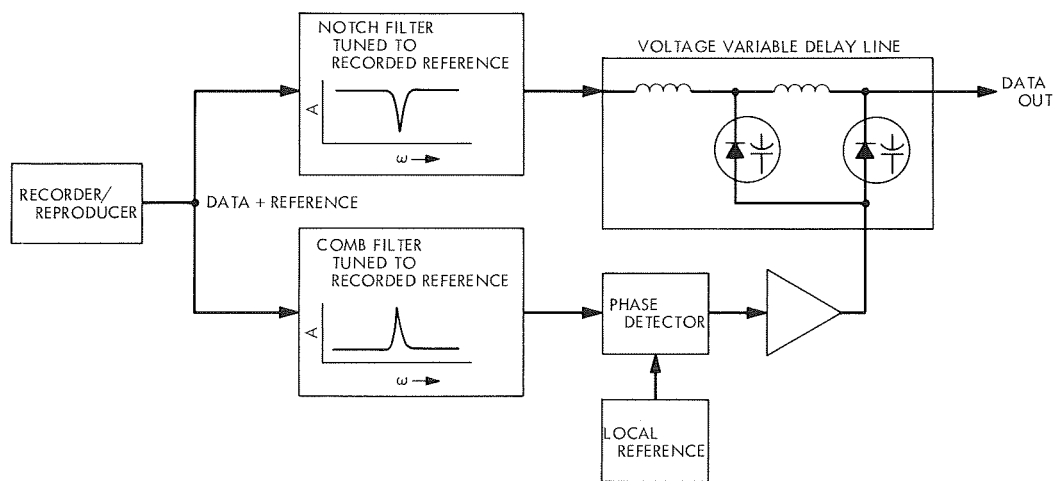**Fig. 13. Reproduce system using reference multiplexed with data**

pared with the local reference; the difference, proportional to the time displacement error, is used to program the voltage variable delay line. In effect, the phase detector generates negative TDE which, when added to the positive TDE in the data, tends to cancel out in the voltage variable delay line.

9. Motor Field Control, T. W. Rathbun

a. Introduction. The 1750-hp motor generator set at DSS 13 is used to supply 400-Hz primary power to the 70-kV high-voltage power supply. It is important that the motor be operated at unity power factor so that the incoming power line is affected as little as possible by load conditions at DSS 13. This minimizes interaction between facilities at Goldstone DSCC, improves voltage regulation, and reduces power costs. Power-factor correction may be accomplished by adjusting field current in the synchronous motor. Originally, the power factor was controlled by a carbon pile regulator. The operation of the carbon pile regulator depends upon sensing low-line voltage caused by the high-line current associated with low-power factor. However, the incoming line to DSS 13 was of such low impedance that the line voltage was not sufficiently affected by low-power factor so the power factor correction did not operate reliably. During the start cycle the synchronous motor is acting as a generator whose output is controlled by field current. It is, therefore, possible to match the voltage output of the motor with the incoming line voltage. In the original installation no provisions were made for matching the line and motor voltage. The result was that the motor's protective circuitry prevented synchronization until man-

Fig. 14. Time-displacement error correction system block diagram

ual adjustment of the field current matched the voltages. This adjustment resulted in a power factor error when the motor was on the line, and readjustment was necessary.

A commercial power factor control unit was tested to determine its suitability to replace the carbon pile regulator. However, the operation of this unit was not satisfactory because of errors in the order of 5% when the motor was lightly loaded.

b. Description of new unit. A new control was designed, breadboarded, and installed at DSS 13. This control contains line-motor voltage matching circuitry (Fig. 15), and a digital phase detector (Fig. 16) for power-factor control after the motor is brought on the line.

The line-motor voltage matching section of the motor field control contains a voltage transducer, which is a full-wave bridge that is linearized by the use of a small value of resistance in parallel with the output resistance. A transducer is used on both the line and motor voltages. The dc voltage output of these transducers is then applied to a voltage comparator circuit whose output controls the motor field-power supply.

The power factor section of the motor field control consists of a digital phase detector, which samples the motor current and motor-voltage phase relationship. The output of the phase detector is zero at unity power factor,
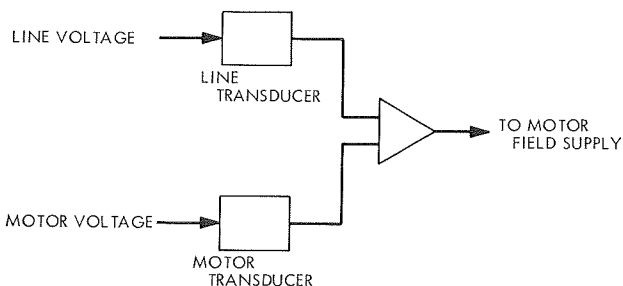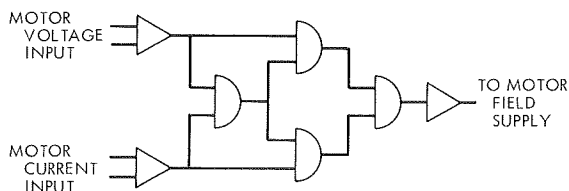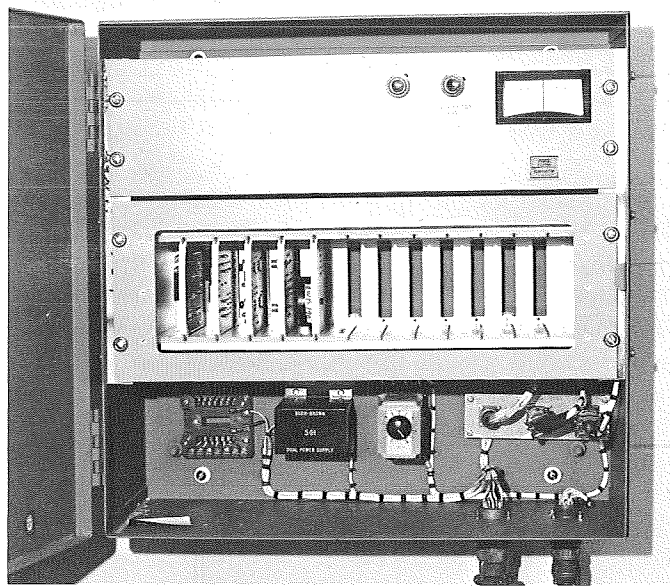

Fig. 17. Prototype motor field control on time-synchronization transmitter

positive for a leading power factor, and negative for a lagging power factor. This output is integrated and applied to an operational amplifier capable of driving the motor field-power supply, resulting in a power-factor control that is not dependent upon line variations nor upon motor loading for control. Laboratory tests of the phase detector showed an accuracy of ±0.5% at worst-case conditions.

The original breadboard has been in operation at DSS 13 in the S-band system for approximately 1 yr with no failures. A prototype (Fig. 17) has been built and installed in the X-band clock synchronization transmitter system of DSS 13. Operation of this unit has been satisfactory for about three months.

c. Future plans. Two production units are scheduled to be delivered during the next reporting period. One of these units will replace the original breadboard model at DSS 13, and the other will be installed at DSS 14 during December of this year.

B. DSN Projects and Systems Development

1. Clock-Synchronization System Performance, *H. W. Baugh*

a. Introduction. A precision clock-synchronization network is being established to meet the requirements of the DSN. The immediate goal for this system was to provide

Fig. 15. Line-motor voltage matching circuit

Fig. 16. Digital phase detector logic

synchronization between all DSSs committed to *Mariner* Mars 1969 to within 20 μs at the time of planetary encounter. A second objective is to provide correlation to the National Bureau of Standards (NBS) or to the U.S. Naval Observatory (USNO) to within 5 μs for the DSN as a whole.

The system uses a computer-controlled transmitter at DSS 13 to send timing signals to the remote DSSs by way of an X-band carrier that is reflected from the surface of the moon. References to previous articles are given in SPS 37-56, Vol. II, pp. 142–143. The most recent article on the system was in SPS 37-57, Vol. II, pp. 151–152. The present article will cover the operations of the system from April 15 to October 10, 1969.

b. Implementation. The installation of clock synchronization equipment at four overseas DSSs was completed during this period. DSS 41 went into operation on June 20. DSS 42 made a gradual transition from the prototype receiver to the new equipment, replacing one assembly at a time. (Its first complete operation using all new equipment took place on June 25.) DSS 62 became operational on July 5, followed by DSS 51 on July 22.

The signal-to-noise performance of the new receivers at DSS 41 and 42 was initially very poor; the cause was determined to be the leakage of 100-kHz pulses into the 100-kHz IF amplifier via the $+12$ Vdc supply line to the oven of the crystal filter. All the new units were rewired to make use of other supply voltages that did not have the 100 kHz noise. Following this change, all the receivers performed satisfactorily and the system could be used to adjust the DSS clocks into close synchronization for the *Mariner* Mars 1969 encounter operations.

c. Calibration. The clock at DSS 14 can be checked by two different measurement techniques. The clock-synchronization receiver provides one means; timing signals direct from the Goldstone Standards Laboratory (via microwave link) provide the other. Since the latter signals are also sent to DSS 13, the offset of DSS 14 with respect to DSS 13 is known to within 1–2 μs. The error of closure between the known offset at DSS 14 and the clock-synchronization receiver measurement gives the sum of the calibration errors of the clock-synchronization system. These errors arise from delays in the equipment, from ephemeris errors, and from large variations in lunar topography. Since earlier results at DSS 42 had been sufficiently stable, it was assumed that calibration data of this sort would not be absolutely necessary. However, a reconfiguring of the sources of reference frequencies at

DSS 13, made about July 15, led to an instability in the transmitter coder that caused the calibration of the system to show jumps of as much as 10 μs from one day to the next.

Consequently, on July 27, the DSS 14 clock-synchronization receiver was activated and DSS personnel were trained in operations and data reduction so as to monitor the system during the *Mariner* Mars 1969 encounter periods.

d. Performance. Figures 18 and 19 show the clock offsets with respect to NBS clock CL-8 during a 10-day period around the two encounter events. The clock-synchronization measurements at the overseas DSSs have been corrected for the closure errors observed at DSS 14. These data are shown in comparison with the time polynomials used in the Orbit Determination Program, which are derived by collating all other forms of timing data, i.e., very-low frequency tracking, simultaneous ranging, and some LORAN-C data. It will be seen that the results are all within the ± 20 μs goal, except at DSS 51 where there appears to be an offset of about 30 μs. Further analysis will be required to resolve this problem, which may be due to errors in assessing the data that led to the time polynomials.

e. Current work. A new transmitter coder has been installed at DSS 13. Initial tests indicate that it is not subject to the instability that disturbed the older unit. Further testing is in process.

The prototype receiver has been returned from DSS 42. After it is refurbished, it will be sent to the USNO. When installation is complete, an extensive evaluation will be made over a period of 1 or 2 mo to assist in determining the nature of the ephemeris-related errors in the system.

2. Multiple-Mission Telemetry System Project,

W. S. Baumgartner, N. C. Ham, W. F. McAndrew, D. W. Brown,
M. L. Yeater, C. A. Holritz, J. T. Hatch, and A. D'Amore

a. Introduction. The Multiple-Mission Telemetry System (MMTS) Project was established in February 1967 to design, test, and install throughout the DSN a telemetry system capable of supporting all foreseeable spacecraft, and with performance close to the theoretical. To provide support for *Mariner* Mars 1969, the equipment was required by mid-1968. These objectives have all now been met. All DSN stations, as well as the Compatibility Test Station at Cape Kennedy and the Compatibility
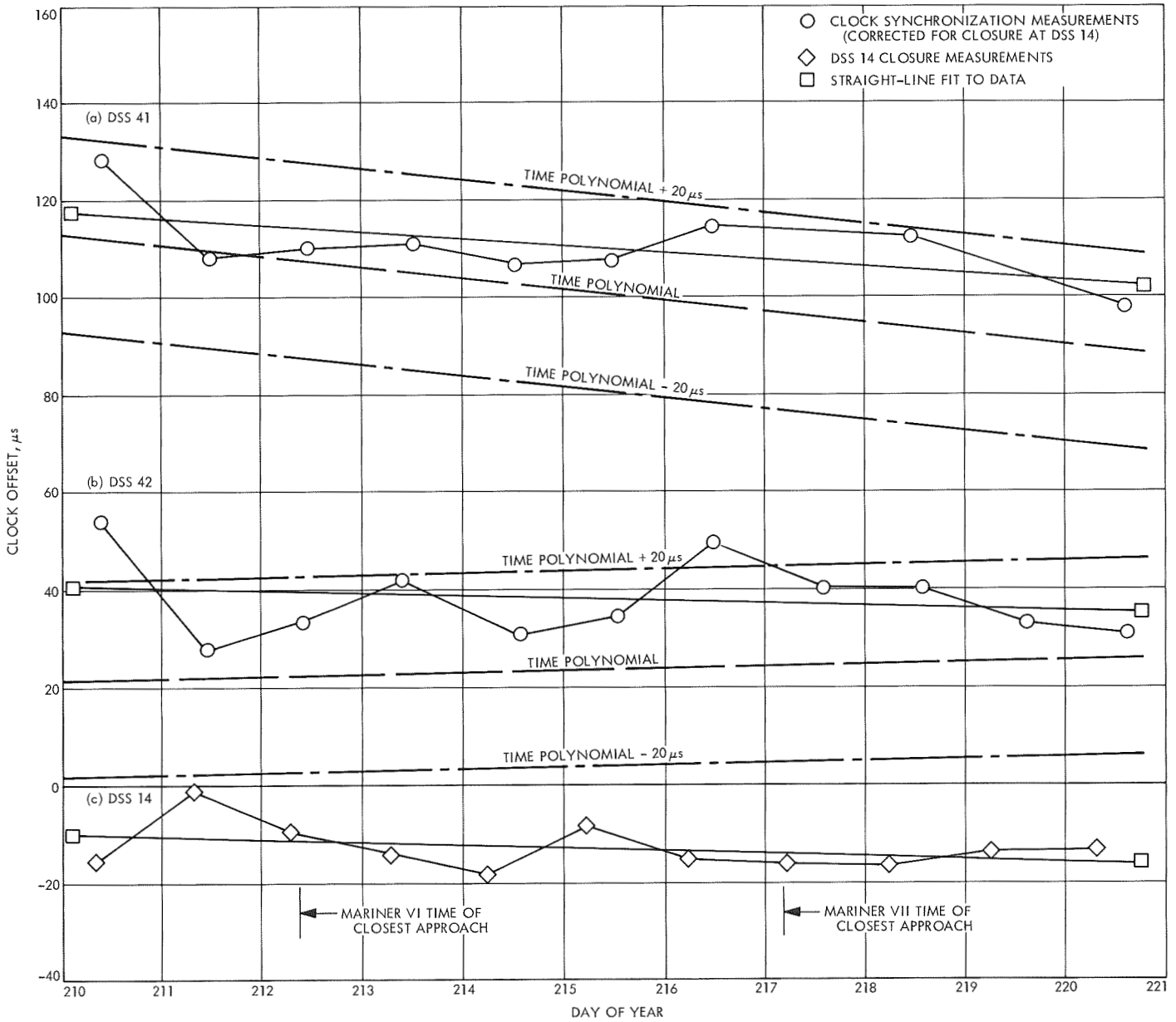
Fig. 18. Clock-synchronization performance for DSSs 41, 42, and 14
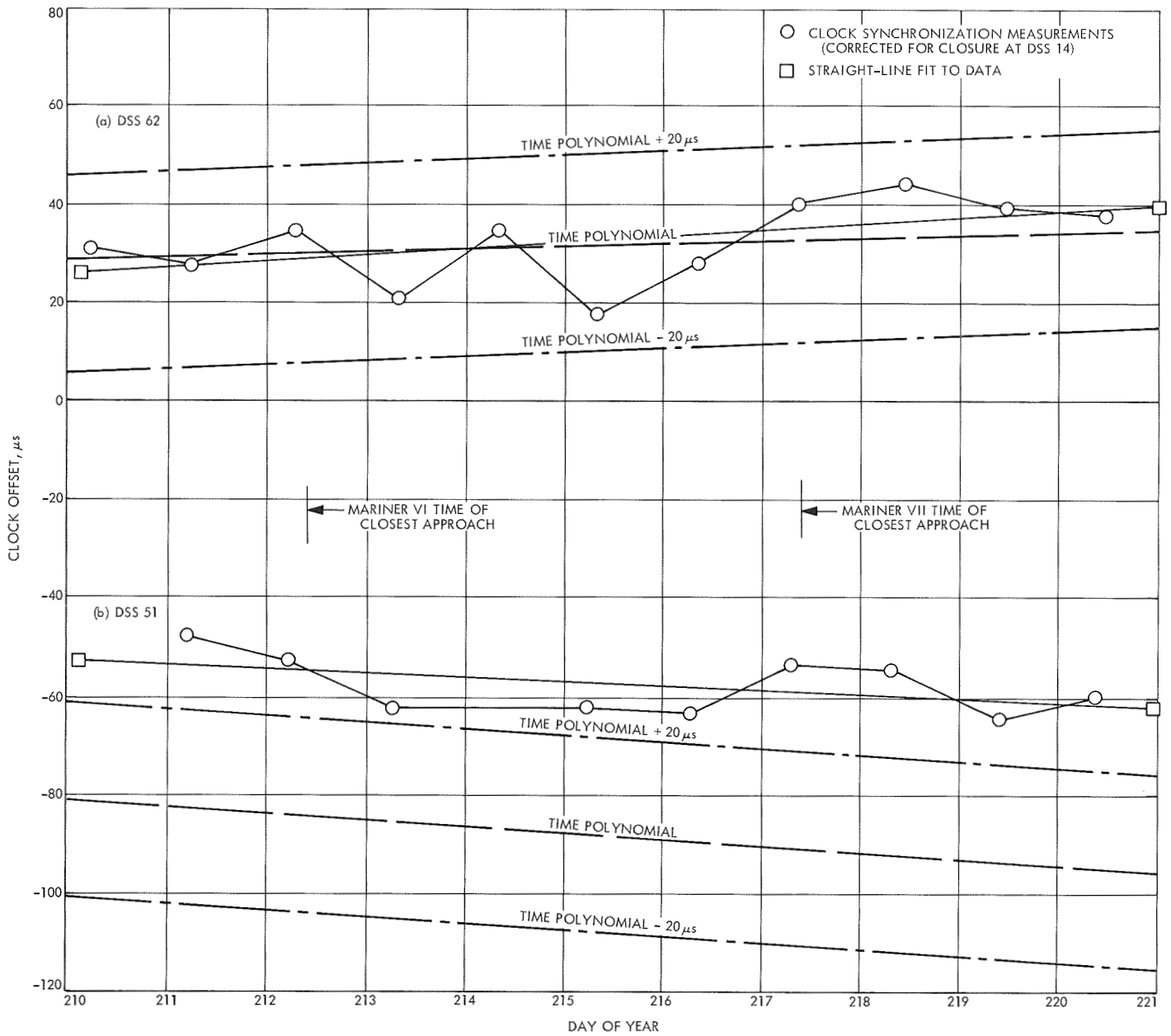
Fig. 19. Clock-synchronization performance for DSSs 62 and 51

Test Area (CTA) at JPL, are equipped with MMTS; the equipment has been extensively evaluated in the laboratory and has successfully supported the *Mariner* and *Pioneer* Projects with performance improved over previous systems.

Detailed analysis and interim test results have been presented in SPS 37-52, Vol. II, pp. 119–143, SPS 37-50, Vol. II, pp. 3–14 and 52-54, SPS 37-49, Vol. II, pp. 98–113, SPS 37-47, Vol. II, pp. 138–142, and SPS 37-46, Vol. III, pp. 175–243. In this article, which will be the final report from the project, an attempt will be made to present the final test results and compare these with the original specifications, outline the present status of the hardware, discuss changes to support future requirements, and report on operational use and results.

b. System verification test.

Performance classification. The objective of this test is to verify the performance of the DSIF MMTS function for non-coded digital pulse-code modulated (PCM) data. Performance is measured by determining the demodulated data probability of error P_e as a function of the overall system's input sideband signal energy per bit-to-noise spectral density ratio ST_B/N_0. Figure 20 is a block diagram of the method used for obtaining measurement data. The input ST_B/N_0 is adjusted for specific values and the detected data is then compared against the input reference data to determine the resultant bit error rate (BER).

To establish a means for evaluating the system's performance characteristics, the system is divided into (1) the receiver assembly, (2) the subcarrier demodulator assembly (SDA), and (3) the telemetry processor assembly.

Specific efficiency coefficients of the assemblies can then define the system's performance characteristics (Fig. 21). The definition of the effective input sideband signal-to-noise for a given bit rate can be stated as

$$R_0 = \frac{ST_B}{N_0}(p)\,(q)\,(r) = \left(\frac{ST_B}{N_0}\right) \text{eff} \qquad (1)$$

In addition to Eq. (1), an additional coefficient m, due to measurement error, is included to normalize the expected test measurements. Therefore,

$$R = R_0(m)$$

$$R = \frac{ST_B}{N_0}(p)\,(q)\,(r)\,(m) = \left(\frac{ST_B}{N_0}\right)\text{eff} \qquad (2)$$

where

$R = $ effective ST_B/N_0

$p = $ efficiency coefficient due to RF receiver tracking loop error

$q = $ efficiency coefficient due to subcarrier reference jitter error

$r = $ efficiency coefficient due to bit synchronization timing jitter error

$m = $ measurement error

(1) RF receiver loop efficiency coefficient p. The equation derived by W. C. Lindsey (Ref. 1) determines the theoretical receiver efficiency coefficient as a function of (ST_B/N_0) eff or R evaluated for various receiver car-
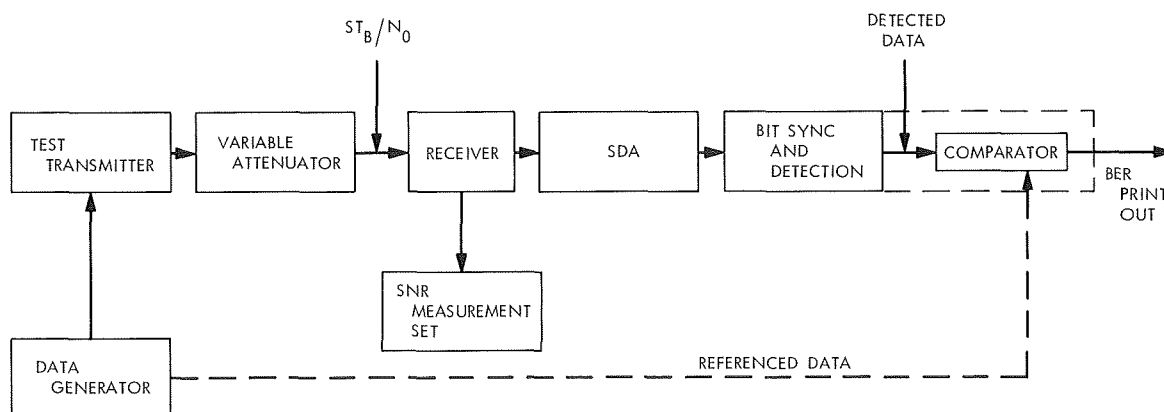

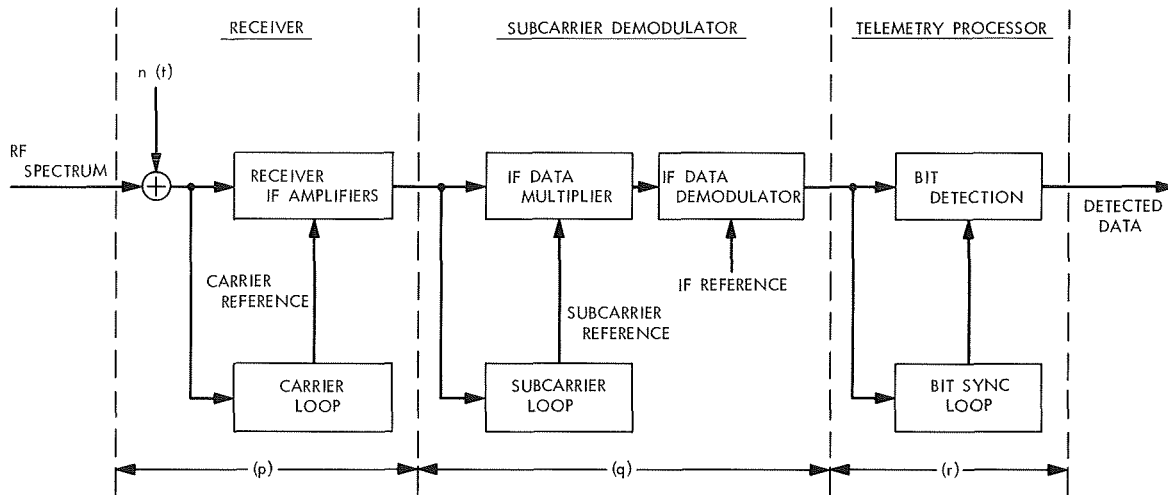Fig. 20. System performance measurement method
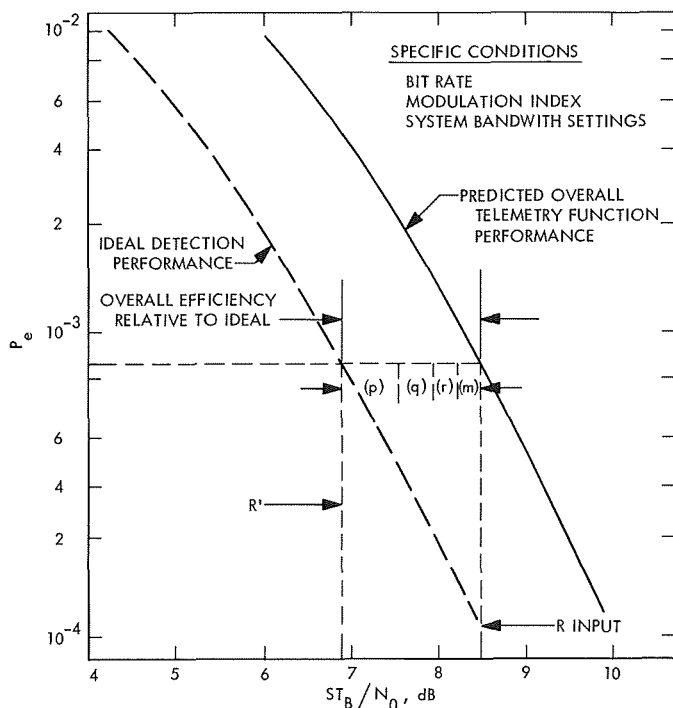
Fig. 21. Simplified system diagram

Fig. 22. Graphical relationship of general efficiency equation

rier loop bandwidth signal-to-noise ratios (SNRs). This equation is expressed as

$$P_E = \int^\pi \frac{\exp{(\rho/\gamma \cos \phi)}}{\pi I_0 (\rho/\gamma)} \text{Erfc} \left[(2R)^{\frac{1}{2}} \cos \phi \right] d\phi \qquad (3)$$

(2) *Subcarrier demodulation efficiency coefficient q.* The ratio of the effective output ST_B/N_0 to the input

ST_B/N_0 of the SDA determines the efficiency coefficient for this assembly. An analysis by M. H. Brockman (SPS 37-46, Vol. III), derives this coefficient as a function of the phase error and is represented by

$$(q) = \frac{\text{output } ST_B/N_0}{\text{input } ST_B/N_0} = \left[1 - \left(\frac{2}{\pi} \right)^{3/2} \sigma_{\theta_n} \right]^2 \qquad (4)$$

where σ_{θ_n} is the rms phase noise error.

(3) *Bit synchronization timing efficiency coefficient r.* The efficiency coefficient due to bit synchronization is more conveniently expressed by the loss in the SNR due to timing jitter of the data correlator. J. W. Layland (SPS 37-46, Vol. III) has derived an expression for determining this loss as follows:

Effective SNR =

$$\frac{ST_B}{N_0} \left\{ 1 - 2 \left(\frac{K}{(1 - K)} \left[\frac{1}{8} \left(\frac{N_0}{ST_B} \right)^2 + \frac{5}{32} \left(\frac{N_0}{ST_B} \right) \right] \right) \right\}^{\frac{1}{2}}$$

(4) *Overall system efficiency.* By combining all the efficiency coefficients, and expressing in units of dB, the overall system efficiency becomes:

$$R(\text{dB}) = S(\text{dB}) + T_B(\text{dB}) + p(\text{dB})$$
$$+ q(\text{dB}) + r(\text{dB}) + m(\text{dB}) - N_0(\text{dB})$$

Figure 22 is the graphical representation of the overall system efficiency equation relative to the ideal detection performance.

Test method. Figure 23 is a block diagram of the system test arrangement used for the verification tests. The telemetry test set provides the reference data for comparison against the detected data and the data-modulated subcarrier for the input test signal. The modulated subcarrier then phase modulates a test transmitter that provides the S-band input signal to the overall telemetry system. The input signal is adjusted to specific values of ST_B/N_0 whose value can be measured by the SNR measurement equipment. After data detection, and comparison to the reference data, the resultant BER is determined.

(1) *Method of establishing input ST_B/N_0.* The technique used for establishing the input ST_B/N_0 consists of accurately measuring the ratio of carrier plus noise power-to-noise power (Y-factor) with the SNR measurement equipment. The power indicator M_1, which measures the power within the 50 MHz bandpass frequency, is adjusted for a reference value with the RF signal source off. Then, the desired ratio $(P_c + P_n)/P_n$ value is inserted in the precision attenuator A_3. With the RF power on and no modulation, attenuator A_2 is adjusted until the power level at indicator M_1 is returned approximately to the reference value. Finally, the true resultant $(P_c + P_n)/P_n$ is accurately measured with A_3. As an example of the adjustment and measurement necessary for a specific test, a typical calculation will be shown. Desired condition:

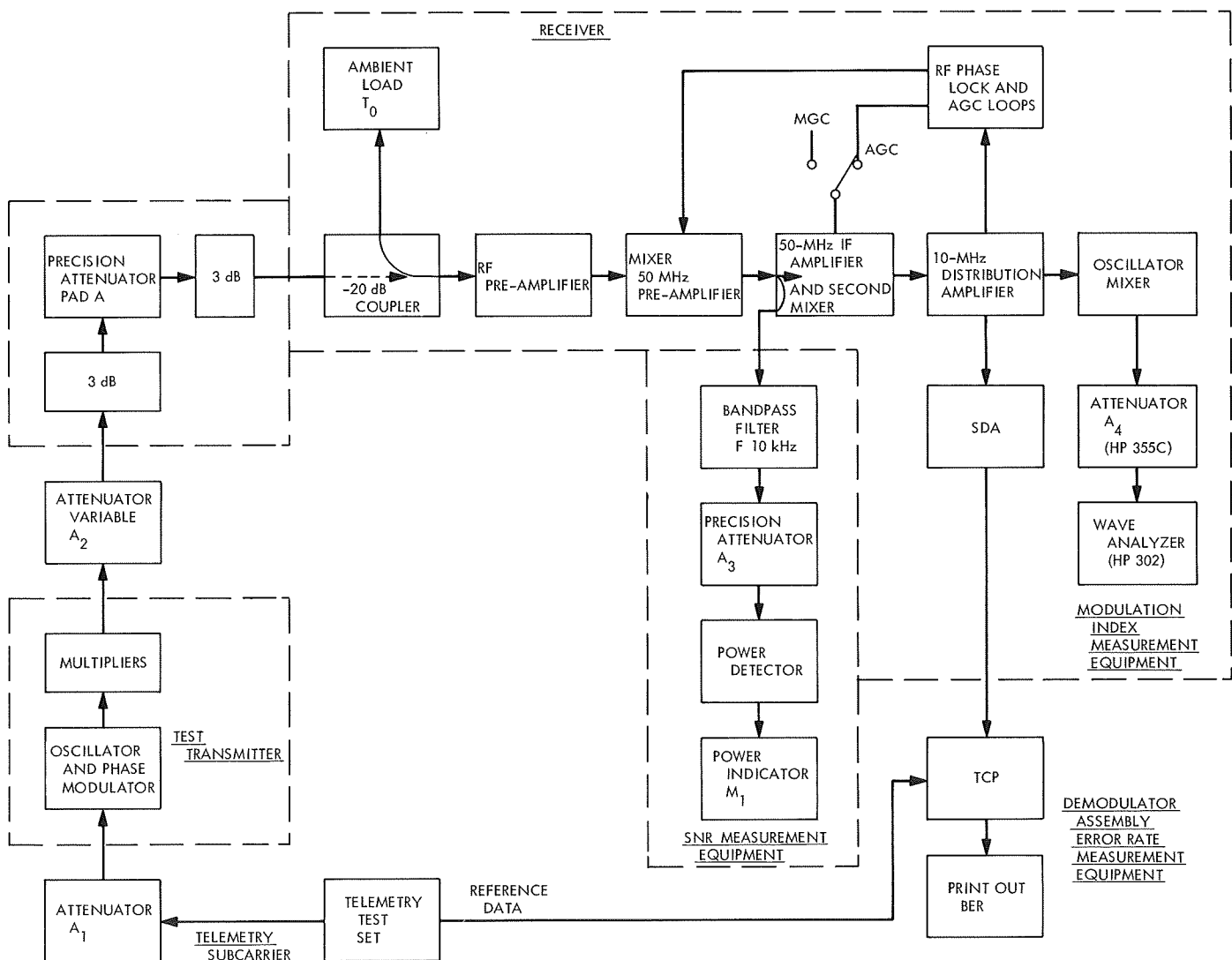$$ST_B/N_0 = 5.2 \text{ dB.} \ (1/T_B = 270 \text{ bits/s})$$

Fig. 23. System verification test arrangement

Then

$$ST_B/N_{0_{ratio}} = 3.311/\text{bit rate duration}$$

$$S/N_{0_{ratio}} = 893.97 \text{ for specific bit rate}$$

$$S/N_{0_{dB}} = 29.51 \text{ dB}$$

$(F, \text{filter bandwidth}) = 9.867 \text{ kHz (typical noise bandwidth value)}$

$\text{Relative bandwidth correction} = 39.94 \text{ dB Hz, } (10 \log 9.867 \text{ kHz})$

Hence, $S/N_{dB} = -10.43$ dB required in 9.867 kHz bandwidth (29.51 dB $-$ 39.94 dB). The desired quantity, S/N, is actually the data SNR or $S/N = P_{data}/P_n$; however, the measured quantity is the carrier SNR without modulation or P_{total}/P_n.

Assuming squarewave modulation and a modulation index of 66.5 deg,

$$\frac{P_{carrier}}{P_{total_{dB}}} = -8.0 \text{ dB;} \left[\frac{P_c}{P_t} = +20 \log \cos 66.5 \text{ deg} \atop \text{carrier suppression}\right]$$

where

$$P_{total} = P_{carrier} + P_{data} \text{ or } 1$$

$$= \frac{P_c}{P_t} + \frac{P_d}{P_t} = \cos^2 \theta + \sin^2 \theta$$

$$\frac{P_{data}}{P_{total_{dB}}} = -0.75 \text{ dB;} \left[\frac{P_d}{P_t} = +20 \log \sin 66.5 \text{ deg}\right]$$

$$\frac{P_{data}/P_n}{P_{data}/P_{total}} = \frac{P_{total}}{P_n}; \frac{P_{total}}{P_{n_{dB}}} = -9.68 \text{ dB}$$

This value would be most difficult to set up and measure directly. Hence, the P_{total} value is set and measured instead at some value above the required value of -9.68 dB. This is accomplished by setting P_{total}/P_n to a modified value with the precision attenuator pad A by-passed (Fig. 24a); then, by replacing the precision calibrated attenuator in the signal line, the proper value P_t/P_n ratio will exist.

Example

Assume that a 20-dB calibrated attenuator is utilized then

$$\frac{P_{total}}{P_n} = -9.68 \text{ dB} + 20.0 = +10.32 \text{ dB}$$

or

$$\frac{P_{total}}{P_{n_{ratio}}} = 10.77$$

and

$$\frac{P_{total} + P_n}{P_{n_{ratio}}} = 10.77 + 1 = 11.77$$

Thus,

$$Y_{dB} = \frac{P_{total} + P_n}{P_{n_{dB}}} = 10.71 \text{ dB}$$

which now becomes the setting of the modified Y-factor value.

(2) Evaluation of measurement errors. The measurement error associated with the determination of the input ST_B/N_0 value is comprised of instrumentation accuracies, human factor error in reading the reference marks, and equipment stability during the time of the measurement and test. A tabulation of the contributing errors is as follows:

Error	Value, dB
Y-factor = attenuator accuracy meter resetability	±0.05 ±0.05
A = precision attenuator pad	±0.05
F = noise bandwidth accuracy	±0.05
MI = attenuator accuracy	±0.10
= meter resetability	±0.05
= system linearity error	±0.05
$P_T(t)$ = time stability of output power for duration of each data point	±0.05
Worst case error total	±0.45

Test results. Verification system test results are shown in Fig. 24a–e. These results are for specific system operational control settings within the DSSs such as receiver loop bandwidth, subcarrier loop bandwidth, and bit synchronization loop bandwidth. The output BER as a function of the input ST_B/N_0 for a specific bit rate and modulation index becomes the variable parameter. The theoretical ideal phase-shift-keyed (PSK) detection characteristic is shown for reference purposes together with the predicted curves that were obtained by combining the theoretical efficiencies of the various elements of the telemetry system. Measured values should then be displaced from the predicted curve no greater than the
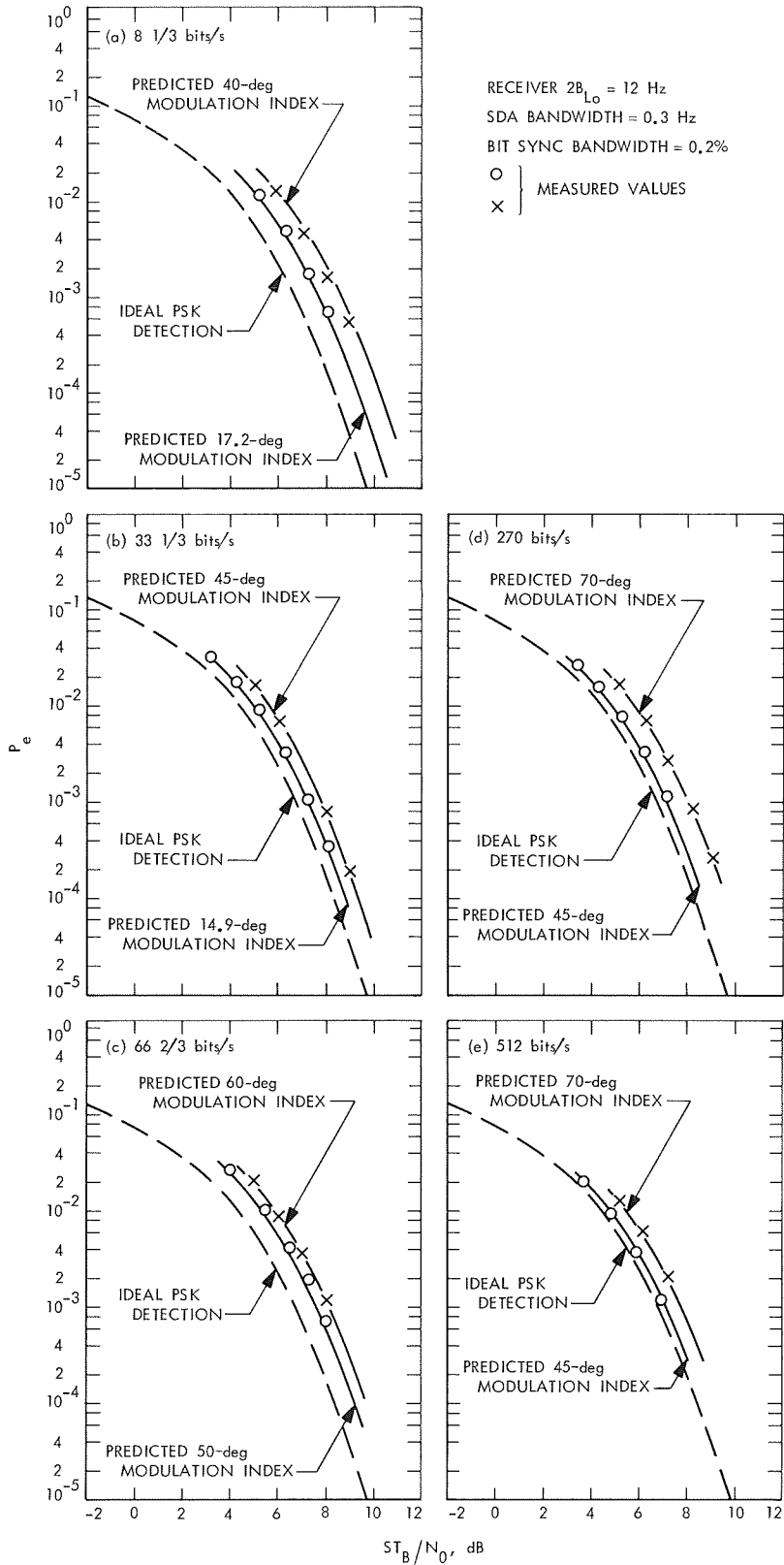
Fig. 24. System verification test results

measurement error if the theoretical analyses for the efficiencies were correct. The results shown on the curves indicate the performance of the MMTS as being very close to theoretical.

c. Receiver modifications. The addition of the SDAs to the receiver–exciter subsystem requires that portions of the receiver–exciter be modified to create an interface to this new equipment.

Prior to the installation of the SDAs, four receiver output signals at 10 MHz were required (Fig. 25). Two of these outputs were assigned to telemetry, one was an undetected output at low level for recording, and the other was a phase detected output providing a baseband signal at high level for recording and further processing. This baseband signal was then processed in the telemetry and command data handling subsystem.

The present method of operation requires SDAs to receive the modulated 10-MHz IF carrier from the receiver. The SDAs then process these signals and extract the data from the telemetry subcarriers. Each SDA requires the following signals from the receiver:

Function	Level
10 MHz reference	$+10$ dBmW
10 MHz IF (receiver 1)	-55 dBmW
10 MHz IF (receiver 2)	-55 dBmW
5 MHz reference	$+10$ dBmW
Switching	28 Vdc
Lamp	24 Vdc

Since the number of SDAs that will be interfaced with the receiver–exciter varies from one to six, the modification kits were designed to handle six SDAs at all sites.

In addition to the 10-MHz modulated signal from the receiver, each SDA requires 10- and 5-MHz reference signals. These were provided in the receiver–exciter interface. Four unused 10-MHz reference signals in cabinet 8 of the receiver–exciter were made available at the cabinet 8 interface plate. The 5-MHz reference signal was utilized only by the receiver–exciter synthesizer and no distribution of this signal was previously made. In order to furnish this reference to the SDAs, a 5-MHz distribution amplifier, similar in construction to the 10-MHz IF signal distribution amplifier, was installed in

a previously unused module location of the receiver–exciter (cabinet 4). The 5-MHz signal from the frequency and timing subsystem (FTS) is distributed to the receiver–exciter synthesizer and to the SDAs from this subassembly (Fig. 26).

The $+28$-Vdc switching supply voltage and the $+24$-Vdc lamp supply voltage were made available on multipin connectors at an interface plate located at the rear of receiver–exciter cabinet 7.

The receiver–exciter subsystem required three new subassembly types to provide the proper signals and levels to the SDAs. When first designed, the SDA interface modification kit had a requirement for 10-MHz modulated IF signals at a level of -66 dBmW. An IF signal distribution amplifier was designed and installed to provide these outputs. This -66 dBmW requirement was subsequently changed to -55-dBmW to provide the capability of handling modulation indices from 11 to 72-deg peak. It was then necessary to design and supply an additional 10-MHz distribution amplifier to increase the interface signal to this new level. The modifications to the receiver consist of the addition of the following three new subassemblies:

10-MHz IF signal distribution amplifier. This subassembly replaces the old 10-MHz IF signal distribution amplifier. It provides eight output terminals at a level of -66 dBmW, three of which are spares. The subassembly is physically located in cabinets 5 and 8, location A402 (the same location as the replaced subassembly).

10-MHz distribution amplifier. This subassembly is required to increase the signal level by 11 dB to -55 dBmW and provide six output terminals for the SDAs. Physically, this subassembly is mounted in a location that formerly held a larger size subassembly. It was therefore necessary to provide an adapter plate for mounting (cabinets 5 and 8).

5-MHz reference distribution amplifier. This subassembly is required to distribute the 5-MHz reference signal from the FTS to the receiver–exciter synthesizer and the SDAs. It is physically located in cabinet 4, location A102, which previously held a blank plate.

The SDA uses a 24-MHz voltage-controlled oscillator (VCO) in the subcarrier tracking loop. In order to accurately set the VCO frequency and eliminate the need to search in order to lock the subcarrier loop, the VCO frequency is held at 24 MHz ±6 Hz maximum.
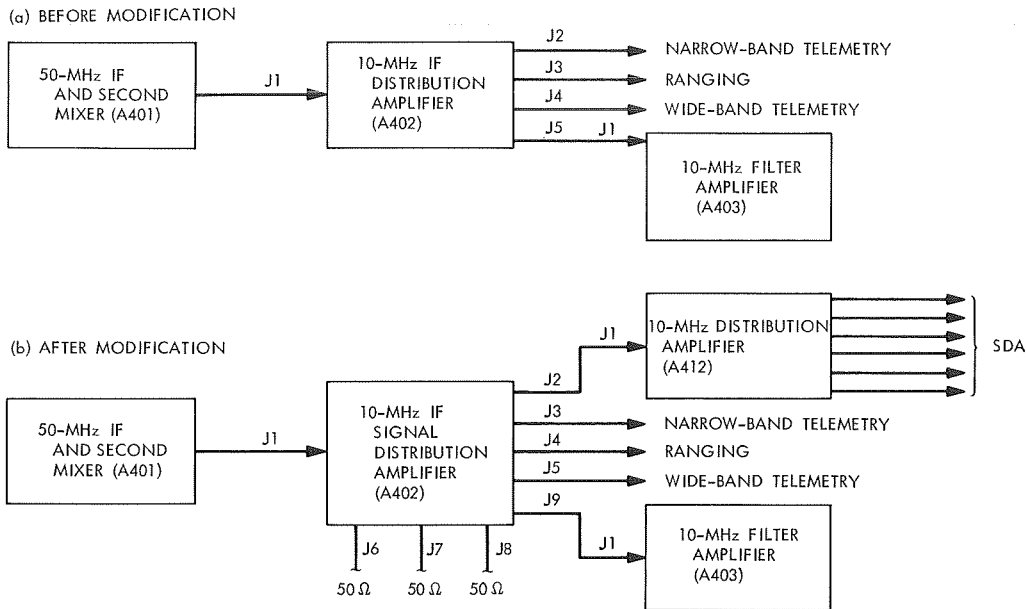
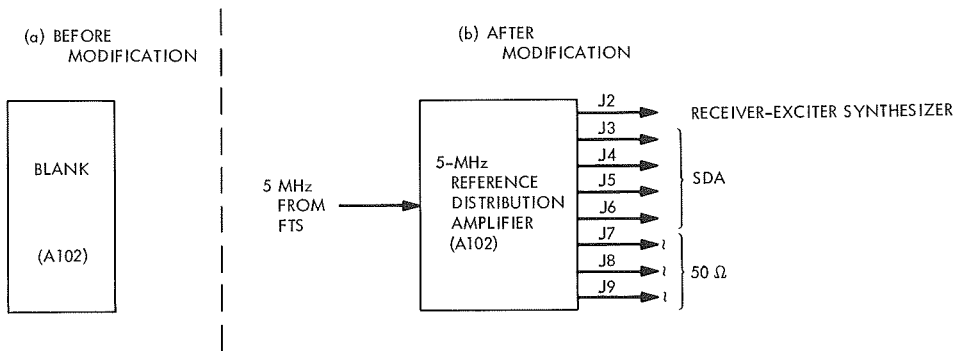**Fig. 25. SDA—receiver—exciter functional interface (cabinets 5 and 8)**

Fig. 26. SDA—receiver—exciter functional interface (cabinet 4)

The receiver–exciter was modified so that the SDA VCO frequency can be monitored on a frequency counter in the receiver control cabinet and adjusted to the proper frequency.

d. SDA. The SDA has had virtually no design changes since the article appeared in SPS 37-49, Vol. II. However, there were two changes made to accommodate the received signal as it became better defined. Each consisted of a temporary measure to be followed by a permanent modification.

Modification 1. The range of modulation indices to be received is in excess of the original 0–12 dB modulation index control provided. The temporary solution has been to increase the signal level at the receiver interface and

to insert a switchable 10-dB attenuator in series with the 0–12 dB control in the SDA. To improve operability and assure future flexibility, the 0–12 dB attenuator is being replaced with a 0–24 dB attenuator.

Modification 2. The nature of the data streams typically used is not compatible with the high pass filtering at the SDA output. This was originally provided to avoid hardware-generated dc offsets at the input to the telemetry and command processor (TCP). During the *Mariner* Mars 1969 period, this filter was bypassed and the offset zeroed out on a daily basis at the data isolation amplifiers at the SDA output. For future applications, the entire high pass filter assembly will be deleted and new design 10-MHz wideband amplitude detectors will be provided with significantly improved dc stability.

Additionally, there have been several design improvements at the subassembly level to improve producibility and reliability.

Since the period covered by the article in SPS 37-52, Vol. II, 20 SDAs have been implemented at nine DSSs and the JPL CTA. These are now operational. Ten additional SDAs are currently under contracted manufacture to implement the tenth DSS as well as added capability at four of the existing sites.

Beginning in the *Mariner* Mars 1971 time period, the MMTS configuration will change significantly. Perhaps the most significant change will be the implementation of symbol synchronizer assemblies (SSA) and associated decoders. Presently, a redesign of the output interface of the SDA is being performed to accommodate the SSA and to improve SDA performance at data symbol rates as high as 270,000 symbols/s. The latter will be accomplished essentially by means of improved frequency response of the data channel and by reduction of incidental time delay in the generation of the "data estimate" as used in the SDA demodulation process.

e. Telemetry and command data subsystem. Figure 27 shows a functional block diagram of a DSS with the MMTS. That part of the MMTS capability residing in the telemetry and command data (TCD) subsystem is the symbol synchronization–detection software described in SPS 37-46, Vol. III. This provided the TCD subsystem with the capability for processing a single telemetry data stream for each TCP (SDS 920) computer.

Future missions require that each TCP computer have a dual MMTS data stream capability. In addition, there is a requirement for higher and more variable data rates, and for handling of biorthogonal comma-free encoded data streams (SPS 37-48, Vol. II, pp. 83–130). Therefore, the expanded MMTS capability to the TCP subsystem will include an SSA, a block decoder assembly, added digital recorders, a 4800-bits/s high-speed data line (HSDL), and a mission-independent software assembly. A project has been established for the implementation of these added capabilities. A functional block diagram of a DSS with the expanded MMTS capability is shown in Fig. 28.

f. Mariner Mars 1969 operational experience.

Mariner Mars 1969 *pre-mission preparation.* A major milestone of the DSN in preparing for the *Mariner* Mars 1969 Mission was the achievement of DSS operational

readiness in November 1968. The information contained herein concerning the MMTS operator training and operational testing programs conducted by the DSIF will provide an insight into the level of effort that was required to implement this new system for *Mariner* Mars 1969 flight support.

(1) *DSIF operator training.* The philosophy for training DSIF operators to support the *Mariner* Mars 1969 Mission was developed by the DSIF Operations Section in August 1967. This philosophy was reflected in the general plan that was incorporated into the *Mariner* Mars 1969 Mission Operations Training Plan. The detailed program and procedures were published in Volume VII of the DSN Test Plan for *Mariner* Mars 1969 Project. While the training program covered all aspects of *Mariner* Mars 1969 operational support by the DSIF, it was heavily MMTS-oriented because of the uniqueness of the new equipment and software.

Prior to commencement of the first phase of the training, a considerable amount of preparation had to be completed. During July and August 1968, the instructors were trained and their course material was prepared. This was accomplished by having the instructors participate in MMTS equipment installation and testing activities at the JPL CTA, during which time they also compiled their course material.

Briefly, the DSIF operator training for MMTS encompassed formal training at the Goldstone DSCC, operational exercises at the JPL CTA, and on-site classroom instruction and training exercises. The training courses at the Goldstone DSCC and the JPL CTA were attended by an operations supervisor and two senior MMTS operators from each *Mariner* Mars 1969 DSS (DSSs 12, 14, 41, 51, 62, and 71). The DSIF Operations Team also participated to the extent that the *Mariner* Mars 1969 Lead Controller attended the Goldstone DSCC course and the entire Net Control Team in the SFOF supported the exercises with the JPL CTA. A brief description of each of the three major phases of the MMTS training is given in the following three paragraphs.

The 2-wk operator training course at Goldstone DSCC was conducted from September 3 through 13, 1968, under the auspices of the DSIF Training Unit. The formal classroom instruction and laboratory exercises covered were the TCP, including the MMTS and related software, and the SDA portion of the MMTS. The objective was to train the operators in operation of the equipment for the *Mariner* Mars 1969 Mission, performance of trouble-
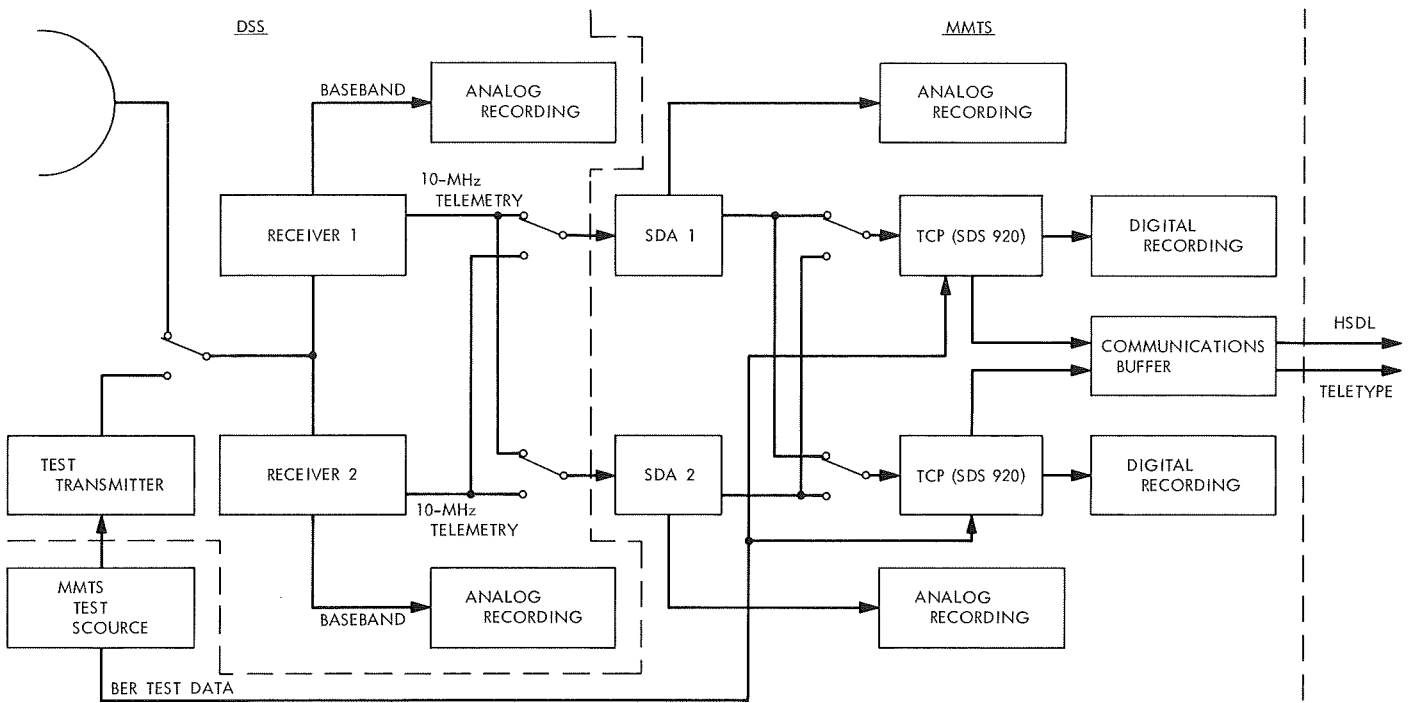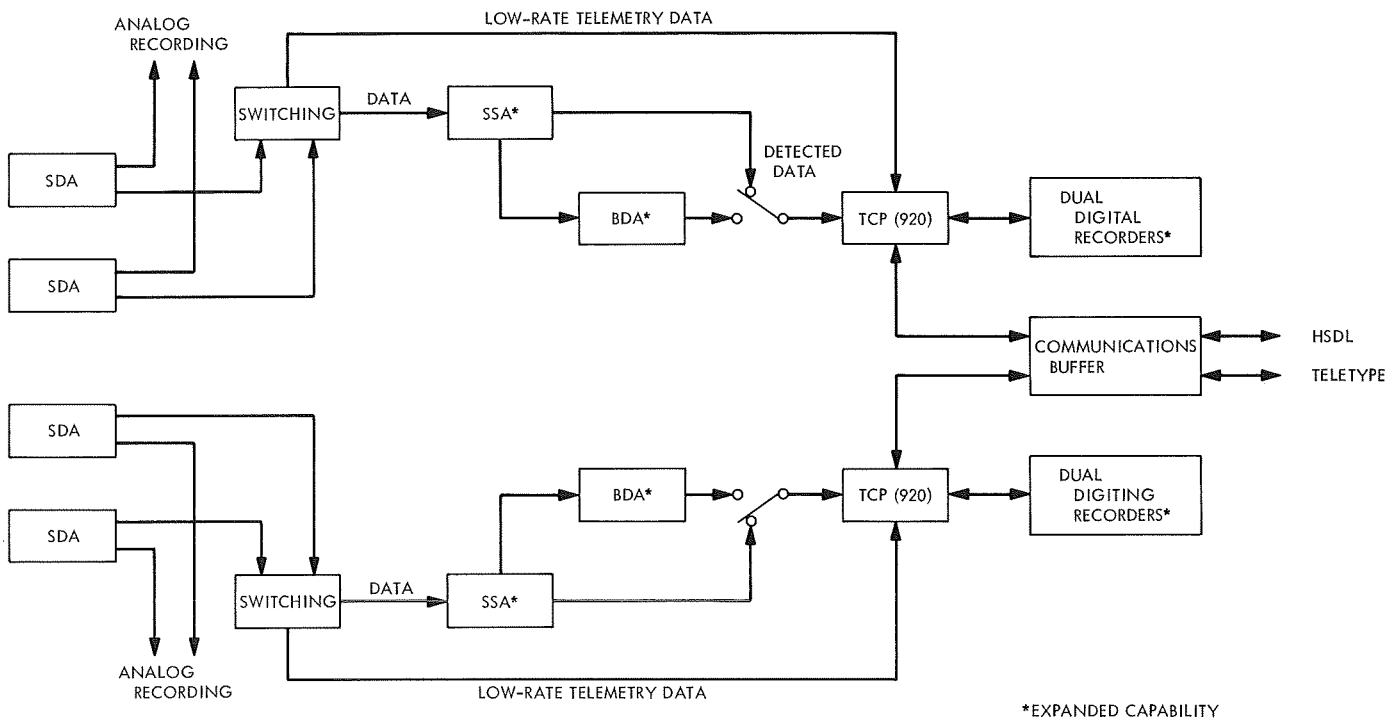
Fig. 27. DSIF MMTS functional block diagram

Fig. 28. TCD subsystem expanded MMTS capability

shooting and preventive maintenance on the equipment, and use and operation of software (computer programs) for the mission, including thorough familiarization with software–equipment interfaces.

Operator training at the JPL CTA, which was accomplished from September 16 through 27, 1968, provided the operators with an opportunity to apply what they had learned during the Goldstone DSCC courses. Under supervision and control of its operations supervisor, each DSS team participated in training exercises in which they operated CTA equipment, utilizing DSIF operating procedures and software for *Mariner* Mars 1969. These exercises included counting down and calibrating the CTA equipment, and then using a live *Mariner* Mars 1969 spacecraft in the Spacecraft Assembly Facility as a data source to perform a simulated track. The DSIF Operations Team also benefitted from this training in the SFOF (DSIF Net Control), which afforded them their first opportunity to participate in realistic *Mariner* Mars 1969 operations and become familiar with the telemetry data formats and operational aspects of the MMTS.

Operator on-site training commenced about October 1, 1968 on return of the above mentioned trainees to their respective DSSs. It consisted of formal classroom instruction (similar to that given at the Goldstone DSCC) and "in house" operational tests designed to exercise the DSS in its *Mariner* Mars 1969 configuration. The program was based on the provision that the limited number of operators trained at the Goldstone DSCC and the JPL CTA would train other operators at their respective DSSs utilizing a training package (course material on the MMTS) supplied by the DSIF Training Unit at the Goldstone DSCC. A continuing and comprehensive program was conducted at each DSS to assure that sufficient qualified MMTS operators were available to support all pre-launch and mission activities.

(2) *DSIF operational testing.* Pre-launch *Mariner* Mars 1969 testing activities involving MMTS operations that were supported by the DSIF included DSIF integration tests, DSIF operational verification tests (OVTs), DSN system tests, DSIF configuration verification tests (CVT), Mission Operations System (MOS) training tests, operational demonstration tests (ODTs), and operational readiness tests (ORTs). Combined with the DSS in-house testing and training exercises, the DSIF, DSN, and MOS testing put a considerable amount of operational running time on the MMTS. The successful and trouble-free use of MMTS to support actual flight operations can be

attributed largely to the thorough shake-down and valuable experience gained during the pre-launch test exercises. This test participation is summarized in Table 4; the amount of MMTS pre-launch operating time is estimated at approximately 300 h/DSS. From the standpoint of DSIF ability to operate the MMTS, the DSIF integration tests and OVTs were the most significant of the tests shown in Table 4. The brief descriptions of integration tests and OVTs given in the following paragraphs will help explain why this is so.

DSIF integration tests, which were critical to the checkout and implementation of the operational MMTS software, were the first used to exercise each DSS in its *Mariner* Mars 1969 configuration. The configuration of each DSS was defined and controlled by Volume VI of the DSN Operations Plan for *Mariner* Mars 1969 Project.

The tests were performed in three phases in accordance with Volume VI of the DSN Test Plan for *Mariner* Mars 1969 Project. The first test, an interface verification test,

Table 4. DSS pre-launch *Mariner* Mars 1969 test participation summary

Test	Number of tests supported						
	DSS 71[a]	DSS 12	CTA[a]	DSS 41	DSS 51	DDS 62	Total
DSIF integration test[b]	1	1	1	1	1	1	6
DSIF OVT	1	11	7	8	8	8	43
DSIF CVT	1	1	1	1	1	1	6
DSN system test	2	2	—	2	2	2	10
MOS system training test	1	1	10[c]	1	1	1	15
MOS ODT[d]	3	3	—	4	3	3	16
MOS ORT	2	2	—	2	2	2	10
Total	11	21	17	19	18	18	106

[a]Not shown are the numerous spacecraft–MOS–DSIF compatibility tests in which these stations participated.

[b]This consisted of a series of tests for a total of 40 h of MMTS operation at each station.

[c]These were Spacecraft Performance Analysis and Command—Technical Analysis Group training exercises using a *Mariner* Mars 1969 spacecraft in the SAF as a data source.

[d]Final test ran for four consecutive 24-h days.

provided final certification that all interfaces with the TCP system operated properly. Next, BER checks were performed to verify proper operation of RF–MMTS–TCP interfaces and provide determination of MMTS performance when operating at or near design threshold levels. Finally, a data flow test (from DSS to SFOF) was run to verify the proper integration of the *Mariner* Mars 1969 TCP program into the DSS and the *Mariner* Mars 1969 software system.

Following completion of the integration tests at each DSS, OVTs were run in accordance with Volume VII of the DSN Test Plan for *Mariner* Mars 1969 Project. These tests exercised not only the DSIF, but also the other elements (GCF and SFOF) of the DSN. They were specifically designed to verify compatibility of the *Mariner* Mars 1969 operating procedures (DSN Operations Plan, Volume VII), equipment, and operational interfaces. They also demonstrated the adequacy of the training of all DSIF operational personnel at the DSSs and in the SFOF.

Successful completion of an OVT was the last step in the process of meeting DSS operational readiness dates. OVTs were run with the DSSs subsequent to their respective readiness dates as required to maintain proficiency and verify the operational capability of newly-trained operators.

Mariner Mars 1969 flight support. As would be expected from the success of the DSIF and DSN pre-launch testing and ability of the MMTS to support the numerous MOS tests, the MMTS performed extremely well during the flight phases of the mission. The few system limitations that were encountered were easily circumvented, either by the use of special operating procedures or by software changes. Some of the more relevant aspects of MMTS performance during flight support operations, including the encounter phase of the mission, are discussed below.

(1) *Telemetry data retrieval.* To date, well over 99% of the telemetry data available during scheduled DSS tracking periods has been retrieved in flight operations. For example, from launch through the midcourse maneuver (February 25 to March 15, 1969) of *Mariner VI*, 99.83% of the telemetry data were retrieved. During the corresponding period for *Mariner VII* (March 27 to April 15, 1969), telemetry data retrieval increased to 99.99%. The negligible amount of data lost by the DSIF throughout the mission is attributed largely to DSS ground receiver out-of-lock conditions, which occurred as a result

of standard tracking procedures associated with turning the ground transmitters on or off.

With two SDAs, two TCPs and recorders, and an FR 1400 recording of the SDA outputs being provided by the standard *Mariner* Mars 1969 DSS configuration, irretrievable loss of data by a DSS was virtually impossible if either of the two ground receivers was in lock. In those cases where communications circuit (HSDL and teletype) outages precluded real-time transmission of data to the SFOF, the MMTS recording capabilities made it possible for a DSS to play a TCP log tape directly back to the SFOF, play an FR 1400 analog tape into the TCP and thence to the SFOF, and mail the TCP log tape to JPL Document Control in the SFOF. All of these methods of retrieving telemetry data were used successfully during the mission.

(2) *Operational performance.* In assessing the overall operational effectiveness of the MMTS, two factors are particularly noteworthy. One is that no emergency changes to the software had to be made for *Mariner* Mars 1969 after completion of the DSIF integration tests. This can be attributed to the thoroughness of the testing and adequacy of TCP program changes made during software development and DSS implementation phases. The other factor is that the original operational program, *Mariner* Mars 1969 TCP Computer Program, was re-written only once after launch. This re-write was accomplished in a very orderly and evolutionary fashion. The new version was thoroughly tested and accepted by the DSIF prior to commencement of the MOS pre-encounter operational tests. Although designed primarily to benefit the *Mariner* Mars 1969 software system, the changes facilitated DSIF–MMTS operations as well.

TCP log tape validation was a problem during the early weeks of the mission. It was found that the information provided by the *Mariner* Mars 1969 TCP computer program regarding quality of the log tape recordings could be misleading. The program printed out the number of "write errors" and records lost on each tape (a "record" consisting of a block of telemetry data). However, it was found that, in many instances, the "write errors" actually were tape recorder "read errors," and that the data actually were properly recorded (no actual "write errors" or "records lost"). The problem still exists with the current version of the software; however, a new TCP computer program (On-site *Mariner* Mars 1969 Log Tape Validation Program) was developed by the DSIF Operations Section to resolve the matter. This

program makes it possible to determine immediately after a DSS tracking period the percentage of good telemetry data that were recorded on each TCP log tape.

The downlink SNR data provided by MMTS proved to be an extremely valuable operational tool during the mission. It is the best indicator of overall telemetry system performance yet seen by the DSIF. As examples, it provided an immediate indication of DSS receiver lock on a sideband and/or wrong spacecraft telemetry bit rate selected for the TCP, and signaled substandard MMTS performance or impending equipment failure so that corrective action could be taken before a telemetry data outage occurred.

(3) *Encounter operations.* MMTS performance during *Mariner* Mars 1969 encounter and playback operations was particularly gratifying. Of special significance were the methods employed by the DSIF Operations Section to operate the Goldstone DSCC/JPL CTA configuration and to overcome a design incompatibility between the MMTS and *Mariner* Mars 1969 spacecraft that affected operations during this period.

The high-rate telemetry (HRT) experiment was an unqualified success from the standpoint of DSIF operations. Six HRT playbacks per spacecraft were accomplished and the data recorded on TCP log tapes by DSS 14. Further, virtually all the data from the first HRT playback of each spacecraft were received and processed in the SFOF in real time. The success of the HRT playbacks (at 16.2 kbits/s) makes it unlikely that the *Mariner* Mars 1969 Project will go to the expense and effort of processing the low-rate (270 bits/s) science log tape recordings made in the SFOF and at the 85-ft-diam antenna DSSs.

The configuration used to support the Goldstone DSCC passes of both the encountering and non-encountering spacecraft was a very complex operational structure. Volume VI of the DSN Operations Plan for *Mariner* Mars 1969 Project details this configuration. Briefly, it involves DSSs 11, 12, and 14 at the Goldstone DSCC and the JPL CTA. The operational employment of MMTS in this configuration is given in Table 5.

During Mode 1 operations (Table 5), DSS 11 was assigned to track the non-encountering spacecraft while, at the same time, DSSs 12 and 14 were tracking the encountering spacecraft. Since DSS 11 was not equipped with a TCP, the SDA 2 output (spacecraft engineering data) was microwaved to the JPL CTA, where the data

were processed in TCP B and then transmitted to the SFOF via HSDL and teletype. For the encountering spacecraft, HRT data were processed in both TCPs (A and B) at DSS 14, normally utilizing the output from SDA 1 (not shown in Table 5). To provide HRT data in real time to the SFOF, the SDA 4 output was microwaved to the JPL CTA where it was processed in TCP A and then transmitted to the SFOF for processing in a Univac 1219 computer and display on television. The output of SDA 2 at DSS 14 was microwaved to DSS 12 where it was processed in TCP B. DSS 12 transmitted either the DSS 14 or its own engineering telemetry data to the SFOF, with the DSS 14 data being "prime."

Not shown by Table 5 is the fact that certain spacecraft telemetry channels were teletyped from the JPL CTA back to DSS 11 and from DSS 12 to DSS 14 in real time. This was required for proper completion of the DSS command readiness procedures.

The foregoing simplified explanation of the MMTS utilization in support of *Mariner* Mars 1969 encounter operations should serve to illustrate the unique and operational situation that faced the DSIF. That the whole operation was 100% successful is a tribute not only to the capabilities of the MMTS, but also to the professional competence of the DSIF operators, both at the DSSs and in the SFOF.

(4) *Special procedures for telemetry mode changes.* The design characteristics of the *Mariner* Mars 1969 spacecraft flight telemetry (TM)–RF subsystems and the DSIF ground receiver (RCV)/SDA subsystems resulted in an inherent incompatibility that affected the ENCOUNTER 2 and PLAYBACK 1 and 2 spacecraft TM modes. This was because of the fact that in these science modes, the exceptionally low spacecraft engineering subcarrier modulation index (11.9-deg minimum as opposed to about 41 deg when science was not present) exceeded the limits of the RCV–SDA ground equipment if the equipment settings established during pre-cals remained unaltered.

Since the problem was caused in part by the characteristics of the spacecraft engineering subcarrier, the capability to process engineering TM was affected at the 85-ft-diam antenna DSSs, as well as at DSS 14, which was the only *Mariner* Mars 1969 DSS capable of processing the 16.2-kbits/s HRT data. Therefore, an operational procedure utilizing a non-standard configuration was initiated to circumvent the problem. This procedure facilitated the altering of the relationship between the RCV attenuator and SDA modulation index settings,

Table 5. MMTS data flow during Goldstone DSCC encounter passes

DSIF mode (No. and purpose)	DSS equipment	Non-encountering spacecraft coverage			Encountering spacecraft coverage		
		DSS 12	DSS 11	CTA	CTA	DSS 14	DSS 12
1 HRT Standard	TCP A TCP B SDA 2 SDA 4		ENG ──→ X		X←┐	HRT HRT ENG ──┘ └─ HRT	ENG X ┌→ X
2 HRT DSS 11 not scheduled	TCP A TCP B SDA 3 SDA 2	ENG X ENG X			X←┐ X←┐	HRT HRT └─ HRT └─ ENG	
3 Science DSS 11 not scheduled	TCP A TCP B SDA 2	SCI X ENG X			X←┐	SCI X ENG X └─ ENG	
4 Science standard	TCP A TCP B SDA 2		ENG ──→ X			SCI X ENG X ENG ──┘	SCI X ┌→X
5 HRT DSS 12 antenna failure	TCP A TCP B SDA 2 SDA 4		ENG ──→ X		X←┐	HRT HRT ENG ──┘ └─ HRT	┌→X ┌→X
6 Science DSS 14 antenna failure	TCP A TCP B SDA 2		ENG ──→ X				SCI X ENG X
7 HRT DSS 11 antenna failure	TCP A TCP B SDA 2 SDA 4				X←┐	HRT HRT ENG ──┘ └─ HRT	ENG X ┌→X

NOTE: X   Indicates on-site processing and standard transmission to SFOF.
    ──→   Indicates microwave link.
    ENG   33⅓ bits/s engineering data.
    SCI   66⅔ or 270 bits/s science data.
    HRT   16,200 bits/s science data.

which were prescribed by Volume VI of the DSN Operations Plan. The detailed operational procedure was published as a change to Volume VII of the DSN Operations Plan.

There were three operational difficulties associated with this design problem. Any change to these modulation settings immediately invalidated the DSS RCV automatic gain control (AGC) prepass calibrations unless additional AGC calibrations were carried out for each anticipated setting prior to a pass. Any change to the SDA setting automatically caused loss of SDA–TCP lock, resulting in loss of TM data from any single DSS. That is, if the settings were changed prior to the spacecraft mode changes, TM data were lost until after the new mode was observed (to ensure receipt of the last available bit of the outgoing TM, a portion of the incom-

ing new mode was forfeited). This problem was obviated by using two DSSs in parallel, whenever possible, with one changing settings before, and one after, the spacecraft TM mode changes. The main operational problem was that the control knobs for these settings, particularly on the RCV, were never intended for real-time operational changes and are physically located such that the RCV operator has to leave his position at the RCV console to carry out the changes at a critical time, when it is imperative that he be able to observe and correct any loss of RCV lock.

The effects of the aforementioned problems on MMTS operations were minimized by the design and issuance of the detailed operational procedure. During the pre-encounter testing, both the DSS operators and DSS controllers in the SFOF practiced the coordination and

developed the proficiency necessary to effect the adjustments without incurring a loss of spacecraft TM data.

g. Pioneer Project operational experience. The *Pioneer* MMTS program was initially produced on a crash basis as a model to demonstrate the real-time telemetry processing capability of the DSN facility at JPL. A minimum amount of manpower effort was expended to design the program. Therefore, the current *Pioneer* Telemetry Processing Program is limited in certain areas and could be improved if the program were redesigned to be used for full operational flight support in place of the current mission-dependent equipment.

The use of the MMTS for support of the *Pioneer* Missions has been limited to the cruise phases of the mission. All data processed have been at the 8-bits/s rate. All MMTS passes for *Pioneer* have been one-way tracking without command capability. The prime support has been provided by DSS 41. Project benefits derived from the MMTS operations have been limited to science data in real-time and analog tapes for backup. The digital recordings could not be processed by the Ames Research Center under the current MMTS configuration.

Systems description. The *Pioneer* Telemetry Processing Program is used to frame sync, decommutate, and display the *Pioneer* telemetry data to the user in real time. The data are received into the IBM 7044 computer from the DSIF. The DSIF site uses a modified *Mariner* Mars 1969 TCP program in an SDS 920 computer to bit-sync and package the telemetry data for transmission to the SFOF. The data are transmitted to the SFOF over Automatic Data Switching System (ADSS) lines. After signal conditioning the ADSS data in synchronizing units, the data are passed to the IBM 7044 computer where they are received by the mission-independent system. The data are then passed to the *Pioneer* Telemetry Processing Program where the actual processing of the data takes place. After the data have been identified, they are passed back to the IBM 7044 mission-independent system for printer formatting and output to the user area.

Software description. The *Pioneer* telemetry data are transmitted from the DSIF site to the SFOF in 600-bit ADSS blocks of data. Each block contains 168 bits of raw telemetry data plus other related data such as spacecraft number, DSIF number, data type, and other related data. The raw telemetry data are transmitted to the SFOF in the order they are received from the *Pioneer* spacecraft. This means that the program in the IBM 7044

computer must synchronize the frames of data from the completely unsynchronized input data blocks. Since a frame of data is 224 bits in length, a frame cannot be held by one ADSS data block alone but requires a portion of another data block. A frame of data could utilize three data blocks for transmission if the beginning of a frame started near the end of an ADSS block. The frame would require the whole (168 bits) of the next block plus a small portion of the following block.

When the ADSS data blocks are received by the IBM 7044 mission-independent system, three header words are attached to the beginning of each block and one trailer is attached to the end of the block. The data blocks are placed into an internal IBM 7044 buffer called ADEBnn, where nn is the spacecraft number of the spacecraft that is sending the data. These buffers are passed to the *Pioneer* Telemetry Processing Program for processing.

The only other inputs to the *Pioneer* Telemetry Processing Program are in the form of punched cards. These cards are used to specify the sync pattern that should be used to synchronize the data into frames, and as a constant to specify to the program the number of telemetry frames to bypass between sending a frame of data to the teleprinters. The "sleeving" of data to the teleprinters is necessary so that the teleprinters do not fall behind in their printing of data frames. Other data inputs to the IBM 7044 computer are directed to the mission-independent system from the message composer units. These messages include process requests, printer and teleprinter output requests, and others.

Program limitation. The current MMTS program for *Pioneer* does not allow for two-way tracking nor will it handle *Pioneer* data rates above 256 bits/s. No consideration was made for interfacing with convolutional coding operations for *Pioneer IX*. Spacecraft AGC and static phase error at the DSS for data rates above 64 bits/s is lost.

The existing program does not output engineering formats required for *Pioneer* operations. Additional limitations in the IBM 7044 area are:

(1) Limited to 4 HSDLs input to the SFOF at one time.

(2) One IBM 7044 will not handle two HSDLs from the same spacecraft (will not process data from both stations during periods of overlap).

(3) Will not output to HSDL.

(4) Writes separate telemetry original data record by project, not by spacecraft.

Pioneer Mission requirements. Future *Pioneer F* and *G* Missions will be dependent both on the redesigned MMTS program, and the upcoming Multiple-Mission Command System Program. Mission-dependent equipment currently used on *Pioneers VI, VII, VIII,* and *IX* will be phased out for the Multiple-Mission Telemetry and Command Systems to be employed at JPL.

Reference

1. Lindsey, W. C., *Performance of Phase-Coherent Receivers Preceded by Bandpass Limiters,* Technical Report 32-1162. Jet Propulsion Laboratory, Pasadena, Calif., Sept. 15, 1967.

V. Operations and Facilities

A. DSN Operations

1. Radio Science Support, T. Sato and D. Spitzmesser

During this period, the DSN supported a general relativity experiment conducted by Doctors D. O. Muhlemann, R. D. Ekers, and E. B. Fomalont of the California Institute of Technology's Owen's Valley Radio Observatory.

The experiment was to attempt to measure, by use of interferometer techniques, the apparent change of angular separation between radio sources 3C273 and 3C279 near the time 3C279 was occulted by the sun. This occurred on October 8, 1969. The maximum-expected shift in separation due to relativity effects is 1″7, but the maximum observable shift would be limited to 0″3 because of the solar corona effects. The above data were obtained from the experimenters.

To implement the experiment, two Goldstone DSCC stations, DSSs 13 and 14, were configured as elements of a phase-sensitive interferometer. The system block diagram is shown in Fig. 1. The frequency of operation was 2388 MHz, and the standard 2388-MHz receivers located at each station were used as the basic elements

of the interferometer. The interferometer baseline was on the order of 10^5 wavelengths.

Experimenter-supplied rubidium frequency standards were installed at each station, and these were used as the reference to synthesize all required local oscillator frequencies. This synthesis was done using the standard modules in each receiver. A 1-MHz reference signal was also microwaved from DSS 14 to DSS 13, where it multiplied to 31.440 MHz, and was phase-compared with basic DSS 13's 31.440-MHz local oscillator frequency. The phase comparison device was a standard Hewlett-Packard vector voltmeter. The phase information obtained was recorded on a strip chart recorder and one channel of a four-channel sequential digital recorder. This information will be used to determine the relative phase difference between the two standards during an observation and to attempt to correct for phase shift introduced in the DSS 14 IF signal by the microwave link.

The IF portion of the DSS 14 receiver was unmodified and the output of the final IF 455- kHz center frequency, with a noise bandwidth of approximately 330 kHz, was
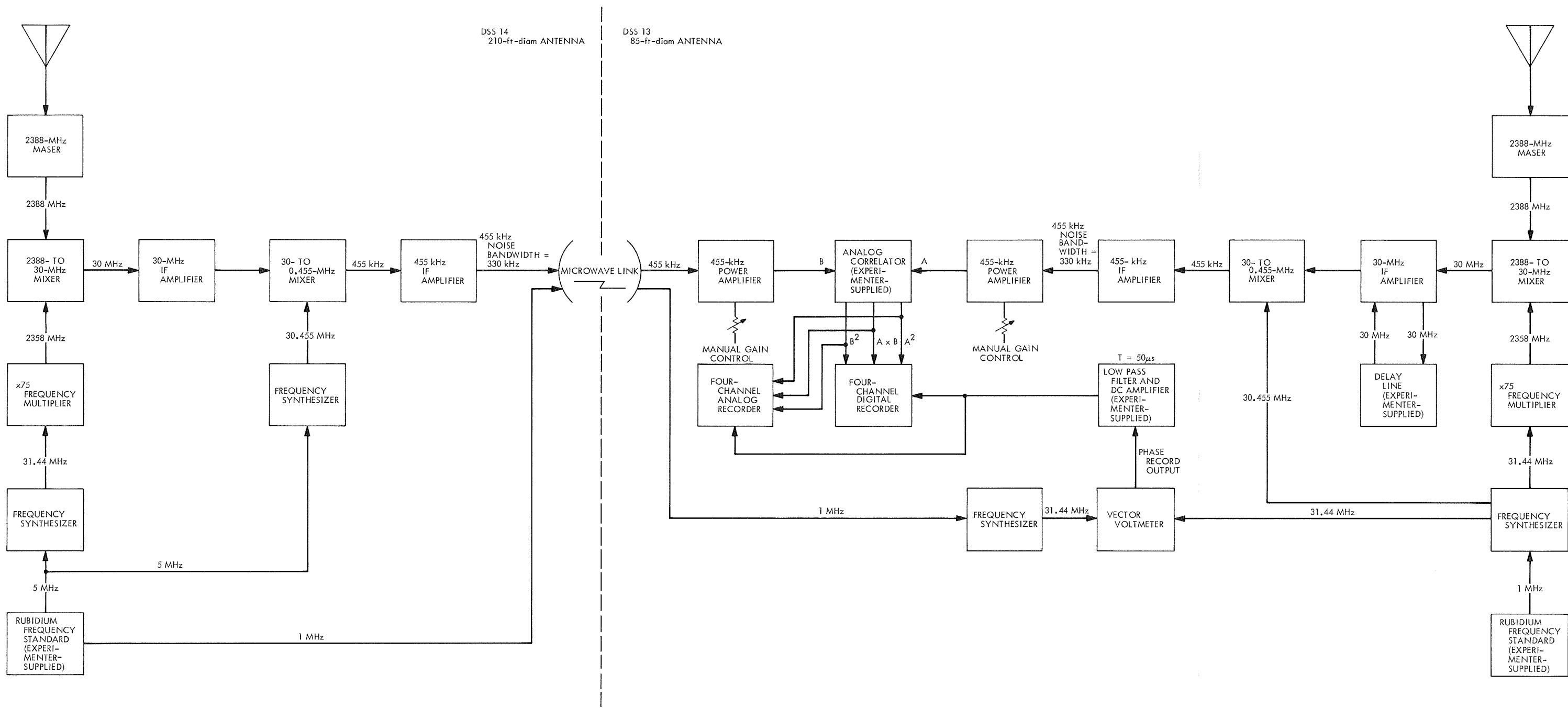
Fig. 1. General relativity experiment system configuration

Page intentionally left blank

sent via the microwave link to DSS 13. The 30-MHz IF amplifier chain at DSS 13 had an adjustable delay line inserted in it. The delay line had a total delay of 126 μs adjustable in 2-μs steps from zero to maximum delay.

The final IF amplifier output at DSS 13, 455 kHz with a noise bandwidth of approximately 330 kHz, was correlated in real time with the 455-kHz signal from DSS 14 in an analog correlator. The analog output of the correlator was then recorded on another channel of the previously mentioned digital recorder. Also recorded on the remaining two channels of the digital recorder were the total power levels of the DSS 14 and DSS 13 receivers. This information may be used to obtain solar scintillation data.

The station provided the experiments with a total of seven observing periods; the first two on September 25 and 26, 1969, from 2100 to 0300 UT, and the one on October 1, 1969, from 0400 to 0900 UT, were used to check system operation. During the September 25 and 26 run, the *Mariner VI* spacecraft was tracked and fringes were observed from the *Mariner* spacecraft carrier. For this test, both stations operated at approximately 2297 MHz. The October 1 run utilized various radio sources and fringes were successfully observed on all sources tracked.

The actual experimental observations of 6 h each took place on October 2 and 3, October 4 and 5, October 6 and 7, October 10 and 11, and October 14 and 15, 1969, from approximately 2000 to 0200 UT.

The data from the general relativity experiment are being processed and evaluated by the experimenters.

B. DSIF Operations

1. RF Spectrum Analysis Technique Utilized by JPL Compatibility Test Area and Cape Kennedy Compatibility Test Station, A. I. Bryan

a. Introduction. One of the requirements of telecommunications compatibility testing of the spacecraft with the tracking and data system is to search the RF spectrum for extraneous, as well as expected, frequencies which are of sufficient amplitude to enable the S-band receiver to obtain phase lock.

The technique previously used to search for these RF signals required the receiver operator to manually tune the receiver and attempt to phase-lock the receiver. The receiver operator had to be able to hear a difference frequency as the receiver passed through a signal in the spectrum, and as a result, data on low-level signals were questionable. Consequently, in December 1967, a system was implemented at DSS 71 utilizing the digital instrumentation system (DIS) phase I digital computer (SDS-920) to provide: (1) S-band receiver voltage-controlled oscillator (VCO) tuning control, (2) frequency monitoring and frequency band power level measurements, and (3) RF spectrum data recorded on the line printer.

b. System configuration and description. A block diagram of the system is shown in Fig. 2. The S-band receiver heterodynes the incoming signal to produce a 10-MHz IF carrier, which is passed through a telemetry bandpass filter and is then mixed with 10.02-MHz to produce a 20-kHz carrier with telemetry subcarriers. The 20-kHz receiver output is input to a wave analyzer, which operates in the normal mode (no automatic frequency control) with a 6-Hz or 200-Hz bandpass.
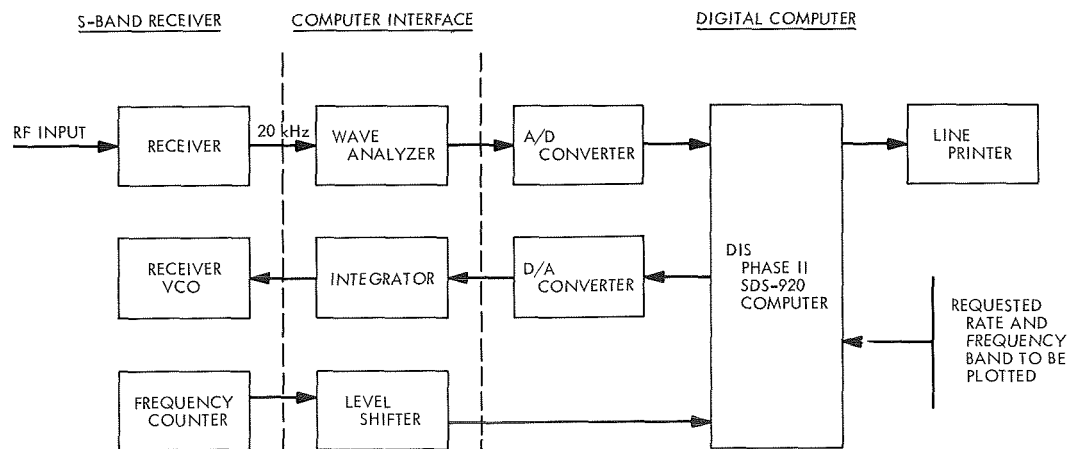

Fig. 2. Block diagram—RF spectrum analysis system

There are two time-multiplexed modes of operation of the system. The specific mode of the system is controlled by interrupts.

The mode with the lowest priority (mode I) is the servo-loop for frequency rate control. This mode provides closed-loop control of the receiver VCO. The digital computer functions as a digital comparator to form the difference between a requested frequency rate and the actual rate of frequency change. The computer then multiplies this difference error by a simple transfer equation. The resulting voltage from the digital-to-analog (D/A) converter drives a lowpass RC filter which provides the control voltage for the VCO. The bandwidth of the integrator is much smaller than that of the VCO, and consequently, the VCO tracks the integrator without significant delay. The RC filter acts to smooth and divide the step signal from the D/A converter.

The VCO frequency is monitored by the counter, which operates in a 1-s interval counter mode. The counter output closes the loop through the digital inputs of the computer. Constants, such as the desired frequency band to be analyzed, starting frequency, and the desired rate of change of frequency, are input to the computer from the typewriter console.

The mode with the highest priority (mode II) is concerned with the computation of the spectrum power. A 14-bit A/D converter samples the wave analyzer output. The computer then sums this information and correlates the sum data with the frequency-band information obtained from the frequency counters. Sampling of the data is sufficiently fast so the Nyquist frequency is not approached.

Mode III includes the output to the DIS line printer and consists of points which are plotted and tagged as to frequency and relative power to carrier level. The plot output is in decibels.

c. System analysis.

Mode I. The block diagram of Fig. 2 can be divided into a discrete and a continuous section, as illustrated in Fig. 3. The discrete section consists of the digital computer and sampler. The continuous section consists of the D/A converter and the integrator. The VCO and the computation time delay within the computer can be ignored due to their relatively high-frequency response in comparison to the desired system frequency response.

This discrete-data control system must be physically realizable with finite settling time and zero steady-state error for an input which is a constant. The condition of a specific input (step function) implies that a "minimal" response design is satisfactory.

Therefore, the closed-loop transfer function of the system (ignoring τ) in Fig. 3 is

$$M(Z) = \frac{C(Z)}{R(Z)} = \frac{D(Z)\,Gp(Z)}{1 + D(Z)\,Gp(Z)}$$

where

$$Gp(Z) = Z[G(S)]$$

$$Z[G(S)] = Z\left[\frac{1 - e^{-TS}}{S}\,\frac{K_1}{S}\right] = \frac{K_1 T}{Z - 1}$$

(1)

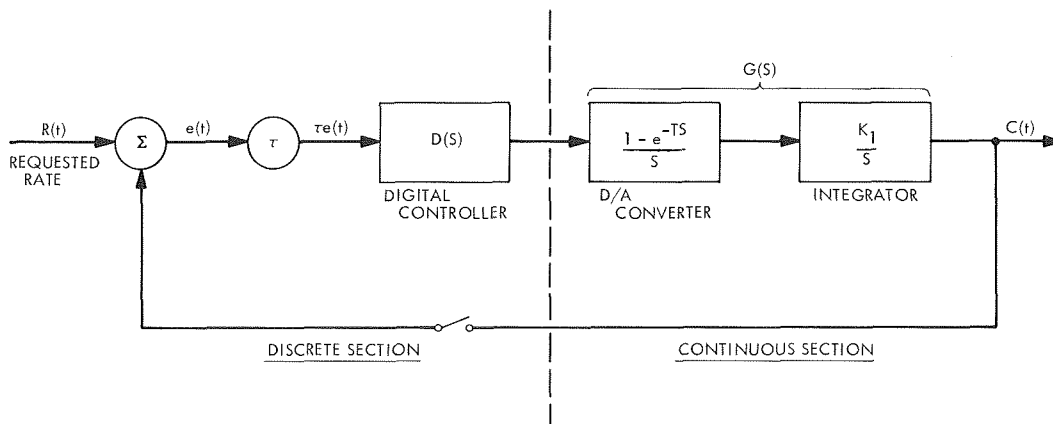where T is the sampling period of 1 s.

Fig. 3. Simplified block diagram—RF spectrum analysis system

Since the process $Gp(Z)$ has no time lag or zeroes (with the simplifying assumptions), then $M(Z)$, the system transfer function, is optimized for a step input by setting $M(Z) = Z^{-1}$ (Ref. 1).

Solving for $D(Z)$ in Eq. (1) yields

$$D(Z) = \frac{M(Z)}{1 - M(Z)} \times \frac{1}{Gp(Z)}$$

and substituting values yields

$$D(Z) = \frac{Z^{-1}}{1 - Z^{-1}} \times \frac{Z - 1}{K_1}$$

$$= \text{constant} \left(\frac{1}{K_1} \right)$$

where $K_1 = 0.0016$. If $D(Z)$ is selected for this value, then the output response is

$$C(Z) = \frac{1}{Z - 1} = Z^{-1} + Z^{-2} + Z^{-3} \cdots$$

The equation for $C(Z)$ implies that the system output will respond to the step input with a delay of one period of the sampling rate.

However, the ± 1 count in the counter does effect the loop; therefore, a variable dampening factor is utilized in the system. The factor $\tau = 1$ when driving the system toward a desired frequency position. The factor $\tau = 0.1$ is then selected by the program when rate and frequency position have been achieved. The value for $\tau = 0.1$ was selected by a system simulation on the SDS 920 and has the effect that $C(Z)$ does not reach zero steady-state for a step input until a delay of 7 sample periods.

The desired S-band frequency rates can be achieved from approximately 2 to 400 Hz/s.

Mode II. The wave analyzer (HP-302 or HP-310A) noise level and the S-band carrier are measured by the computer program and stored as constants. The frequency relationships to these data points and to the data points of the swept spectrum are obtained from the counters.

The voltage signal from the wave analyzer represents the signal power within the selected noise bandwidth

of the analyzer. The sampled output of a particular spectrum interval (i.e., 5 Hz, if a 5-Hz/s rate is selected) is summed, squared, and expressed in volts. Then a comparison is made with the previously measured carrier power to form a relative level expressed in dB.

A machine language subroutine (SDS-920 symbolic) is required to speed the operation of handling the sampled data. The sample rate is a constant 333 samples/s. A 1-ms pulse from the station timing system is used to initiate the sample interrupt.

The graphic display of the RF spectrum allows real-time observation, as well as a permanent record of power and frequency measurements. Any portions of the spectrum may be further examined by plotting an expanded section (i.e., sweeping the spectrum at a slow rate) of the area in question. Results have shown that at power levels of -40 dB below the carrier, relative accuracies of ± 1 dB are obtained. An example of the output is illustrated in Fig. 4.

d. Development. To reduce the time involved in analyzing the spectrum, it is proposed to use the fast discrete Fourier transform (DFT) to examine the S-band spectrum. Preliminary testing has been successful in utilizing the Welch (SPS 37-40, Vol. III, pp. 6–8) version of the DFT to examine the spectrum from the carrier to approximately 160 kHz. The data obtained are comparable to the analog technique presently used. The time involved in a spectrum observation is reduced by a factor of 10 to 20.

Reference

1. Kuo, D. C., *Analysis and Synthesis of Sampled-Data Control Systems.* Prentice-Hall, Inc., Englewood Cliffs, N. J., 1963.

C. Facility Engineering

1. SFOF Emergency Power Subsystem, R. V. Phillips

a. Introduction. The SFOF emergency power subsystem discussed in SPS 37-50, Vol. II, pp. 189–191, SPS 37-51, Vol. II, pp. 170–171, and SPS 37-57, Vol. II, pp. 170–173, is incrementally becoming a reality. The uninterruptable power system (UPS) began on-line operation on May 3, 1969, and the engine-driven standby power plant is scheduled for completion in early 1970. The installation of the central supervisory monitor and control system is in process and will be operable with completion of the standby power plant.

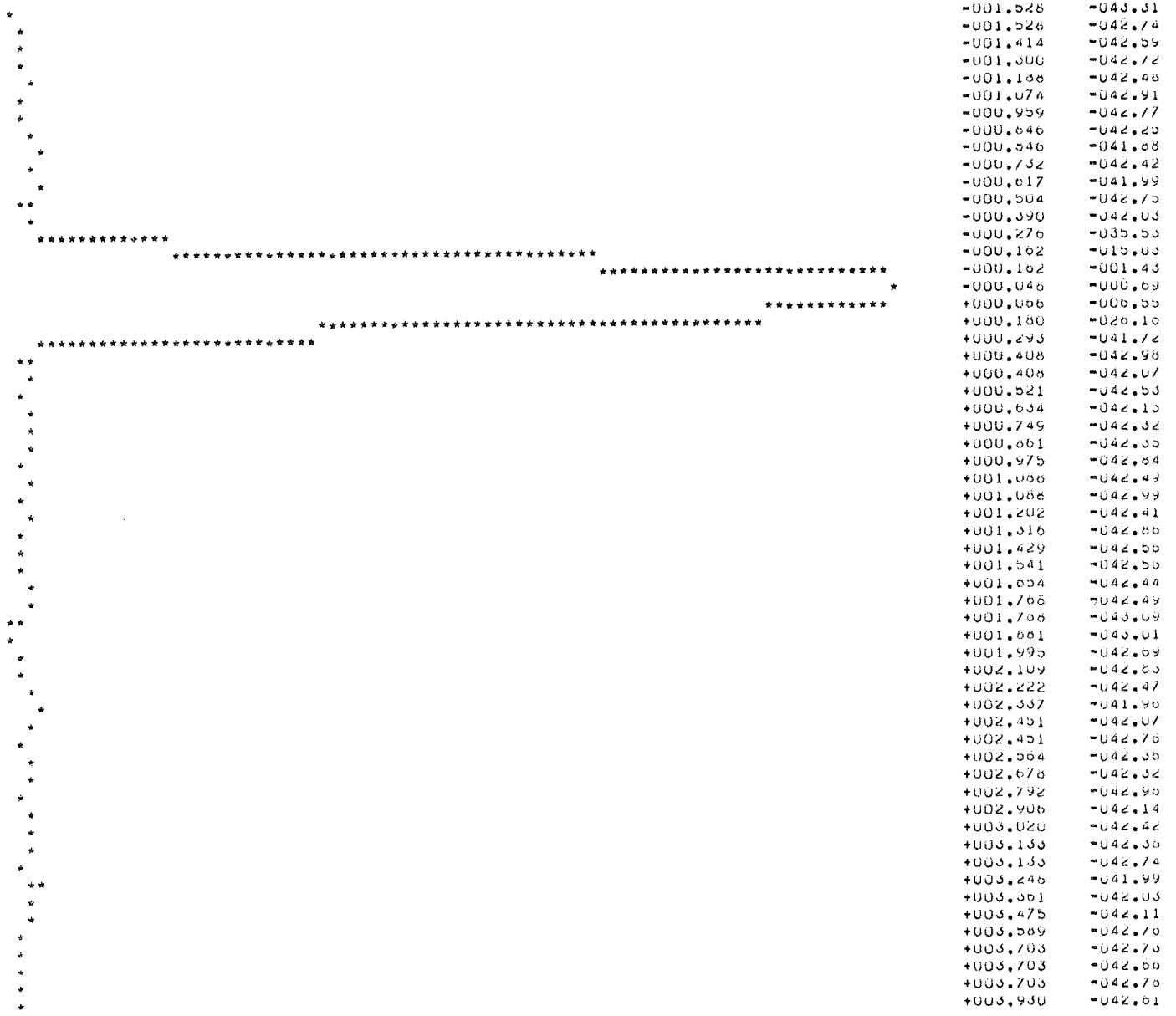|	
-001.528	-043.31
-001.528	-042.74
-001.414	-042.59
-001.300	-042.72
-001.188	-042.48
-001.074	-042.91
-000.959	-042.77
-000.846	-042.23
-000.546	-041.88
-000.732	-042.42
-000.617	-041.99
-000.504	-042.73
-000.390	-042.03
-000.276	-035.53
-000.162	-015.03
-000.162	-001.43
-000.046	-000.69
+000.066	-006.55
+000.180	-026.10
+000.293	-041.72
+000.408	-042.98
+000.408	-042.07
+000.521	-042.53
+000.634	-042.13
+000.749	-042.32
+000.661	-042.33
+000.975	-042.84
+001.088	-042.49
+001.088	-042.99
+001.202	-042.41
+001.316	-042.86
+001.429	-042.55
+001.541	-042.56
+001.654	-042.44
+001.766	-042.49
+001.766	-043.69
+001.881	-043.01
+001.995	-042.69
+002.109	-042.83
+002.222	-042.47
+002.337	-041.96
+002.451	-042.07
+002.451	-042.76
+002.564	-042.36
+002.678	-042.32
+002.792	-042.96
+002.906	-042.14
+003.020	-042.42
+003.133	-042.36
+003.133	-042.74
+003.246	-041.99
+003.361	-042.03
+003.475	-042.11
+003.589	-042.70
+003.703	-042.73
+003.703	-042.66
+003.703	-042.73
+003.930	-042.61

Fig. 4. Portion of *Apollo 11* frequency spectrum (DIS spectrum plot; 2287.5-MHz carrier; rate = 100 Hz/s)

b. Uninterruptable power system. The dependable on-line operation of the UPS before and during the *Mariner* Mars 1969 encounter period attests to the significant advancement made towards providing "computer reliable" power to the SFOF. The installation of the UPS was completed at the SFOF in April 1969. During extensive acceptance tests made in April and May, the UPS exceeded all requirements outlined in the bid specifications.

The UPS is composed of rectifiers, inverters, and batteries. The utility power is connected through the UPS to the critical loads to maintain constant and disturbance free power. Four 480-V, 3-phase, 60-Hz rectifier units produce 405 Vdc and are connected to a 2,000-A bus. Current from the bus feeds through four dc-to-ac inverter units to the critical load. An impedance inserter is installed on the output of each inverter to clear the circuit in case of a fault in the inverter. Two banks of batteries are connected to the 2,000-A bus parallel with the rectifier output. One battery bank consists of 184 Gould FT 15 cells with 804-A capacity on an 8-h basis. The other bank consists of 184 C&D LCU 27 cells with 1940-A capacity at an 8-h rate.

To determine the UPS acceptability with respect to the specifications and manufacturer design parameters,

Table 1. UPS test results: input requirements

Parameter	Specifications	Test results
Harmonic	15% current distortion	5% circuit $1B_3$, carrying 520 A
Voltage	460 V, 3-phase, 4W ±10%	System performed satisfactorily when varied from 420 to 508 V
Frequency	57–63 Hz	System performed satisfactorily when varied from 56 to 63 Hz
Current in-rush	25 to 100% of full-rated load over 15 s	In-rush on 2 rectifiers = 300 A; full load on 2 rectifiers = 1208 A; UPS returns to rated load in 15 s
Total system efficiency	80% with supply at 0.8 pF; load at 0.8 pF lagging	91% at 750 kV-A, 08-pF load; 67% at 200 kV-A, 09-pF load

Table 2. UPS test results: output (steady-state)

Parameter	Specifications	Test results
Voltage (steady-state)	120/208 Vac ±2%, 3-phase, 4 wire, adjustable ±5%	With stepped load increases 0–150–300–468–480 kW, voltage changed from 215 to 212 V; negligible under steady-state; adjusts to 190-224 V
Frequency	Continuously adjustable 57–63 Hz ±0.5% stability; when operating free-running, oscillator shall hold inverter output frequency to ±0.5% for both steady-state and transient conditions; total frequency deviation, including short-time fluctuations and drift, shall not exceed ±0.5% from rated frequency during 24-h period	±1/10 Hz or 0.16%
Harmonic content	Maximum 5% rms	2.09% at 750 kV-A, 0.8-pF load
	Maximum 3% single harmonic	1.55% at 750 kV-A, 0.8-pF load
Unbalanced load	Inverter output voltage shall not differ between phases by more than 3% or line-to-neutral voltage by more than 5% with unbalanced phase to neutral kV-A loads of 15%; frequency stability shall not be adversely affected under this condition	Phase to phase, 2%; phase to N, 2.8%; loads per phases A,B,C, respectively: 250, 250, 287 kV-A
Phase displacement	Phase displacement of inverter output voltage shall be maintained at 120 ±5 electrical deg with unbalanced phase to neutral kV-A loads of 15%	2 deg with unbalance, as noted above

simulated and real tests were performed during installation and initial operation. The results of the tests are delineated in Tables 1–3.

Several voltage dips from commercially supplied power have been recorded. Table 4 lists these occurrences and the effects.

The UPS meets or exceeds all specifications, as shown by the documented tests, performance during malfunctions, and voltage dips. The stability and accuracy of this trouble-free power system will reduce the number of critical power failures and provide confident mission support.

c. Standby power. The standby power plant is in the process of completion. The engine-generators are in place. The power control center has been delivered. Installation of ancillary items and connections to the major equipment are now in process. The basic major construction is scheduled for completion in January 1970.

d. Central supervisory monitor and control system. Installation of the central supervisory and monitoring system is complete except for the connections of alarm points in the standby power plant. Completion of the basic unit is scheduled for December 1969.

Table 3. UPS test results: output (transient)

Transient cause	Maximum deviation at rated voltage, $\pm\%$ [a]	Test results
187.5-kV-A load steps to 750-kV-A total load	8	Maximum 5.3%
Loss of ac input power or excursions of input power in excess of system tolerances (750-kV-A load)	5	Negligible
Return of ac input power (750-kV-A load)	5	Negligible
Dropping one power converter off output power line by switching (750-kV-A load)	8	Maximum 3%
Bringing one power converter onto output power line by switching (750-kV-A load)	8	Maximum 3%
Dropping one power converter off output power line as a result of an internal fault, e.g., silicon-controlled rectifier or diode short (500-kV-A load)	8	Maximum 4.5%

[a]The UPS shall regulate voltage transients for the output load changes and switching actions to the limits indicated when all four modules are on the line.

Table 4. Voltage transients induced by commercial power

Voltage dip, V	Time	Cause	Remarks
30-40 (dips and spikes)	5-11-69 (all day)	Weather conditions	No equipment loss or adverse effects noted as had previously been reported under similar conditions
130	5-14-69 (08:21)	Boom of construction crane touched 66-kV transmission line, reflecting transient into commercial power	Systems on UPS power not affected
80	5-14-69 (10:40)	Transient from MacNeil Substation	Systems on UPS power not affected